JAERI-Review
94-005

JAERI TIARA ANNUAL REPORT
1993 (VOL. 3)
April 1993-March 1994

November 1994

Advanced Radiation Technology Center

日本原子力研究所
Japan Atomic Energy Research Institute

本レポートは，日本原子力研究所が不定期に公刊している研究報告書です。
入手の問合わせは，日本原子力研究所技術情報部情報資料課（〒319-11 茨城県那珂郡東海村）あて，お申し越しください。なお，このほかに財団法人原子力弘済会資料センター（〒319-11 茨城県那珂郡東海村日本原子力研究所内）で複写による実費頒布をおこなっております。

This report is issued irregularly.
Inquiries about availability of the reports should be addressed to Information Division, Department of Technical Information, Japan Atomic Energy Research Institute, Tokai-mura, Naka-gun, Ibaraki-ken 319-11, Japan.

編集兼発行　日本原子力研究所
印　　刷　いばらき印刷㈱

JAERI-Review 94-005

JAERI TIARA Annual Report
1993 (Vol.3)
April 1993 - March 1994

Advanced Radiation Technology Center

Takasaki Radiation Chemistry Research Establishment
Japan Atomic Energy Research Institute
Watanuki-cho, Takasaki-shi, Gunma-ken

(Received October 7, 1994)

This annual report describes research activities which have been performed with the JAERI TIARA (Takasaki Ion Accelerators for Advanced Radiation Application) facilities from April 1, 1993 to March 31, 1994.

Summary reports of 80 papers and breaf descriptions on status of TIARA in the period are contained. A list of publications, the type of research collaborations and organization of TIARA are also given as appendices.

Keywords: JAERI TIARA, Ion Accelerators, Solid State Physics, Radiation Effects in Materials, Materials for Space, Semiconductors, Organic Materials, Inorganic Materials, Nuclear Fusion Reactor, Functional Materials, Radiation Chemistry, Radiation Biology, Nuclear Medicine, Biotechnology, Radioisotope Production, Nuclear Chemistry, Accelerator Shielding, Materials Analysis, Accelerator Technology, Safety Control

---

Editors: Isao Ishigaki, Ryuichi Tanaka, Tadao Seguchi, Isamu Nashiyama, Hiroshi Naramoto, Hideki Omichi, Akio Toraishi, Hiromasa Watanabe, Hiroshi Watanabe, Tsuneo Sasuga

原研イオン照射研究施設（ＴＩＡＲＡ）平成５年度年次報告

日本原子力研究所高崎研究所
放射線高度利用センター

（1994年10月７日受理）

本年次報告は、原研イオン照射研究施設で、1993年４月１日から1994年３月31日までの間に行われた研究活動の概要をまとめたものである。

１）宇宙用半導体、２）バイオテクノロジー、３）放射線化学、４）有機材料、５）無機材料、６）材料解析、７）核化学およびラジオアイソトープ製造、８）加速器の遮蔽、９）加速器技術の９部門にわたる80編の研究報告に加えて、施設の運転・利用状況、公表された文献、企業・大学等との研究協力関係、研究開発・施設運営組織を収録する。

高崎研究所：〒370－12　群馬県高崎市綿貫町1233

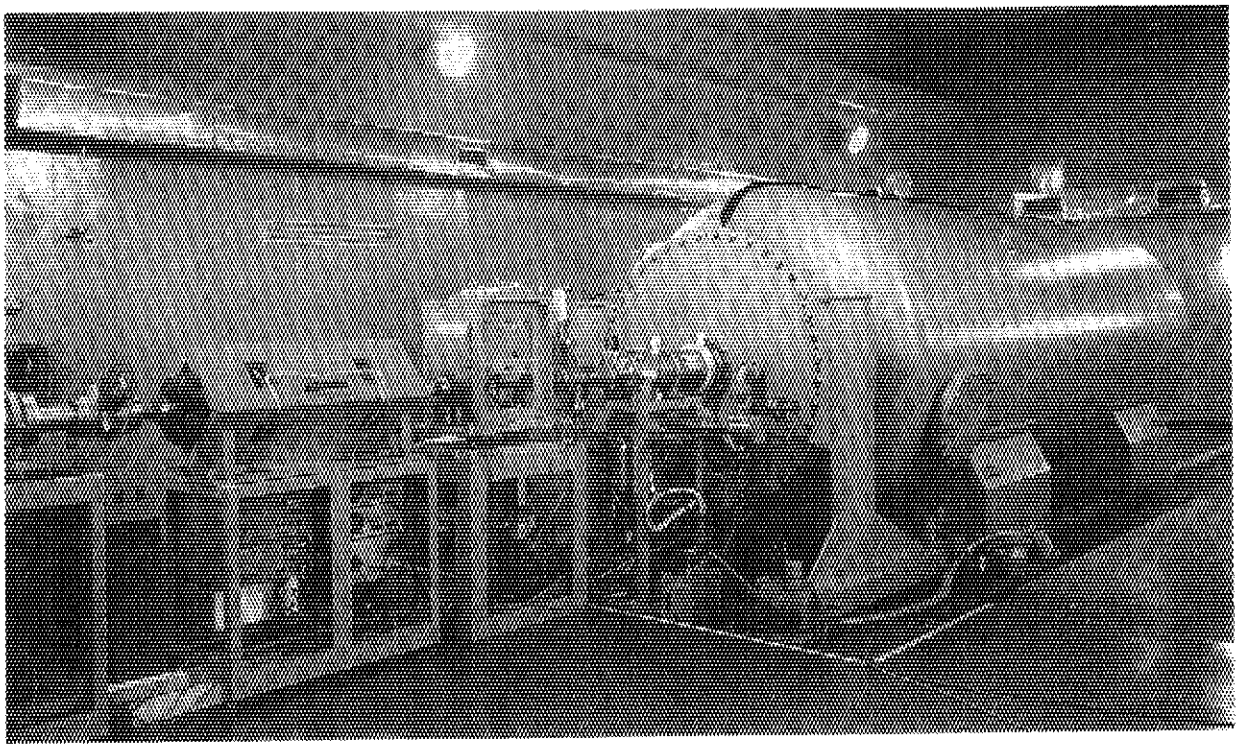

3MV Single-ended Accelerator

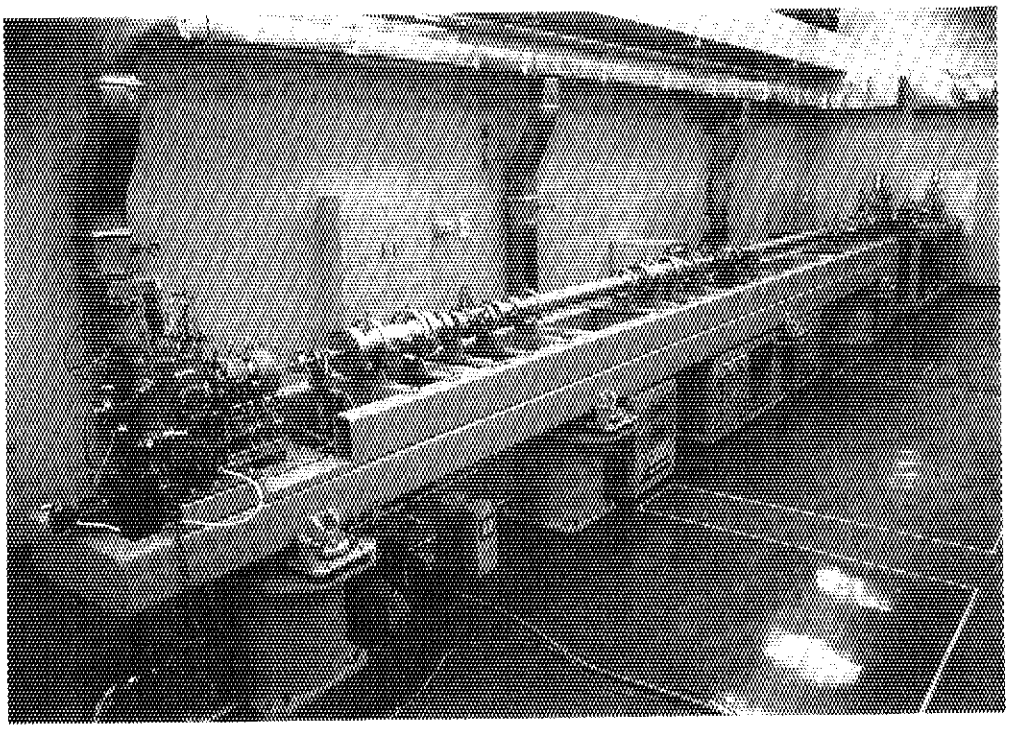

Submicron Microbeam Line (Target Room 3)

PREFACE

This report covers research and development activities which have been conducted with TIARA (Takasaki Ion Accelerators for Advanced Radiation Application) during the period from April 1993 until March 1994, and also gives an outline of the operation and utilization of TIARA in the same period.

The AVF cyclotron and the 3MV tandem accelerator have been operated satisfactorily through the period, though the latter was stopped from January to October 1993 because of the construction of a new beam line connected to a newly constructed target room. Other two accelerators, i.e. the 3MV sigle-ended accelerator and the 400kV ion implanter were installed and they started serving to research activities from January 1994.

The Third TIARA Research Review Meeting was held on June 28 and 29 1994 at Takasaki, the subjects were reported in this issue. 29 oral and 44 poster papers, and two invited lectures were presented; 253 persons including 124 from outside of JAERI participated the meeting: In contrast with the first and the second meetings, munerous results of TIARA utilization were presented, suggesting the TIARA is now becoming a fruitfull facility. We owe this to advices of the Consultative Committee for the Research and Development of Advanced Radiation Technology, the Consultative Committee for the JAERI/Universities Collaborative Project Research Program, the TIARA General Program Committee, and their subcommittees.

I sincerely hope the utilization of TIARA will be more prosperous and successful in coming years.

Isao Ishigaki
Director
Department of Advanced Radiation Technology,
Takasaki Radiation Chemistry Research Establishment

Contents

1. Semiconductors for Space

1.1 DEVELOPMENT OF ENERGETIC HEAVY-ION IRRADIATION METHOD FOR SINGLE-EVENT TESTING

Isamu NASHIYAMA, Yousuke MORITA, Toshio HIRAO,
Hisayoshi ITOH, and Masahito YOSHIKAWA
Department of Materials Development, JAERI

I. INTRODUCTION

Modern artificial satellites are equipped with sophisticated electronic circuits, where various kind of highly integrated semiconductor devices are used for the control of the satellites and for realizing their scientific and commercial missions such as satellite communication, broadcasting, survey of the earth surface. The most serious problem which these semiconductor devices suffer is the effects of strong nuclear radiation in space. Most of semiconductor devices have been developed for very mild environments on the surface of the earth, and these devices especially highly integrated circuits, are quite sensitive to nuclear radiations. Since the beginning of the outer space age and the finding of van Allen radiation belts surrounding the earth, intense efforts have been made on developing radiation hard semiconductor devices, which involves series of irradiation testing, study of radiation effects on semiconductors, and R&D of new device process. For these purposes, some artificial radiation sources and suitable irradiation techniques are required. Energetic heavy ions with high energy purity, homogeneity, and low back-ground are especially required for the testing of single-event effects.

In the present work, we have developed several irradiation techniques for radiation hardness testing of semiconductor devices.

II. SCATTERED BEAM IRRADIATION

Experimental set up of the scattered beam irradiation method was illustrated in references 1 and 2. Heavy ions with the energies of a few hundred MeV from TIARA AVF cyclotron accelerator are scattered forward with a thin (~1μm) gold foil and scattered ions are irradiated on test devices placed at angles of 20 to 40 degrees. Using this method, we can conveniently decrease the beam intensity and provide homogeneous ion beams.

Advantages of the scattered-beam irradiation method are, 1) beam intensity can be reduced by a several order of magnitude to a level convenient for SEU testing, 2) homogeneous irradiation fluence within the chip area of the device under test, 3) accurate evaluation of the fluence. Figure 1 (a) shows 175MeV argon beam incidence on an 1μm Au foil and scattered into 40 degree with an energy of 145MeV, where 40 MeV recoil Au atoms hit the specimen as well as the scattered argon ions. By applying a 12.5μm thick Kapton absorber in front of the device under test, the recoiled Au peak disappears, and the scattered argon ions degrade their energy in the absorber as shown in FIg. 1(b).

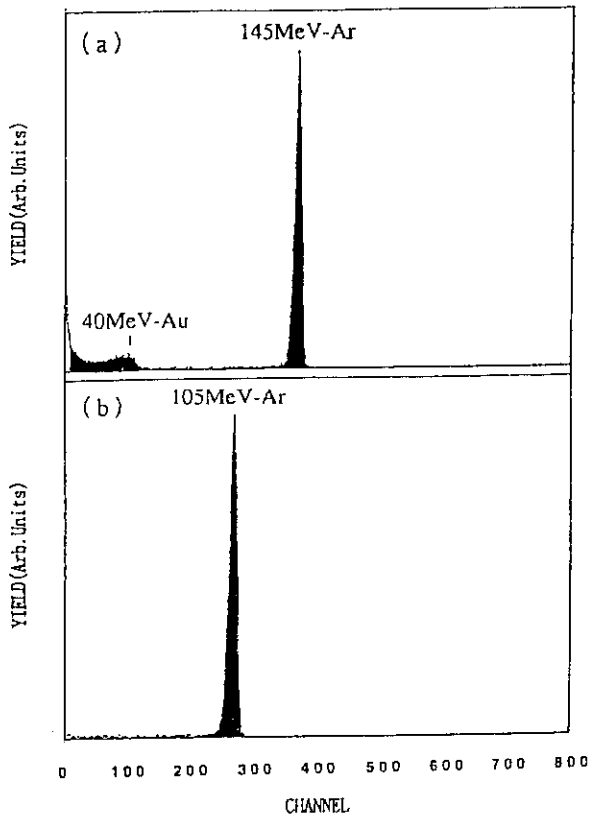

Fig.1 Energy spectra of scattered argon ions with and without Kapton absorber. The incident argon ion energy is 175MeV.

III. DIRECT BEAM IRRADIATION

In the case of very high energy heavy-ions of E/M > 10 MeV/amu, a strong nuclear reaction occurs between incident ions and the Au scatterer. Therefore, we can not apply the scattered-beam irradiation method based on Rutherford scattering principle. In this case, A direct-beam irradiation method is applied instead, where the beam intensity is reduced by a beam attenuator, and the beam is defocused in order to obtain uniformity of irradiation fluence. Direct and scattered beam spectra are shown for 330MeV argon ion beam incidence in Fig.2. A sharp energy profile is obtained in the case of direct-beam irradiation.

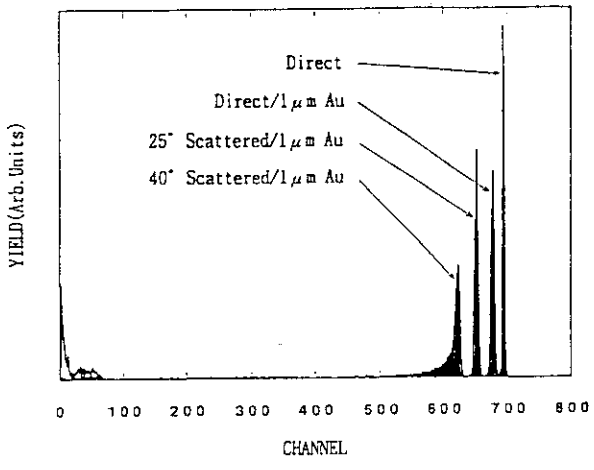

Fig.2 Energy spectra of direct and scattered argon ions. Incident ion energy is 330MeV.

IV. RECOIL PARTICLE IRRADIATION

Since TIARA AVF AVF cyclotron can not accelerate metal ions at present., LETs from 20 to 30 MeV/(mg/cm^2) are not available for single-event testing. Therefore, we developed the recoil atom irradiation method. For this purposes, very high energy krypton beams and metal target are used. Figure 3 shows a typical example of this method, where 520MeV krypton ions are guided into a 5μm nickel target and we can obtain 300MeV nickel ions into the recoil angle of 20 degree as shown in Fig.3(b). The 450MeV krypton ions scattered with 1μm thick gold foil into 20 degree is shown in Fig.3(a) for comparison. Disadvantages of this method are poor energy purity, low fluence rate, and higher background.

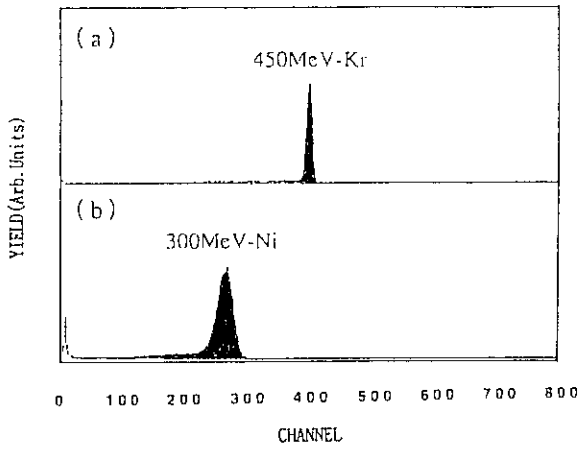

Fig.3 Energy Spectra of the recoil nickel atoms and the scattered krypton ions.

REFERENCES

1) H.Itoh, T.Hirao, Y.Morita, I.Nashiyama, TIARA Annual Report, 1 (1992) 97.
2) I.Nashiyama, Y.Morita, T.Hirao, H.Itoh, M.Yoshikawa, TIARA Annual Report, 2 (1993) 3.

1.2. STUDY OF ION-BEAM INDUCED LUMINESCENCE IN ALUMINA AND SILICON CARBIDE

Hisayoshi ITOH, Toshio HIRAO, and Isamu NASHIYAMA
Department of Materials Development, JAERI

I. INTRODUCTION

The impingement of high-energy ions on semiconductors generates dense electron-hole pairs along ion tracks. It is well known that the recombination of excited electron-hole pairs induces photon emission (luminescence) in semiconductors and insulators. The study of the relaxation processes accompanied with luminescence gives us the information about the density and lifetime of electron-hole pairs induced by irradiation. The knowledge of defects in irradiated materials is also obtained from the analysis of luminescence data. In addition, the clarification of electronic excitation and relaxation occurred in semiconductors by ion irradiation is essential to understand the fundamental processes of single-event phenomena, since electron-hole pairs cause the single-event phenomena such as soft-error, latch up, and burn-out in semiconductor devices.[1,2]

We have studied ion-beam induced luminescence in alumina by 175MeV-Ar^{8+} ions accelerated by the AVF cyclotron. Also, we have investigated luminescence induced in silicon carbide (SiC) semiconductor by the irradiation. In this paper, we show the results of ion-beam induced luminescences in alumina and SiC, and discuss the recombination processes of electron-hole pairs in those samples.

II. EXPERIMENTAL PROCEDURES

Samples used were single crystalline SiC with 0.03mm thickness and sintered alumina with the thickness of 1mm. The SiC samples with zinc blende structure were grown epitaxially on Si substrates at 1400°C by chemical vapor deposition.[3] These samples were mounted on a cryostat holder on a two-axes goniometer installed in a chamber HE1. The temperature of samples was variable in a range between ≈20K and room temperature (RT) by using Iwatani Cryo-Mini D310/CW303. Details of the vacuum chamber HE1 have been described in a previous paper.[4] Ion-beam induced luminescences were obtained by measuring photons emitted from samples during irradiation. The transient intensity of emitted photons was acquired by a streak camera system[5] (Hamamatsu C1587/C3140), which has an detection region of photon wavelength 200-850nm. An energy profile of photons was also obtained by using a monochromator[5] (Jovin Yvon HR250). In the time-resolved optical measurements, the trigger signals of the AVF cyclotron were used to start acquiring data.

III. RESULTS AND DISCUSSION

Figure 1 shows typical luminescence spectra induced in alumina samples at RT by 175MeV-Ar^{8+} irradiation (beam current ≈3nA). Two bands at 430nm and 330nm are clearly seen in the spectra shown in Fig.1(a) and 1(b), respectively. The full width of half maximum of the 430nm band was about 60nm, and that of the 330nm band was approximately 30nm. Similar spectra were observed in photoluminescence[6] and ion-beam excited luminescence[7] of sapphire samples. Lee *et al.*[5] reported 3eV and 3.8eV photoluminescence bands, which were caused by radiative recombinations associated with the F and the F^+ centers in neutron bombarded Al2O3, respectively. Here, the F and the F^+ centers are the neutral oxygen vacancy (V_O^0) and the positively charged V_O (V_O^+), respectively. The photon energies of 330nm (3.8eV) and 430nm (2.9eV) bands observed in our experiments agree well with those emitted from the F^+ and the F centers, respectively. Thus, we can conclude that the 330nm and 430nm bands induced in alumina samples by 175MeV-Ar^{8+} irradiation are ascribed to radiative recombination of excited electron-hole pairs through oxygen vacancies. A time-resolved intensity of the 330nm band during the ion irradiation is shown in Fig.2.

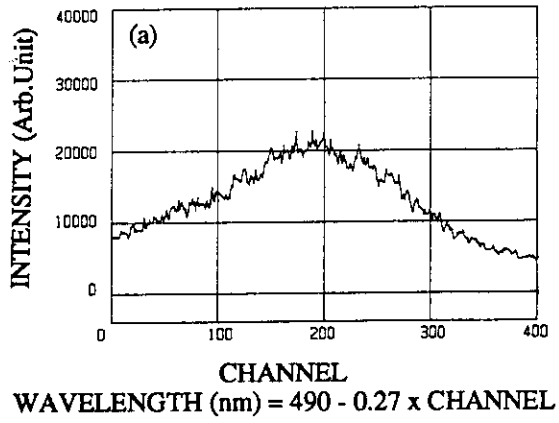

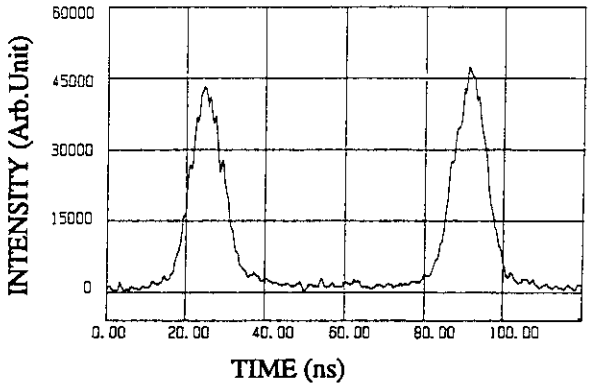

Fig.2 Time-resolved luminescence-signal induced in alumina by Ar ion irradiation.

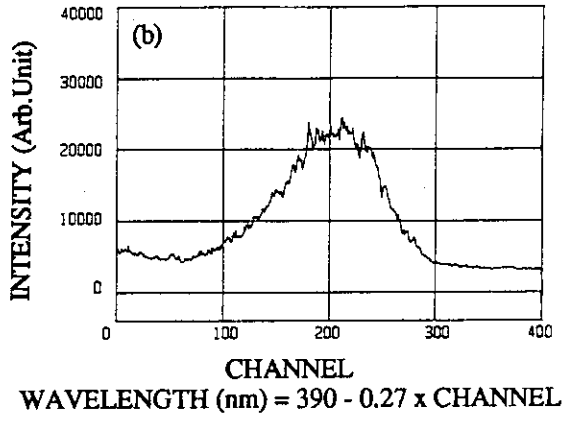

Fig.1 Ion-beam induced luminescence spectra for alumina. The observed wavelength region: (a)490-380nm, (b)390-280nm

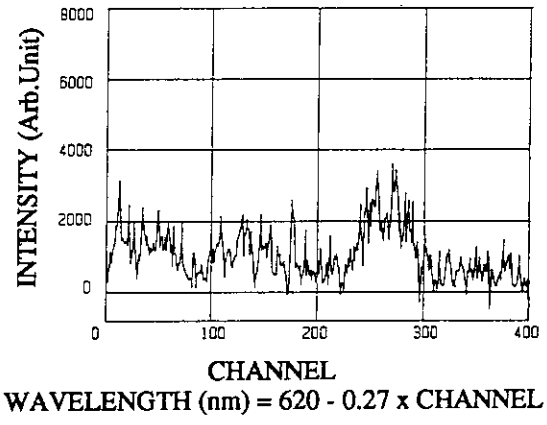

Fig.3 Ion-beam induced luminescence spectrum for SiC.

The interval of the obtained signals was estimated to be 66ns, which is in good agreement with that of 175MeV-Ar^{8+} pulses from the AVF cyclotron. In addition, the pulse width of the observed signals was 9ns, which is very close to the width of the Ar ion-beam pulses. Taking account of the time resolution of our measurements, the lifetime of electron-hole pairs excited in alumina samples by Ar ions is estimated to be shorter than 1ns.

Figure 3 shows a luminescence spectrum observed in SiC samples at 30K by 175MeV-Ar^{8+} irradiation (beam current ≈30nA). In this spectrum, a weak band was observed at 550nm. No significant photon emission due to ion irradiation was observed for Si samples. Thus, the observed band is thought to be emitted from only SiC whereas 175MeV-Ar ions (the mean ion depth ≈45μm in SiC) penetrate to the Si substrate under a thin SiC layer. The photon energy of this band is approximately 2.3eV, which corresponds to the band gap of SiC (2.4eV at 4K). This result suggests that the 2.3eV luminescence is caused by the electron-hole recombination between the conduction band and the valence band. Phonons are probably incorporated in the recombination process from the fact that SiC has an indirect energy-band structure. Further investigations are needed to clarify the emission processes of photons in SiC. It was also found that the intensity of the 550nm band decreased with the fluence of Ar ions. This result can be explained by the generation of non-radiative recombination channels in SiC by the irradiation.

IV. SUMMARY

We have performed wavelength- and time-resolved optical measurements of luminescences induced in sintered alumina and SiC semiconductor by 175MeV-Ar^{8+} irradiation. Two luminescence bands were observed at 330nm and 430nm in the wavelength-resolved spectra for alumina samples. The photon energies of the 330nm and 430nm bands agree well with those of luminescences[6,7] accompanied with the F^+ (V_O^+) and the F (V_O^0) centers in sapphire, respectively. Thus, it can be concluded that these bands arise from the electron-hole recombination associated with oxygen vacancies. We obtained the time-resolved signals of the ion-beam induced luminescence (330nm emission) for alumina samples. The shape of the time-resolved signals suggests that the lifetime of electron-hole pairs excited in alumina by ion irradiation is shorter than 1ns. A luminescence band at 550nm was first observed in the ion-beam induced luminescence in SiC. This result can be accounted for by the recombination between electrons in the conduction band and holes in the valence band in SiC.

REFERENCES

1) E.L.Petersen, in the Text of Tutorial Short Course in IEEE 1983 Nuclear and Space Radiation Effects Conference, held on July 17, 1983, in Gatlinburg, TN, USA.
2) J.C.Pickel, in the Text of Tutorial Short Course in IEEE 1983 Nuclear and Space Radiation Effects Conference, held on July 17, 1983, in Gatlinburg, TN, USA.
3) S.Yoshida, K.Endo, E.Sakuma, S.Misawa, H.Okumura, H.Daimon, E.Muneyama, and M.Yamanaka, Mat. Res. Symp. Proc. 97 (1987) 259.
4) H.Itoh, T.Hirao, Y.Morita, I.Nashiyama, TIARA Annual Report, 1 (1992) 97.
5) H.Itoh, T.Hirao, I.Nashiyama, TIARA Annual Report, 2 (1992) 134.
6) K.H.Lee and J.H.Crawford,Jr. Phys. Rev. B19 (1979) 3217.
7) A.Al.Ghamdi and P.D.Tawnsend, Nucl. Inst. & Methods Phys. Res. B46 (1990) 133.

1.3 AN EVALUATION OF THE SINGLE EVENT UPSET EFFECT BY HEAVY ION ON SRAM FOR SPACE APPLICATION

Ichiro NAITO*, Takashi TAMURA*, Sumio MATSUDA*,
Isamu NASHIYAMA**, Toshio HIRAO**,Hisayoshi ITOH**
*National Space Development Agency of Japan,
**Department of Materials Development,JAERI

I.Introduction

In space application, probability of upsets are important to determine the reliability of the system. In order to predict event rates for SEU in space based on experimental measurement, it is at least necessary to measure both saturated cross-section and LET threshold. These two parameters are measured with ion beam perpendicular to the chip of the device under test and are used directly as the experimental upset cross-section and LET threshold parameters.

Space radiation particles trapped by the Earth's magnetic fields have seriously effects on artificial satellites. These radiation belts, Van Allen belts have double structured fields surrounding the Earth. The inner zone of the Van Allen belts has altitude of 2,000-5,000km on the equator and the outer zone extends over 10,000-20,000km.

In addition to the trapped radiation, the galactic cosmic rays and solar radiation induced by solar activity can also have effects on artificial satellites.

The satellites in low earth orbit (400km - 900km) and in geostationary orbit (about 36,000km) are exposed to electrons, protons and heavy ions. In case of memory devices, single event upset induced with heavy ions have very serious effects on satellites.

II. Sample and irradiation method

(1)Samples

The samples used for the test are 256Kbits SRAM and 64Kbits SRAM those are qualified by NASDA for space usage. Table 1 shows the specification of test samples.

(2) Irradiation Method

The "scattered ion beam" is used in order to get uniform fluence at a sample. Fig.2 shows the concept of this test system.SSD is used for counting particles Au is used as scattering material. The particle energy is measured by pulse height analyzer (PHA) which is connected to the SSD through pre-amplifier. Further, polyimide film is placed in front of the sample in order to absorb the scattered Au particles. Scattering angle is 30 degree both for the test device and SSD. Using this scattered ion beam, three samples could be tested simultaneously. On the other hand the ion beam is directly irradiated to a test device in case of the energy purity of the beam is important.

III. Measurement results

(1) Beam Spectra

The normalized beam spectra are shown in Fig.3. In this figure, some of the scattered beam spectra are broad. As shown in Fig.1, the upset cross-section in the low LET region changes radically, LET spectrum must be sharp. However, by inserting the polyimide film, the beam spectrum becomes broad. From this reason, in case of measuring the saturated cross-section the scattered ion beam is used and in case of measuring LET threshold direct irradiated ion beam is used.

(3) Upset Cross Section

Fig.3 shows the upset cross section versus LET. From these figures LET threshold and saturated cross-section are obtained. These values are listed in Table2. Applying these value to CREME CODE, upset rates of the devices in the space environment are predicted. Table 2 also shows the results of this calculation.

IV. Conclusion

LET threshold and upset cross-section are obtained for 256K bits SRAM and 64Kbits SRAM. Their upset rates in space environment are predicted.

We plan to evaluate another devices such as DRAM, FPGA, Flash Memory in order to investigate the possibility of usage of these devices in space.

Reference

1) Adams, Jr. and James H., NRL Memorandum Report 5901 (1987).

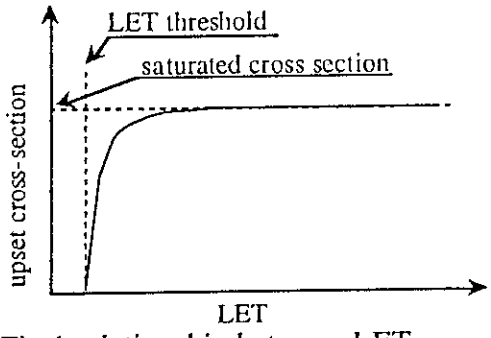

Fig.1 relationship between LET and upset cross section

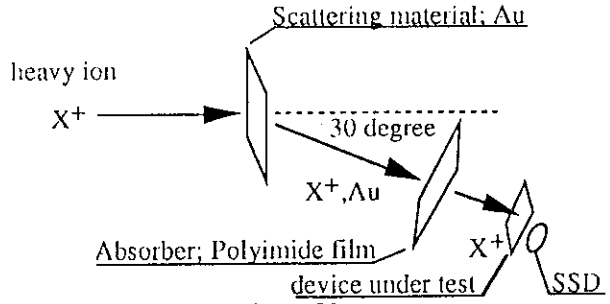

Fig.2 Schematics of beam scatter and absorption of Au

Table 1 Specification of test sample

Devices	64K bits SRAM	256K bits SRAM
Part Number	NASDA 38510/92001XBD	NASDA 38510/92001XBD
Technology	CMOS	CMOS
Words	8,192	65,536
Bits	8 bits	4 bits
Access Time	200ns (Max)	45ns (Max)
Package	28 pin 600 mil Ceramic Dip	24 pin 400 mil Ceramic Dip

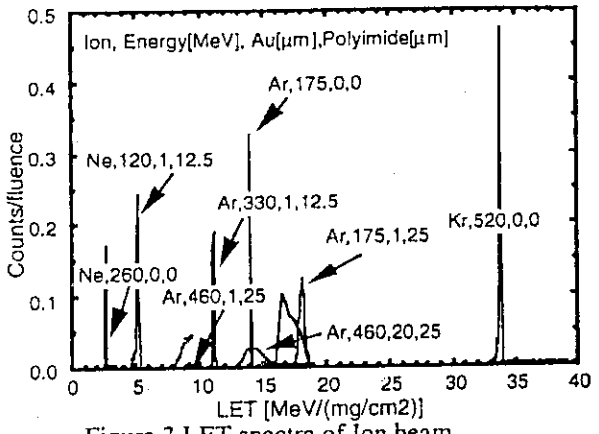

Figure.3 LET spectra of Ion beam

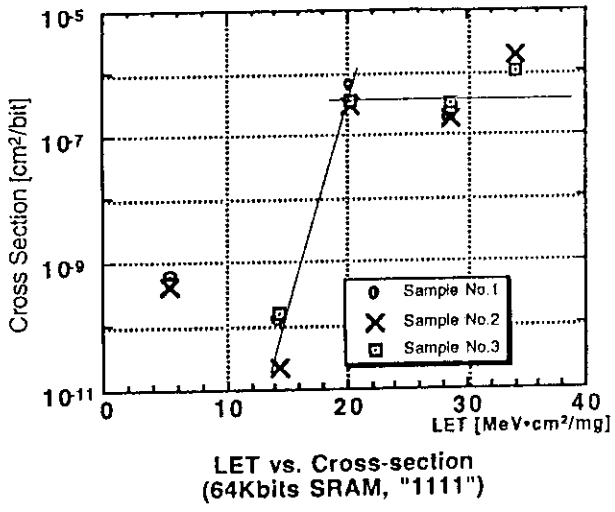

LET vs. Cross-section (64Kbits SRAM, "1111")

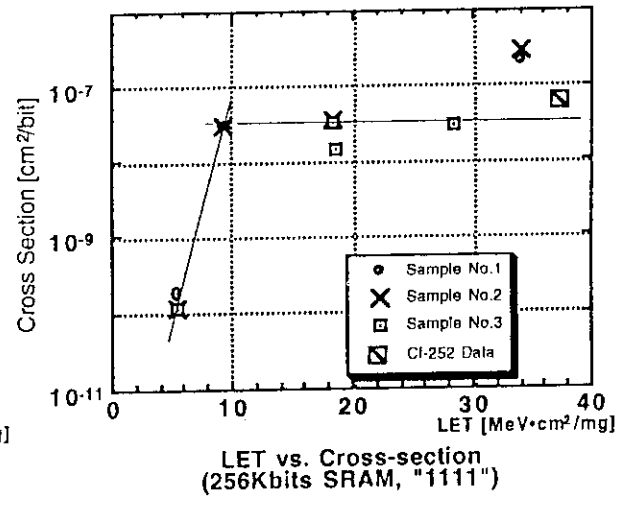

LET vs. Cross-section (256Kbits SRAM, "1111")

Table.2 Results

	LET threshold [MeV/(mg/cm^2)]	cross-section [cm^2]	Event rate [upsets/(bit day)]		
			LEO1*1	LEO2*2	Geostational Orbit
256Kbits SRAM	6.4	3.2e-8	8.61e-8	1.70e-7	7.58e-7
64Kbits SRAM	17	3.9e-7	7.09e-9	1.33e-8	8.47e-8

*1:Hight 400km,inclination 28.8deg, *2:Hight 500km inclination 51.6deg

1.4 EFFECT OF RADIATION DAMAGE ON SINGLE-EVENT TRANSIENT CURRENT MEASUREMENT.

Toshio HIRAO, Toshiji NISIJIMA*, Tomihiro KAMIYA,
and Isamu NASHIYAMA
Department of Materials Development, JAERI
*Electrotechnical Laboratory

1. INTRODUCTION

Single-event upset (SEU) is triggered when an amount of electric charges induced by energetic ion incidence exceeds a value known as a critical charge in a very short time period.

Therefore, accurate evaluation of electric charges and understanding of basic mechanisms of SEU are necessary for the improvement of SEU tolerance of electronic devices.

Several attempts have been made for the direct measurements of extremely fast transient currents induced by single ion strikes on a p/n junction, and charge collection mechanisms such as drift, funneling, and diffusion effects have been studied. [1,2,3,4]

Last year, we reported in the TIARA Research Review Meeting that measurements of transient currents were made in success for 6 MeV helium and 15MeV heavy-ion incidence on a p/n SEU diode at various bias voltages. We have obtained detailed information about the charge collection[5, 6].

2. EFFECTS OF RADIATION DAMAGE

It is found in the previous work[6] that collected charge increases with increasing the bias voltage and LET. We compared experimental values with theoretical values of collected charges as shown Figure 1, where the theoretical values are calculated using screened McLean-Oldham's (Mc. & O) model[7,8]. Mc.&O.model are reproduces the experimental values fairly well for the He-ion incidence. For heavy ions, however, experimental values do not show such strong bias voltage dependence as the Mc. & O. model prediction. We consider that this discrepancy is due to the effect of radiation damage.

In our experiments, Transient currents were measured using the 40GHz wide-band sampling oscilloscope (Textronix model CSA803) which requires at least 512 trigger events to produce a complete wave form. Therefore, we consider that radiation damage is introduce during measurements.

Figure 2 shows how the wave form of the transient current changes with the repetition number of the measurement for 15MeV Fe-ion irradiation.The peak height of the transient current decreases with increasing radiation damage. The whole shape of wave form, however, does not change much by irradiation. In the case of 6 MeV helium incidence, we did not observe significant radiation damage.

3. RADIATION DAMAGE CONSTANT

In order to evaluate the effects of radiation damage, we assume that the amount of the collected charges is proportional to the minority carrier mobility (μ) and that the degradation of the mobility is expressed by the equation, $\mu^{-1}=\mu_0{}^{-1}+ K\mu\phi$, where $K\mu$ is mobility damage constant and ϕ is the fluency of the incident ion beam. Then we obtain the relation, $(Q/Q_0)^{-1} = 1 + Kn\ N$, between normalized collected charge Q/Q_0 and the repetition number of measurements N. Reciprocals of normalized collected charges are plotted in Figure 3 as a function of the repetition number of the measurements for 15MeV C-, O-, and Fe-ions irradiation.

As is expected, experimental values lie in straight lines and we can obtain the damage constant Kn from the slope of the lines by the least square fit to the experimental values. Obtained values of Kn are normalized by the value for 6 MeV helium ion irradiation and tabulated in Table 1. Relative values of theoretical damage constants are also tabulated, which correspond to the values of dpa (displacement per atom) calculated by assuming Coulomb potential and Kinchin-Pease damage model. The agreement between the experimental and theoretical damage constants is excellent. This indicates that the decrease in the collected charge is

due to the degradation in minority carrier mobility and that we can theoretically evaluate the effect of radiation damage introduced during the measurements.

4. SUMMARY.

We found that irradiation effects on the total collected charges can be explained by the introduction of displacement atoms calculated using Coulomb potential and Kinchin-Pease model. In order to avoid the radiation damage, a single-ion hit technique seems necessary for SEU experiments.

The authors would like to acknowledge Mr. Tajima who spent many long hours operating the accelerator for us.

REFERENCES

1) C.M.Hesieh et al., IEEE Electron Dev. Lett. EDL-2(1981)103
2) F.B.McLean et al., IEEE Trans.Nucl. Sci.Vol.NS-29, No.6(1982)2028
3) R.S.Wagner et al., IEEE Trans.Nucl. Sci. Vol.NS-34, No.6(1987)1240
4) R.S.Wagner, et al., IEEE Trans. Nucl. Sci. Vol.NS-35, No.6(1988)1578
5) Toshio Hirao et al.TIARA annual Report.Vol.1(1992)100
6) Toshio Hirao et al.TIARA annual Report.Vol.2(1993)9
7) T.R.Oldham et al., IEEE Trans.Nucl. Sci.Vol.NS-33, No.6(1986)1646
8) C.Hu et al., IEEE Electron Dev.Lett. EDL-3, No.2(1982)31

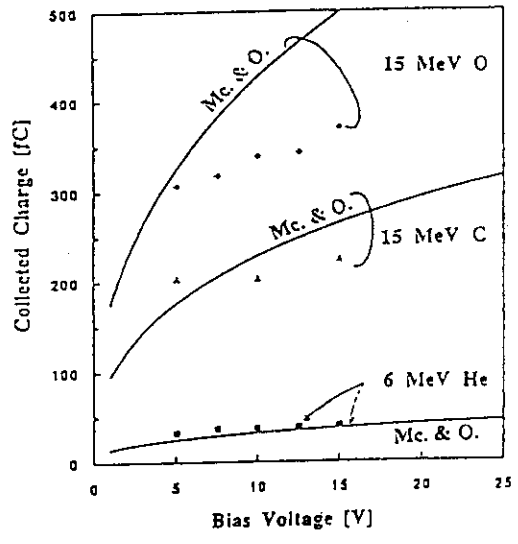

Fig. 1 Relation between collected charge and bias voltage. Solid lines are calculated using screened McLean and Oldham's model mechanism of SEU.

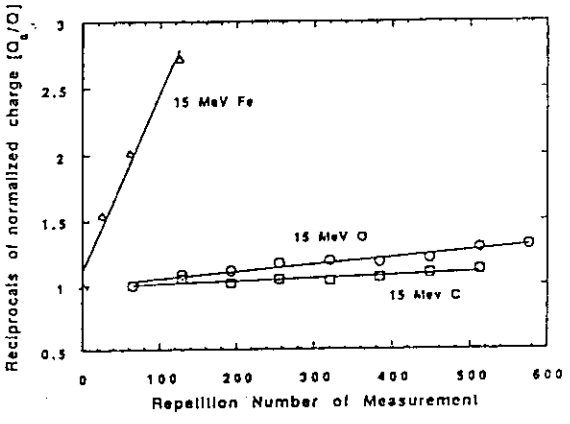

Fig.3 Analysis of radiation damage effects. Reciprocals of the normalized charge show linear dependence on repetition number of measurement.

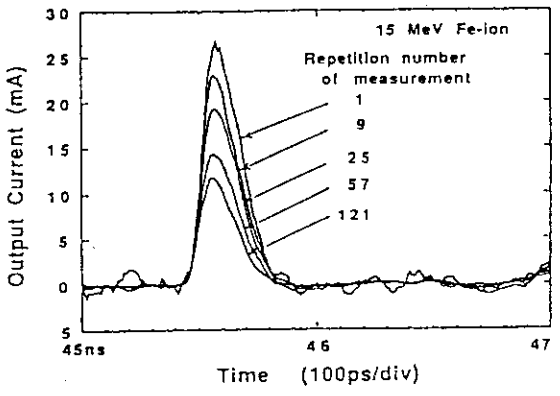

Fig.2 Effect of radiation damage on the current transients for a p/n junction diode with $2x10^{16}cm^{-3}$ substrate doping level.

Table 1 Relative radiation damage constants for collected charges. Experimental and theoretical values are compared.

Ion Type (Energy)	Damage Constant	Relative Value	Theoretical values
Alpha (6 MeV)	1.7×10^{-5}	1	1
Carbon (15MeV)	2.2×10^{-4}	12.7	12.2
Oxygen (15MeV)	5.4×10^{-4}	31.4	29.2
Iron (15MeV)	1.67×10^{-2}	977	1076

1.5 Proton Irradiation Effects of Amorphous Silicon Solar Cell for Solar Power Satellite

Y. Morita, S. Sasaki[1], A. Ushirokawa[2]
Dep. of Materials Development,JAERI, Institute of Space and Astronautical Science(ISAS)[1], Tokyo Engineering Univ.[2]

Introduction

The plan of the Solar Power Satellite named SPS 2000[1)] is made as a conceptual design for a 10 MWatt scale satellite at ISAS. It aims to demonstrate the feasibility of the SPS as an energy system in terms of whether it will resolve the problems of the global environment and energy. For the SPS 2000, amorphous silicon(a-Si) solar cell, a thin film type developed for ground use, is selected as a potential candidate for its power generator, because of convenience of transportation from ground, and assembly in space.

Amorphous-Si solar cells have not used before in space, owing to their photodegradation, and low conversion efficiency compared with those of the crystalline cells. However, as a high conversion efficiency over 10% was achieved in recent development of the a-Si solar cells, the studies of radiation resistance of the a-Si solar cells comes to be reported for the purpose of using in space[2)].

In this report, the radiation resistance of a-Si solar cells, which is very important problem in the realization of SPS 2000 plan, was studied by a simultaneous irradiation of 10 MeV proton beam and light of a solar simulator.

Experimental

Fig. 1 shows a schematic diagram of the simultaneous irradiation system for the a-Si and the c-Si cells. Incident angles of proton beam and light beam(1 solar in Air mass 0) of the solar simulator to the solar cell samples were a right and 40.5 degree, respectively. The irradiation of proton(10 MeV) to the solar cells was carried out by scanning the 1cmϕ spot beam (~80nA) in the area of 10x10 cm^2.

The electric output power (Pmax=(IxV)max) of the solar cells was measured by the instrument of I-V measurement system, which is connected to the solar cell samples. Fig. 2 shows the schematic diagram of the cross section of a flexible a-Si solar cell(size: 113x120x0.25mm^3, Sanyo Elec. Co., Ltd.) used in this test. The a-Si cell was deposited on poly-ethylene-terephthalate(PET) film (0.05mm thick) by chemical vapor deposition (CVD) method. A thickness of p-i-n junction of the cell is as very thin as ca. 1μm. Crystalline silicon (c-Si) solar cell(size: 20x20x0.1mm^3, Sharp Co., Ltd.) was used as references for the a-Si solar cell.

Results and Discussion

Fig. 3 shows the relative retentions of Pmax of the a-Si and the c-Si solar cells, which were irradiated simultaneously by 10 MeV proton and light from the solar simulator. Although the number of the test cells are limited, the results indicate that the a-Si cells have a higher radiation resistance by 180 times than the single crystalline cells. One of the reasons for the higher resistance could come from extremely thin structure of the a-Si cell layer.

The equivalent damage fluence during 1 year for SPS 2000 on the 1100 km equatorial orbit is estimated as 2.1x10^{10}protons/cm^2 at 10 MeV, which is calculated for crystalline Si solar cell referring to the Solar Cell Radiation Handbook by NASA JPL[3)]. The a-Si solar cell tested are degraded typically by 5-10% with the fluence of 2x10^{13}proton/cm^2 at 10MeV, which corresponds to the total fluence for the SPS 2000 during over 100 years. But, if the c-Si solar

cell is adopted for the SPS, the fluence($7x10^{10}$ protons/cm^2) at 5-10% degradation of the Pmax in c-Si cell corresponds to the total fluence for the SPS 2000 during 3.5 years. However, as high energy protons pass through the thin a-Si cell, it is necessary for the a-Si cell to be tested by irradiations of lower energy protons, which are stopped in the p-i-n junction of the cell.

Fig. 4 shows the recovery of Pmax of the irradiated a-Si cells after storing them at ambient temperature. Pmax of the a-Si cells irradiated by proton recovered rapidly immediate after the irradiation, and gradually to its initial value in the term of 40 days. In the same irradiation and storing conditions, Pmax of c-Si cell samples do not recover at all. In c-Si solar cell, degradation of its electrical property by the irradiation is caused by formation of the various defects in silicon crystalline. The most of these defects are not annealed at ambient temperature region. On the other hand, degradation of a-Si solar cell is caused by formation of Si dangling bonds which are generated by breaking Si-Si and Si-H bonds in a-Si by electronic interaction between proton and a-Si. As these dangling bonds react with hydrogen migrated in a-Si, and generated by the irradiation of PET[4], it is considered that the degradation of the Pmax in the irradiated a-Si solar cells recover rapidly at ambient temperature.

Conclusion

The effects of the high energy proton(10 MeV) irradiation on the a-Si solar cells which are the potential candidate for SPS 2000 have been investigated by the method of the simultaneous irradiation of proton beam and light from the solar simulator. It has been found that the a-Si solar cell has a higher radiation resistance than the c-Si cell. And, the electric property of the a-Si cell recovered rapidly immediate after irradiation at ambient temperature. From these results, the irradiation effects of the a-Si cell are completely different from those of the c-Si cell.

For SPS 2000, it is concluded that the a-Si solar cells are quite promising for SPS use if the conversion efficiency and a photodegradation is improved as is now expected.

References

1)M.Nagatomo and K.Ito; 2nd International Symposium SPS 91, Paris, 1991.
2)J.J.Hanak et al., Report of 19th IEEE Photovoltaic Specialists Conference,1987.
3)H.Y.Tada et al., Solar Cell Radiation Handbook Third Edition, NASA JPL, California, USA, 1982.
4)T.Sito et al., JAERI-M 89-096 ('89)

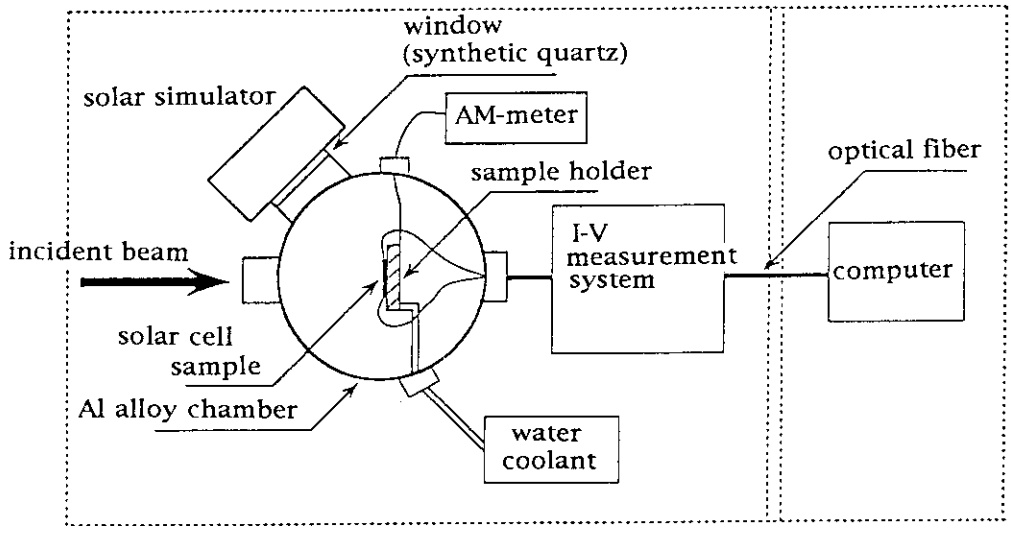

Fig. 1 Schematic drawing of proton irradiation system

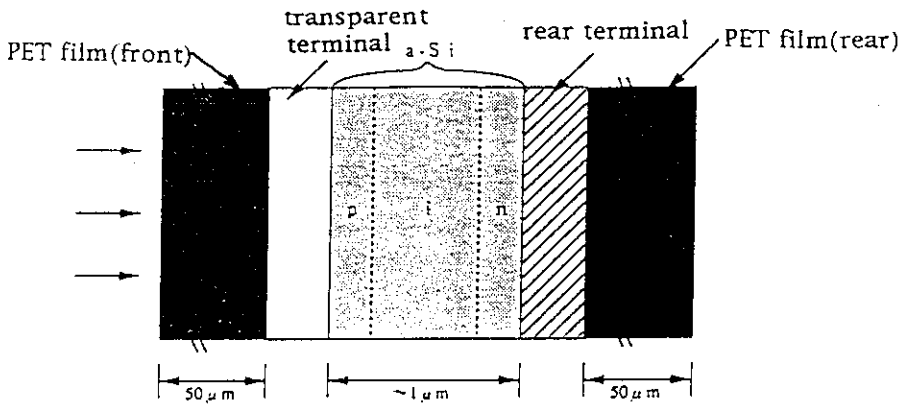

Fig. 2 Schematic drawing of cross section of flexible a-Si solar cell

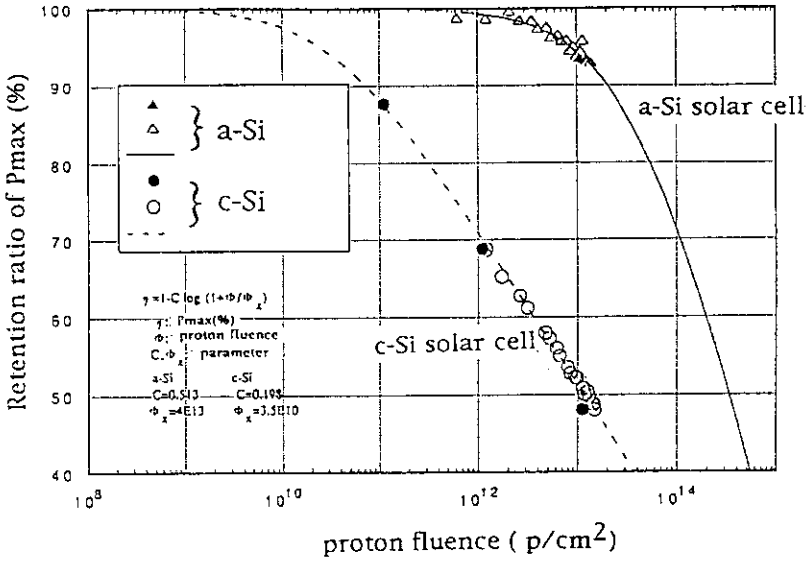

Fig. 3 Change in Pmax of solar cell irradiated by 10 MeV proton
proton; 10 MeV, 20~160 nA. Pmax at 28°C

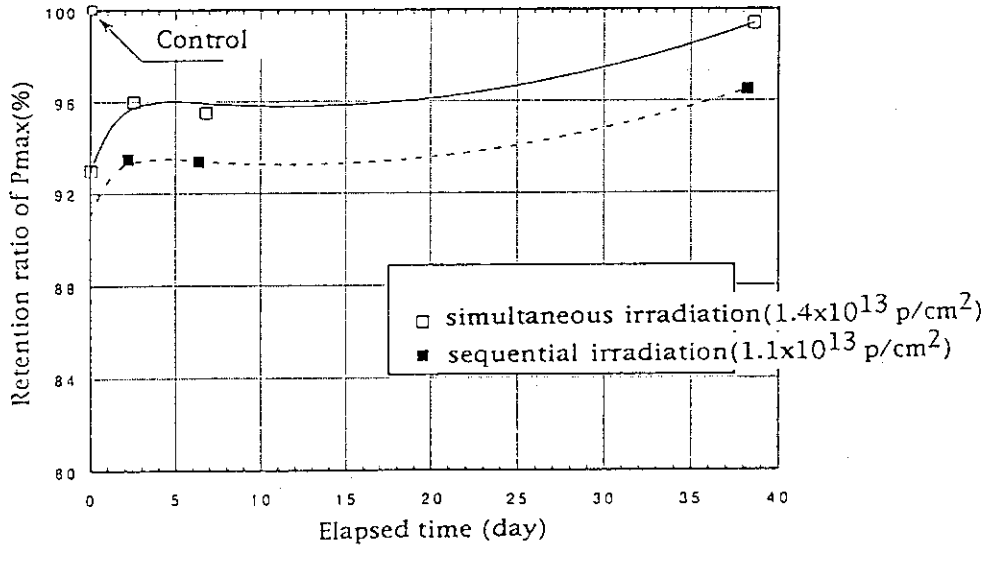

Fig. 4 Time dependence of Pmax of irradiated a-Si solar cell
stored at ambient temperature.
proton; 10 MeV, 60~160 nA, Pmax at 28°C

1.6 Radiation Effects of Solar Cells for Space Use

Sumio MATSUDA*, Yasunari YAMAMOTO*, Osamu KAWASAKI*
Yousuke MORITA**, Isamu NASHIYAMA**
*National Space Development Agency of Japan (NASDA)
**Department of Materials Development, JAERI

I. Introduction

Solar cells on the satellites are important for supplying electric power to the satellite systems. Electrical performance of solar cells degrade with time because of radiation in the space environment. Degradation of electrical performance depends on the kind of radiation, its energy and fluence. When we use solar cells in space, it is important to know their resistance to irradiation.

Engineering Test Satellite-V (ETS-V) was launched on 27 August 1987 and put into geostationary orbit. ETS-V was equipped with the Solar Cell Monitor (SCM). SCM is composed of 24 solar cells and measures radiation effects on various solar cells in the space. These cells differ in cell thickness, cell structure, epitaxial layer growth method, cover glass thickness and cell material (Gallium Arsenide and Silicon) to investigate the radiation effects on these properties.

Fig. 1 shows the degradation data for three different types of solar cells, Gallium Arsenide (GaAs) cell made by Liquid Phase Epitaxy (LPE) method, Silicon with a Back Surface Field and Reflector structure (Si BSFR) 200μm cell and Si BSFR 50μm cell. The vertical axis indicates the percentage of the normalized short circuit current (Isc), which is also called remaining factor (RF) of Isc. The RF doesn't start from 100% because of degradation of the solar cells by radiation belts on the transfer orbit.

This data shows significant degradation due to solar flares from August to October in 1989.

We performed tests to investigate radiation effects on solar cells.

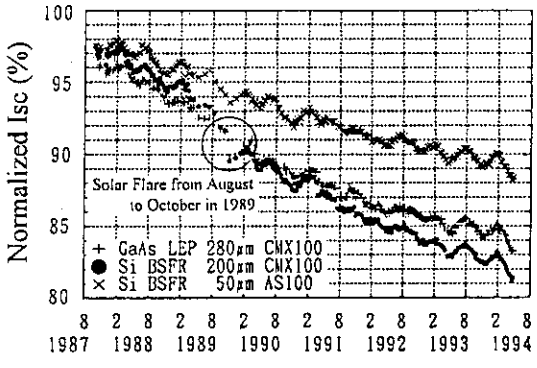

Fig. 1 Flight data of three solar cells in SCM

II. Sample and Irradiation Method

The samples are Si BSFR and GaAs solar cells. The Si BSFR solar cell is 2cm × 2cm × 100μm. The GaAs solar cell is 2cm × 2cm × 200μm. Neither cells have cover glasses.

The irradiation method is describe below. We adjusted the shape of a proton beam to about 1cm diameter and scanned the beam in the region of 10cm × 10cm. Solar cells are fixed to a 10cm × 10cm aluminum board with double-sided adhesive tape. Using this method, 6 to 12 cells can be irradiated simultaneously.

We measured beam charge in order to determine ion fluence, which is evaluated by

subtracting the secondary electron charge from the measured beam charge. The secondary electron charge is about 10% of the total charge.

Ⅲ. Test Results

Fig. 2 and Fig. 3 show the 10MeV proton fluence dependence of normalized electrical performance about Si and GaAs solar cells. Electrical performance parameters are Isc, Voc (open circuit voltage) and Pmax (maximum power). Electrical performance degrades with increase in proton fluence. Normalized electrical performance can be expressed by eq.(1)[1].

$$\eta = 1\text{-}C \times \log(1+\phi/\phi x) \quad (1)$$

η :normalized electrical performance, ϕ :fluence, C, ϕx:fitting parameters

Table 1 shows the fitting parameters (C, ϕx) derived from an approximation of the least square of eq.(1). Here, ϕx indicates the threshold of degradation of electrical performances, and C indicates the gradient of the fitting curve.

Fig. 4 shows the difference of Isc degradation behaviors in Si and GaAs solar cells between 1MeV electron irradiation and 10MeV proton.

We can find that GaAs and Si solar cells suffer similar degradation when irradiated by electrons, but GaAs solar cells suffer less degradation than Si when irradiated by protons.

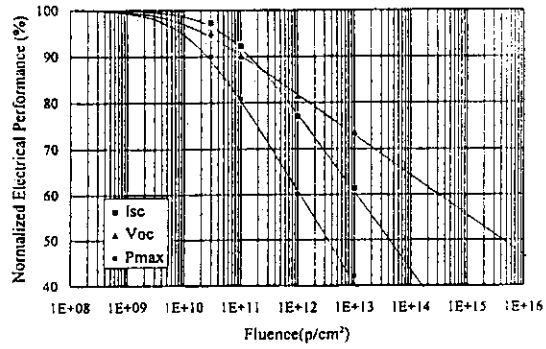

Fig. 2 Degradation of Si solar cell by 10MeV proton irradiation

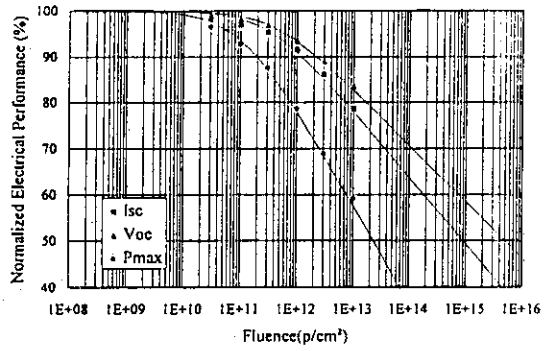

Fig. 3 Degradation of GaAs solar cell by 10MeV proton irradiation

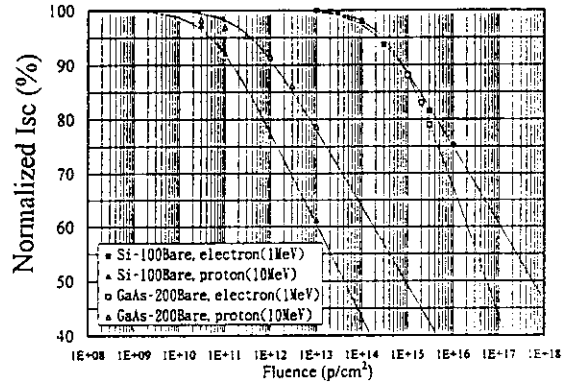

Fig. 4 Degradation of solar cells by electron and proton irradiation

Table 1 Fitting parameter of eq.(1) in irradiation of 10MeV proton

	Si-100 Bare		GaAs-200 Bare	
	C	ϕx	C	ϕx
Short circuit current (Isc)	1.72E-01	5.13E+10	1.44E-01	3.04E+11
Open circuit voltage (Voc)	8.76E-02	8.30E+09	1.22E-01	3.93E+11
Maximum power (Pmax)	2.05E-01	1.24E+10	2.11E-01	9.91E+10

This phenomenon is expected to relate with cell structure, and we will investigate continuously.

We shall confine our attention to the dependence of Isc on solar cell thickness. Fig. 5 shows the normalized Isc of Si solar cells. Thin solar cells (Si-50) suffer less degradation than thick (Si-200) solar cells at low fluence. At high fluence, however, thin solar cells suffer more degradation than thick solar cells.

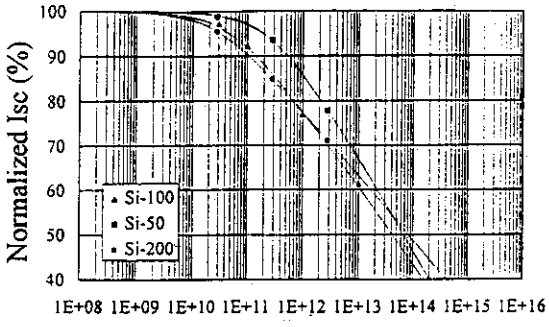

Fig. 5 Effects of thickness of Si solar cells on their degradation by 10MeV proton

We performed 20MeV proton irradiation tests to investigate the dependence of degradation on proton energy. Fig. 6 and Fig. 7 show the dependence of degradation of Si-100 and GaAs-200 by 10 and 20MeV proton at the same fluence. We found that degradation of electrical performance decreases with increasing proton energy in Si solar cells, though

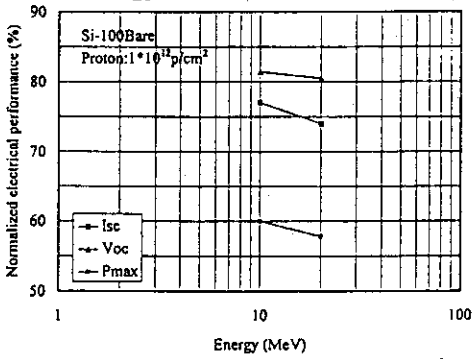

Fig. 6 Effects of proton energy on the degradation of Si solar cell

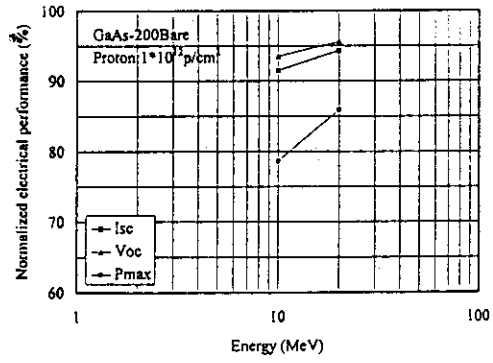

Fig.7 Effects of proton energy on the degradation of GaAs solar cell

degradation increases with increasing proton energy in GaAs solar cells. NASA previously performed similar tests on Si solar cells with different results. However, we tested relatively in narrow range of proton energy, so we will perform more tests over a wide range of energy.

IV. Conclusion

Fitting parameters of Si and GaAs solar cells were obtained by the irradiation of 10MeV proton. GaAs solar cells were more resistant to proton radiation than Si solar cells. Si solar cell degradation depends on cell thickness.

Further, we plan to obtain degradation dependence of Si and GaAs solar cells on proton energy.

Acknowledgment

We would like to thank Mr. T. Nakao and Mr. Y. Wakow of A.E.S for their useful advice.

Reference

1) "Solar Cell Radiation Handbook" H.Y. Tada, Carter Jr., B.E. Ansqaugh, and R.G. Downing, JPL Publication, Jet Propulsion Laboratory (1982)

1.7 Charge Distribution in a Small Sensitive Volume due to the Si(p,x) Nuclear Reactions. (II)

Y.Takami, Y.Morita[1], I.Nashiyama[1], T.Tamura[2], M.Uesugi[2]
Institute for Atomic Energy, Rikkyo University, Department of Materials Development, JAERI[1], NASDA[2]

Recoil energy spectra, both experimental and computed, for 40 MeV protons are illustrated in Fig.1. Round circles indicate experimentally measured values, while stepwise solid lines is computed values for whole non-elastic recoil events and smooth solid line is the one for elastic recoil events.

The elastic recoil spectrum was converted, through kinematic calculation, from differential cross sections of elastic scattering obtained by the optical model. The recoiled nuclei spectrum by non-elastic reactions include all energetically allowed reactions, except for elastic reaction. They were computed by the MCEXCITON code[1]. In the computation, energy deposition by emitted light particles is not taken into account. This caused a part of the discrepancy at the high energy region between experiments and computed results. This discrepancy is evident in the energy region above 5 MeV.

Another factor in the high energy region discrepancy is long proton trajectories scattered in a Si detector. The radiation sensitive region of the detector was 10^4 μm and $2x10^4$ μm in thickness. A considerable portion of the scattered protons are likely to travel long paths, which are closely parallel to the detector faces, before leaving the sensitive depleted region of the detector.
Experimental values show a steep increase at the energy region below 1 MeV. On the contrary, computed values by elastic scattering give extremely steep rise of up to 10^8 mb/MeV at the vicinity of 0 MeV. This is attributed to the fact that the so-called "folding" was not made for the computed values regarding the actual energy resolution of Si detectors and the associated electronic system. However, experimental recoil energy spectra agree quite well with the spectra computed by the MCEXITON code. Consequently, the computed nuclear reaction cross section by the code is satisfactory for the prediction of SEU rates.

SEU cross sections of the 93L422 (LTTL, RAM, 256x4 bits, AMD) were experimentally measured in the proton range of 10 to 70 MeV by a cyclotron[2].
Assuming the sensitive volume dimensions to be 39x39x2 μm^3, the energy deposit for emitted alpha particles and protons were computed and shown in Fig.2. In the calculation range-energy relations of Ziegler's data table[2] were used as a main reference.
Deposit energy distributions in the sensitive volume are now computed and known for the protons of 40, 30, 20, 10 MeV. After integrating deposit energy distribution from energy E_c to $E\infty$, one can obtain the relation between critical energy deposit E_c and upset cross section. Fig.3 shows computed upset cross section vs. critical energy deposit E_c, for 40 MeV protons and a sensitive volume of 39x39x2 μm^3. Individual upset cross sections for major nuclear reactions are also illustrated together with the total upset cross sections.
Our computed values of SEU cross sections of 93L422 for 40-, 30-, 20-, and 10-MeV protons are tabulated with Shimano et al.'s cyclotron data[3] in table 1.

References

1. N.Kishida and H.Kadotani, "On the Validity of the Internuclear-Cascade and Evaporation Model for High Energy Proton Induced Reactions", Proc. Int. Conf. on Nuclear Data for Science and Technology, Mito, May 1988, p.1209

2. J.Ziegler, "Stopping Powers and Ranges in All Elemental Matter" Pergamon Press, New York

3. Y.Shimano, T.Goka, S.Kuboyama, K.Kawachi, T.Kanai and Y.Takami, "The Measurement and Prediction of Proton Upset", IEEE, Trans., Nucl., Sci., Vol.36, No.6, p.2344 (1989)

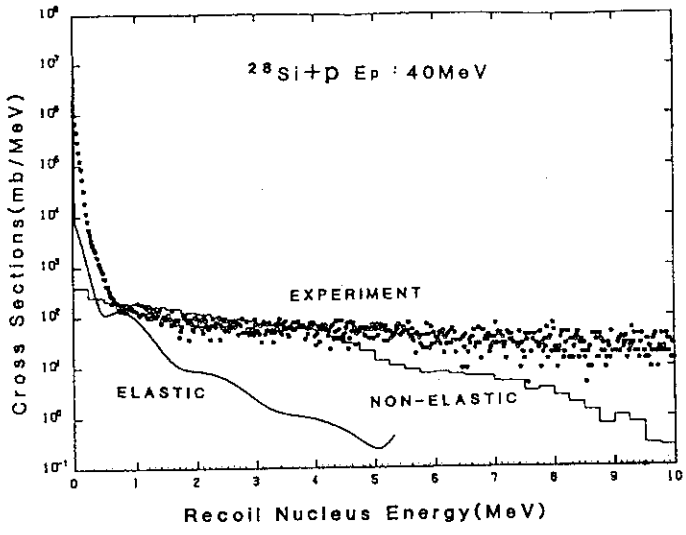

Fig. 1 Recoil energy spectra for 40 MeV protons. Open circles are experimental values; and solid lines, computed values.

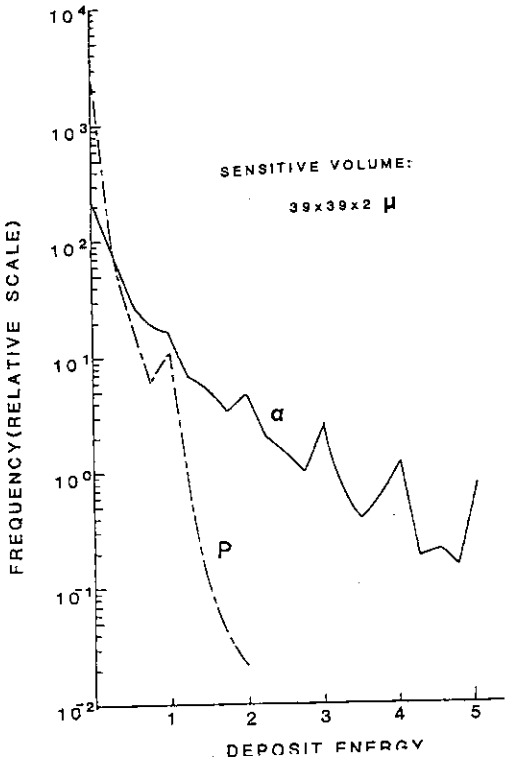

Fig. 2 Deposited energy spectra for emitted alphas and protons by 40 MeV protons in a sensitive volume of 39x39x2 μm^3.

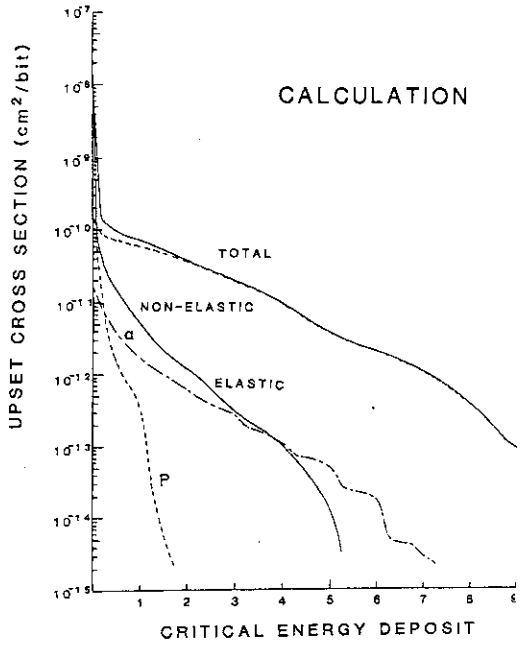

Fig. 3 Computed SEU cross sections vs. critical energy deposit, Ec, for 40 MeV protons and a sensitive volume of 39x39x2 μm^3. Individual cross sections for major nuclear reactions are illustrated together with the total upset cross section.

Table 1 Experimental and computed cross sections in cm^2/bit. For 93L422(LTTL, RAM, 256x4 bit, AMD), assuming 39x39x2 μm^3 sensitive volume.

E_p(MeV)	Experimental values by Shimano et al.[3].	Computed values by our model
40	1.05×10^{-10}	0.77×10^{-10}
30	0.73×10^{-10}	0.80×10^{-10}
20	0.37×10^{-10}	0.69×10^{-10}
10	0.05×10^{-10}	0.12×10^{-10}

1.8 ESR Studies of H^+ Ion Implanted Synthetic Diamond Crystals

J. Isoya, S. Wakoh, M. Matsumoto, and Y. Morita*
University of Library and Information Science,
*Department of Materials Development, JAERI

Introduction

Although relatively large synthetic diamond crystals of high-quality are now available as a result of recent developments in high-pressure synthesis, applications are still limited to those utilizing the unique physical properties such as hardness, high thermal conductivity and optical transparency in wide range. To develop applications to electronic or optic devices, incorporation of new impurities which create useful properties is required. While p-type semiconducting crystals are easily obtainable by incorporating boron, growth of n-type crystals is not established yet. Since incorporation of dispersed impurities at the growth stage is so far limited to only a few elements (N, B, Ni) and since doping by thermal diffusion does not seem possible, ion implantation is interesting as a potential method of introducing new impurities into diamond. Impurities which are implanted may not necessarily be incorporated as isolated impurities. Moreover, lattice damages are created by the irradiation. Microscopic structural analysis of ion-implanted diamond crystals should be helpful for searching conditions to create isolated substitutional impurities by ion-implantation. We use ESR technique to identify the local structure of implanted ions and that of implantation-induced defects. In this paper, we present results of ESR measurements of high energy H^+ ion implanted synthetic diamond crystals.

Experimental

For the H^+-implantation, synthetic diamond crystals were bombarded with H^+ ions (10 MeV, 45 MeV) from an AVF cyclotron (JAERI Takasaki) at room temperature. Diamond crystals are classified into four types, type-Ia, Ib, IIa, and IIb, according to the concentration and the form of nitrogen impurities. Boron-doped crystals belong to type IIb. Various synthetic crystals with various concentrations of impurities (N, B, Ni) were implanted. The ESR measurements were performed on a Bruker ESP300 X-band spectrometer by using an Oxford Instrument ESR-900 to control the sample temperature.

Results and Discussion

After H^+ implantation, several kinds of ESR signals which are likely to be arising from vacancy-related defects (isolated vacancy, vacancy-complex, vacancy-impurity-complex) were observed. It has been found that the kinds of implantation-induced defects are different among the different types of diamond crystals. So far, no ESR signals exhibiting hydrogen hyperfine structure have been found for all the crystals studied. Thus, it is likely that hydrogen implanted exists mostly in a non-paramagnetic form.

The ESR signal of amorphous carbon was not detected. After H^+ implantation, the ESR signal intensities of impurities which had been incorporated at the growth stage changed. However, broadening of the linewidth which should be induced if the lattice was highly disturbed is not noticeable.The fluence dependence ($1\sim7\times10^{15}$ H^+/cm^2) has been studied for 10 MeV H^+implantation. It is noted that the increase of the ESR signal intensities of vacancy-re-

lated defects with the increase of the fluence has a tendency of saturation at higher fluences. In a crystal grown from metal solvent of Ni-2%Ti, with the increase of fluence, the signal intensity of isolated nitrogen decreased and that of interstitial Ni^+ increased (Fig.1). In a type-IIb crystal, the signal intensity of interstitial Ni^+ decreased with the increase of the fluence. These changes in the signal intensity are likely to be caused by the changes in the charge state of the impurities.

The isolated lattice vacancy is the primary defect that is produced upon irradiation with energetic particles. In H^+-implanted type-IIa crystals, the A1 spectrum[1] was dominantly observed at low temperature (Fig. 2) while the R1 spectrum[2] was strongly observed at room temperature (Fig. 3). The A1 center was originally found in electron irradiated type-IIa crystals.[1] In type-IIa crystals, it is likely that the neutral vacancy which is nonparamagnetic is the major radiation damage induced by H^+-implantation as in the case of electron irradiation. The negatively charged vacancy is produced in type-Ib synthetic crystals after 2 MeV electron irradiation.[3] In H^+-implanted type-Ib crystals, negatively charged vacancy was dominantly produced. With lower nitrogen concentration, the A1 spectrum was also observed at low temperature (Fig. 1) while the R1 and R2 spectra[2] were observed at room temperature (Fig. 3). In H^+-implanted type-IIb crystals, the NIRIM-3 spectrum (S=1/2, tetragonal symmetry, $g_{//}$ =2.0009 and $g_{\perp}$ = 2.0022 at 4 K) which was originally found in type-IIb crystals after 2 Mev electron irradiation[4] was strongly observed at low temperature (4 ~20K). Since the NIRIM-3 center dominates in boron-doped crystals after irradiation with high energetic particles, the spectrum might be related to the positively charged vacancy. However, the spin density (0.05) on each of four carbons giving the ^{13}C satellite lines ($A_{//}$ =1.17 mT, and $A_{\perp}$ = 0.75 mT at 4 K) is likely to be too small for the nearest-neighbors of isolated vacancy unless the wavefunction of the unpaired electron is considerably delocalized.[4] Thus, the microscopic identification of the NIRIM-3 center has not yet been established. While the NIRIM-4 center (S=3/2, orthorhombic symmetry, the principal values of the g-tensor: g_1=2.0050, g_2=2.0042, g_3=2.0059, the principal values of the ^{11}B hyperfine tensor: A_1=1.16 mT, A_2=1.52 mT, A_3=0.90 mT) is observed in boron-doped crystals after electron irradiation[4], the A1 center was observed in boron-doped crystals after H^+ implantation (Fig.2).

The amount of the point defects created with 45 MeV H^+-implantation was much lower than that with 10 MeV H^+-implantation.

Acknowledgment

The synthetic diamond crystals used in the present work were grown by Dr. H. Kanda.

References

1) Y. M. Kim and G. D. Watkins, J. Appl. Phys. 42, 722 (1971)

2) E. A. Faulkner, and J. N. Lomer, Phil. Mag. 7, 1995 (1962)

3) J. Isoya, H. Kanda, Y. Uchida, S. C. Lawson, S. Yamasaki, H. Itoh, and Y. Morita, Phys. Rev. B45, 1436 (1992)

4) J. Isoya, H. Kanda, and Y. Morita, in *Proceedings of the Fourth International Conference on the New Diamond Science and Technology, Kobe, 1994* , in press

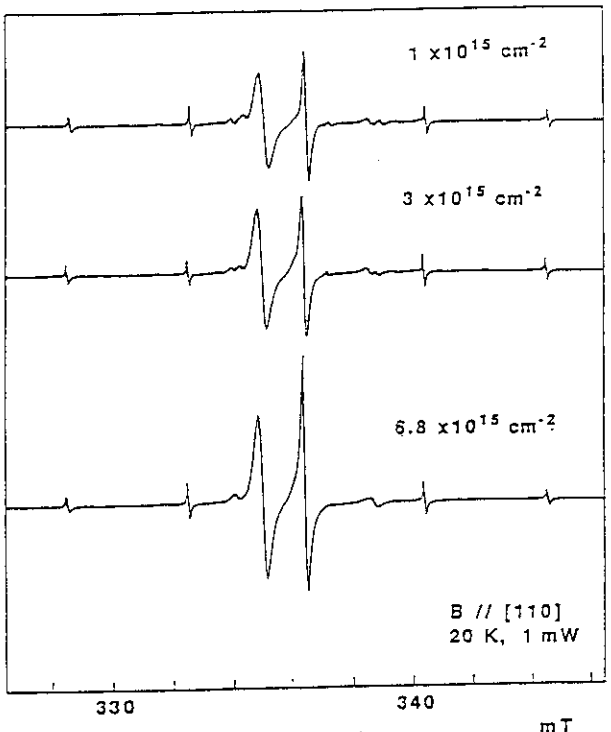

Fig. 1 ESR spectra of H^+-implanted synthetic diamond crystal grown from Ni-2%Ti solvent

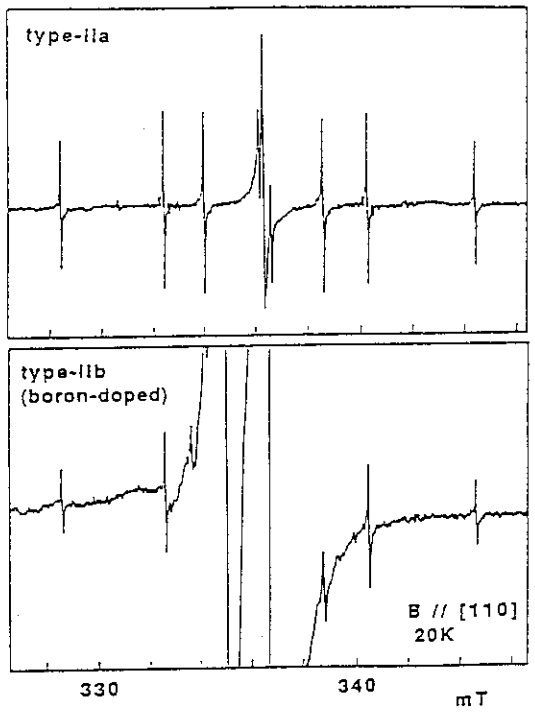

Fig. 2 ESR spectra of H^+-implanted synthetic diamond crystals

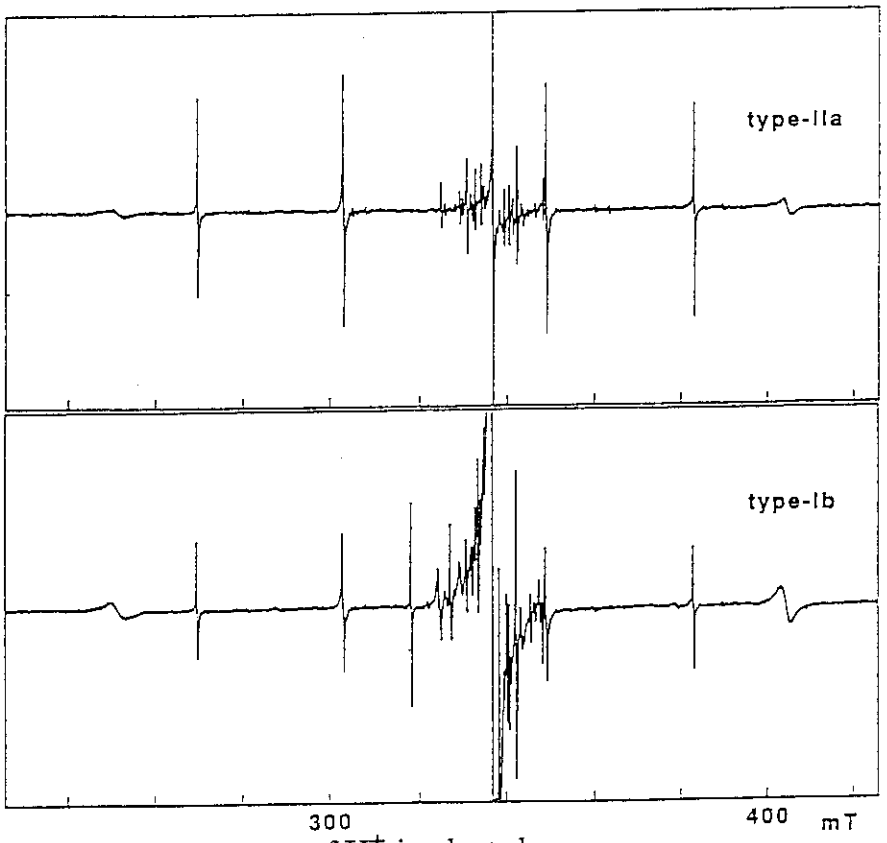

Fig. 3 ESR spectra of H^+-implanted synthetic diamond crystals measured at room temperature

2. Biotechnology

2.1 Ion Beam Apparatus for Biological Samples (III) Penetration Controlled Irradiation Technique

A. Tanaka[1], T. Shimizu[2], M. Kikuchi[1], Y. Kobayashi[1], and H. Watanabe[1]
[1] Department of Radiation Research for Environment and Resources, JAERI
[2] Department of Advanced Radiation Technology, JAERI

(1) Introduction

Irradiation Apparatus for Cell (IAC), which has been connected to a beam line of 3MV tandem accelerator, was made up for ion irradiation of biological samples by controlling the range[1]. Ion beams can be taken out through a kapton film of 7.5μm thickness from vacuum chamber and can reach the target such as biological samples in atmosphere. In this experiment, the range was measured as a function of the distance from beam window using cell lethality and radiochromic dosimeter (RCD) film. From the result, we confirmed that the ion range in a target could be controlled by changing the distance from beam window to a target instead of changing the initial incident energy of ion beams.

(2) Materials and Methods

The ion beams used in this experiment were 6MeV He^{2+} and 18MeV C^{5+}. Two kinds of targets were used for the measurement of the range of ion beams, i.e., RCD film for He ions and aluminum-cell system for He and C ions. RCD film (50μm in thickness), lying perpendicular to ion beams, were irradiated with more than 20kGy, and the depth of blue-colored range was measured using optical microscope. On the other hand, lyophilized cells of *Deinococcus radiodurans* that were monolayered on φ50mm filter were used for aluminum-cell system. As shown in Fig.1, the filter was covered by several pieces of aluminum foils with successively inscribed squares. The aluminum-cell was irradiated perpendicular to ion beams with around 50kGy which is enough dose for cell death if ion beams could reach to monolayered cells through the aluminum foils. Inscribed six pieces of aluminum foils of 3μm thickness were used for He ion irradiation, and eight pieces of foils of 0.8μm thickness were used for C ion irradiation. After 3 day incubation of cells on the filter which was put on TGY agar medium, survivals of cells were measured. Theoretical range of ion beams was calculated by ELOSS code as a constituent of IRAC code system[2].

(3) Results and Discussion

Fig.2 shows the result of the ranges of He ions measured by RCD film. Range of ion beams in film decreased linearly with increasing distance from beam window. Furthermore, each range approximately agrees with calculated value. Whereas, the range in aluminum-cell system also decreased linearly with the distance from beam window,

however, the ranges were about 2~3 μm shorter than calculated ranges (Fig.3 and Fig.4). Fig.5 shows the range converted to biological material using the results of Fig.3 and Fig.4. It can be seen that the range in biological material could be controlled linearly in the range from about 1 μm to 30μm by changing the distance from beam window to the target. However, the difference of range at about 3μm was found between the converted value and the calculated value, even considered the 1μm thickness of cell as shown by slashed line in Fig.5. As shown in Fig.4, cells could survive even after irradiation at 13mm or above distance from beam window where ion beams was expected to penetrate the cells from theoretical calculation. Therefore, some factors such as fluence and LET that affect the cell lethality may affect the difference between experimental result and calculated result.

References

1) M.Kikuchi et al. (1992) JAERI TIARA Annual Report 1:159-162
2) S.Tanaka et al. (1992) JAERI TIARA Annual Report 1: 76-79

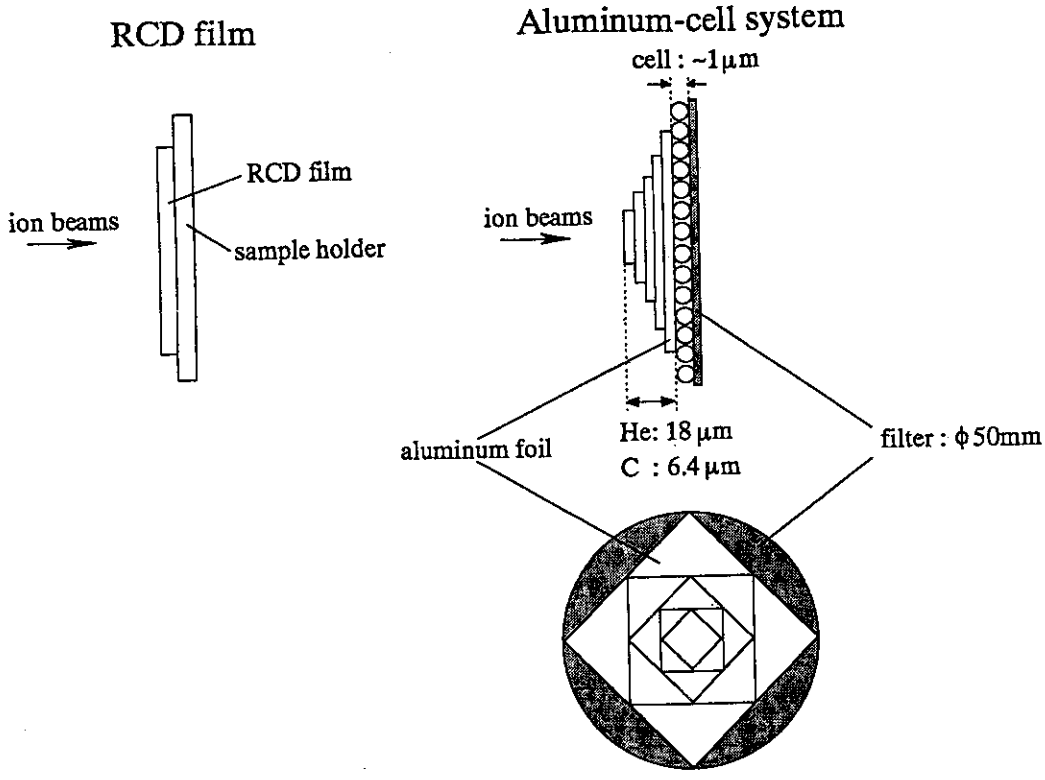

Fig. 1 Scheme of irradiation of RCD film and aluminum-cell system.

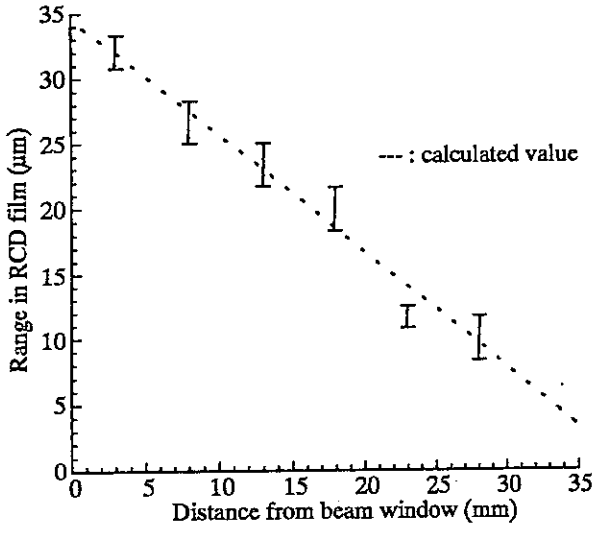

Fig. 2 Range of 6MeV He ion in RCD film at different distance from beam window.

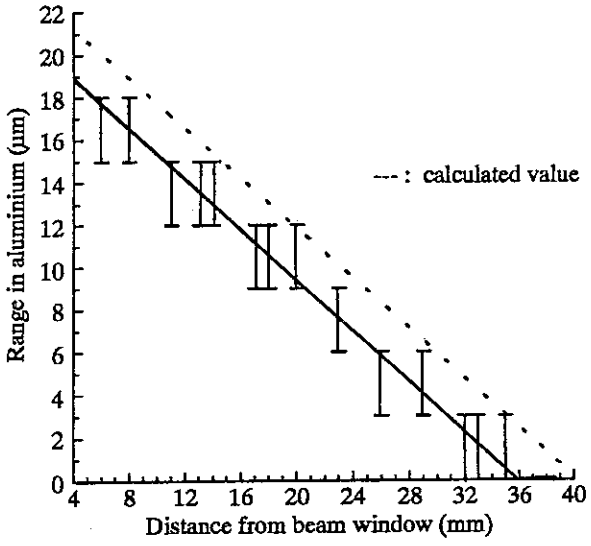

Fig. 3 Range of 18MeV C ion in aluminum by aluminum-cell system.

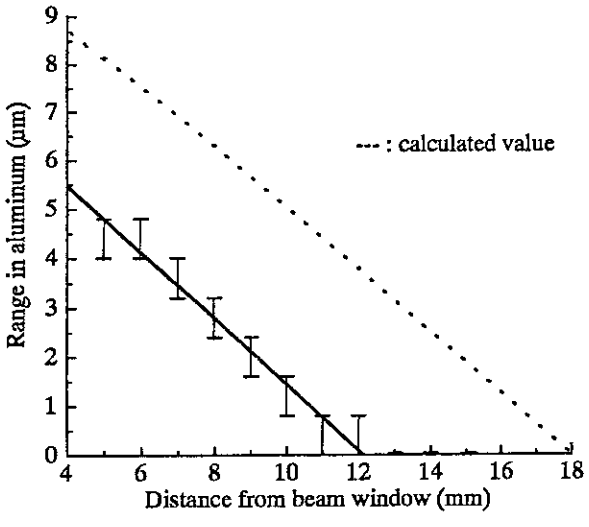

Fig. 4 Range of 6MeV He ion in aluminum by aluminum-cell system.

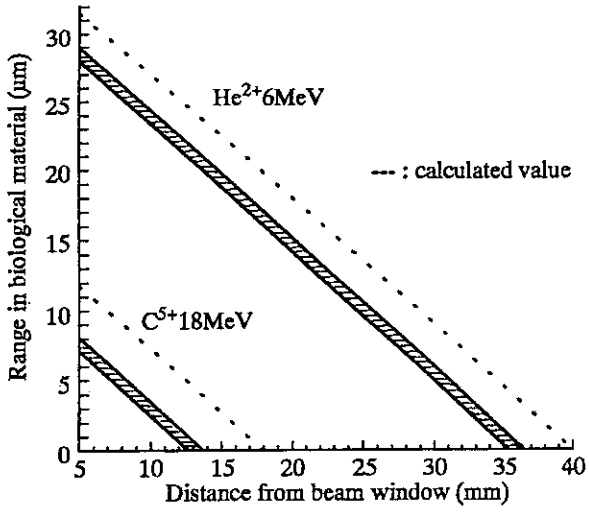

Fig. 5 Converted range in biological material of He and C ion from results of aluminum-cell system.

2.2 Mutations induced by ion beam (C^{5+}) irradiation in barley

I. Kishinami
A. Tanaka, H. Watanabe[2]
Plant Bioeng. Res. Lab. Sapporo Breweries,
JAERI, Takasaki, Biotech. Lab.[2]

Ion beams, which belong to high LET (linear energy transfer) radiations, are considered to be efficient mutagenic agents applicable to mutation breeding of barley plant. The present studies were initiated aiming to obtain mutants with practically useful traits. However, little has been studied the effect of ion beam irradiation on induction of mutation in barley. Therefore, we have examined survival rate after irradiation and have inspected mutation spectrum induced by ion beam (C^{5+}).

Dry seeds of barley (Hordeum vulgare cv Haruna Nijyou) were irradiated with ion beam (C^{5+}) at various doses. While irradiation, embryo side of the seeds were kept facing toward ion beam. Irradiated seeds were sown and grown to maturity in a greenhouse. Survival rate was measured 4 months after sowing. Self-polimated seeds (M_2) were harvested, then next year those seeds were sown in an experimental plot. Mutated barley plants were inspected in M_2 generation, and mutation rate induced by ion beam was calculated. Even as high as 100 krad irradiation, almost all barley seeds were able to germinate. However, they could not grow further. About 1 month after germination, those plants were all died. Therefore survival rate was calculated by the formula, number of plants grown to maturity /number of sown seeds irradiated with ion beam. Table 1 shows that survival rare of barley seeds irradiated at various doses. At 10 krad irradiation, 80% of seeds could germinate and have grown to maturity. At 20 krad irradiation, survival rate markedly decreased to 5%. Above 30 krad irradiation, almost all seeds could not survive. A few M_1 plants were survived at 20 krad irradiation. They were all morphologically distorted and were completely sterile. M_1 plants obtained from irradiation over 5 krad had somewhat clear aberations such as crooked leaves and extraordinal formation of tillers. But no mutation of chlorophyll deficiency was observed in M_1 plants. As fertility of M_1 plants irradiated at 10 krad was over 90%, enough M_2 seeds were able to be obtained from 10 krad irradiated plants. Those M_2 seeds were used for the check of occurrence of mutations in M_2 generation. The germination rate of those seeds was about 98%. Therefore we used barley seeds irradiated at 10 krad for investigate mutation spectrum. Mutations induced by ion beam (C^{5+}) were almost all chlorophyll deficient mutations such as albino, xantha and stripe (Table 2). We could not find any obvious mutants other than chlorophyll deficient mutants. This might be the reason that we did not apply any selection pressure to M_2 plant population. Mutaion rate of the whole chlorophyll deficient mutants was about 2% in M_2 generation.

Thus, mutations induced by ion beam (C^{5+}) in barley were found to be relatively high in M_2 generation. This result suggest that ion beam can be a potent mutagen to induce useful trait in barly. Now, we are going to isolate disease resistant mutants of barly by ion beam.

Table 1. Effect of ion beam (C^{5+}) irradiation on the survival of barley (cv haruna Nijyou)

Dose (Krad)	0	5	10	20	30	50	100
Survival rate (%)	100	94	80	5	1	0	0

Survival rate was measured 4 months after sowing.

Table 2. Frequency of chlorophyll deficient mutants appeared in M_2 generation

Ion beam	Dose (Krad)	Number of M_2 plants	Frequency of chlorophyll deficient mutants
C^{5+}	10	6,000	2.1%

2.3 Effects of Ion Beams on the Germination and Survival Rate in *Arabidopsis thaliana*

A. Tanaka[1], Y. Yokota[2], H. Watanabe[1], N.Shikazono[1] and S. Tano[1]
1) JAERI, Advanced Sci. Res. Center at Takasaki, 2) Beam Operation Co.

(1) Introduction

Ion beams with high LET are thought to have the high relative biological effectiveness (RBE) compared to low LET radiations such as X- or gamma rays, because of concentrated deposition of the energy in biological materials. From the biological standpoint of view, ion beams may have the following characteristic effects: 1) difference in the induced mutation spectrum, 2) difference in the frequencies of the induced mutations, 3) frequency and size of the induced chromosome deficiencies and 4) difference in nature of the DNA strand breaks and their repair mechanisms. However, only a little information is available on plant material[1),2)] until now.

In order to elucidate the biological and genetic effects of ion beams on the plant material, a basic research was conducted by using *Arabidopsis thaliana*. This plant is very convenient for the biological investigations, because it has the following characteristics: 1) short generation time (4-6 weeks), 2) possible self- and cross-pollination, 3) mutants may be easily obtained, because of the small plant size, small genome size, and little repeating sequences in DNA, 4) the chromosome and RFLP maps are available, 5) Ti and Ri plasmids can be used to transform DNA, 6) plant regeneration is possible from the protoplast, and 7) the seed and gene banks have been established.

(2) Materials and Methods

Seeds of two ecotypes of *Arabidopsis thaliana,* Columbia (Col) and Landsberg erecta (Ler) were irradiated by various ion beams from the AVF cyclotron.

The ion beams used were $^{4}He^{2+}$ (50MeV), $^{4}He^{2+}$(20MeV), $^{12}C^{5+}$ (220MeV) and $^{20}Ne^{7+}$(260MeV). Electrons(2MeV) were used as a low LET radiation. About 300 seeds were sealed between kapton films to make monolayer of the seeds for homogenous irradiation. After irradiation using the irradiation apparatus for seed at HY-1 beam port, these seeds were placed on the moistened filter paper in petri dish and kept at 4°C for 3 days. The germination rate was measured when the cotyledons were expanded after 3 day incubation at 23°C under continuous light (2,500 lux). In the case of the survival rate, the irradiated seeds were sown in pots and the survived plants were counted when the true leaves were expanded after one month under the same culture conditions.

(3) Results and Discussion

Energy, LET and range of each ion beam and electron were listed in Table 1. The size of *Arabidopsis* seed is about 0.2 x 0.5 mm, therefore, all ion beams and electrons can pass through the seed. Fig.1 shows the germination rate against the irradiated dose of each ion. In case of germination, 37% inhibition dose became small according to the increase of LET value. And the response to ion beam irradiation was different between the two tested strains, i.e., Ler strain showed higher sensitivity than Col strain to all kinds of ion beams used in this test.

Relationship between LET and the biological effects such as DNA strand breaks and lethality has been studied mainly in the microbials and the mammalian cells[3),4)]. It is generally accepted that the maximum effect is observed between 100-200keV/μm among various kinds of ions. In case of the germination rate in this experiment, Ne ions showed the highest effect compared to other ions. On the other hand, the difference between two strains was not observed in case of the survival rate. Fig.2 shows the relationship between the survival rate and the dose in Col strain. In this case, C ions gave higher effect than He and Ne ions. In this figure, Ne ions showed clearly different nature which did not have a shoulder in the survival curve. This result suggests that Ne ions may have the different radiobiological effects.

From the results obtained, the relationship between LET and RBE, based on the dose which gave the 37% germination and the survival fraction, was presented in Fig.3. No clear peak was observed in case of the germination rate, but the maximum peak for the survival rate was observed around LET of 100 keV/μm.

It was suggested that the radiobiological effects of various kinds of the heavy ions may be different each other. Therefore, many kinds of the mutant lines induced by ion beams should be established to proceed the genetic analysis of the effects of ion beams to *Arabidopsis thaliana.*

References

1) Fuji, T., M. Ikenaga and J.T. Lyman (1966) Radiation effects on *Arabidopsis thaliana* I I , *Radiat. Botany* , 6: 297-306

2) Bork, U., K. Gartenbach, C. Koch and A.R. Kranz (1987) Heavy ion induced lethality in *Arabidopsis*, *Arab. Inf. Serv.*, 9-14

3) Blakely, E.A. (1992) Cell inactivation by heavy charged particles. *Radiat. Environ. Biophys.*, 31: 181-196

4) Weber,K.J. and M. Flentje (1993) Lethality of heavy ion-induced DNA double strand breaks in mammalian cells. *Int. J. Radiat. Biol.*, 64: 169-178

Table 1 Properties of electrons and ion beams used in this experiment.

ion	Energy (MeV)	Energy (MeV/u)	LET (keV/μm)	Range (mm)
e	2	2.0	0.2	9
He	20	5.0	71	0.2
He	50	12.5	15	1.5
C	220	18.3	111	1.0
Ne	260	13.0	504	0.3

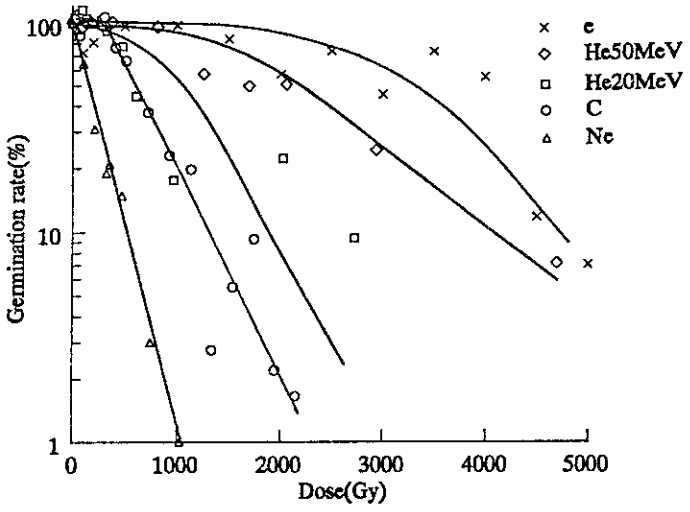

Fig.1 Dose response curves for germination rate of Ler strain seeds.

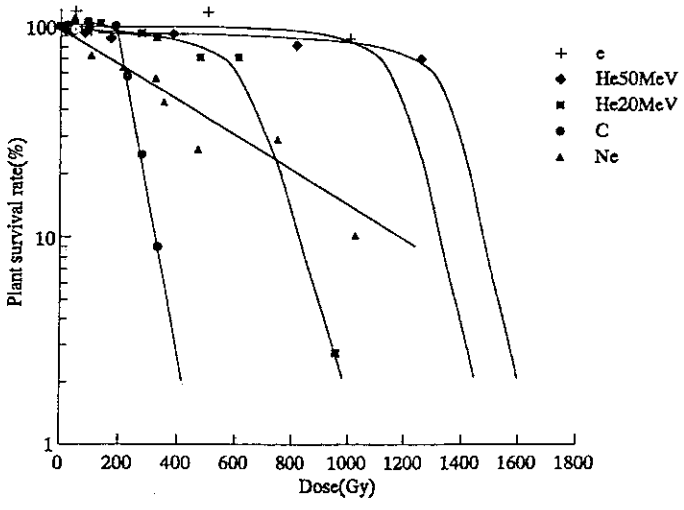

Fig.2 Dose response curves for survival rate of Col strain plants.

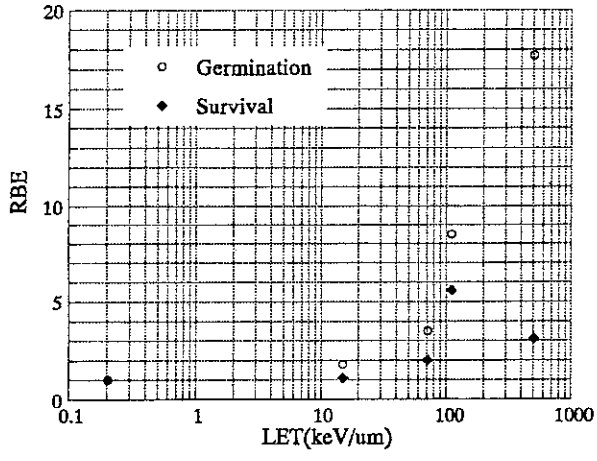

Fig.3 Relationship between LET and RBE. RBEs were determined as the ratio of D_{37} values to D_{37} obtained from electron beams.

2.4 Survival of Dry Cells of *Deinococcus radiodurans* after Heavy Ion Irradiation

Y. Kobayashi[1], T. Shimizu[2], A. Tanaka[1], M. Kikuchi[1], G. Taucher-Scholz[3] and H. Watanabe[1]

[1]Biotechnology Lab., Takasaki, JAERI; [2]Department of Advanced Radiation Technology, Takasaki, JAERI; [3]Biophysik, GSI-Darmstadt

The extraordinary radiation resistance of *D. radiodurans* has been ascribed to the ability to repair all DNA lesions including double strand breaks(DSBs) induced with doses up to 5 kGy[1]. It was reported that this bacterium was also resistant to ion beam irradiation and the survival curves had large shoulders[1]. In the previous studies the cells of *D. radiodurans* had been irradiated under wet conditions involving indirect action from water radicals.

In order to distinguish between direct and indirect radiation effects on lethality, cells were irradiated under dry condition in our experiments. Cross sections for cell inactivation were calculated from the exponential part of the survival curves. Values of relative biological effectiveness(RBE) for inactivation of dry cells of *D. radiodurans* were determined from the ratios of inactivation constants obtained for heavy ions and 2 MV electrons.

When the cells were exposed to heavy ions, all survival curves had a large shoulder. The plots of RBE versus LET showed no obvious peaks at LET values up to 500 keV/μm.

Materials and Methods

D. radiodurans R_1 strain was cultivated in TGY liquid medium with shaking at 30°C for 24hrs. Stationary phase cells were lyophilized on membrane filters(0.22 μm, Millipore Co.) as a monolayer and irradiated in the atmosphere with heavy ions listed in Table 1.

Exposure to He, C, Ne and Ar ions from AVF cyclotron was carried out at TIARA in JAERI using Irradiation Apparatus for Seed[2](IAS); exposure to Ne, Ar, Ni, Xe and Au ions was carried out at the UNILAC in GSI-Darmstadt. The dry cells were also irradiated with 2 MV electron beams from a Cockcroft-Walton accelerator at JAERI. Particle fluences were determined using track detector (CR-39 film and glass). LETs were calculated with ELOSS code developed in JAERI.

Following the irradiation, dry cells were transferred onto TGY agar plate and surviving colonies were counted after 2-3 days incubation at 30°C. Cross sections and F_{37} for cell inactivation were calculated from the exponential part(final slope) of the survival curves plotted against particle fluences. The inactivation constants(D_0) were calculated from F_{37} and corresponding LET. Values of relative biological effectiveness(RBE) for inactivation of dry cells were determined from the ratios of inactivation constants obtained for heavy ions and 2 MV electrons.

Results and Discussion

Figure 1 shows the response of the dry cells of *D. radiodurans* R_1 to heavy ion irradiation carried out at TIARA. The particle energies on the target and LETs for our experiments are listed in Table 1. In the case of C and Ne ions irradiation, the beam energies were degraded with absorbers to obtain various LET values on the target. All survival curves had a large shoulder; about 10 kGy after irradiation of He and C ions, about 20 kGy for Ne ions.

Figure 2 is a plot of the inactivation cross sections as a function of LET. The cross sections were determined from the final slope of the survival curves given in Figure 1. This plot is not showing the saturation of inactivation cross section at LET values up to 10^4 keV/μm, however, charactristic hooks begin in the data points for Ne and Ar ions.

Figure 3 is a plot of the RBE for inactivation of dry cells of *D. radiodurans* as a function of LET. In the case of mammalian cells it has been reported that the RBE maximum for cell-killing after exposure to heavy ions occurs at LET values around 100 keV/μm[3], however, no obvious RBE peaks are shown in Figure 3 at such LET values

It is widely accepted that the critical radiation-induced DNA lesion finally causing cell inactivation is the non-repaired DNA double strand breaks. The pattern of the effect of LET on the induction of DSBs is comparable to the shape of the LET response for cell lethality[4], therefore, the RBE pattern shown in Figure 3 seems to reflect the ability of this bacterium to repair all DNA lesions including DSBs.

On the other hand, Figure 3 shows an unexpected RBE peak with

Table 1 Cell inactivating effects of heavy ions

Particle	Enenergy on Target (MeV/u)	LET (keV/um)	F_{37} (p/cm^2)	cross section (um^2)	D_0 (kGy)	RBE
He	11.7	14.3	9.1E10	1.1E-3	2.1	0.96
He	4.1	42.8	2.4E10	4.3E-3	1.6	1.24
He	1.5	100	1.5E10	6.8E-3	2.4	0.86
C	17.3	116	9.1E9	1.1E-2	1.7	1.18
C	12.1	158	7.7E9	1.3E-2	1.9	1.02
Ne	14.4	310	4.1E9	2.4E-2	2.0	0.98
Ne	10.8	466	2.5E9	4.0E-2	1.9	1.06
Ne	7.6	596	1.9E9	5.3E-2	1.8	1.12
Ne	3.1	1030	2.1E9	4.8E-2	3.4	0.58
Ar	88	252	5.5E9	1.8E-2	2.2	0.9
Ar	5.5	1940	9.1E8	1.1E-1	2.8	0.7
Ar	2.8	2630	1.1E9	9.1E-2	4.6	0.44
Ni	13.8	2320	9.7E8	1.0E-1	3.6	0.56
Ni	5.9	3410	8.6E8	1.2E-1	4.7	0.42
Xe	9.05	7990	2.1E8	4.8E-1	2.7	0.76
Xe	4.44	9170	1.6E8	6.1E-1	2.4	0.84
Au	8.9	12480	3.3E8	3.0E-1	6.7	0.3
Au	5.4	13890	2.3E8	4.4E-1	5.0	0.39

the data points for Xe ions at very high LET, suggesting that either production of non-repairable DNA lesions or inactivation of repair processes may occur especially at very high LET although differences between particles cause disparate results at the same LET.

References
1.Kitayama,S. *et al.*:*Agric. Biol. Chem.16*,583(1977)
2.Kobayashi,Y.*et al.*:TIARA Annual Rep.,*2*,27(1992)
3.Blakely,E.A.:*Radiat.Environ.Biophys.31*,181(1992)
4.Lett, J.T. :*Radiat. Environ. Biophys. 31*, 257(1992)

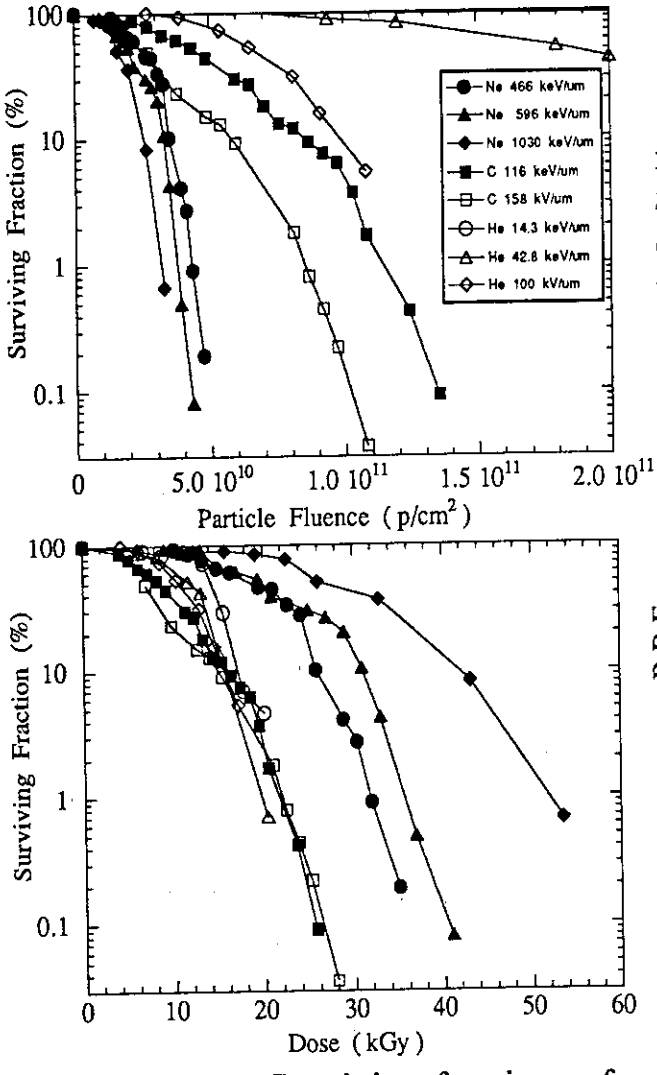

Figure 1. Surviving fractions of dry cells of *D. radiodurans* R_1 as a function of particle fluence(top) and dose in kGy(bottom) after irradiation of heavy ions listed in Table 1.

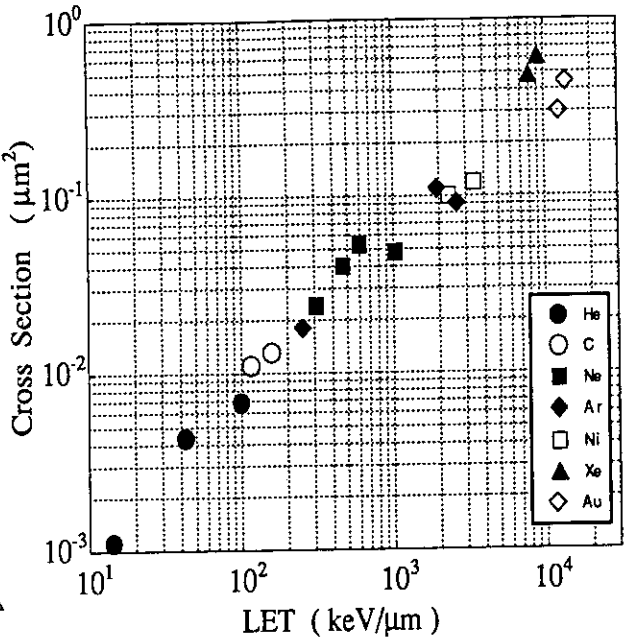

Figure 2. Cross sections for inactivation of dry cells of *D. radiodurans* R_1 as a function of LET. Cross sections were calculated from the exponential part of the survival curves given in Figure 1.

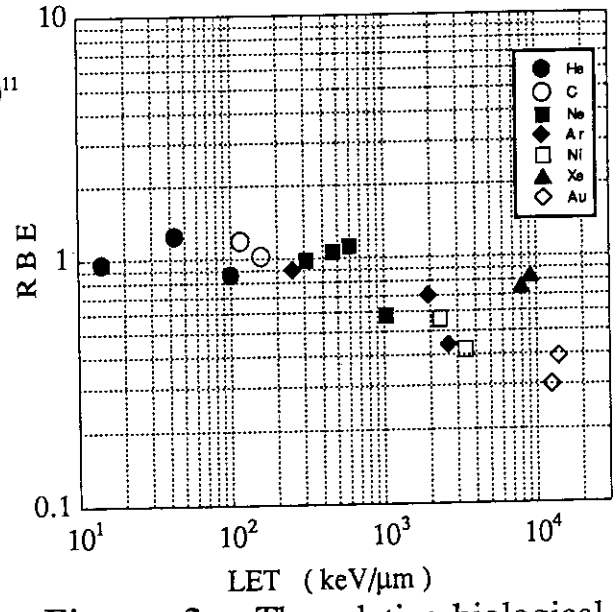

Figure 3. The relative biological effectiveness(RBE) for inactivation of dry cells of *D. radiodurans* R_1 as a function of LET. RBE values were determined from the ratio of inactivation constants obtained for heavy ions and electrons.

2.5 Biological Effects in Dry Seeds of *Triticum*, *Brassica* and *Allium* Exposed to 12.5 MeV/n of Particle Beams of He Ions

H. Ohara, N. Inomata, [1]
H. Watanabe, A. Tanaka, Y. Kobayashi, M. Kikuchi[2]
Okayama Univ., General Education Dept., [1]
JAERI, Takasaki, Biotech. Lab.[2]

(1) Introduction : Biological action of a high energetic particle beam may be primarily due to its high density of localized energy deposition occurred within a living cell, which will suffer soon or later from the injuries caused in the most critical target , DNA. The features of cellular radiation injuries have been noted by the induction of molecular and structural changes in DNA, which can be detectable as the radiation induced events of cells at various levels. In molecular basis, it is well known that ionizing radiations produce single and double strand breaks of DNA as one of the most important initial events, which correlate intimately with biological effects[1]. The radiation induced chromosome aberrations can be recognized as the most impressive and visible event of radiation effects in both of plant and animal cells. The studies on the radiation induced chromosome aberrations, of which structural changes thus primarily originates from initial events of molecular damages to DNA, are thought to indicate the nature of the damage to DNA[2] . The major aim of the study is to understand the nature of radiation quality. This kind of studies[3,4]are now capable in such a institute like JAERI, Takasaki, which can provide a variety of light and heavy ion beams with different radiation quality.

In the present study, some preliminary results on the biological effects of 12.5 MeV/n of particle beams of helium ions are to be described, which included radiobiological chracerization of three different species of crops; wheat, rape and onion in dry seeds.

(2) Materials & methods: The dry seeds used for the present experiments were from the following three species of crops.

1. *Triticum aestivum* L. cv. Chinese spring.
2. *Brassica napus* L. ssp. *oleifera* cv. Wester.
3. *Allium cepa* L. cv. Senshu-chuko-kitamanegi.

The experimental seed samples were attached to the central area (3 cm^2) of a dish for irradiation, in which abour 60-100 grains of seeds were lined up one by one, and irradiated by using the seed irradiation apparatus devised at Biotech. Lab.,JAERI,Takasaki, with different doses to establish a dose dependent-response on each of some useful radiobiological observation indexes.

The subjects of the observation for the irradiated samples were those tests for (1) the ability of germination, (2) the growth of roots and (3) the ability of cell division at tip of the roots. For germination test, seeds were placed on the water dipped filter paper in a glass dish and kept in the dark at 25℃. For cytology of cells in division, root tip cells were stained with Feulgen solution and examined details of cell division by the traditional way of squash

method [3,4,5].

The physical descriptions of He^{2+} ion beams will not be described here but else where in other report. The high energy of He beams used for the present study seems to be sufficient to cover a wide spread of dose range for such relatively radioresistant samples like plant seeds.

(3) Effect of He ions on seed germination: It was not perfect in the dose schedules to cover the whole of the radiation response to elucidate the radio-sensitivity in all of the experimental plants. The wheat seeds (*Triticum*) showed relatively high degree of radioresistance that 95.7 % were still the survivors capable of germinating even under the exposure of 400 Gy. The rapes (*Brassica*) and onions (*Allium*) showed complete inhibition of germination against exposure of 500 Gy. Further, *Allium* seeds showed only 20 % for germination against exposure of 100 Gy, while remarkable inhibition was not observed against the exposures up to 20 Gy (Fig. 1). In comparison, *Triticum* seeds seems to be the most radioresistant, being followed by the those of *Brassica* and *Allium* in order.

(4) Effect on growth of roots in terms of elongation: The selected dose range was 100 - 500 Gy, during which *Triticum* seeds was the most sensitive to reach maximally about 50 % of growth when compared to those non-exposed controls. In *Brassica*, growth of germinated seeds showed dose dependent change, i.e., 91.8 % of elongation for 100 Gy, 46.9 % for 300 Gy, and none for germination and growth. In contrast, *Allium* showed no inhibition of growth unless the germination was inhibited. The exposure to 100 Gy allowed *Allium* seeds only less than 20 % for germination. The growth, however, of root tips was not seen to be inhibited, being comparable to those of non-exposured controls.

(5) Cytological effects on chromosomes and cell division: The cytological observation was only concerned with those of *Allium* cells which were capable of growng even after exposure to He ions. The main subject of present cytology was to elucidate the dose dependent fluctuations in the frequencies of such aberrant cells like those cells containing chromosome aberrations. For this purpose, the frequencies of the cells containing such structural abnormalities in chromosomes like bridge formation, fragmentation, lagging in polar movement, multipolar formation or division, and ring formation, etc., were examined and analysed for the variation of the dose between 50 and 500 Gy. It was found that the frequencies of aberrant cells increased with increasing dose to form a maximum peak around 300 Gy, and began to decrease remarkably at 400 Gy and more decreased at 500 Gy. This decrease may be due to the effect of a high dose of irradiation which causes almost complete inhibition of cells to enter mitotic phase, which is apparently the indication of cell death before entering mitosis, and also leads to a remarkable decrease in the frequency of cells at mitosis. The other findings were that the frequency of chromosome aberrations were also increased with increasing irradiation dose, and that almost all types of aberration were multiplied to increase the frequencies of abnormality of chromosomes in a cell beyond the exposure

chromosome aberration analysis are shown in Fig. 2.

(6) Summary: The radiosensitivity of three different species of crops, i.e., *Triticum*, *Brassica*, and *Allium*, in terms of growth inactivation of dry seeds was roughly estimated by experimental exposures to high energetic (12.5 MeV/n) particle beams of helium ions produced by AVF cyclotron of JAERI, Takasaki. In *Allium*, an appropriate range of exposure dose of He ions was discovered for the analysis of chromosome aberrations. Therefore, the next step of study to elucidate the dose response in aberration frequencies at metaphase plate could be possible.

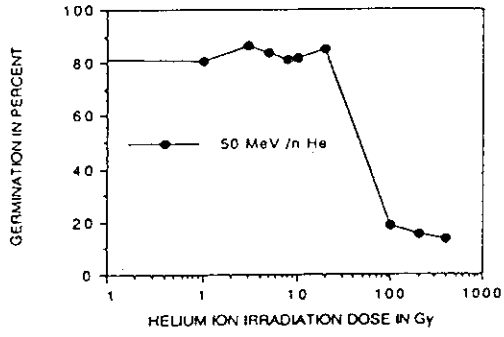

Fig.1. Change in rate of seed germination against dose of He ions in *Allium cepa*.

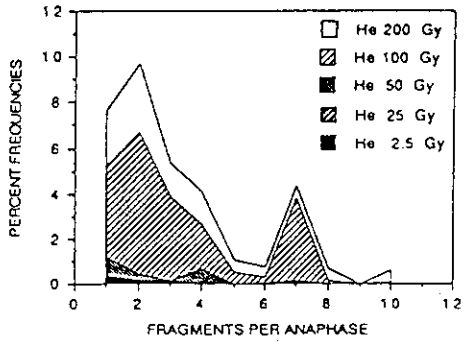

Fig. 2. Dose-response analysis of chromosome fragmentations at anaphase of *Allium* root tip cells irradiated by various doses of He ion beams. High dose curves were characterized by two modal peaks.

References:

1) D.T. Goodhead, Int. J. Radiat. Biol. 65 (1994), 7.
2) C.R. Geard, Radiat. Res. 104 (1985), S-112.
3) E.E. Edwards, D.C. Lloyd, J. Pinnon, and J.E. Monquet, Int. J. Radiat. Biol. 50 (1986), 137.
4) S. Matsubara, H. Ohara, T. Hiraoka, K. Ando, H. Yamaguchi, Y. Kuwabara, M. Hoshina, and S. Suzuki, Radiat. Res. 123 (1990), 82.
5) A. Marshak, J.C. Hudson, Radiology 29 (1937), 669.
6) K. Sax, Genetics 41 (1956), 639.
7) N.S. Cohn, Genetics 41 (1956), 639.

2.6 STUDIES ON INDUCED MUTATIONS BY ION BEAM IN PLANTS

H.Nakai, H.Watanabe*, A.Tanaka*, S,Kitayama**, T.Asai and K.Shindoh
Shizuoka univ., *JAERI, **RIKEN

We have studied on the biological effect of thermal neutrons and found that the high LET radiation is useful as a mutagen for induction and development of new plant genetic resources to be used in plant breeding.[1, 2] The present studies were initiated aiming at application of various ion beams, of which LET is higher than that of thermal neutrons, to plant mutation breeding. In the studies, some preliminary experiments are required for accumulating basic data on radiobiological effects of the ion beams on plants, since there is little data previously obtained on this matter. This paper pertains to effects of an ion beam, He^{2+}, on the pollen and seed fertility of rice plants in the first generation after irradiation (M_1).

Dry seed lots of rice, Oryza sativa L., c.v. Koshihikari, were irradiated by ion beams (He^{2+}) from the AVF cyclotron in JAERI operating at 50 MeV. On the other hands, for comparison, the seeds were exposed to thermal nutrons with a flux of 2.5×10^9 Nth/cm/sec for 0-6 hr in the heavy water facility of Kyoto University Reactor operated at 5000 kW, and exposed to gamma- rays of 0-600 Gy from a ^{60}Co source. After irradiation with three mutagens, the seeds were brought back to Shizuoka University to grow in the isolated experimental field. At flowering time of the M_1 plants, the glumous flowers were collected from every plant and pollen fertility was measured by staining the pollens from the glumous flowers with aceto carmine. Seed fertility per panicle (percentage of ripening) was also measured after maturity of the M_1 plants.

The effects of gammar-rays, the ion beams (He^{2+}) and thermal neutrons for pollen fertility and seed fertility are presented in Fig.1 and Fig.2. In the figures, the dose-response curves were drawn by the equation, $S=e(-\text{alpha} \times D - \text{beta} \times D^2)$, where S and D means degree of radiation damage relative to control and absorbed dose, respectively, and alphe and beta are a constant to be calculated by experimental data.[3] As seen in Fig.1 and Fig.2, the dose-response curves of gamma-rays and the ion beams (He^{2+}) on both the traits were sigmoidal or somewhat sigmoidal, whereas those of thermal neutrons were rather exponential. The M_1 damage per unit of dose caused by thermal neutrons appeared to be larger than that by the ion beams (He^{2+}). RBE (relative biological effectiveness) values of the ion beams and thermal neutrons relative to gamma-rays were calculated by the formula, D_{50} of gamma-rays /D_{50} of relevant radiation, where D_{50} means a dose which reduces the average values of pollen and seed fertility to 50% of control. The RBE values of the ion beams (He^{2+}) on pollen and seed fertility were 2.5 and 2.6,

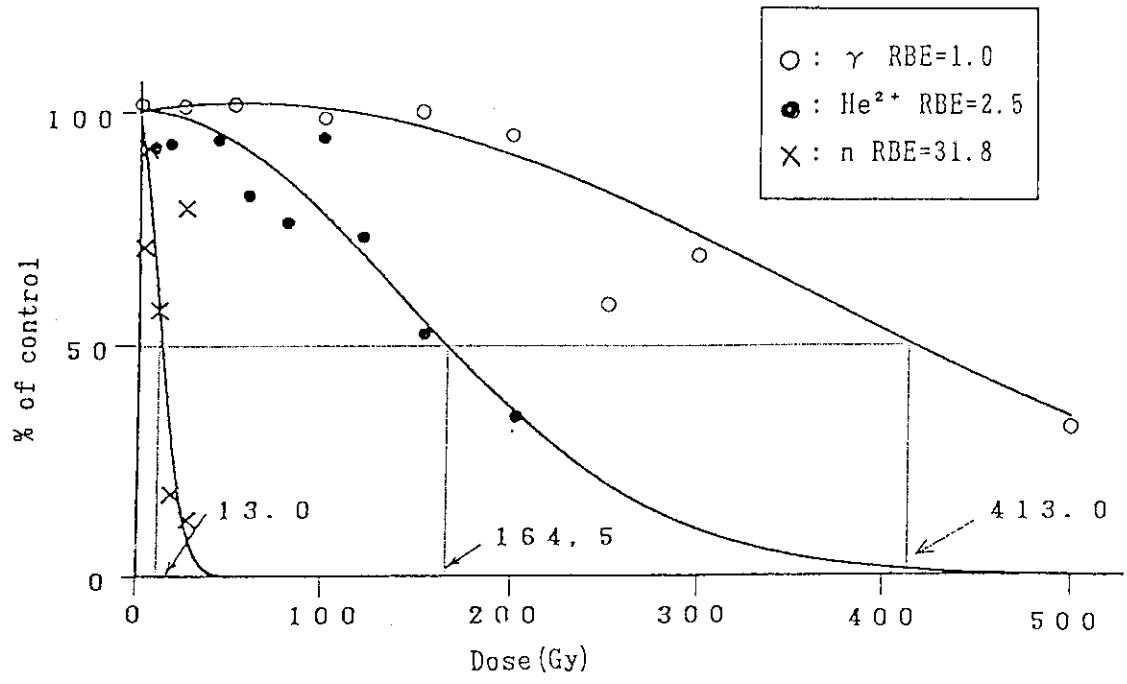

Fig.1 Dose-response of gamma-rays, ion beams (He^{2+}) and thermal neutron on pollen fertility in M_1 plants.

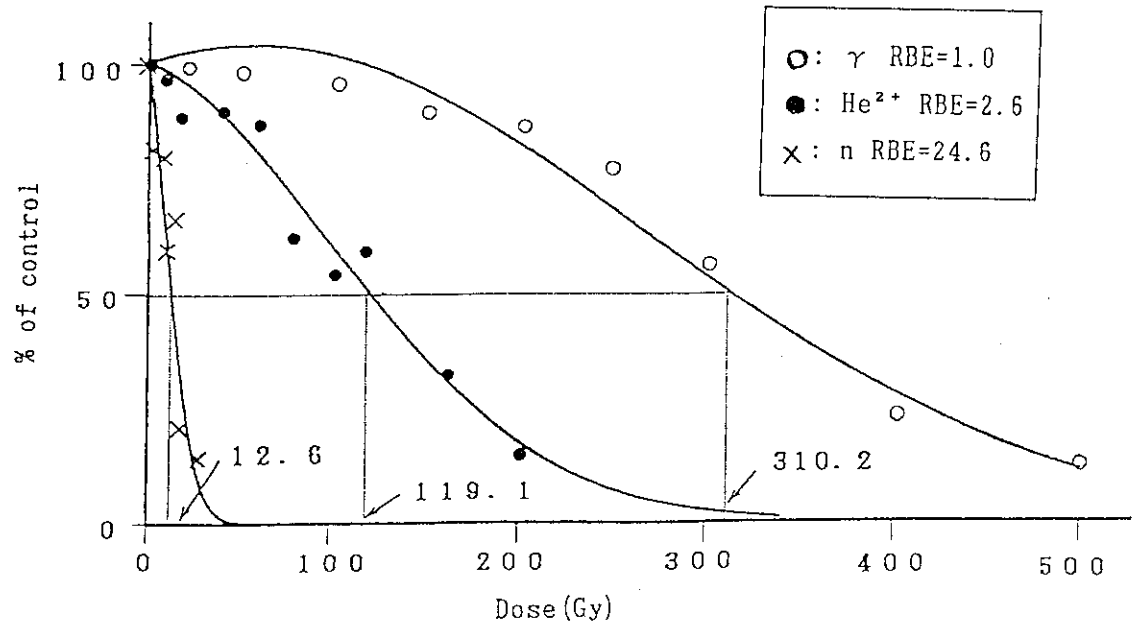

Fig.2 Dose-response of gamma-rays, ion beams (He^{2+}) and thermal neutrons on seed fertility in M_1 plants.

Table 1. RBE of ion beams(He^{2+}) and thermal neutrons relative to gamma-rays on some traits.

Mutagen	He^{2+}	Thermal neutron	Gamma -ray
Root length	2.9	18.6	1.0
Seeding height	3.5	15.1	1.0
Pollen fertility	2.5	31.8	1.0
Seed fertility	2.6	24.6	1.0

respectively. It is noted that these RBE values of the ion beams were low comparing with those of thermal neutrons, supporting the previously reported data on RBE values for root length and seedling height.[4] RBE values of the mutagens used on pollen and seed fertility were listed in Table 1, along with those on root length and seedling height which were previously reported. As seen in Table 1, RBE values of ion beams(He^{2+}) were similar on all the traits concerning vegetative growth (root length, seedling height) and reproduction (pollen and seed fertility) of M_1 plants, whereas those on the traits concerning reproduction, in case of thermal neutrons were signficantly higher than those on the traits concerning vegetative growth. It is assumed from this result that biologicalactions of ion beams(He^{2+}) might be different from those of thermal neutrons, suggesting a possibility to induce some specific mutations useful to plant breeding with ion beams. Further experiments in detail on the biological effects of ion beams are in progress.

REFERENCES

1) H. Nakai, M. Saito and H. Yamagata, Env. and Exp. Bot. 20 (1980) 191.
2) H. Nakai and M. Saito, ibid. 25. (1985) 385.
3) H. K. Chadwick and H. P. Leenhouts, The Molecular Theory of Radiation Biology, Springer-Verlag, New York (1981).
4) H. Nakai et al., TIARA Annual Report Vol. 2 (1992) 54.

2.7 Interspecific Hybridization between *Nicotiana gossei* Domin and *N.tabacum* L., using $^4He^{2+}$-irradiated Pollen

M.Inoue,H.Watanabe[2],A.Tanaka[2] and A.Nakamura[3]

Department of Agriculture, Kyoto Prefectural University, Takasaki Establishment, JAERI[2], Department of Agriculture, University of Osaka Prefecture[3]

In order to introduce a desirable gene(s) from wild plants to cultivar, many works have been carried out, particularly in relation to disease- and insect-resistance. However, it is very difficult or almost impossible to get a viable hybrid plant(s) between distantly related species, because of cross incompatibility and/or hybrid inviability. It has been demonstrated that pollen irradiation with ionizing radiations is effective for overcoming these barriers in sexual reproduction, and that some of viable hybrid plants have been produced[1)~4)].

We have been investigating on the efficient procedure for producing interspecific hybrid in *Nicotiana*[1),4)]. In the present experiment, two viable hybrid plants between *N.gossei* and *N.tabacum* were obtained from the *in situ* cross with $^4He^{2+}$-irradiated pollen. It is known that in this species-combination hybrid seedlings from the cross with non-irradiated pollen are lethal in the early stage of growth.

Mature pollen of *N.tabacum* cv Bright Yellow 4, was collected immediately after anthesis, and kept in a desicator for one day. The collected pollen was held between kapton films(8.5μm thickness, Toray-Dupon Co.Ltd.) on the one layer, and irradiated with $^4He^{2+}$ of 800Gy from 3MV Tandem Electrostatic Accelerator(6MeV) and AVF Cyclotron (50MeV). The flowers of *N.gossei* were emasculated before anthesis, and pollinated with the irradiated pollen. Then, each flower was sealed, and cultivated at the temperature of about 30℃ in a glass house. After 3~4 weeks, capsules were harvested, and F1 seed fertility was measured. F1 seeds with the non-irradiated pollen were obtained by means of identical procedures to those in the irradiated pollen.

In F1 generation, seed germination and seedling cultivation were permitted in the growth chamber controlled at 25℃. Thereafter, survival plants were transplanted and cultivated in the glass house with the temperature of about 30℃. Chromosome pairing in pollen mother cell(PMC) was analyzed by aceto-carmine staining and squash method.

Table 1 shows the results on F1 seed formation and hybrid viability. In the crosses with $^4He^{2+}$-irradiated pollen, only 2.3% of crosses produced capsules with fertile seeds. Most(92.5%) of F1 seeds developed to germinate, and, finally, two(5.4%) of the resulting seedlings grew up to flowering. Accordingly, the yield of viable hybrid plants was $1.1x10^{-3}$. On the other hand, in the crosses with non-irradiated pollen, many F1 seeds were obtained, and they germinated at the rate of 76.7%. However, no seedling

Table 1 Effect of $^4H^{2+}$-irradiation to pollen on the production of viable F_1 plants

Irradiation	Frequency of fertile capsules (%)	Germination rate of F_1 seeds (%)	Survival rate of F_1 plants (%)	Yield of flowering F_1 plans
non	66.7	76.7	0	0
$^4H^{2+}$ 800Gy	2.3	92.5	5.4	$1.1x10^{-3}$

could survive over the period of about one month after germination.

The characters in interspecific hybrids were different from those in parents(Fig.1, Table 2). Particularly, some characters, e.g. flower petal twist and leaf shape, were different between hybrid plants.

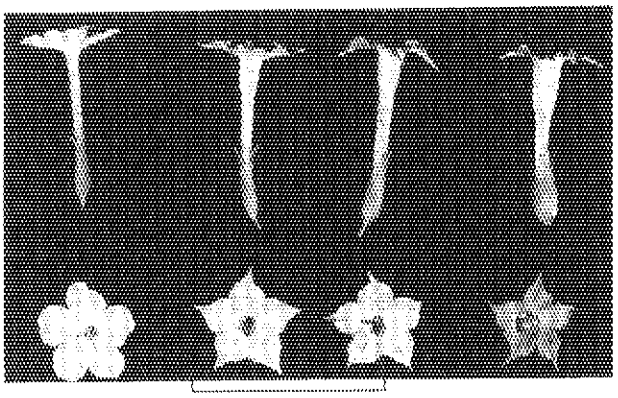

N.gossei F1 *N.tabacum*

Fig.1 Flower of *N.gossei*, *N.tabacum* and F_1 plant

Table 2 Characteristics of *N.gossei*, *N.tabacum* and F_1 plant

Character	*N.gossei*	F1 Plant-1	F1 Plant-2	*N.tabacum*
Flower type				
color	white	palepink	palepink	pink
shape	star	star	star	star
petal tip	smooth	sharp	sharp	sharp
petal twist	-	-	+	++
calyx twist	-	-	-	-
trichome	++	+	+	-
Leaf type				
shape	spatula	long ellipse	ellipse	ellipse
tip	smooth	sharp	sharp	sharp
margin plait	+	+	+	-
petiole	-	+	+	++

++,+ and - indicate the degree in each character.

The results on chromosome pairing in PMC of hybrid plants were shown in Table 3. *N.tabacum* has 48 chromosomes(2n) and TS genome. *N.gossei* has 36 chromosomes(2n) and its genome has not been identified. From the another results on crossability and hybrid inviability, it is clear that these two species are distantly related. As shown in Table 3, frequency of PMC with only 42 univalent chromosomes(42 I), PMC with 40 univalents and 1 bivalent(40 I +1 II), PMC with 38 univalents and 2 bivalents(38 I +2 II) and PMC with 36 univalents and 3 bivalents(36 I +3 II), were 24.2, 23.0, 18.7 and 13.0%, separately. About half of PMCs had bivalent of 1 to 3, suggesting that $^4He^{2+}$-irradiation can induce chromosome damage.

It was also observed that hybrid plants had no fertile pollen and no seed by selfing and back crosses with parents.

Table 3 Frequency of partial chromosome pairings in pollen mother cells of F_1 plants

Chromosome composition	Relative frequency
42 I*	24.2 ± 13.9 ***
40 I + 1 II **	23.0 ± 9.6
38 I + 2 II	18.7 ± 6.8
36 I + 3 II	13.0 ± 7.4
34 I + 4 II	7.9 ± 6.2
32 I + 5 II	5.1 ± 4.3
30 I + 6 II	2.5 ± 2.0
28 I + 7 II	2.2 ± 2.9
26 I + 8 II	1.8 ± 1.5
24 I + 9 II	0.4 ± 0.5
22 I + 10 II	0.7 ± 1.3
>11 II	1.1 ± 1.7

*, univalent chromosome.
**, bivalent chromosome.
***, mean value ±S.D.

References

1) Inoue et al., The use of pollen irradiated with helium ion beam for interspecific hybridization in *Nicotiana*, TIARA Annual Report, vol.2, 50-53(1992).

2) Pandey et al., Sexual transfer of specific genes without genetic fusion, Nature, vol.256, 310-313(1975).

3) Shintaku et al., Interspecific hybridization between *Nicotiana repanda* Willd. and *N.tabacum* L. through the pollen irradiation technique and the egg cell irradiation technique, Theor. Appl. Genet., vol. 76, 293-298(1988).

4) Yakushiji et al., Characters of interspecific hybrid between *Nicotiana gossei* Domin and *N.tabacum* L., using gamma-irradiated pollen, Jpn. J. Breed., vol. 40(Suppl. 2), 444-445(1992).

2.8 Studies on the Cold Tolerance of Malvaceae Plants

Alejandro Vazquez Tello, Makoto Hidaka, Takeshi Uozumi,
Yasuhiko Kobayashi[2] and Hiroshi Watanabe[2]
Department of Biotechnology, The University of Tokyo
Biotech. Lab., Takasaki Institute, JAERI[2]

Introduction

Hibiscus rosa-sinensis is a tropical plant which bears large and beautiful flowers of a brilliant color, but it can not endure winter in Japan, where the minimum temperature becomes lower than 5°C. In the same *Malvaceae* family, *Lavatera thuringiaca* is cold tolerant and survives the minimum temperature of at least -3°C. We have been trying to give cold tolerance to the tropical *Hibiscus* by cell fusion with *L. thuringiaca* (1). In case of ordinary cell fusion, all the chromosomes of both plants will be maintained in the fusant cells, and the hybrid will inherit some undesirable traits, such as small flower and dull appearance of the leaves intrinsic to *Lavatera*. Irradiation by ionizing radiation of the plant cells before or after cell fusion may result in partial loss of chromosomes that have undesirable genes, and may be useful to get a fusant that has a combination of desirable characters of both parents.

One important approach in plant breeding consists in the asymmetric fusion of protoplasts, one of which is exposed to irradiation in order to inactivate the nucleus, aiming to obtain cybrid cells combining one nucleus with a different cytoplasm. Such approach has been useful for localization of the cytoplasmic male sterile factor in plants, and its transmission to other species by asymmetric protoplast fusion. Another important application of irradiation consists of the generation of somatic mutations, either for getting mutant plants with commercially interesting phenotypes, or aiming the identification of a specific gene and its role in the plant cell.

Conventionally, gamma rays have mostly been used in such applications, but they present a major inconvenience, namely that relatively high doses of irradiation must be used to increase the probability of hitting a specific gene target, and consequently it is also likely that other genes in the genome are affected as well, causing extensive damage to the DNA. In addition, other undesirable effects may occur, such as general cell damage and low cell survival rates. On the other hand, little research has been done with ion beam irradiation on plant cells. One advantage of the ion beam irradiation over the conventional one is that the former possesses a much higher linear energy transfer (LET) to the target than the latter; in other words, the amount of total irradiation required may be considerably lower than that used with the conventional irradiation, to obtain the change or loss of a specific chromosome. It is therefore important to determine the effects of different doses of ion beam irradiation on plant tissues and its potential use for plant breeding. In this research, we have investigated the effects of the ion beam irradiation of 220 MeV $^{12}C^{+5}$ on protoplasts, cell suspensions and calluses of *L. thuringiaca*.

Results

The results of several doses of irradiation on the embryonic potential of

a cell suspension were determined, to establish up to which dose the cells can be exposed safely without compromising the plant regeneration capability. In case of the *L. thuringiaca* cell suspension, the embryogenic potential decreased concomitantly with increasing irradiation doses. Exposure to doses of 5.0 Gy or higher caused a severe inhibition in the embryogenic potential of the cells. At 20 Gy, the embryogenesis rate dropped to only 5.5% of the non exposed control (100%).

The effect of several doses of irradiation on the percentage of cell survival and cell division of isolated protoplasts was also determined. The percentage of protoplast survival did not change markedly even at 20 Gy. The highest irradiation dose tested on the protoplasts (50 Gy) caused a decrease of cell survival to approximately 55% of non-exposed control (100%). This result suggests that the ion beam $^{12}C^{+5}$ may cause less cell damage than the conventional irradiation. The effect of irradiation on protoplast division was more evident. The percent cell division decreased in parallel to the increase in irradiation dose; the dose needed to inhibit cell division 50% was determined to be 5.0 Gy.

Finally, the extent of callus growth exposed to different doses of irradiation was measured after 13 days post treatment, and the results were expressed as % of cell growth as compared to the untreated control (100 %). We observed a gradual decline in cell growth with increasing doses of irradiation. The decline was approximately linear from 0 to 1.0 Gy. However, higher irradiation doses caused a sharp growth inhibition of callus. The dose calculated to cause a 50 % growth inhibition in the exposed callus was 2.5 Gy.

Discussions

We have achieved protoplast fusion of *H. rosa-sinensis* and *L. thuringiaca* (1). The somatic hybrid cells formed calluses and some of them showed an intermediate cold tolerance between the parents. However, regeneration of hybrid plant was not successful, so far. As the original *Lavatera* suspension culture is embryonic and can be regenerated to the plant, some of the chromosomes from *Hibiscus* seems to inhibit the regeneration of the hybrid plant.

In this research, we have elucidated the effect of $^{12}C^{+5}$ beam irradiation on the survival and cell division of the calluses, suspension cultured cells and protoplasts of *L. thuringiaca*, and found appropriate doses for each material. Next step will be irradiation of the somatic hybrid cells between *Hibiscus* and *Lavatera*, to make selected loss of some chromosomes in order to achieve regeneration of hybrid plants. Irradiation of protoplasts of one plant before fusion with non-irradiated protoplasts of another plant will be an alternative approach to get hybrid plants with partial loss of chromosomes originating from only one of the parents.

References

1) A. Vazquez-Tello, M. Hidaka and T. Uozumi, "Protoplast fusion and selection of somatic hybrids of *Hibiscus rosa-sinensis* X *Lavatera thuringiaca* by the use of kanamycin and hygromycin resistance", Abstracts of XV International Botanical Congress, Yokohama, 1993, p.549

2.9 Electron Microscopic Analysis of *Deinococcous radiodurans* irradiated by Heavy Ions

S.Inaba, K.Osawa, Y.Koizumi, T.Oota,
H.Watanabe*, A.Tanaka*, Y.Kobayashi* and M.Kikuchi*
Radioisotope Center, Tokyo Univ. of Agriculture, and
*Biotechnology Lab., JAERI/Takasaki.

Deinococcous radiodurans R1 was isolated as an extraordinaly radiation-resistant bacterium. The radiation resistance of this bacterium has been attributed to its exceptional repair capabilities, though little was revealed about repair enzymes. From these studies, it was shown that the survival curve of R1 strain was sigmoidal.

It is thought that high LET radiations takes place heavy damages in not only DNA but also cell structure which gives an environment desirable for DNA repair. However, little has been studied the change of cell structure after ion beam irradiation. Therefore, we have examined the effect of Ar, He and C ion beams on the dry and wet cells of *D. radiodurans* R1 strain. The change in cell structure after direct or indirect action of ion beams were observed using transmission electron microscope(TEM).

(1) Radiosensitivity

The cells of *D. radiodurans* R1 were irradiated with Ar^{13+}, C^{5+} and He^{2+} ions under both dry and wet conditions. The LETs of Ar^{13+}, C^{5+} and He^{2+} were 1800, 120 and 14 keV/μm, respectively. Figure 1 shows the survival curves. The highest sensitivity was found in the wet cells irradiated with He^{2+} ions. The radiosensitivities of wet and dry cells were increased in the order of decreasing ion mass and LET. On the other hand, all wet cells were more sensitive to ions than dry cells, indi- cating a contribution of indirect action of water. The degree of indirect action was the highest in Ar^{13+} ions and the lowest in C^{5+} ions.

(2) TEM observation

Changes in the cell structure were observed with the TEM picture of thin section and DNA prepared by Miller technique from irradiated dry and wet cells.

Cell envelope

Slime layer: Electron density was more dense in wet cells than in dry cells. Significant damages were observed in wet cells (Phot.1 ~ 4).

Cell wall: Significant damages of morphological structure were observed in the wet cells. In particular, the large deformations of walls were caused by all ion beams used, especially by He^{2+} ion beams at 10.0 kGy.

Cytoplasmic granules

Cytoplasmic granules were also destroyed by He^{2+} ion irradiation, consequently the size of granules became about half. The effect of irradiation on the decrease of size was more significant in wet cell than in dry cells. On the other hand, the effect of irradiation on decrease of size was more significant in C^{5+} ions than He^{2+} ions.

Significant destructions of cytoplasmic granules were not observed after Ar^{13+} irra diation on both wet and dry cells.

Cell nucleus

As shown in Phot.1 ~ 4 when the thin sections prepared from irradiated cells. No significant differences of morphological structures were observed between the unirradiated cells and dry cells irradiated with 5.4 kGy of Ar^{13+} ion beams, while the partially broken cell nucleus was observed in the wet cells irradiated with 5.4 kGy of Ar^{13+} ions. Compared with cell survival, these decomposition of nucleus would be recovered during the incubation of post-irradiation. On the other hand, irradiation of dru cells with 10 kGy of He^{2+} ions did not cause any significant changes in the nucleus as shown in Phot.3. However, when the wet cells were irradiated with the same dose, the broken nucleus was observed as shown in Phot.4.

DNA by Miller technique

Specimens prepared by Miller spreading technique were rotary shadowed with Pt, followed by shadowing with carbon at an angle of 30°. Phot.5 and -6 show the chromosomal DNA was observed in the wet cells from unirradiated and with 10.0kGy

of C^{5+} ions. Once in a while the partially and finely broken chromosomal DNA was observed in the wet cells irradiated with 10 kGy C^{5+} and He^{2+} ions.

Research

These results indicates that partially broken nucleus could be recovered, but heavily broken nucleus could not, and further indicate that the increased sensitivities and decomposition of cell nucleus (chromosomal DNA) under the wet condition would be due to indirect action of water radicals.

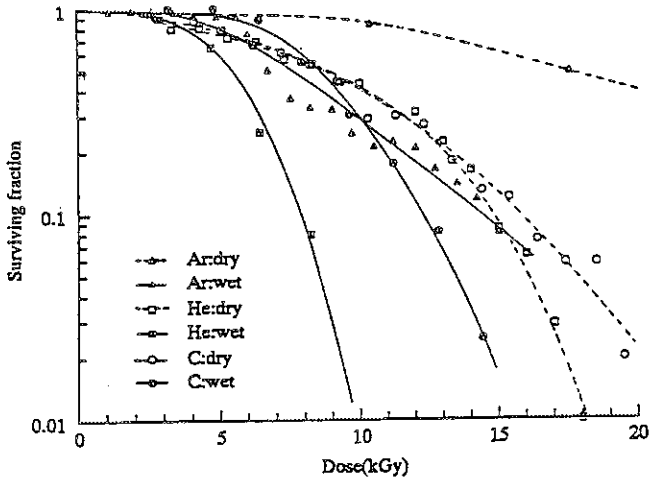

Fig.1 Survival curves of *D. radiodurans* R1 cells irradiated with Ar, He and C ions under both dry and wet conditions.

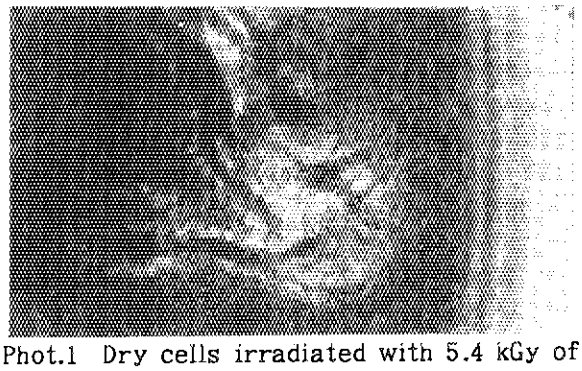

Phot.1 Dry cells irradiated with 5.4 kGy of Ar ions.

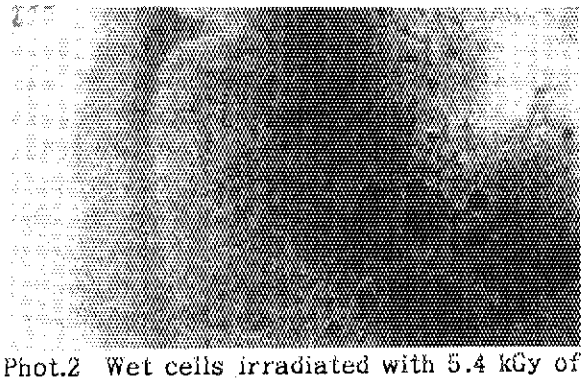

Phot.2 Wet cells irradiated with 5.4 kGy of Ar ions.

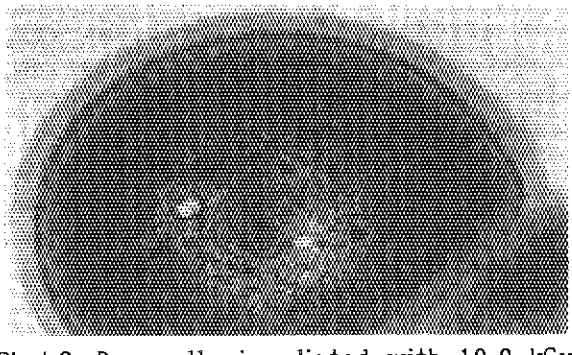

Phot.3 Dry cells irradiated with 10.0 kGy of He ions.

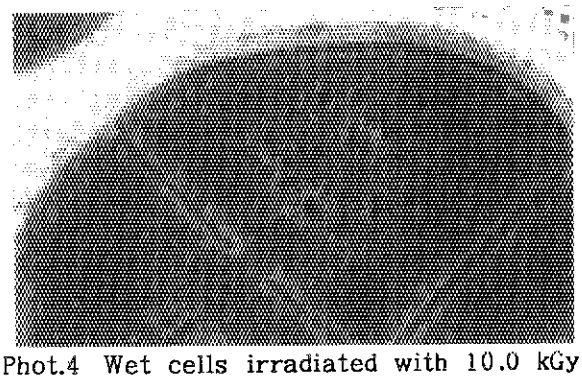

Phot.4 Wet cells irradiated with 10.0 kGy of He ions.

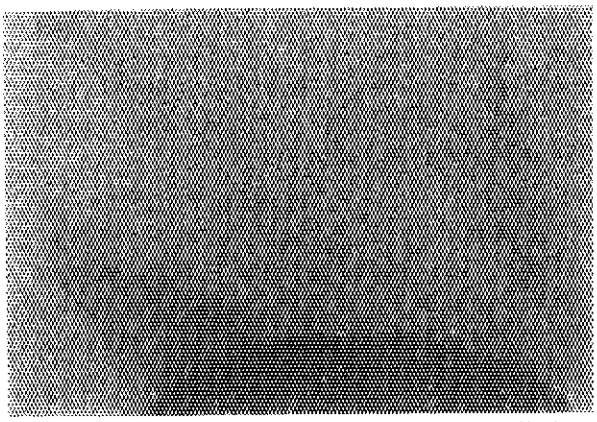

Phot.5 Chromosomal DNA in unirradiated cell.

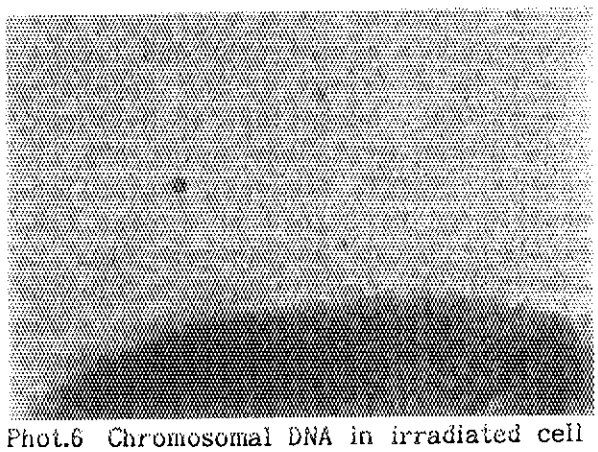

Phot.6 Chromosomal DNA in irradiated cell with 10.0 kGy of C ions.

2.10 Recovery of Transforming Activity in Lyophilized Cells of *Deinococcus radiodurans* Irradiated with Various High-LET Ions

N. Mizuma, T. Kikuchi,
H. Watanabe[2], Y. Kobayashi[2], A. Tanaka[2], M. Kikuchi[2]
Res.Reactor Inst.,Kyoto Univ., JAERI,Takasaki,Biotech.Lab.[2]

Deinococcus radiodurans is extremely resistant to the lethal effects of ionizing radiation and many other agents that damage DNA. Although the repair of DNA damage in *D. radiodurans* is known to be extraordinary efficient,the molecular mechanisms for repair of radiation-induced DNA damage have not been well characterized. It has been demonstrated that *D.radiodurans* was able to repair double-strand breaks in the DNA[1]. It was proposed that the exceptional radiation resistance of *D.radiodurans* must be due to the high efficiency of its recombination repair systems, but the its detailed mechanisms remain largely obscure. Recombination ability can be assayed by measuring the level of transformation.

This paper described mainly the results of the recovery rate of transforming activity (TA) in the lyophilized cells irradiated with sublethal dose (2~3 kGy, Fig.1) of various kinds of high-LET ion beams (Table). The recovery rate of TA is analyzed by short time treatment with protein synthesis inhibitors (chloramphenicol;CM,tetracycline;TC) at the various times during the postincubation as shown in Fig.2. Cells harvested on a millipore membrane filter were frozen and lyophilized in a freeze-drying apparatus (~0.03 TOR). Except $^4He^{2+}$(6 MeV)ions, irradiation with ions using AVF cyclotron (JAERI,Takasaki establishment) were performed at a room temperature under helium-gas flow to suppress the radiation activation of sample in an automatic-sample-exchanging apparatus(IAS) with remote-control system. Using He^{2+}(6MeV) ion beems accelerated by 3 MeV tandem electrostatic accelerator, lyophilized cells were also irradiated through a Kapton film of 8.5 μm thickness in a Irradiation Apparatus for Cells (IAC). The TA was assayed by the same procedures using rifampicin resistant marker as previously described [2)3)].

As shown in Fig.1, the length of shoulder on the survival curve decreased and the final slope was somewhat steeper as LET increased. These results indicate that higher LET ions give more lethal effects. The results in Fig.2 show that *de novo* protein synthesis seems to be required for the recovery of TA and the inhibitor suppresses specifically the recovery at early time of postincubation. TA of the recipient cells irradiated with ion beams was recovered during the postincu-bation under the growth condition. In the previous works,the recovery rate of TA in the cells irradiated with high-LET boron neutron captured beam (BNCB) decreased more than that in the cells irradiated with γ-rays. The recovery times for TA of cells irradiated with different LET radiations were shown in Fig.3. The recovery times for TA of the cells irradiated with 14 to 200 keV/μm LET ions were not so different, but about 90 minutes. The recovery time for LET over 200 keV/μm increased gradually with LET.

1)Kitayama S. et al,POSSIBILITY OF THE REPAIR OF DOUBLE-STRAND SCISSIONS IN *Micrococcus radiodurans* DNA CAUSED BY GAMMA-RAYS, Biochem. Biophys. Res. Commun., 33, 418-422 (1968)

2) Mizuma N. et al, DAMAGES AND THEIR REPAIR OF THE CELLS IRRADIATED WITH HIGH LET RADIATION, Proc.Scientific Meeting.Res.Reactor Inst. Kyoto Univ., 27, 61-66 (1993)

3) Kikuchi T. et al, REPAIR OF TRANSFORMING CAPACITY OF CELLS IRRADIATED WITH HIGH-LET IONS IN A RADIATION RESISTANT BACTERIUM, *Deinococcus radiodurans* , TIARA Annual Report, Vol.2, 42-45 (1992)

Table. Ion beams used for irradiation

Beam	Energy (MeV)	LET (keV/μm)	Facility
$^{4}He^{2+}$	50	14	Cyclotron
$^{4}He^{2+}$	20	42	Cyclotron
$^{4}He^{2+}$	6	112	Tandem
$^{12}C^{5+}$	220	121	Cyclotron
$^{20}Ne^{7+}$	260	430	Cyclotron
$^{40}Ar^{13+}$	460	1800	Cyclotron
γ-ray		0.3	^{60}Co
BNCB* α		200	Reactor
^{7}Li		300	

*$^{10}B(n_{th},\alpha)^{7}Li$

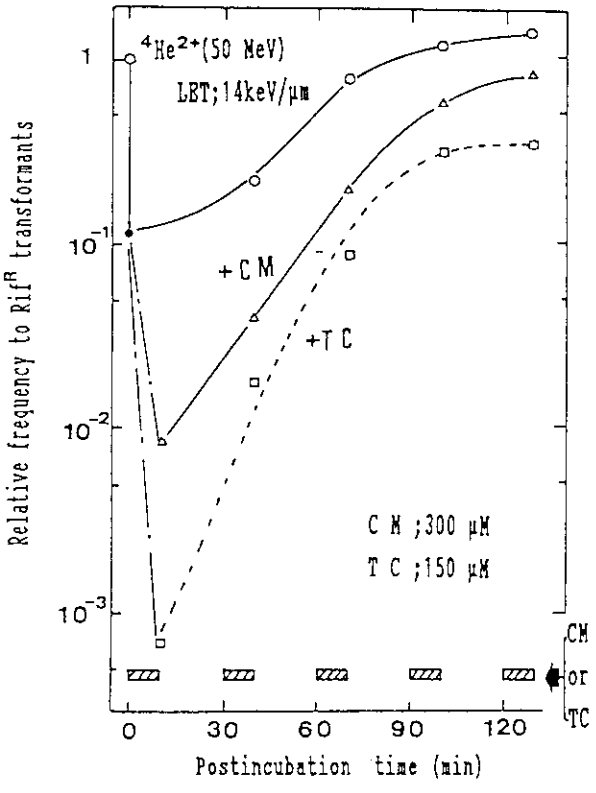

Fig.2. Recovery rate of transforming activity estimated by short period treatment with protein synthesis inhibitors during postincubation.

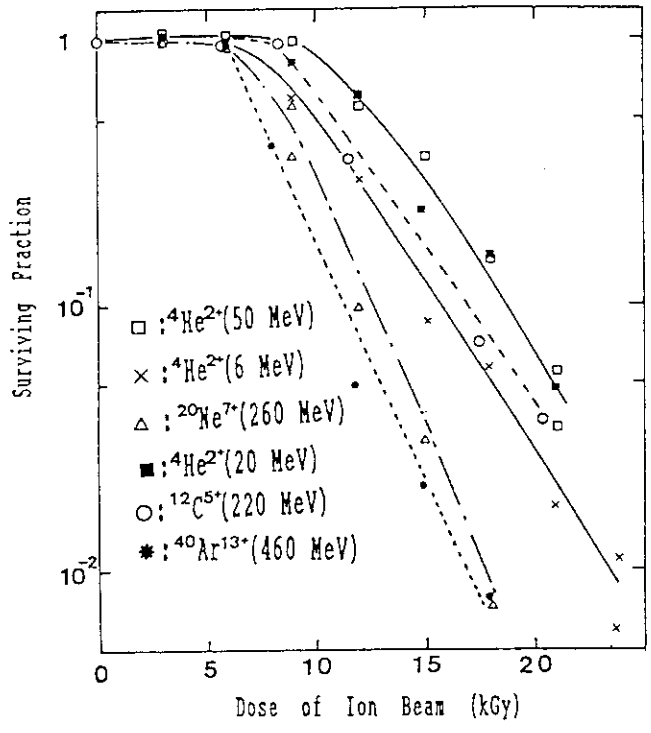

Fig.1 Ion beam survival curves for lyophilized cells of *D.radiodurans* .

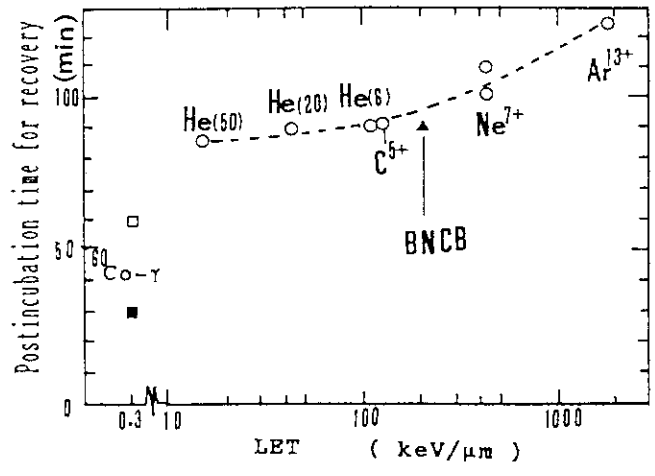

Fig.3. Relationship between the recovery times of transforming activity and LET values of ion beams. Numbers in parentheses indicate energy (MeV) of the ion beams. Closed and open symbols denote the recovery times of cells irradiated as cell suspension or after the lyophilization, respectively.

2.11 Method of Mutation Spectrum Analysis on DNA Irradiated with Ion Beams Using Shuttle Vector Plasmid pZ189

K. Harada, T. Nakano,
H. Watanabe[2], Y. Kobayashi[2], A. Tanaka[2] and M. Kikuchi[2]

Div. of Mol. Life Sci., PL Botanical Inst. PL Gakuen Women's Jr. College, JAERI, Takasaki, Biotech. Lab.[2]

We have been studying the subject of "the mechanisms of the DNA injury by ion beams and its repair on radioresistant bacteria (II)" in "the Advanced Radiation Technology Project by Ion Beam in JAERI", and we have already reported the results[1,2]. In this report we improved the assay method of the mutation in DNA base sequence to research the effect of BNC (Boron Neutron Captured) beams (α-particles) and ion beams ($^{12}C^{5+}$) on plasmid DNA.

A shuttle vector plasmid pZ189 was used as a plasmid DNA. The pZ189 DNA contains the pBR327 replication origin, β-lactamase gene, bacterial suppressor tRNA (*supF*) gene which serves as a mutagenesis target, and the SV40 early region (Fig. 1). Then, this plasmid DNA can be used in studying the mechanisms in eucaryotic and procaryotic mutation induction.

The plasmid pZ189 DNA was dissolved in Tris-EDTA buffer containing 0.3 M ^{10}B-enriched boric acid ($H_3{}^{10}BO_3$) at a concentration of 0.5 μg/μl. After then, the DNA was irradiated with BNC beams by ^{10}B (n, α)^{7}Li nuclear reaction of thermal neutron (3×10^9 n/cm^2/sec) in the heavy water (D_2O) facility of KUR operated at 5 MW. The dose rate was about 3.2 kGy/hr. On the other hand, the dried plasmid pZ189 DNA on the paper disk was irradiated with carbon ions ($^{12}C^{5+}$; 220 MeV, LET = 121 keV/μm) generated from AVF cyclotron in TIARA, JAERI Takasaki.

The irradiated plasmid pZ189 DNA was transformed in *Escherichia coli* wild type strain KY40 and DNA repair deficient mutant strain KY46 (*uvrA*$^-$) according to calcium chloride procedure. The SOS function of these strains was beforehand induced by UV-C irradiation. The two *E. coli* strains containing the irradiated plasmid pZ189 DNA were incubated during overnight for fixation of mutation.

The relative number of bacterial colonies was observed after 15 hrs incubation at 37°C on LB agar plates containing ampicillin as the surviving fraction after irradiation. As for α-particle exposure, the dose-effect curves of plasmid pZ189 DNA included in KY40 and KY46 were almost the same, and each D_{10} value was about 5 kGy. The mutation frequencies of pZ189 at D_{10} dose in KY40 and KY46 were about 3×10^{-5} and 6×10^{-5}, respectively[3]. Though the dose-effect curves of the plasmid irradiated with carbon ions were almost same between KY40 and KY46 strains, the dose-effect curves indicated the shoulder and each D_{10} value was above 15 kGy (Fig. 2). The difference of D_{10} value between plasmids irradiated with α-particles and carbon ions may be due to the cell condition, that is, wet cell or dried cell.

As shown in Fig. 1, the pZ189 DNA isolated from these *E. coli* strains was transfected into *E. coli* MBM7070/pKY241 cells. A plasmid pKY241 carries the *gyrA* gene of *E. coli* with amber mutation and chloramphenicol resistant marker. The transformants carrying mutation on *supF* gene in plasmid were selected as a nalidixic acid resistant and white colonies on LB agar plates with X-gal and IPTG[2-6].

From these results, we could obtain the pZ189 *supF* mutants efficiently, and started the next step analysis, that is, DNA base sequence analysis. From the data obtained up to the present, we found that 91.9 % of the plasmid mutation was base substitutions. Also, one-base deletions of 5.4 % and deletions of 2.7 % were detected (TABLE 1). Among

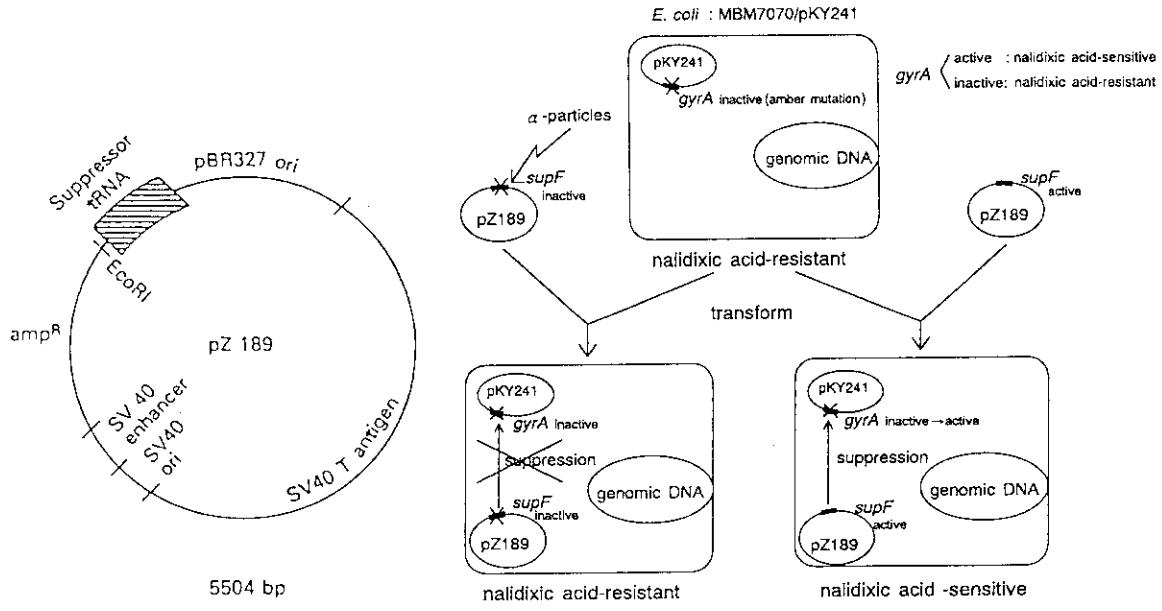

Fig. 1 Scheme of Shuttle Vector Plasmid pZ189 and Mutation Assay Method on pZ189 DNA.

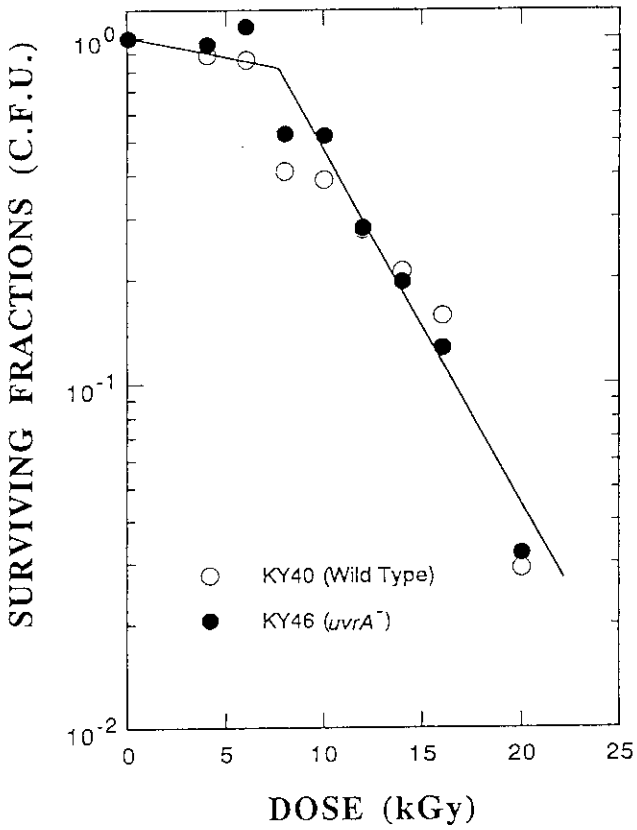

Fig. 2 Surviving Fractions of pZ189 Irradiated with $^{12}C^{5+}$ Ions.
Surviving fractions were obtained from the relative number of bacterial colonies of *E. coli* KY40 (wild type; open symbol) or *E. coli* KY46 (*uvrA*$^-$; closed symbol) transformed by ion beam-irradiated pZ189 DNA.

TABLE 1
DISTRIBUTION OF α-PARTICLES INDUCED *supF* MUTANTS BY CLASS

Type of Mutation	Number Observed	% of Total Mutations
Base Substitution	68	91.9
1 base	65	87.8
2 base	3	4.1
One-Base Deletion	4	5.4
Deletion	2	2.7
Total	74	100

these base substitutions, transversions predominated and no A:T to G:C transitions were detected (data not shown).

We are grateful to Dr. Kumio Okaichi, Dr. Hideki Matsumoto and Dr. Takeo Ohnishi (Nara Medical University) for providing us with biological materials and for their technical teaching. We are also grateful Patriarch Takahito Miki (Church of Perfect Liberty) for constant kind guidance and encouragement during this work. This work is a part of studies presented at the 3rd TIARA Research Review Meeting on June 29, 1994 (Takasaki)[6].

REFERENCES

1) K. Harada, R. Kimura, T. Nakano, H. Watanabe, A. Tanaka and M. Kikuchi, TIARA Annu. Rep. 1992 (1993) p. 46.
2) K. Harada, Proc. 5th Radiat. Process Symposium (in Japanese) (1993) p. 28.
3) K. Harada, T. Nakano, M. Saito and N. Mizuma, KURRI Prog. Rep. 1993 (1994) in press.
4) T. Nakano and K. Harada, PL G. W. J. C. Bull. **20** (1993) 46.
5) K. Harada, T. Nakano, R. Kimura, N. Mizuma and M. Saito, Proc. Sci. Meeting of KURRI (in Japanese) (1994) p. 81.
6) K. Harada, T. Nakano, H. Watanabe, Y. Kobayashi, A. Tanaka and M. Kikuchi, Abst. 3rd TIARA Res. Rev. Meeting (in Japanese) (1994) p. 70.

2.12 TRANSPORT IN A PLANT OF POSITRON-EMITTING TRACER PRODUCED WITH AVF CYCLOTRON

T.Fujimura[1], K.Adachi[1], H.Omichi[1], H.Uchida[2], T.Omura[2], T.Yamashita[2], H.Matsuoka[3], N.Shigeta[3], A.Osa[3], T.Sekine[3], M.Fukawa[4], H.Kobashi[4], K.Omasa[5], H.Yamaguchi[6]

[1]Department of Materials Development, JAERI, [2]Hamamatsu Photonics, [3]Dept.of Radioisotopes, JAERI, [4]Faculty Engineering, Gunma University, [5]The National Institute for Environmental Studies, [6]Dept. of Radiology, Komazawa Junior College

Positron-emitting tracers and positron emission tomograpny have been used for diagnosis in the medical field. In the plant science field, small number of studies have been performed with positron-emitting tracers[1-5]. The transport of a positron-emitting tracer in a plant can be monitored by detecting a pair of gamma-rays produced following annihilation of the positron. From the end of 1993, we have started to study for the transportation of positron-emitting tracers produced with high energy cyclotron in plants.

The aqueous solution of the positron-emitting ^{18}F tracer was directly produced with the reaction of $^{16}O(\alpha,pn)^{18}F$ by bombarding ultrapurified water with 1μA of 50MeV α-particles from a high energy cyclotron. The beams were emerged from vacuum through a Ti window into water. The planar positron camera has two detectors made from 23x27 scintillator array, composed of $Bi_4Ge_3O_{12}$ (BGO) crystals, the size of which is 2mmx2mmx20mm, coupled to a position sensitive photomultiplier tube (Hamamatsu R3941-2). The kidney bean plants (Phaseolus vulgaris L.) were cultivated with hydroponics.

At the time of experiment with positron camera, the kidney bean plant was illuminated with two incandescent lamps with attached filters to remove heat. The luminous intensity was 200μmol photon $m^{-2}s^{-1}$ at the leaves. The root of this plant was immersed in distilled water containing 70 MBq of ^{18}F at the beginning.

The two detectors of positron camera were positioned vertically 12 cm apart with the plant positioned in the mid-plane. After feeding the tracer to the root, the planar image was recorded for a leaf of the plant. Some image of a low concentration of the tracer spread on a leaf was observed.

REFERENCES

1)Jahnke,S., Stoecklin,G. and Willenbrink,J.
Planta 153, 56-63(1981)
2)Caldwell,C.D. et al.
J. exp. Bot. 35,431-443(1984)
3)Jaeger,C.H. et al. Physiol. Plant. 72,588-594(1988)
4)Roeb,G and Britz,S.J.
J. exp. Bot. 42,469-475(1991)
5)Mckay, R.M.L. et al.
Plant, Cell and Environment 11, 851-861(1988)

2.13 EFFECT OF ION BEAM IRRADIATION ON RABBIT RED BLOOD CELLS

K.Adachi[1], T.Fujimura[1], H.Watanabe[1], H.Omichi[1], M.Fukawa[2], H.Kobashi[2], M.Tamura[3]

[1]JAERI Takasaki, [2]Faculty of Engineering, Gunma University, [3]Hokkaido University

I.INTRODUCTION

Some studies of the gamma-ray irradiation effect on purely isolated hemoglobin solution established that methemoglobin(Fe^{3+})is formed from hemoglobin (Fe^{2+}) by radiation oxidation.[1] There have been little data of spectrophotometric study of irradiation effect on red blood cells containing hemoglobin. Recently, we have found that methemoglobin is also formed from hemoglobin in gamma-irradiated red blood cells in suspension. We have reported optical absorption spectra of red blood cells irradiated with $^{40}Ar^{13+}$ beams.[2] During ion-beam irradiation, we could observe reactions induced by irradiation inside organisms, by optical detection technique. For a step of the studies along this line, we will report here the irradiation effect on red blood cells irradiated with $^{4}He^{2+}$ beams.

II.MATERIALS AND METHODS

Red blood cells were separated from fresh blood taken from rabbits in the mornig of the experimental day. Phosphate buffer(pH 7.3) containing 1% heparin was added to the fresh blood and centrifuged at 2500 r.p.m. for 5min. This treatment was successively cycled three times. Thus obtained condensed red blood cell suspension was coated on pure quartz glass plate. The sample was irradiated in air by $^{4}He^{2+}$ ion-beams from AVF cyclotron. The ion-beams were ejected from beam line to atmosphere through thin Ti foil. After the irradiation, the buffer was added to the sample and the irradiated red blood cells were washed out and poured into an optical cell. The optical measurements of the samples thus obtained were performed.

The Yunisoku USP 410 spectrophotmeter was used for photometrical study. Light source was a 100-W halogen lamp. Light shorter than 500 nm from source was eliminated with a cut-off filter, then monochromated with a diffraction grating, and the monochromatic light was introduced to the sample for the measurement. The transmitted light was detected with a photomultiplier by the photon counting method.

III.RESULTS AND DISCUSSION

The spectra of rabbit red blood cells dissolved in the buffer after irradiation with $^{4}He^{2+}$ ions are shown in Fig.1. The energy of the ion beams was 20MeV and the current was 10nA. These spectra are the difference between the irradiated one and nonirradiated one. The increase of the absorption band around 630 nm can be seen clearly. This absorption band is attributable to methemoglobin (Fe^{3+}). The decrease of the absorption band around 576 nm can also be seen clearly. This absorption

band is due to oxyhemoglobin (Fe^{2+}) in red blood cells. These observation show that methemoglobin is formed from oxyhemoglobin in red blood cells by radiation oxidation induced by the irradiation with $^4He^{2+}$ beams.

Fig.2 shows the irradiation time dependence of the peak height ratio for methemoglobin(630 nm) and oxyhemoglobin(576 nm). This ratio maintained an almost constant value for the change of various beam currents and irradiation times. The result indicates that similar reactions took place in the all present experimental range.

The numbers of molecules of methemoglobin and oxyhemoglobin can be obtained from the peak heights of the bands using molecular extinction coefficient of methemoglobin and oxyhemoglobin. Recently, we have made clear that in the red blood cells in suspension irradiated with low dose rate gamma-rays, one molecule of methemoglobin was produced from one molecule of oxyhemoglobin. Only one reaction took place in this case. In the present study, for the red blood cells irradiated with $^4He^{2+}$ ion beams, the number of molecules produced from one molecule of oxyhemoglobin was less than one. This result indicates that the other reactions occur at the same time.

ACKNOWLEDGEMENT

The authors wish to express their thanks to Dr. A. Tanaka and Mr. T.Shimizu of JAERI for their technical assistance in handling of ion irradiation chamber.

References

1)Z.Szweda-Lewandowska, M.puchala, and P.A.Osumulski, Radiat.Environ.Biophys. 28(1989)39.

2)T.Fujimura, N.Ishihara, H. Watanabe, H.Omichi, H.Kobashi M.Tamura JAERI-M 93-241 (JAERI TIARA Annual Report vol.2)(1992)p57.

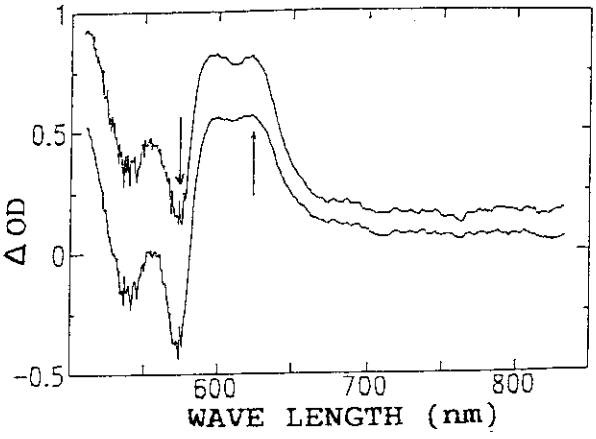

Fig.1 Optical absorption spectrum of rabbit red blood cells dissolved in the phosphate buffer after irradiation with 20 Mev, 10 nA $^4He^{2+}$ ion beam. Irradiation time; upper spectrum 1 min., lower spectrum 2 min. These spectra are the difference between the irradiated one and nonirradiated one.

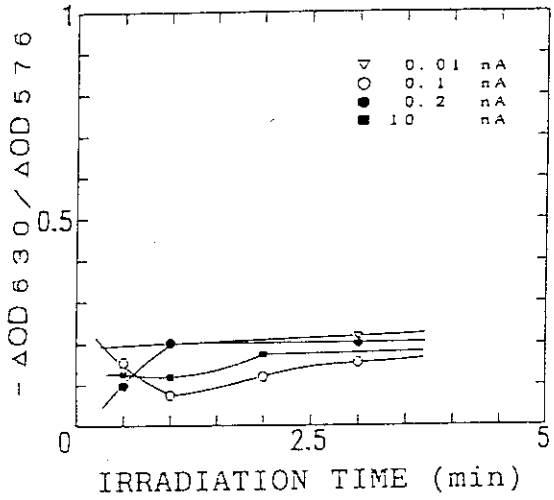

Fig.2 $^4He^{2+}$ ion beam irradiation time dependence of the peak height ratio for methemoglobin (ΔOD_{630}) and oxyhemoglobin(OD_{576}). The energy of ion beams was 20 MeV.

3. Radiation Chemistry

3.1 The Relationship between Chemical Structural Change and Energy Profile for Polymers Irradiated by Ion-beams.

Y.Hama, K.Hamanaka, H.Matsumoto,
T.Seguchi[2], T.Sasuga[2], H.Kudoh[2]
Advanced Res. Cent. for Sci. & Engn., Waseda Univ.,
JAERI, Takasaki[2]

Introduction.

Ion-beam has larger stopping power compared with γ-ray or electron-beams. Different irradiation effects from that by low stopping power beams has been expected. The energy deposition profile of the ion beam in a material should be represented by the Bragg curve along the track. If the ion beam stops in the material, the energy deposition of the ion beam comes to be different along the track. Therefore, if the stopping power effect (LET effect) is remarkable for polymers, the different chemical structural change along the track should be expected. This would be important for the degradation of polymers by ion-beam irradiation.

This work is concerning the depth profile of the change of the chemical structure induced in the slab of some polyolefins by heavy ion-beam irradiation.

Experimental.

Samples: In this work, low density polyethylene (LDPE), high density Polyethylene (HDPE) and polypropylene (PP), which were formed in a slab of 2 mm thick, were used.

Irradiation: Each sample was irradiated in vacuum by 10MeV, 20MeV H^+, 20MeV He^{2+} or 175MeV $^{40}Ar^{8+}$ with AVF cyclotron in JAERI Takasaki (TIARA). The absorbed dose at the surface of the sample estimated by the beam current.

Micro-FT-IR measurement: The sample irradiated was sliced along the cross-section to the slab surface and a thin film of some hundreds of μm could be obtained. The depth profile of the chemical structural change induced by irradiation was measured by using Micro-FT-IR spectrometer.

Results and discussion.

Structural change by ion-beam irradiation.

When LDPE or HDPE was irradiated in vacuum and then measurement was carried out in air, predominant chemical species induced were trans-double bond ($\sim$964cm^{-1}), carbonyl group ($\sim$1720cm^{-1}) and hydroxyl group ($\sim$3200cm^{-1}). The depth profiles of these species are similar to Bragg curve as shown in Figs.1 and 2. The fact that the carbonyl group could be observed and the profile was similar to Bragg curve, nevertheless irradiation

was carried out in vacuum, indicates that the formation of carbonyl groups comes from the reaction of allyl radicals with oxygen molecule which is occurred after the irradiated sample is exposure to air after irradiation. Moreover, the yield of carbonyl group for HDPE was higher than that for LDPE. This indicates that the allyl radical in HDPE is more stable than that in LDPE in vacuum at room temperature, as noted also by many other works.

The large yield of trans-double bond for PE suggests that LET effect is remarkable in ion-beam irradiation.

In PP, slight yield of double bond, carbonyl group and hydroxyl group were observed.

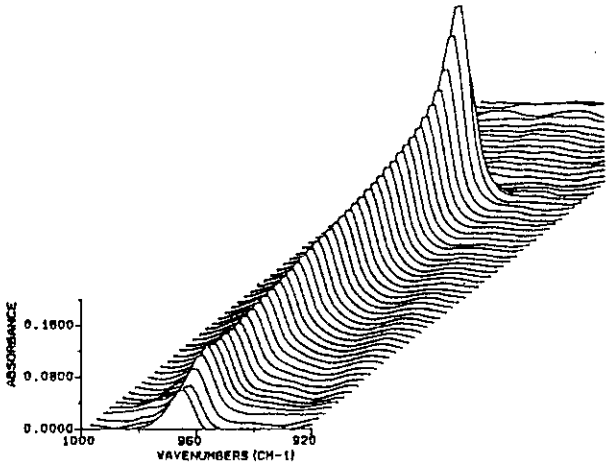

Fig.1. Depth profile of the absorption due to trans-double bond for LDPE irradiated to a dose of 0.5 MGy by 10 MeV H^+.

Relation between structural change and energy profiles.

It is important for LET effect that one supposes the relation between chemical structural change and stopping power. Figs.3 and 4 shows the particle energy dependence of the IR absorbance and the G-value for trans-double bond produced in LDPE and stopping power, in irradiation of 20 MeV He^{2+} and 175 MeV Ar^{8+}. In both cases, the peak of G-value and absorbance should be found to appear at higher energy than the peak in stopping power curves calculated by Bethe Formula or TRIM-code. This indicates that in the region under so much stopping power the chemical structural change which should be detectable by FT-IR observation is hardly induced. Very complex reaction

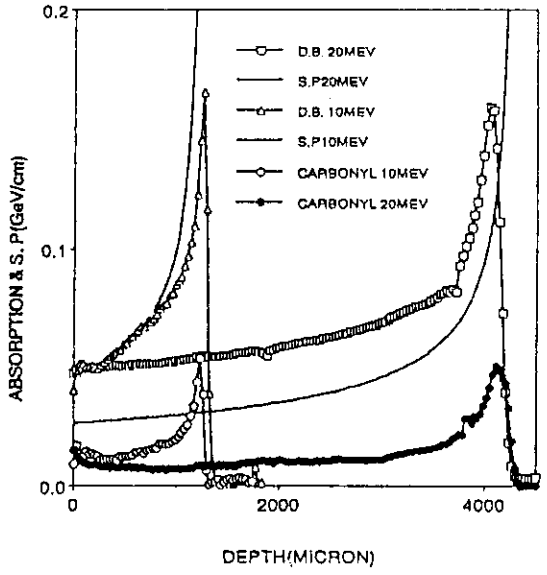

Fig.2. Depth profile of the trans-double (D.B) and carbonyl group for LDPE irradiated to a dose of 0.5 MGy by 10 MeV or 20 MeV H^+. The stopping power (S.P.) claculate are shown in solid lines.

would be occurred in high density excitation, especially in solid material.Up to date, we could not assign the chemical reaction in high stopping power region, yet.

Conclusion.

The irradiation effects of ion-beams for PE and PP are different from that of low LET beam such as γ-rays or electrons. The depth profile of the chemical structural change by ion-beam irradiation is similar to Gragg curve, though it is not correlative exactly with the energy profile. This may be due to complicated reactions in the heavy ion track in polymers. The further analysis should be required for the reaction process in the high stopping power region.

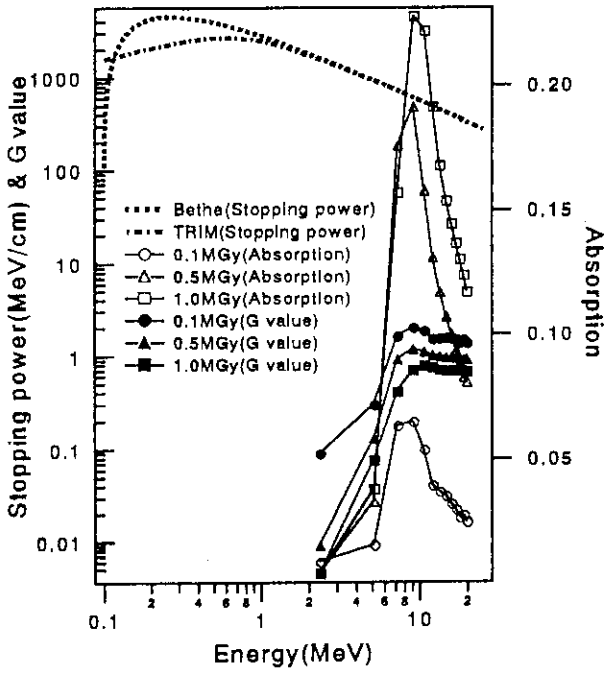

Fig.3. The particle energy dependence of the absorption and the G-value of trans-double bond for LDPE irradiated by 20 MeV He^{2+}, together with the stopping powers calculated based on Bethe fomula and TRIM-code.

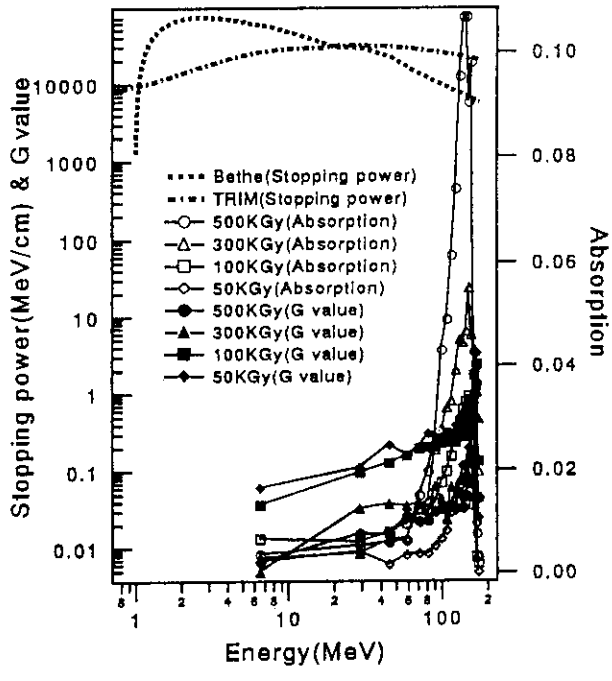

Fig.4. The particle energy dependence of the absorption and the G-value of trans-double bond for LDPE irradiated by 175 MeV Ar^{8+}, together with the stopping powers calculated based on Bethe fomula and TRIM-code.

3．2 Ion Beam Irradiation Effects on Hole Drift Mobility of Polysilanes

Shu SEKI, Seiichi TAGAWA, Youichi YOSHIDA,
Hisaaki KUDOH*, Tsuneo SASUGA*, Tadao SEGUCHI*,
Hiromi SHIBATA**, and Kenkichi ISHIGURE***

The Institute of Scientific and Industrial Research,
Osaka University.
*TRCRE, JAERI.
**The Research Center for Nuclear Science and Technology,
The University of Tokyo.
***Department of Quantum Engineering and System Science,
Faculty of Engineering, The University of Tokyo.

High hole drift mobility of polysilanes may be one of the most practical prospect for applicational view in the field of engineering of polysilane derivatives, and R&D have been intensively carried out for this characteristics of polysilane derivatives. The reason why carriers can quickly transport in a polysilane media, which has only single bonded silicon skeleton, seems to be closely connected to unique electronic structures of polysilanes, that is so-called s-conjugated system.

The values of hole drift mobility in poly(methylphenylsilane) ; PMPS were obtained by the conventional DC Time-of-Flight (TOF) measurement, and the mechanism and potential of high hole drift mobility will be discussed in the present paper in relation with the suggested model of electronic structures and their changes with ion beam irradiation.

The values of hole drift mobility obtained here corresponded to several previous data[1-4], and the value was estimated for PMPS to be 4.0×10^4 $cm^2/V \cdot sec$ at room temperature. The temperature dependence;

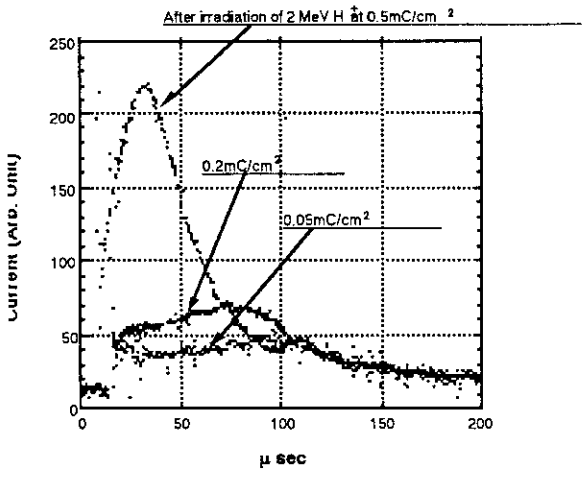

Fig. Changes in transient current pulse shapes of irradiated poly(methylphenylsilane) at 298K, 3.3x10 V/cm

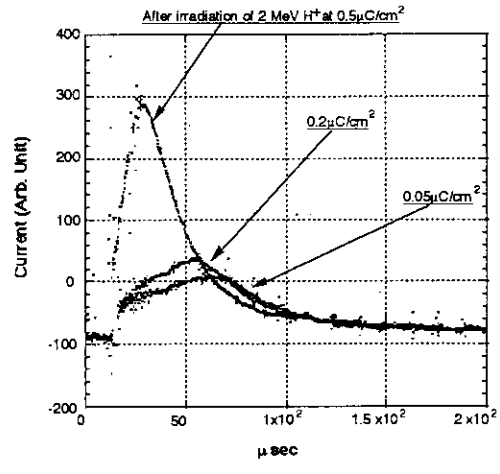

Fig. Changes in transient current pulse shapes of irradiated poly(methylphenylsilane) at 298K, 4.2x10⁴ V/cm

Facilities and Instruments
TIARA Cycrotron Accelerator

Reserch Field
Radiation Chemistry, Solid State Physics

Arrhenius plot and the field dependence of hole drift mobility can be well explained by Poole-Frenkel model which is similar to the model for PVK. Further, the value of activation energy for PMPS was obtained to be 0.39eV. This value reasonably supports the charge resonance model suggested in our previous works[5].

Ion beam irradiation was carried out for PMPS using Van de Graaff accelerator in RCNST, University of Tokyo and AVF cyclotron, Takasaki JAERI, and the values of carrier mobility were compared before the irradiation with that after. The irradiation makes charge carriers in polysilanes highly mobile, and the observed flight time of the carriers was distributed for shorter time region. The acceleration and multi-compornent mobility seems to be basically explained by a simple model of 3-dimensional like network structure induced by ion beam irradiation, which is also suggested in our previous studies[6]. Namely, intramolecular potential gap was reduced with extended s-conjugatied system. Further, electron conduction, which had been never observed for polysilane derivetives, was detected for the ion beam irradiated PMPS, and the transient pulse shape will be also reported.

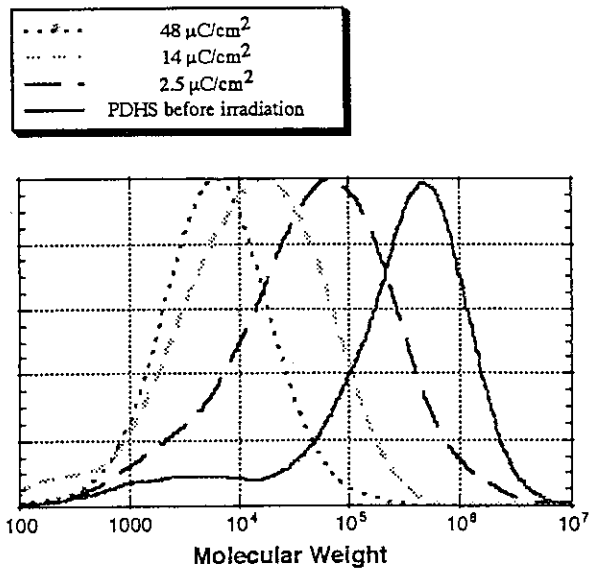

Fig. Molecular weight changes of PDHS with the irradiation of 45MeV H^+ Beam

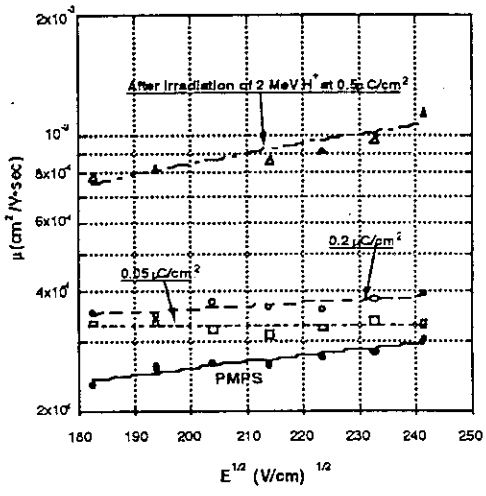

Fig. Semilogarithmic plot of hole drift mobility μ against $E^{1/2}$ $(V/cm)^{1/2}$ in ion beam irradiated poly(methylphenylsilane) films at 298K

References

1 Kepler, R. G.; Zeigler, J. M.; Harrah, L. A.; Kurtz, S. R. Phys. Rev. B 1987, 25, 823.

2 Fujino, M. Chem. Phys. Lett. 1987, 136, 451.

3 Stolka, M.; Yuh, H. J.; McGrane, K.; Pai, D. M. J. Polym. Sci., Polym. Chem. Ed. 1987, 62, 547.

4 Abkowitz, M. A.; Knier, F. E.; Yuh, H. J.; Weagley, R. J.; Stolka, M. Solid State Commun. 1987, 62, 547.

5 Ushida, K.; Kira, A.; Tagawa, S.; Yoshida, Y.; Shibata, H. Proc. ACS PMSE 1992, 66, 299.

6 Seki, S.; Shibata, H.; Ban, H.; Ishigure, K.; Tagawa, S. Macromolecules, To be published.

3．3 Radiation Effects of Ion Beams on TCNB in PVA Films.

H.Hiratsuka, R.Tomita, Y.Matsumoto,
M.Taguchi †, H.Namba † and Y.Aoki †
Department Chemistry, Gunma University
† Takasaki Radiation Chemistry Research Establishment, JAERI

It has been confirmed that the radical anions of TCNB were produced by the ion beam irradiation of Ar^{11+}, Ar^{8+} and C^{5+}, and its dose dependence of the radical anion formation was examined.

INTRODUCTION

We have studied radiation effects of He^+ ions on triphenylmethanol doped in poly(vinyl butylal)film. He^+ ions were generated by Takasaki Ion Beam Implanter and was accelerated by 200 keV. By the simultaneous irradiation with He^+ ions and 337-nm light from a nitrogen laser, fluorescence emission of triphenylmethyl radicals was observed. Dose dependence of the emission intensity was examined and reaction cross section was calculated [1]. In this year, we have studied radiation effects of ion beam form AVF cyclotron of JAERI on organic molecules doped in polymer films by measuring UV-VIS absorption spectrum.

RESULTS AND DISCUSSION

Figure 1 shows UV-VIS absorption spectra of TCNB doped in poly(vinyl alcohol) [PVA] film irradiated with 220-MeV C^{5+} ions. For comparison, absorption spectra of TCNB irradiated with 1-MeV electron beam and ^{60}Co γ-ray are shown. These spectra show peaks around 464 nm and 377 nm, and are similar to that observed for TCNB irradiated with ^{60}Co γ-ray in MTHF glass at 77 K [2]. It is safely said that the radical anion of TCNB is produced in PVA film by ion-beam irradiation.

Figure 2 shows the absorption spectrum of TCNB irradiated with 330-MeV Ar^{11+} ions. The 464-nm peak is observed, where, the other peaks in the shorter wavelength region are obscured by the back-ground absorption which gradually increases towards 300 nm. This may be due to carbonation of the film with increase of dose.

Dose dependence of radical anion formation was examined. Figure 3 is the plot of absorbance at 464-nm peak against the dose of 330-MeV Ar^{11+} ions. The absorbance increases with increase of dose, and shows maximum value of OD=0.03 at about 20 kGy and then decreases. As shown in Figure 4 lifetime of the radical anion produced by ^{60}Co γ-ray with dose of 10 kGy is about 4h in PVA film. Such a long lifetime may be also expected for the radical anion produced by ion-beam irradiation. By considering the long lifetime, the decrease of the 464-nm peak due to the radical anion observed in Figure 3 is ascribable to the annihilation of radical anion by collision with ions. Study of dose dependence is now progress for

electron beam and ^{60}Co γ -ray. Radiation effects of ion beam will be discussed in comparison with γ -ray and electron beam irradiation.

References

[1] M.Taguchi, Y.Aoki, H.Namba, S.Nagai, H.Maeoka and H.Hiratsuka, The 36th symposium on radiation chemistry (Hachiouji)2O13.

[2] T.Shida Electronic Absorption Spectra of Radical Ions. Elsevier (Amsterdam)

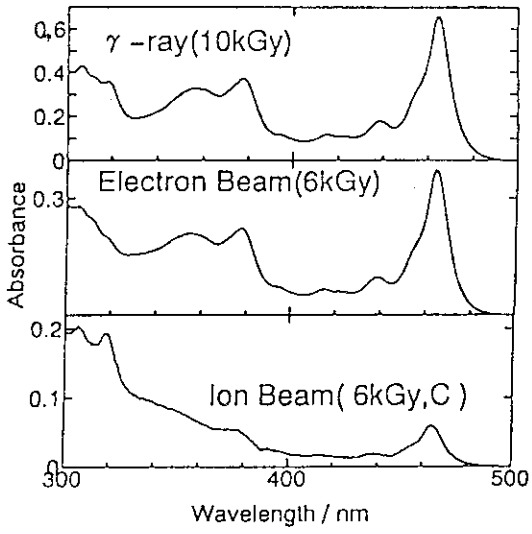

Figure 1. Absorption spectra of TCNB in PVA film irradiated with 220-Mev C^{5+} ions, 1-MeV electron beam and ^{60}Co γ -ray.

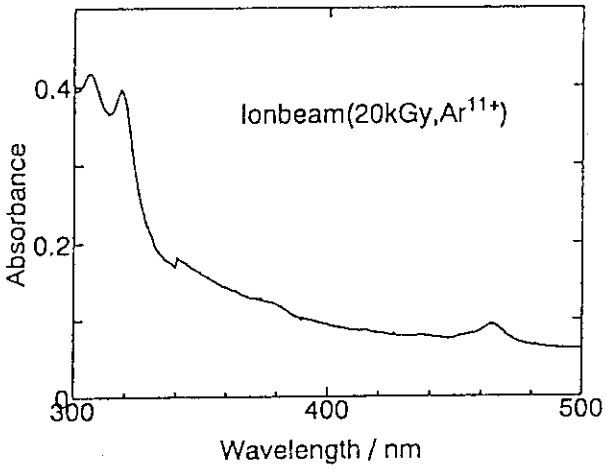

Figure 2. Absorption spectrum of TCNB in PVA film irradiated with 330-MeV Ar^{11+} ions.

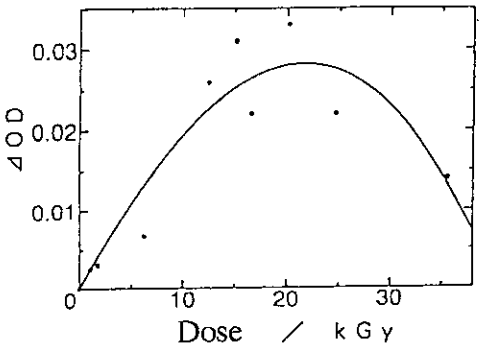

Figure 3. Dose dependence of the absorbance at the 464-nm peak of TCNB radical anion.

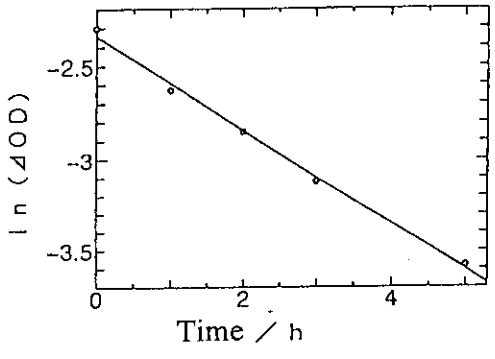

Figure 4. Time dependence of the absorbance at the 464-nm peak of TCNB radical anion produced by γ -ray irradiation.

3．4 LET Effect on Radical Formation in Ion-Irradiated Alanine

H. Koizumi[1], T. Ichikawa[1], H. Yoshida[1],
H. Namba[2], M. Taguchi[2], T. Kojima[2]
Fac. Engineering, Hokkaido University[1], JAERI, Takasaki[2]

Radiation effects depend on quality of radiation. It is mainly due to difference in local distribution of deposited energy. Reactive intermediates form with a distribution according to the local dose distribution. If their reaction probability depends on their concentration, the radiation effects alter. We are aiming to clarify relation between the radiation effects, the local distribution of intermediate, and the quality of radiation. Ion beams are usefull to study this subject. The local dose distributions for ion beams are much different from those for low LET radiations. The distribution can be altered with changing the energy and the spices of the ions. We have previously investigated radical formation in alanine irradiated with 0.5-3MeV H^+ and He^+ ions[1]. The radical yields depend on energy and species of the ions. We have estimated average radii for the radical distribution from the relationship between the radical yields and ion fluence. The radii are 4-6nm for these ions. In this work, we have investigated radical formation in alanine irradiated with 175MeV Ar^{8+} and 460MeV Ar^{13+} ion beams to get further insight into radiation effects of ion beams.

Experimental

Samples used are alanine film dosimeters, which have been developed at JAERI[2]. The dosimeters are made of low-density polyethylene(LDPE) as binder and alanine powder. Two kinds of the dosimeters have been used. One is the film of 160μm thickness with the 50:50 weight % ratio of alanine/LDPE (AL1). The other is the film of 220μm thickness with the 60:40 weight % ratio of alanine/LDPE (AL2). The densities of AL1 and AL2 are 1.22 g cm^{-3} and 0.812 g cm^{-3}, respectively. Irradiation was carried out at the HX1 port of TIARA. Pieces of the sample films (ca. 10mm × 10mm) were placed on a holder in a vacuum chamber. 175MeV Ar^{8+} and 460MeV Ar^{13+} ion beams were generated with the AVF cyclotron, and were irradiated to the samples. The ranges of 175MeV Ar^{8+} and 460MeV Ar^{13+} ions in AL1 are 61 and 226μm and those in AL2 are 92μm for and 340μm, respectively. 175MeV Ar^{8+} ions stop within the first film, while 460MeV Ar^{13+} ions stop within the second films. The currents of the beams were measured with a Faraday cup on the holder plate just before and after the irradiation. ESR spectra of radicals in the ion-irradiated films were measured with X-band spectrometers at JAERI Takasaki and at Hokkaido university. Radical concentrations were calculated by double integration of the ESR spectra and they were calibrated with DPPH as a reference.

Results and discussions

Figures 1 and 2 show radical yield in the alanine films irradiated with the Ar ion beams as a function of ion fluence. The yields are constant in the lower fluence than $2\text{-}3\times10^{10}$ ions cm^{-2}, whereas the yields decrease with increasing fluence in the higher fluence than it. This decrease is ascribed to overlap between ion tracks. Radicals generated within a shorter distance than a certain one will react and become products undetectable with ESR. As increasing the fluence, distances among ion tracks decrease. In fluence higher than the critical one, a part of radicals generated in an ion track reacts with radicals generated in another ion track. This causes decrease in the radical yield. The reciprocal of the critical fluence hence gives average cross section for the radical distribution along the ion tracks. The critical fluence, $2\text{-}3\times10^{10}$ ions cm^{-2} gives the radius of 30-40nm. This is 5-10 times larger than those for the H^+ and He^+ irradiated alanine. The yields in the lower fluence give G-values of 2.3 and 4.2 for alanine irradiated with 175MeV and 460MeV Ar beams, respectively.

The difference between the radii for Ar ion irradiated alanine and those for H^+ and He^+ irradiated ones is due to the difference in local

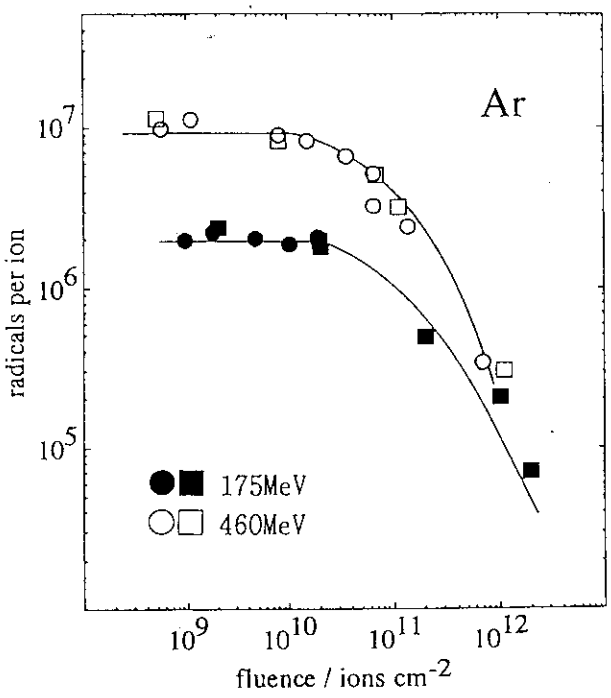

Figure 1. Radical yield in alanine dosimeter as a function of ion fluence for 175MeV (●■) and 460MeV (○□) Ar ions.

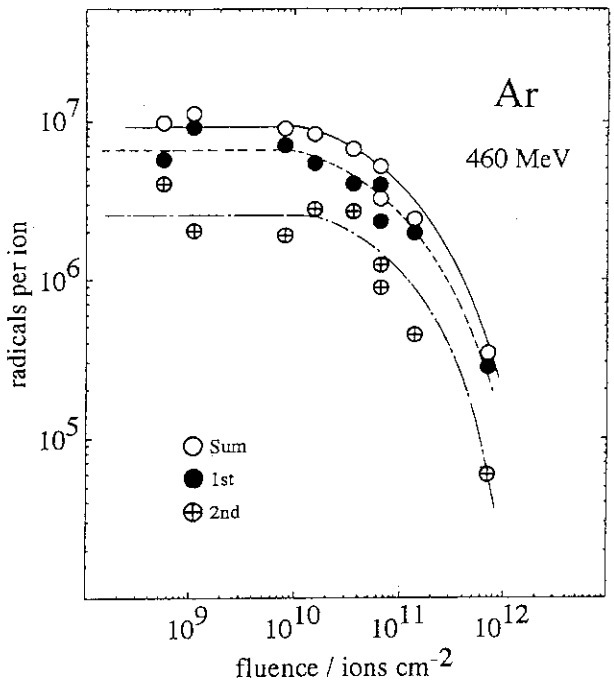

Figure 2. Radical yield in alanine dosimeter irradiated with 460MeV Ar ions. The yield in the first film (●), in the second film(⊕) and the sum of the yields in the two films(○).

dose distribution in ion tracks. Figure 3 shows radial dose distribution in the ion tracks of these ions. They are calculated with an equation proposed by Chatterjee et al.[3, 4] If the yield of the radicals varies in response to the local dose and it is the same function of dose irradiated with low LET radiation, the radius at the dose of 5×10^4Gy will a measure of the radius of radical distribution. Since G-value for radicals in gamma-irradiated alanine start to decrease at the critical dose of 10^5 Gy[1], overlap of the region higher than 5×10^4Gy exceeds the critical dose and the yield hence decreases. The radii of 5×10^4Gy are 1-3nm for the H^+ and He^+ ion beams, whereas it is 10-20nm for Ar ion beams. This can explain the difference in the experimentally obtained radii.

The G-values of radical yields are plotted in figure 4 as a function of average LET (<LET>). This plot shows that the G-value is not a simple function of <LET>. The G-values tend to decrease with increasing <LET> among H^+ and He^+ ion-irradiated alanines. However, the G-values for alanine irradiated with Ar ions, whose <LET> are about 10 times larger than those of He^+ ion-irradiated ones. This is due to the large radii in Ar ion-irradiated alanine. LET is deposited energy per unit length along ion trajectory. This energy radially extends to a certain radius in ion tracks. As shown above, the radii for Ar ions are 5-10 times larger than those for H^+ and He^+ ions. G-values are a function of local dose rather than <LET>. If we estimate the local dose with a simple cylindrical model shown in figure 5, average dose in ion tracks (<dose>) is

$$<\text{dose}> = \frac{E_i}{\pi r^2 L} \qquad (1),$$

where E_i is the initial energy of the ions, L is the range of the ions, and r is the radius of the ion tracks. Since <LET> = E_i / L, the equation (1) is

$$<\text{dose}> = \frac{<\text{LET}>}{\pi r^2} \qquad (2).$$

The values of <LET> for the Ar ions are 10 times larger than those for the He ions, and they are 30-100 times larger than those for the

H ions. The radii for the Ar ions are 5-10 times larger than those for the H and He ions. The values of <dose> for the Ar ions are then 0.1-0.4 of those for the He ions, and they are comparable to those for the H ions. The G-values for the Ar ions are hence analogous values to those for the H ions.

In conclusion, local dose distribution in ion tracks and G-values for low-LET radiation explain the dependence of radical formation in alanine on ion beams. The knowledge of local dose distribution in ion tracks and G-values in high dose region is then important to estimate the radiation effects in ion-irradiated materials.

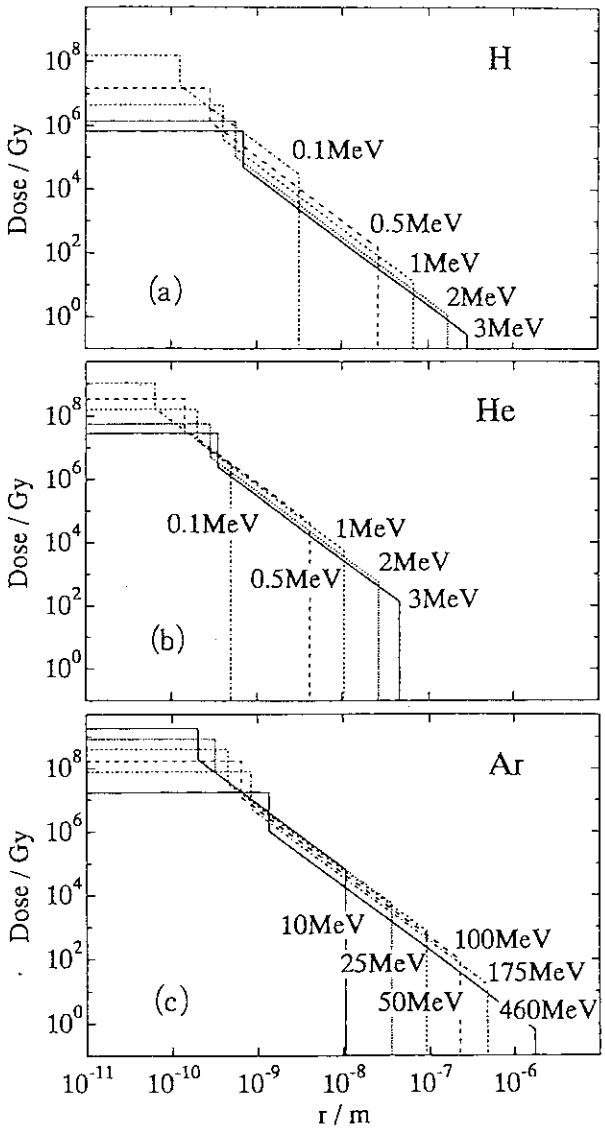

Figure 3. Radial dose distribution in ion tracks: (a) H ions, (b)He ions, and (c) Ar ions.

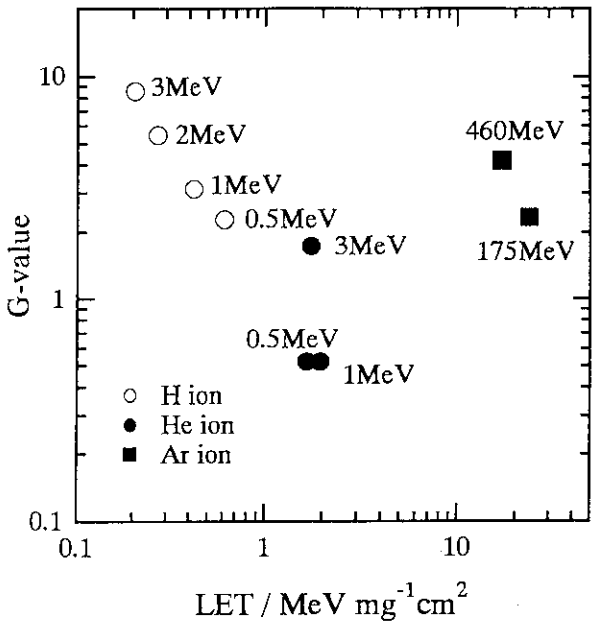

Figure 4. G values for radical formation in alanine plotted as a function of average LET.

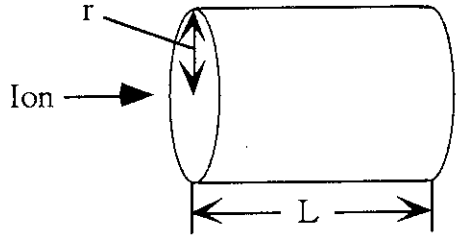

Figure 5. Cylindrical model for ion tracks.

References

1)V. V. Krushev, H. Koizumi, T. Ichikawa, H. Yoshida, H. Shibata, S. Tagawa, and Y. Yoshida, Radiat. Phys. Chem., 44 (1994) 521.

2)T. Kojima, H. L. A. Ranjith, Y. Haruyama, S. Kashiwazaki, and R. Tanaka, Appl. Radiat. Isot., 43 (1993) 41.

3)A. Chatterjee and H. J. Schaefer, Radiat. Environm. Biophys., 13 (1976) 215.

4)J. L. Magee and A. Chatterjee, *Track reactons of radiation chemistry,* in *Kinetics of nonhomogeneous processes,* G.R. Freeman, Editor, (John Wiley & Sons, New York, 1987) p. 171.

3.5 MICRODOSIMETRY WITH HEAVY IONS (II)

Hideki Namba, Mitsumasa Taguchi, Katsutoshi Furukawa[2], Yasushi Aoki and Shin-ichi Ohno[3]

JAERI,Takasaki,Biotech.Lab., JAERI,Tokai,Laser-Chem.Lab.[2], Tokai Univ.,Inst.Res.Develop.[3]

I. INTRODUCTION

Irradiation with high energy heavy ions gives rise to ununiform energy deposition to the materials to make so-called "track structure". Ionizations and excitations by the energy deposition will be successive to the direction of incident ions; while, to the vertical direction of incident ions, there exist "physical core", which is produced directly by incident ions, and "penumbra", which is caused by secondary electrons.[1] It is very important for the Radiation Chemists to get the information of energy deposition in order to clarify the "chemical effects" followed by the energy deposition or "physical effect". However, there are only a few research works to investigate the energy deposition directly because of experimental difficulty.

We have installed an experimental apparatus for basic study on radiation chemistry with heavy ions (EA-BRACHI) at HX1 port of AVF cyclotron in TIARA,[2] and started to measure the spatial distribution of energy deposition to gaseous Ar induced by high energy Ar ion beams.[3]

II. EXPERIMENTAL

The experimental apparatus for this research is essentially the same as we have reported before.[3] Figure 1 shows a schematic diagram of the main part of experimental apparatus, the third chamber of EA-BRACHI connected to a vertical beam port of AVF cyclotron in Second Heavy Ion Irradiation Room. EA-BRACHI has differential pumping system

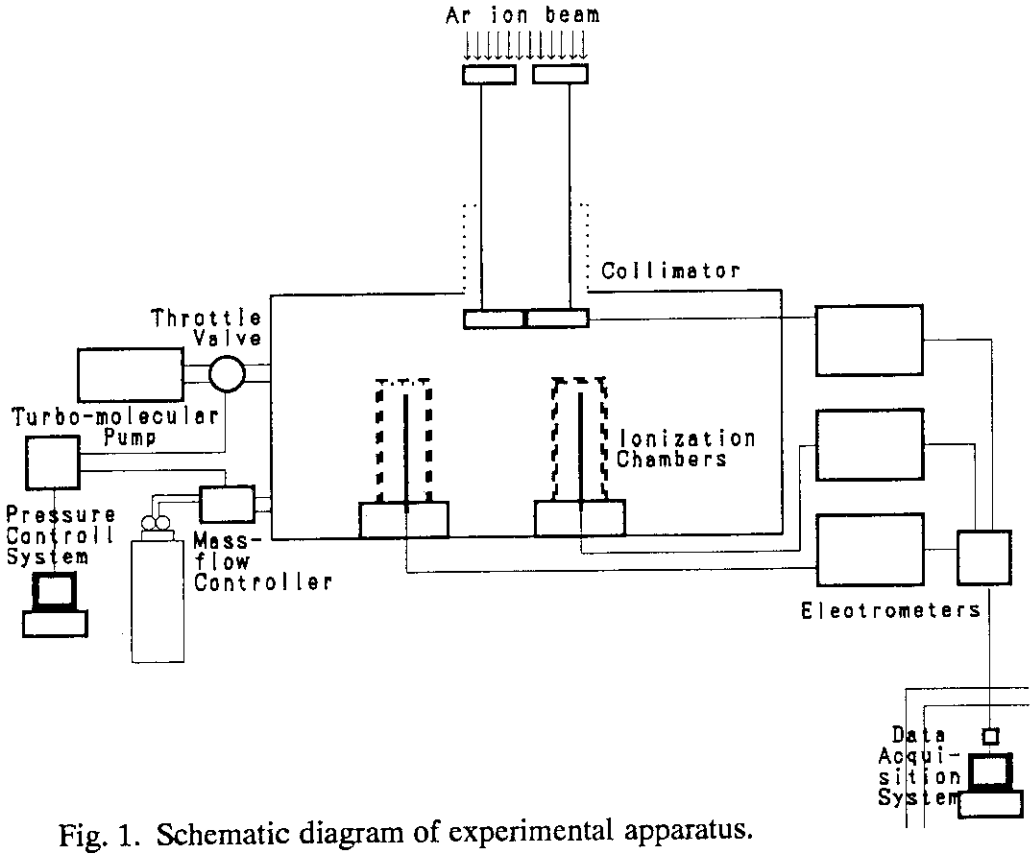

Fig. 1. Schematic diagram of experimental apparatus.

with turbo-molecular pumps, tantalum collimators and pressure control system. It is possible to control the pressure in the third chamber with this system during ion beam irradiation.

Gaseous Ar is introduced to the third chamber with controlling its flow rate by mass-flow controller (MKS 147B). The pressure of the gas is measured with pressure sensors (MKS Baratron 122A and 127A), and controlled with pressure controller (MKS113A) by pumping through throttling valve (MKS 253A-2-4CF-2) connected to the turbo-molecular pump (Osaka Vacuum TG1000M) in the third chamber.

Heavy Ar ion beam (175MeV) from the cyclotron are introduced to the EA-BRACHI through a bending magnet of HX1 port. The beam monitoring and position setting were done as described before[2]. The ion beam was introduced through the collimator (0.1mm) connected to the third chamber.

Two small ionization chambers, as shown in Fig. 1, were set on a stage, which are possible to move all directions with an accuracy of 5μm. The details of the ionization chambers were reported in former publication.[3] The distance from the center of ion beam was changed with moving the stage. Ionization current induced by Ar ion beam was measured by two electrometers (Keithley 617) connected to the collecting electrodes of ionization chambers. D.C. voltage was supplied to the high voltage electrode from high voltage power supplies (Hamamatsu C3350). The signals were transferred by an optical fiber to the neighboring operation room, and were accumulated by a computer (NEC PC9801NA) with 10 times sampling after the current being steady state.

The intensity of the incident ion beam has about ±10% fluctuation during the irradiation, therefore, the intensity was monitored by another electrometer (Keithley 617) and make corrections.

III. RESULTS AND DISCUSSION

Fig. 2 shows the applied voltage dependence of ionization current induced by 175MeV Ar beam irradiation in 6.2 torr Ar gas at 100mm from the beam center. The applied voltage region between 40 to 80V, the current became constant (saturation region), whereas the ionization current increased rapidly at more higher voltage. The applied voltage dependence of ionization current at 71.5mm is shown in the same figure. There was a saturation region also at more than 40V; the saturation current at 71.5mm was larger than 100mm. There was no amplification region at 71.5mm. It will be ascribed space charge effect in the chamber.

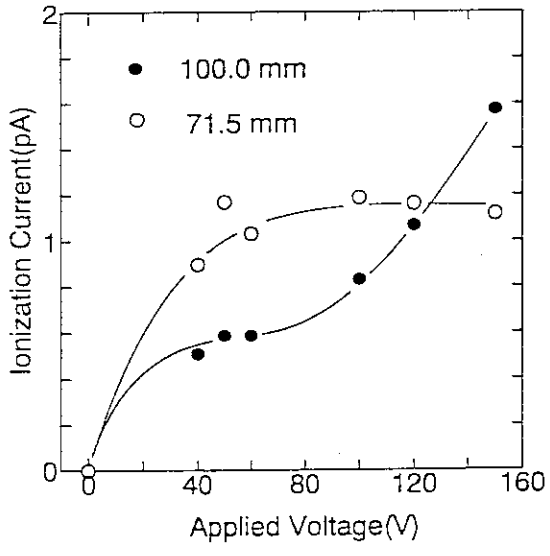

Fig. 2. Applied voltage dependence of induced ionization current.

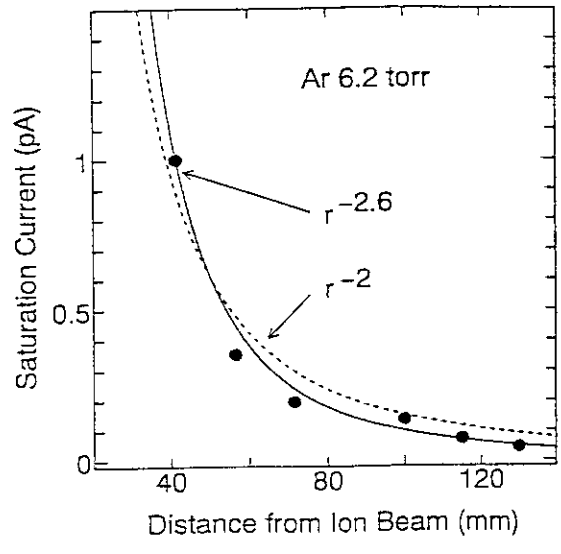

Fig. 3. Saturation current at different distances from the center of ion beam.

The saturation current at different distance from the center of ion beam is shown in Fig. 3. The current is corresponds to the amount of ions produced inside of the ionization chambers. The amounts of produced ions are predicted[3] to be proportional to reciprocal square of the distance (r). The dotted line in the figure indicates the curvature of r^{-2}. The solid line in the figure is the result of the least square fitting: the best fitting was $r^{-2.6}$. It needs more studies both experimentally and theoretically to clarify the steep decrease of saturation current.

REFERENCES

1) J. L. Magee and A. Chatterjee. Track reactions of radiation chemistry. Kinetics of nonhomogeneous process (J. Wiley & Sons), edited by G. R. Freeman, 171 (1987).
2) H. Namba, Y. Aoki, M. Taguchi and K. Furukawa, experimental apparatus for basic radiation chemistry with heavy ion beams, JAERI TIARA Annual Report *1*, 163 (1992).
3) H. Namba, M. Taguchi, K. Furukawa, S. Ohno and Y. Aoki. Microdosimetry with heavy ions, JAERI TIARA Annual Report *2*, 69 (1992).
4) R. Katz, B. Ackerson, M. Homayoonfor and S. C. Sharma, Inactivation of cells by heavy ion bombardment, Radiat. Res., *47*, 402 (1971).

3.6 CHARACTERISTICS OF VARIOUS FILM DOSIMETERS FOR ION BEAMS II

Takuji KOJIMA, Haruki TAKIZAWA, Hiroyuki TACHIBANA, and Hiromi SUNAGA
Advanced Radiation Technology Center, JAERI

I. INTRODUCTION

Absorbed dose is a common measure for interpretation and comparison of radiation effects on organic materials and biomaterial samples, and detailed dose distribution in materials, especially in depth is also required for it.

We have developed precise dosimetry techniques both for ^{60}Co gamma-rays and electron beams of energies from 0.15 to 3 MeV so far. On the basis of these techniques, preliminary studies on dose response characterization of film dosimeters and depth dose profile measurement using various film dosimeters have been carried out for ion beams from the AVF cyclotron in TIARA[1]. Alanine-PE[2], Gaf film(GAF Chemicals Co.)[3], Radiachromic film (RCD, FWT-60, Far West Technology)[4], and cellulose triacetate dosimeter(CTA, FTR-125, Fuji Photo Film Co., Ltd.)[5] with about 10 to 200 μm in thickness are well-characterized for ^{60}Co gamma-rays and electron beams, and now being applied to ion beam dosimetry.

In parallel with these studies, design and development of dosimetry technique are in progress for precise on-line fluence monitoring, accurate characterization of irradiation fields, and absorbed dose calibration.This technique is on the basis of simultaneous measurement of energy fluence, particle fluence, and absorbed dose by using a total absorption calorimeter, a Faraday cup, and stacks of uncalibrated thin film dosimeter, respectively[6].

This paper focuses on some depth-dose profile measurement studies with high spatial resolution in depth by using film dosimeters, and on comparison of measured depth-dose profiles with those obtained by simulated calculations.

II. EXPERIMENTAL

For depth-dose profile measurement, dosimeter samples were prepared by two methods;

(1)film dosimeters were stacked one on one up to the thickness enough to stop ion beams completely,

(2)one sheet of film dosimeter was put beneath a wedge-shaped polymer phantom with different thick steps up to the thickness enough to stop ion beams completely, by equivalent thickness to one sensitive layer of film dosimeter.

These methods may have limitation in resolution in depth due to the thickness of dosimeter itself, however, the method(2) using Gaf dosimeters, which consists of 8-μm thick sensitive layer and inert base polymer, will provide higher resolution than the method(1) as fine as thickness of the sensitive layer of dosimeter.

Ion beams irradiations of above dosimeters samples were done with 100 x 100 mm^2 scanning beams of 10, 20-MeV protons and 20, 50-MeV helium ions from the cyclotron in the evacuated "wide-area ion irradiation chamber"[7]. Beam currents were 200 nA for CTA dosimeters and 20 nA for others. Fluence uniformity on irradiation area is approximately within ±3%. The dosimeter samples were irradiated to about 40 and 2 kGy at the surface for CTA dosimeters and

others, respectively. Dosimeter responses of alanine-PE dosimeter and others were analyzed in terms of electron spin resonance (ESR) spectral amplitude per unit mass and optical density change per unit thickness at specified wavelengths, respectively.

Simulated calculations of depth-dose profiles were carried out by using ELOSS code. It is one of the modified OSCAR code[8] and gives energy deposition in interest materials by steps of input resolution on the basis of initial energy at the surface of the interest layer and mass collision stopping power data[9].

III. RESULT AND DISCUSSION

The depth profiles of energy deposition or dose response for 20-MeV protons and helium beams are shown in Fig.1 and 2, respectively. The former is measured by the method(1) using CTA dosimeters (thickness of one dosimeter is 125 μm, 16.1 mg/cm^2) and the latter is measured by the method(2) using Gaf film(0.96 mg/cm^2 thick sensitive layer coated on 100-μm thick polyester) with polyimide phantoms with 1.16-mg/cm^2 thick steps. Dose responses of CTA and Gaf film are plotted against depth in the materials with histogram of solid line and black closed circle(•), respectively.

Calculation results with two different depth resolution: one dosimeter thickness and its 1/10, are shown in the figures with the histograms of dotted line and solid line curves, respectively.

Depth dose profiles curve obtained by experimentally and calculation are in good agreement in position of the peak: 250 mg/cm^2 for 20-MeV protons and 39 mg/cm^2 for 20-MeV helium beams, and in shallow part of Bragg curves with different depth resolutions of calculation. Calculation results with the same depth resolution agree with measured profiles. The difference in absorbed dose between experimentally and theoretically is mainly attributed to depth resolution and averaging in interested

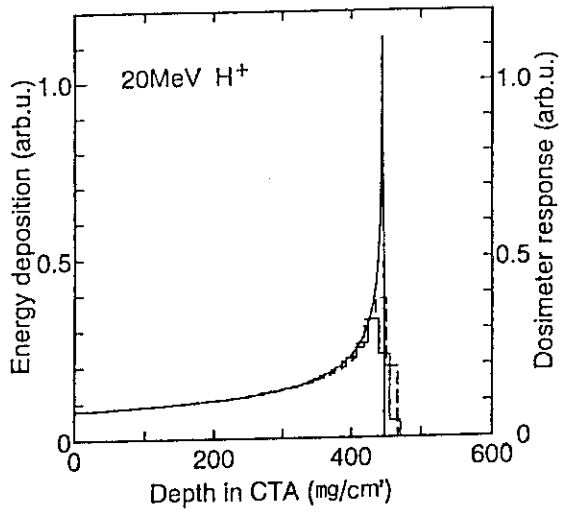

Fig.1 Depth dose profiles for 20-MeV protons. The histograms of solid line and dotted line are measurement by stacked CTA dosimeters(thickness: 16.1 mg/cm^2) and ELOSS calculation with resolution of 16.1 mg/cm^2, respectively. The solid line curve is calculation with resolution of 1.61 mg/cm^2.

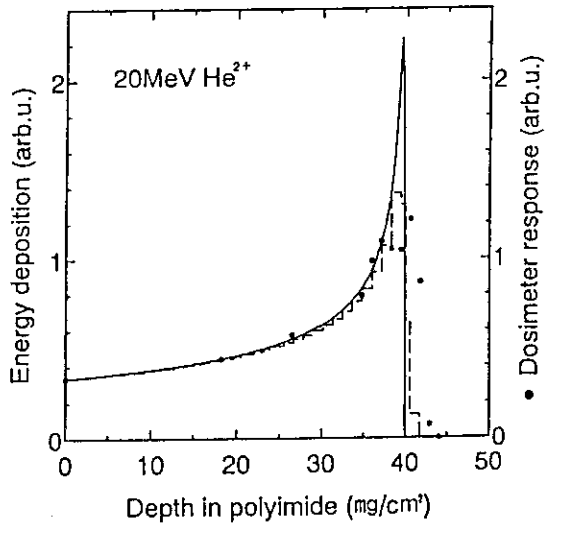

Fig.2 Depth-dose profiles for 20-MeV helium beams measured by Gaf films irradiated through polyimide phantoms, and ELOSS calculation results.Thickness of one polyimide film is 1.16 mg/cm^2. The closed circles are film measurements. The histogram of solid line is ELOSS calculation with resolution of 1.16 mg/cm^2. The solid line curve is calculation with resolution of 0.2 mg/cm^2.

depth extent. There is also contribution of increase of mass collision stopping power from about 300 to 2,000 MeV/mg/cm^2 along with depth in materials up to the peak, which affects on dose responses[1], besides limitation in effective correction of difference in dosimeter thickness and uncertainty in mass stopping power data.

IV. SUMMARY

The depth dose profile measurements with high resolution in depth were studied for 10, 20-MeV protons, and for 20, 50-MeV helium beams comparing with calculation results. Dose profiles measured by using film dosimeter for these beams nearly agree with those calculated using ELOSS code.

The theoretical calculation may not be fully adequate and can profitably be supplemented with experimental measurement. Especially for heavier ion beams with short penetration range, for instance C^{5+} and Ar^{8+}, estimation of initial energy or mass collision stopping power value at the surface of interest material layer may have large uncertainty. Calculation code and data base have to be improved and supplemented by experiments.

ACKNOWLEDGEMENT

The authors would express their appreciation to T.Sasuga, H.Kudo and S.Tanaka of JAERI for discussion in ion beam irradiation and ELOSS calculation.

REFERENCES

1)T.Kojima, H.Sunaga, H.Takizawa and J. Okamoto: TIARA Annual Report Vol.2, JAERI-M 93-241(1993) 65
2)T.Kojima, A.Ranjith H.L., Y.Haruyama, S.Kashiwazaki and R.Tanaka: Appl. Radiat.Isot.44,(1993) 41
3)R.D.H.Chu, G.Van Dyk, D.F.Lewis, K.P. J.O'Hara, B.W.Buckland and F.Dinelle: Radiat.Phys.Chem.35,(1990) 767
4)W.L.McLaughlin, A.W.Boyd, K.H. Chadwick, J.C.McDonald and A. Miller: "Dosimetry for radiation processing"(Tailor & Francis, London, 1989) 167
5)H.Sunaga, R.Tanaka, K.Yoshida, and I. Kohno: RIKEN Accel.Prog.Rep.22(1988) 130
6)T.Kojima, H.Takizawa, H.Tachibana and H.Sunaga: Abstracts of the 3rd TIARA research review meeting(1994) 84
7)T.Sasuga, H.Kudo, T.Seguchi: TIARA Annual Report Vol.1, JAERI-M 93-047 (1992) 117
8)K.Hata and H.Baba: JAERI-M 88-184 (1988)
9)J.F.Ziegler, J.P.Biersack and U.Littmark: "The stopping and range of ions in matter" Vol.1(Pergamon press, Oxford, 1985)

4. Organic Materials

4.1 HIGH ENERGY ION IRRADIATION EFFECTS ON POLYMER MATERIALS(II)

H.Kudoh, T.Sasuga and T.Seguchi

Takasaki Radiation Chemistry Research Establishment
Japan Atomic Energy Research Institute
Takasaki, Gunma, 370-12 Japan

1. Introduction

Artificial satellites and space stations need polymer and fiber reinforced plastic as the thermal insulators and structural materials. To apply polymer materials in space environment of the radiation field of high energy ions and electrons, the knowledge about the degradation induced by ions is essential. We have studied the high energy proton irradiation effects for several polymers and compared with those of electron irradiation in the previous report[1] and LET (Linear Energy Transfer) effect was scarcely observed for the tensile test of PE (polyethylene) and PTFE (polytetrafluoroethylene), whereas a LET effect was observed for PES (polyethersulphone) and UPS (bis-phenol A type polysulphone). In this work, the changes in flexural strength induced by proton irradiation for PMMA (polymethylmetacrylate) and GFRP (glass fiber reinforced plastic; Glass/bisphenol-A type epoxy resin) were studied and compared with those of Co-60 gamma rays irradiation. For further high LET ions such as He^{2+} and C^{5+} ions, the irradiation effects on PE, PTFE, PES and UPS were investigated.

2. Experimental

Films of PE of 0.5mm thick, PTFE, PES and UPS of 0.1mm thick were used for tensile test. Those of PMMA of 3mm thick and GFRP of 2mm thick were for flexural test, respectively.

Ion beams of 10mm diameter from the Cyclotron accelerator were scanned uniformly in 100mm x 100mm area. Ion energy was selected as shown in Table 1 in order that ions pass through the materials. The materials were put on the water cooled holder and irradiated under vacuum. Absorbed dose(D) was calculated as the product of fluence(Q) and Bethe's mass stopping powers(S) shown in Table 1. The formula is D=Q/q*S. To compare the effect with proton irradiation, 2MeV electron

Table 1 Ions, ion stopping power(S;MeVcm^2/g) and ion penetration range(mm)

Polymer	Ion	S	Range
PE	10MeV H^+	43.0	1.35
	50MeV He^{2+}	142.5	2.03
	20MeV He^{2+}	304.5	0.39
PTFE	10MeV H^+	36.5	0.68
	50MeV He^{2+}	121.4	1.02
PES	10MeV H^+	39.7	1.02
	50MeV He^{2+}	132.0	1.69
	220MeV C^{5+}	598.0	1.47
UPS	10MeV H^+	40.5	1.11
	20MeV He^{2+}	284.8	0.32
PMMA	45MeV H^+	11.5	19.2
	30MeV H^+	16.3	9.02
GFRP	30MeV H^+	16.1*	7.84*

* values for CTA

irradiation was carried out for PE, PTFE, PES and UPS under vacuum at room temperature, and Co-60 irradiation for PMMA and GFRP was performed in nitrogen gas atmosphere at room temperature.

In additon to mechanical property test, glass transition temperature of PES, UPS and GFRP was measured by DSC (Differential Scanning Calorimetry). Molecular weight of PMMA was measured by GPC (Gel Permeation Chromatography).

3. Results and Discussion

(1)PMMA:

Figure 1 shows the change in flexural strength of PMMA measured at RT as a function of absorbed dose. The flexural strength decreases with dose above 0.1MGy, and this behavior is the same among gamma rays, 45MeV and 30MeV protons. Figure 2 shows the change in Molecular weight(Mn) as a function of absorbed dose. The Mn decreases in the same way among gamma rays, 45MeV and 30MeV proton irradiations. The ratio of weight average molecular weight to number average one, Mw/Mn, was around 2 after a small dose irradiation, which means that the molecular weight distribution is random. The G value of chain scission of PMMA calculated

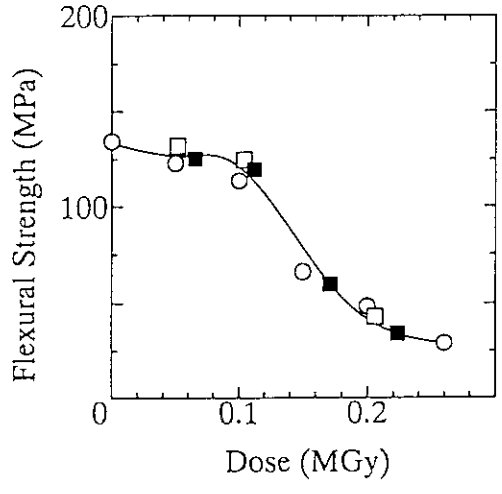

Fig. 1 Flexural strength of PMMA (○;gamma ray,□;45MeV proton,■;30MeV proton)

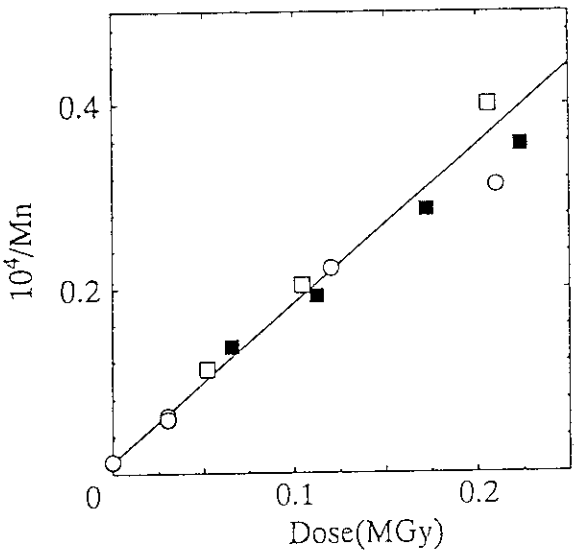

Fig. 2 Number average molecular weight(Mn) of PMMA (○;gamma ray,□;45MeV proton, ■;30MeV proton)

from Fig. 2 is 1.7 and agrees well with values in literatures[2]. The experimental results of flexural strength, Mn and Mw/Mn indicate that the chain scission takes place in the same way among the irradiations of gamma rays and 45MeV and 30MeV protons, and that the decrease in mechanical properties depends only on the dose. LET effect on PMMA degradation is not observed in our experiments. On the other hand, Yates et al.[2] and Schnabel et al.[3] reported that G value of scission of PMMA decreases in large LET at 60 eV/A by 90MeV Oxygen.

(2)GFRP:

Figure 3 shows the change in flexural strength of GFRP measured at RT as a function of absorbed dose. The radiation resistance of GFRP is attributed to the degradation of matrix resin. Figure 4 shows the change in glass transition temperature, Tg, of epoxy resin, determined by DSC. The decrease of Tg means the degradation of network structure of epoxy resin. The scission probability is the same between gamma rays and 30MeV proton irradiations.

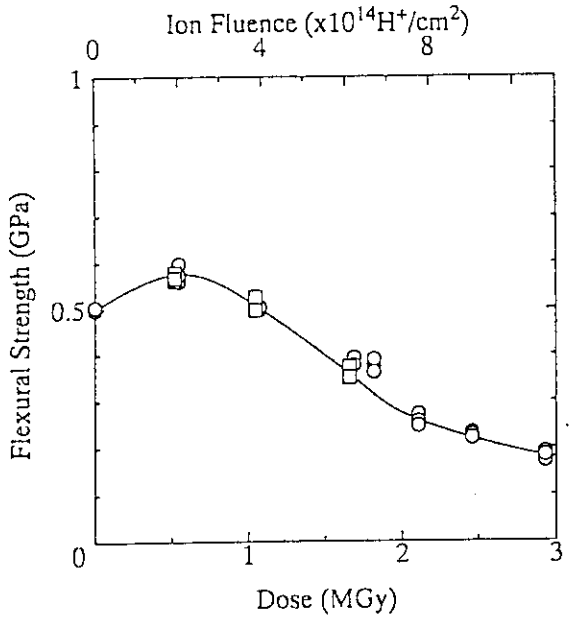

Fig. 3 Flexural strength of GFRP
(○;gamma ray,□;30MeV proton)

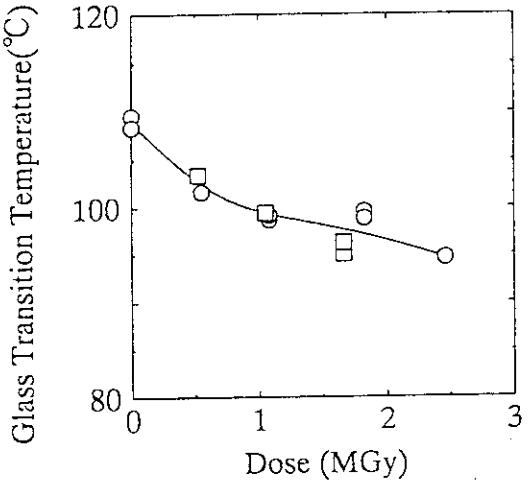

Fig. 4 Glass transition temperature(Tg)
of GFRP(○;gamma ray,□;30MeV proton)

(3)PE, PTFE, PES and UPS:

Table 2 shows the dose at degradation, the dose at which the elongation at break decreased to the indicated value. The results of PE irradiated by 50MeV or 20MeV He^{2+} and PTFE by 50MeV He^{2+} were the same with that of 10MeV H^+. Those of PES irradiated by 50MeV He^{2+} and 220MeV C^{5+} showed the similar dose dependence, but the degradations were less than that of 10MeV H^+. For UPS irradiated by 20MeV He^{2+}, the change in elongation against dose was less a little, but not so different from that of 10MeV H^+. These experimental results did not show the clear LET effects on the degradation of polymer materials in terms of mechanical property.

Table 2 The Dose at Degradation[1] in tensile test of PE, PTFE, PES and UPS

Polymer	Ion	Degradation	Dose
PE	10MeV H^+	$0.5Eb_0$[2]	0.2MGy
	50MeV He^{2+}		0.2
	20MeV He^{2+}		0.2
	2MeV e^-		0.2
PTFE	10MeV H^+	$0.6Eb_0$	4kGy
	50MeV He^{2+}		4
	2MeV e^-		4
PES	10MeV H^+	$0.9Eb_0$	0.1MGy
	50MeV He^{2+}		0.4
	220MeV C^{5+}		0.4
	2MeV e^-		0.2
UPS	10MeV H^+	$0.6Eb_0$	2MGy
	20MeV He^{2+}		3
	2MeV e^-		2

1) The dose at which the elongation decreased to the indicated value. (Ex., for PE, the dose at which the elongation decreased to the half of the initial elongation.)
2) Eb_0 denotes the elongation at break of the unirradiated sample.

References

1) H.Kudoh, T.Sasuga and T.Seguchi, JAERI-M 93-241, 79, 1993
2) B.W.Yates and D.M.Shinozaki, J.Polym.Sci.B, vol.31, 179, 1993
3) W.Schnabel and S.Klaumunzer, Radiat.Phys. Chem, vol.37, 131, 1991

4.2 IRRADIATION EFFECTS ON MECHANICAL PROPERTIES OF CFRP FOR SPACECRAFT

KOZO YUDATE and YOSHIKI MORINO
Office of Research and Development, National Space Development Agency of Japan

AKIRA UDAGAWA, HISAAKI KUDOH, TSUNEO SASUGA and TADAO SEGUCHI
Department of Material Development, Japan Atomic Energy Research Institute

I. INTRODUCTION

Composite materials, particularly Carbon Fiber Reinforced Plastic (CFRP), offer substantial advantages for large space system applications, because of their superior strength, specific stiffness and low coefficient of thermal expansion. CF/Epoxy resin composite (CF/Ep) is being increasingly utilized as a structural material for space use.

NASDA is now conducting R&D efforts on reentry winged vehicle "HOPE". CF/Polyimide resin composite (CF/Pi) is expected as the first candidate material for the primary structure of this "HOPE". CF/Pi composite resists higher temperature than CF/Ep composite. These superior characteristics of CF/Pi would contribute to weight saving of HOPE structure.

Resistance to space environmental effect such as proton and electron radiation as well as mechanical properties of CFRP is the most important characterization to apply to structural material for space use. Irradiation effects (proton, electron) on mechanical properties were studied for CF/Ep and CF/Pi composites.

II. EXPERIMENTAL PROCEDURE

(i) Samples

The samples used were two kinds of CFRP (CF/Ep and CF/Pi). These CFRP were prepared as follows. The UD (Uni-directional) preimpregnated sheets were laminated and cured. 20 plies of sheet for CF/Ep and 16 plies of sheet for CF/Pi were laminated. These laminates consisted of plies with 0 and 90 degree fiber orientation. The thickness of CFRP (CF/Pi and CF/Ep) was 2 mm. Table-1 shows the mechanical properties of CFRP. CF/Pi has a high Tg(glass transition temperature indicating that it is a high temperature resistant composite. Polyimide resin is PMR-15[1].

Table 1. Mechanical Properties of CFRP

CFRP	Flexural Strength(MPa)	Flexural Modulus(GPa)	ILSS (MPa)	Tg (℃)
CF/Ep	684	133.3	47.6	145
CF/Pi	1051	87.8	74.6	354

(ii) Irradiation

Irradiation was performed by 45 MeV protons from a AVF cyclotron and 2 MeV electrons from an electron accelerator installed in the JAERI Takasaki Radiation Chemistry Research Establishment. The proton fluence rate was 2.5×10^9 p/cm²/s and the total absorbed dose (D) was max 1.22 MGy for CF/Ep and max 1.80 MGy for CF/Pi. The electron fluence rate was 1.16×10^{13} e/cm²/s and absorbed dose (D) was 5 ~60 MGy. To avoid rising temperature during the electron irradiation, the samples were stuck on the irradiation table with water cooling jacket.

(iii) Measurement of mechanical properties

After proton/electron irradiation, 3 point flexural test was carried out at temperatures from RT to 250℃ for CF/Pi, from RT to 100 ℃ for CF/Ep. The size of sample was 102 mm(L) X 10 mm(W) X 2 mm(T) and span length was 64 mm. Interlaminar shear strength(ILSS) was also measured at room temperature, the size of sample was 20 mm(L) X 10mm(W) X 2 mm(T) and span length was 12 mm. The glass transition temperature(Tg) of sample was determined by visco-elasticity measurement.

III. RESULTS AND DISCUSSION

(i) Proton and electron irradiation in low dose region

Figs. 1 and 2 show flexural strength and modulus at room temperature for CF/Pi as a function of proton-dose and those for CF/Ep, respectively.

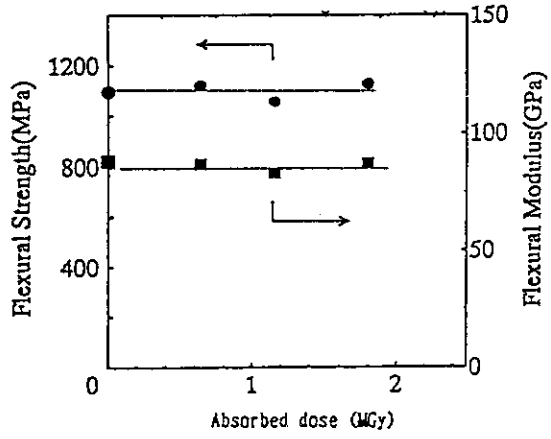

Fig. 1 Flexural strength and Modulus vs. proton dose for CF/Pi at RT

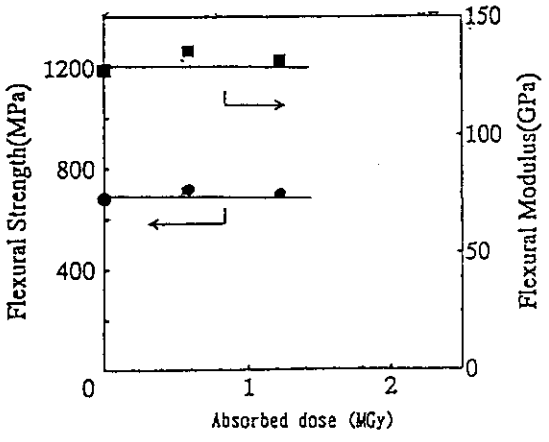

Fig. 2 Flexural strength and Modulus vs. proton dose for CF/Ep at RT

The degradation of mechanical properties were not observed for CF/Pi and CF/Ep.

Electron irradiation were carried out in the equal absorbed dose (0~1.8 MGy) as with proton irradiation for comparison. No degradation were also observed up to 1.8 MGy electron irradiation. From these results it is concluded that CF/Pi and CF/Ep are stable to both proton and electron irradiations up to 1.8 MGy.

(ii) Electron irradiation in high dose region

Figs. 3 and 4 show flexural strength for CF/Pi as a function of electron-dose, and flexural modulus, respectively. The measurement temperature were from RT to 250 ℃. Fig 5 shows ILSS at RT. Although the flexural strength at high temperatures was lower than that at low temperatures, it did not decrease with electron dose. CF/Pi had equal flexural modulus at high temperatures and with absorbed dose.

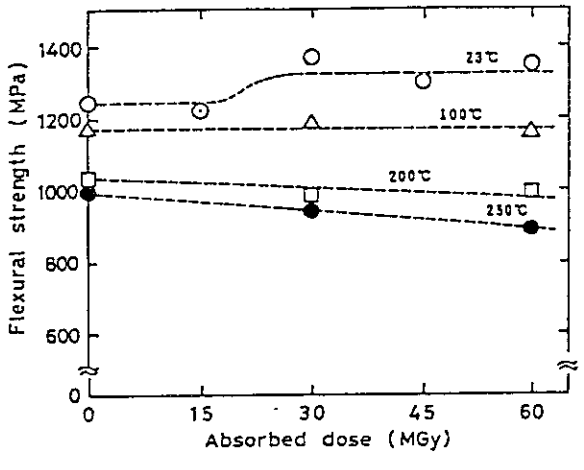

Fig. 3 Flexural strength vs. electron dose for CF/Pi at temperatures from RT to 250℃

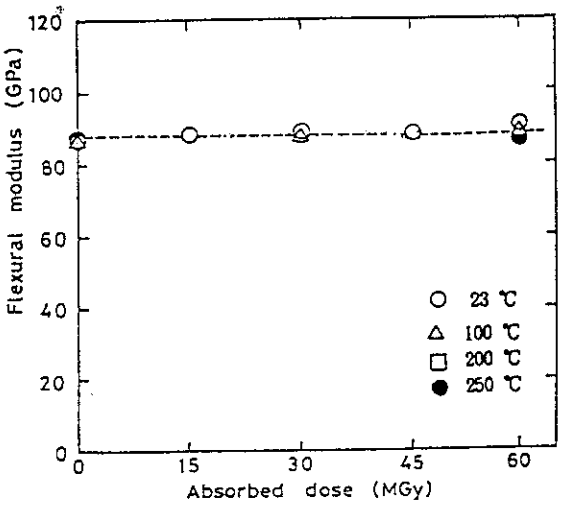

Fig. 4 Flexural modulus vs. electron dose for CF/Pi at temperatures from RT to 250℃

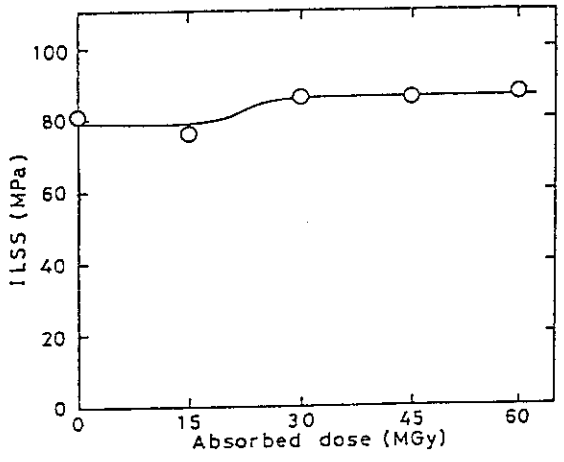

Fig. 5 ILSS vs. electron dose for CF/Pi at RT

ILSS increased slightly with dose. Tg increased by 16 ℃ to 370 ℃ by 60MGy electron irradiation From these results, CF/Pi is excellently stable to electron irradiation. Tg increased by electron irradiation, indicating that Polyimide resin was classified as a crosslinking type polymer under electron irradiation.

Figs. 6 and 7 show flexural strength for CF/Ep as a function of electron-dose, and flexural modulus, respectively. The measurement temperature were from RT to 100℃. Flexural strength and modulus decreased steeply at higher temperatures temperatures with increasing electron dose.

Fig 8 shows ILSS at RT. ILSS decreased above 15 MGy of electron dose. The Tg decreaed by 26℃ to 119 ℃ by 30MGy irradiation, resulting that Epoxy resin is classified as a bond-scission type under electron irradiation. It is

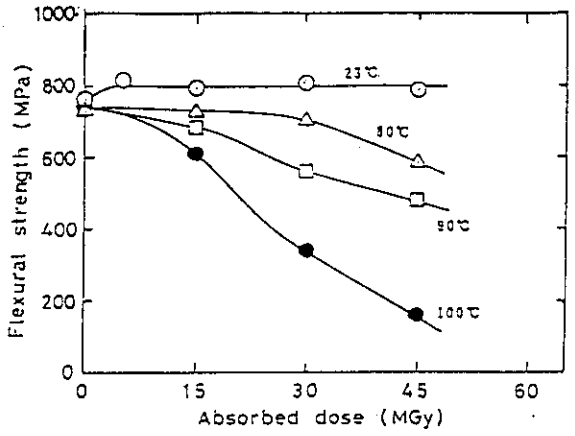

Fig.6 Flexural strength vs. electron dose for CF/Ep at temperatures from RT to 100℃

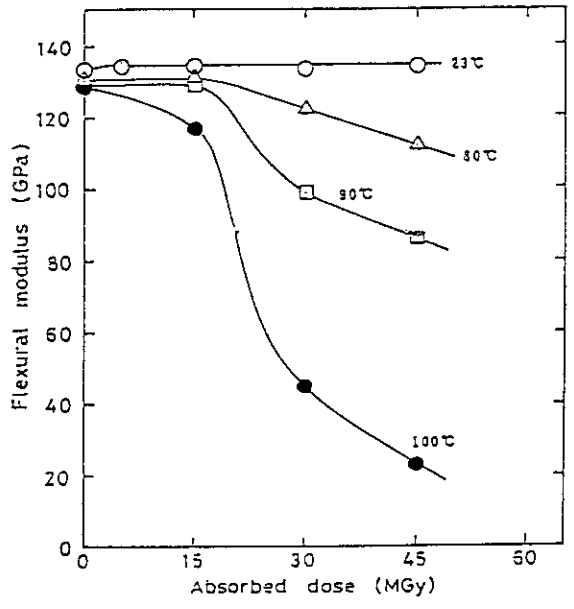

Fig.7 Flexural modulus vs. electron dose for CF/Ep at temperatures from RT to 100 ℃

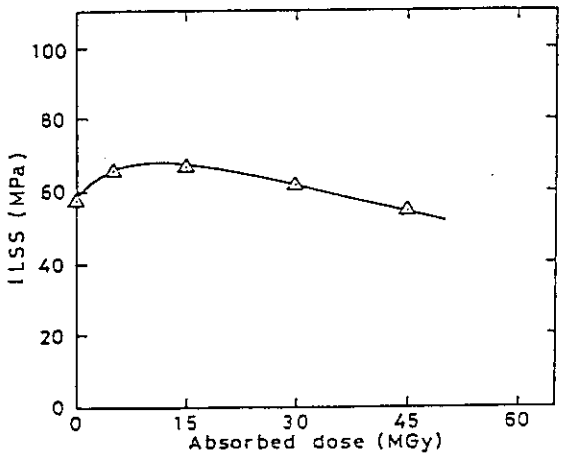

Fig. 8 ILSS vs. electron dose for CF/Ep at RT

verified that CF/Ep was degraded by electron irradiation.

The degradation of mechanical properties was observed at high temperatures with increasing electron dose for CF/Ep. Tg decrease , which was caused by Epoxy resin dissociation under electron irradiation, was also observed. These dissociated bonds rearranged at temperature of decreased Tg , resulting in degradation of Epoxy resin [2] . CF/Ep degradation is probably due to Epoxy resin degradation.

(iii) Evaluation of CFRP for space use

It is estimated that spacecraft surface in the geostationary orbit with altitude of 36000 km is irradiated by electron maximum 10MGy (CFRP) for 30 years [3] . From the present work, no degradation was observed by 1 ~2 MGy proto irradiation for CF/Pi and CF/Ep. On the other, it was verified that CF/Ep was degraded by electron irradiation (above 15 MGy), and CF/Pi showed no degradation up to 60 MGy electron irradiation.

Ⅳ. CONCLUSION

(i) CF/Pi has high electron-radiation resistance Polyimide resin (PMR-15) is a crosslinking type polymer under electron irradiation. No degradation was observed up to 1.8 MGy proton irradiation.

(ii)CF/Ep has low electron-radiation resistance. The degradation was observed above 15 MGy electron irradiation. Epoxy resin is a bond-scission type polymer under electron irradiation. No degradation was observed up to 1.2 MGy proton irradiation.

REFERENCE

(1) R.W.Lauver; Journal of Polymer Science, Polymer Chemistry Edition. Vol.17, 2529-2539 (1979)

(2) A.Udagawa et al; Kobunsi-Ronbunsyu, 44, 8 631-639 (1987)

(3) Seehra, S., Benton. D., Rosen, J., and Goundor, 29th National SAMPE Symp., pp157-168 (1984)

4.3 Development of a new nuclear track detector

M. Asano[1], M. Yoshida[1], M. Tamada[1], H. Omichi[1],
N. Nagaoka[2], H. Kubota[2], R. Katakai[2], T. Hattori[3],
K. Ogura[3]

1) Department of Materials Development, Takasaki Radiation Chemistry Research Establishment, JAERI
2) Department of Chemistry, Faculty of Engineering, Gunma University
3) College of Industrial Technology, Nihon University

INTRODUCTION

Diethyleneglycol-bis-allylcarbonate (CR-39) film has been widely applied to the field of nuclear particle detection, track radiography and microfilter production, because of its high sensitivity to ion beams and charge resolution. The sensitivity of polymeric track detector is known to be affected by various factors such as purity of monomer, molecular structure of polymer[1], polymerization conditions[2], environmental conditions during irradiation and etching conditions[3]. In order to develop a new polymeric track detector of high sensitivity, we investigated a copolymer of CR-39 monomer with methacryloyl-L-alanine methyl ester (MA-AlaOMe).

EXPERIMENTAL

The copolymer film of CR-39 and MA-AlaOMe was fabricated by a cast polymerization. A mixture of MA-AlaOMe and CR-39, containing 3 % BPO as an initiator, was poured into a cast consisting of two glass plates separated by the spacer of 100 μm thick film of polyethylene terephthalate. The monomer mixture in the cast was polymerized at 75°C for 24h (Fig. 1). The copolymer films were irradiated under vacuum condition with 1×10^3 He^{2+} ions of 5 MeV/n, C^{5+} ions of 18.3MeV/n, Ne^{7+} ions of 13 MeV/n, Ar^{13+} ions of 11.5 MeV/n at the AVF cyclotron (TIARA) and with 1×10^6 Au ions of 13.4 MeV/n at the UNILAC heavy ion accelerator

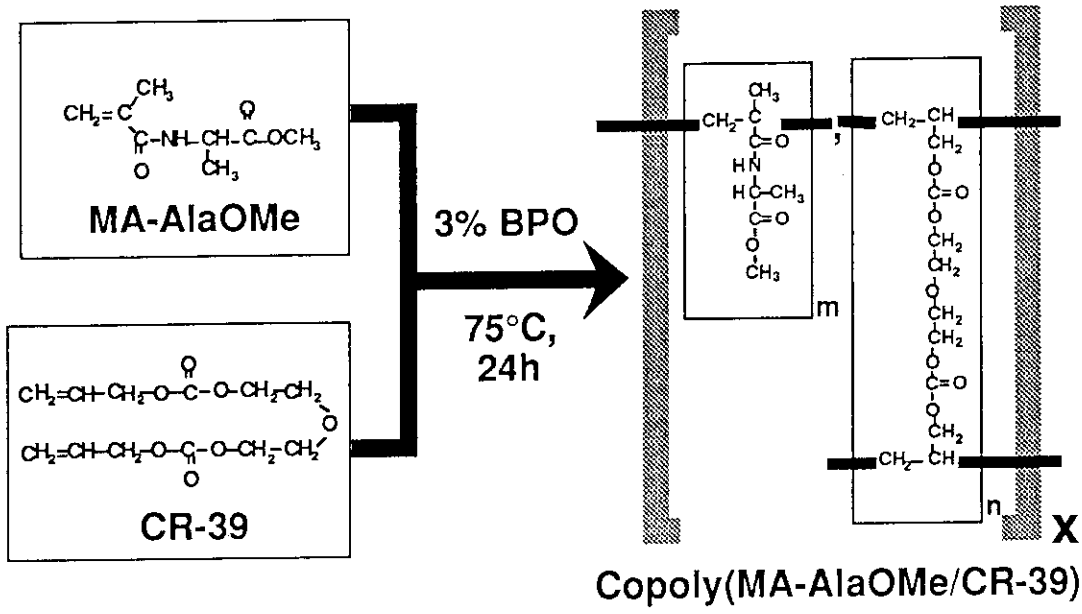

Fig. 1 Structural formula of MA-AlaOMe, CR-39, and copoly(MA-AlaOMe/CR-39).

(GSI). The irradiated films were etched in a concentrated NaOH solution. The sensitivity was expressed as $(V_t/V_b)-1$, where V_t is track etch rate and V_b bulk etch rate obtained from the observation of scanning electron microscopy with the irradiated films.

RESULTS

The track formation is due to the energy transfer from the irradiated energetic ion to the material. In this case, there is a minimum energy called REL(restrited energy loss) below which no track formation is detected.

High REL region

Copolymer films of CR-39 and MA-AlaOMe in the compositions of 100/0, 95/5, 90/10, 85/15, 80/20, 70/30, 60/40, and 40/60 in weight ratios, were irradiated by 13.4 MeV/n ^{197}Au ions at normal incident angle to the copolymer surface. Then the copolymer films were etched in 6N NaOH solution at 60°C. A conical shape of the etched structure provided V_t and V_b as reported in our previous paper[4].

Fig. 2 shows the effect of MA-AlaOMe content on the sensitivity. The introduction of MA-AlaOMe to CR-39 was effective in increasing the sensitivity of CR-39 to 13.4 MeV ^{197}Au ions in the region of MA-AlaOMe content less than 40 %. The maximum sensitivity was obtained with the copolymer containing about 10 wt-% of MA-AlaOMe. This value was 2.1 times that of

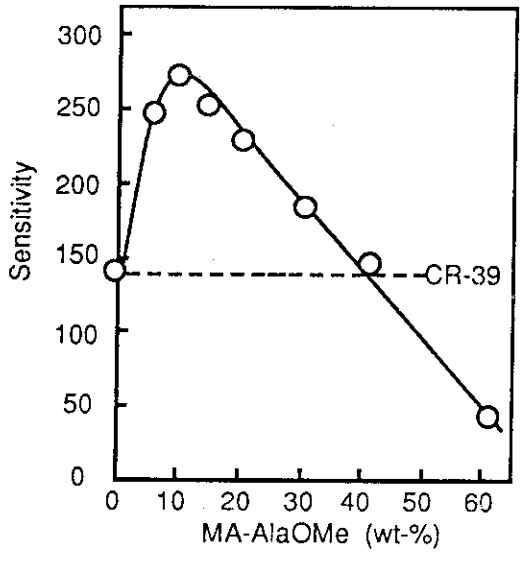

Fig. 2 Effect of MA-AlaOMe content on the sensitivity. The films were irradiated by 13.4 MeV/n ^{197}Au ion and then were etched with 6N NaOH solution at 60°C.

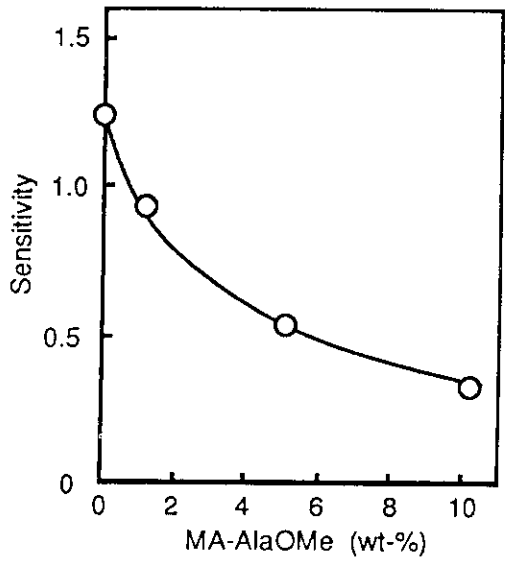

Fig. 3 Effect of MA-AlaOMe content on sensitivity. The films were irradiated by 13 MeV/n ^{20}Ne ion and then were etched with 7N NaOH solution at 70°C.

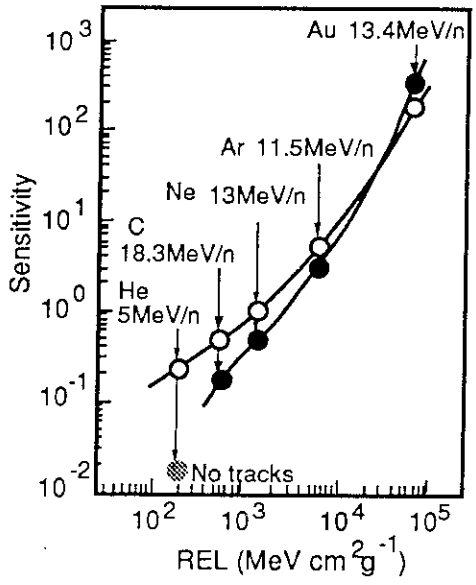

Fig. 4 Response curves of copoly(MA-AlaOMe/CR-39) film and Poly(CR-39) film; (O) CR-39 and (●) MA-AlaOMe/CR-39 (10/90 wt%).

pure CR-39.

Low REL region

Fig. 3 shows the effect of MA-AlaOMe content on the sensitivity of copolymer films for 13.0 MeV/n ^{20}Ne ions. The sensitivity was simply reduced with increasing MA-AlaOMe content. The sensitivity of the copolymer with 10wt-% MA-AlaOMe was about 1/3 of pure CR-39.

Fig. 4 shows the sensitivity curves as a function of REL of the copolymer containing 10 wt-% MA-AlaOMe. From the figure, it is clearly observed that the copolymerization of CR-39 with 10 wt-% MA-AlaOMe is effective in increasing the sensitivity of CR-39 to high LET particles in the region of REL higher than 3×10^4 MeV cm^2/g. In the region less than 3×10^4 MeV cm^2/g, on the other hand, the copolymerization with MA-AlaOMe reduces the sensitivity.

For the next step, we intend to develop a copolymer with a high sensitivity to low REL region.

REFERENCES

1) J. Stejny, and T. Portwood, Nucl. Tracks., **12**, 59-62 (1986)
2) P. B. Price, E. K. Shirk, K. Kinoshita, and G. Tarle, Proc. 16th Int. Cosmic Ray Conf., **11**, 80-85 (1979)
3) S. A. Amin, and L. Henshaw, Nucl. Instr. Meth., **190**, 415-421 (1981)
4) M. Tamada, M. Yoshida, M. Asano, H. Omichi, R. Katakai, C. Trautmann, J. Vetter, and R. Spohr, Nucl. Tracks. Radit. Meas., **20**, 543-547 (1992)

4.4 The formation of metallic complex by sputtering Cu or Ni on the simultaneously deposited film of Phthalocyanine and Stearic acid

K.Orihara,K.Tsuchiya,K.Nouchi,K.Aoki,
F.Hosoi [2] ,H.Omichi [2]
Dept.of Materials Science,Yamagata Univ. of Engineering. Takasaki
Radiation Chemistry Research Establishment, JAERI.[2]

Introduction

We tried to evaporate the metal(Cu or Ni) by sputtering method on the deposited mixed film of Phthalocyanine(Pc) and Stearic acid(SA) evaporated simultaneously on the bare glass in vacuum. By this method we tried to form metallic complex of Pc(MPc).

H.Omichi et.al [1] had tried to form the MPc by the deposition of Cu by sputtering method on the previously deposited Pc film on the bare glass in vacuum. Though CuPc was not formed by the way [1].The Pc film evaporated in vacuum shows highly regular stacking for the growth direction[2]. So the reason of the result seems to be that Cu atom can not arrive at Pc molecule in the highly oriented Pc film .

On the other hand K.Orihara et.al had tried to evaporate each metal(Ni,Cu, Al,Sn,In and Au) and Pc simultaneously from dual sources in vacuum. As a result an interesting example was found in the case of the deposition of Ni and Pc. That is,the sample showed a possibility of NiPc complex formation [3]. But in almost all samples Pc component was damaged by the metal evaporated simultaneously. Furthermore samples deposited together with Paraffin(Pa) from triple sources in vacuum have been also investigated.As a result,the sample consisting of Ni,Pc and Pa showed better possibility of NiPc complex formation compared with the previous sample obtained with double sources.[4] Additionally the sample consisting of Cu,Pc and Pa also showed a possibility of the complex formation[4]. Almost amorphous structure of these three-component mixed films[5]seemed to induce those suitable results.Probably such an amorphous structure should induce active thermal movement of the metallic atoms and Pc molecules.

In this study we tried to apply the active character of the mixed deposition to form a metal-organic complex. Firstly almost amorphous film of Pc was fabricated by evaporating with SA. Secondly on the mixed film ,the metal(Cu or Ni) was deposited by sputtering method.The chemical structure of Pc in the fabricated samples(Pc*SA ←M) was analyzed with XPS and UV-V.

Experiment

Firstly the mixed organic films were deposited in vacuum. SA was evaporated with Pc simultaneously for 420sec in vacuum of $1.3X10^{-2}$Pa.The temperature of evaporating source was 400℃ for the Pc and 90℃ for the SA.The substrate temperature was 13 ℃.The distance from evaporating sources to substrate was 11.5cm. Cu and Ni were deposited on the above organic film by the sputtering method with the apparatus making hybrid membranes at Takasaki.The accelerative voltage of sputtering Cu by Ar^+ was 0.5kV,and that of Ni was 1.0kV.The sputtering time of Cu was 30min,and Ni was 20min.

The tertiary structure of the samples was analyzed by using reflective X-ray diffraction method. The chemical structure of Pc in the samples was analyzed by using XPS and UV-V spectrophotometer.

Results and Discussion

The reflective X-ray diffraction patterns of the mixed film consisting of Pc and SA(Pc*SA) is shown in fig.1 by full line and that of deposited pure Pc film by dot line. The diffraction peak intensity of Pc*SA decreases clearly and its HW becomes wide compared with that of the pure Pc film.These results suggest the low crystalline and the small size of Pc cluster in Pc*SA compared with that in the pure Pc film.

Figure 2(a) shows the XPS spectrum for N 1s electron of Pc*SA←Cu. A single sharp peak 1 with HW of 1.3eV is observed at 404eV accompanied with three weak satellites. Figure 2(b) shows the XPS spectrum for N 1s of the ready-made CuPc

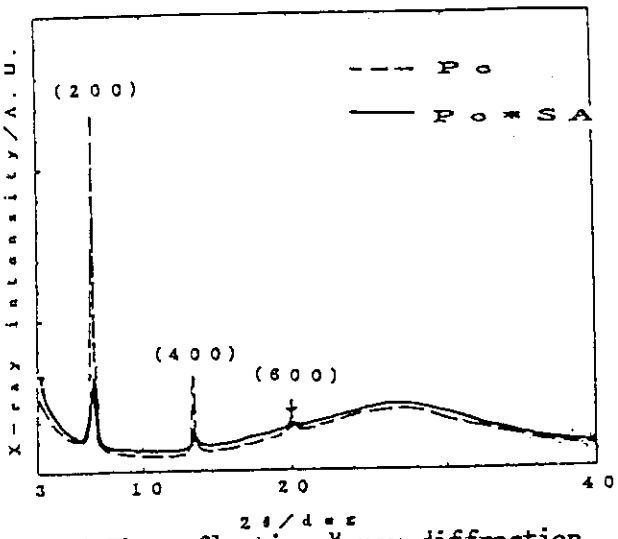

Fig.1 The reflective X-ray diffraction patterns of the Pc*SA(——) and the deposited pure Pc film(---)

complex film. A single sharp peak 1 with HW of 1.2eV is observed at 399.15eV. The single peak in Fig.2(b) corresponds to four aza nitrogens and four nitrogens coordinating with Cu in CuPc molecule [6]. Figure 2(c) shows the XPS spctrum for N 1s of the deposited pure Pc film sputtered by Cu(Pc←Cu).Two peaks 1 and 2 are observed at 407.8 and 409.05eV respectively.The chemical shift between them is 1.25eV and their intensity ratio is 0.27. Figure 2(d) shows the XPS spectrum for N 1s of the deposited pure Pc film.Two peaks are observed at 398.6 and 400.1eV. The chemical shift between two peaks(1 and 2) is 1.5eV and intensity ratio of them is 0.33.These two peaks correspond to six aza nitrogens and two pyrrole nitrogens in Pc molecule respectively [6]. The difference of binding energy zone among (a) ~(d) may due to the difference of the tertiary structure in each sample.The clear difference of the spectrum is found between the sample of Pc*SA←Cu(a) and the pure Pc film(d).The profile of the single sharp peak 1 in (a) is rather similar to that of the ready-made CuPc film(b), and satellite peak 2 in both figures,(a) and (b) at lower binding energy of the peak 1 is also shown in both films.On the other hand the spectra (c) and (d) show almost same chemical sift between two peaks,1 and 2.From these results,only Pc*SA←Cu seems to show a possibility of the formation of CuPc co-

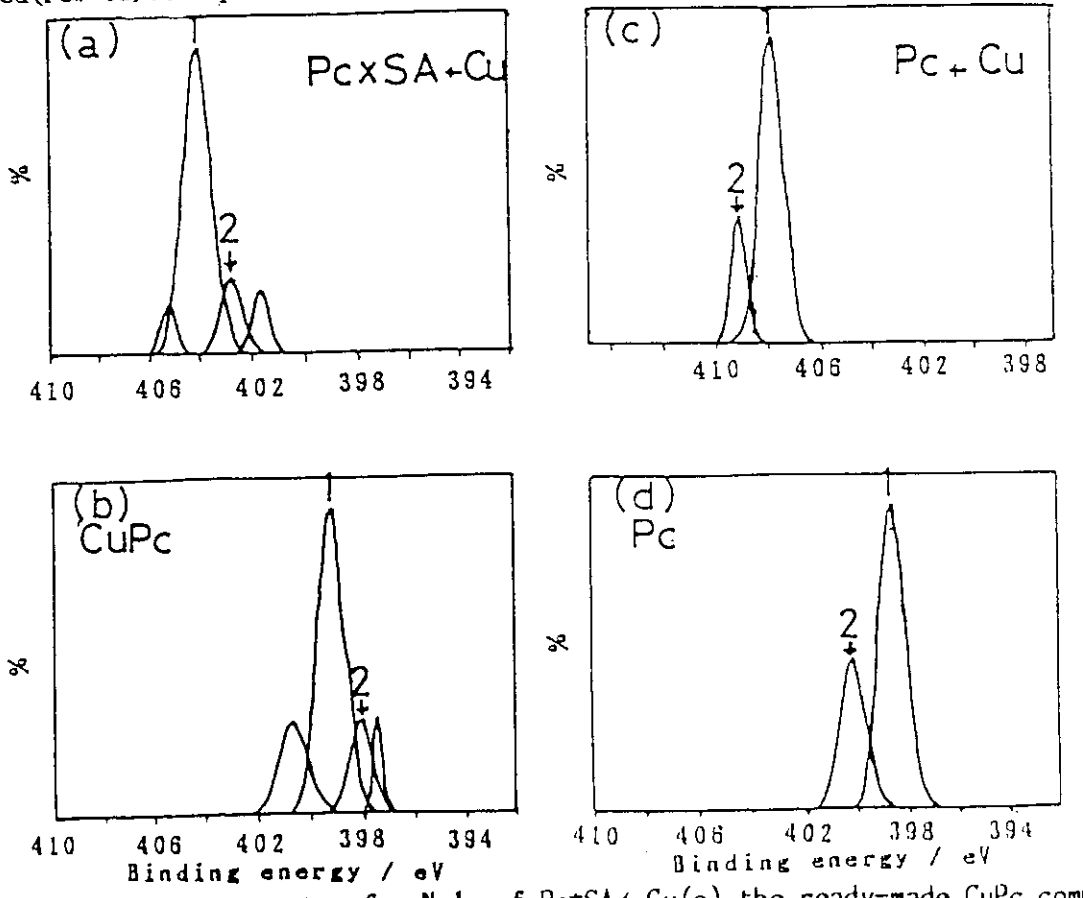

Fig.2 The XPS spectra for N 1s of Pc*SA←Cu(a),the ready-made CuPc complex film(b),the Pc←Cu(c) and the deposited pure Pc film(d)

mplex.

Figure 3 shows the UV-V spectra of the deposition of Pc*SA←Cu,Pc*SA and ready-made CuPc.The profile of the spectrum of Pc*SA←Cu is similar to that of Pc*SA. But the depression of 263nm in Pc

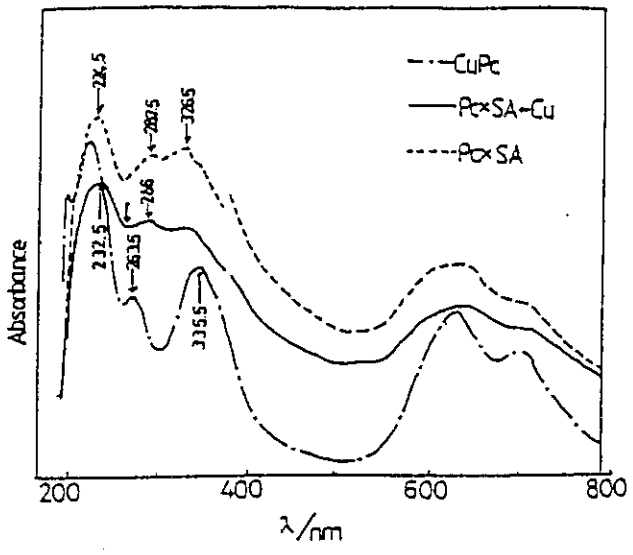

Fig.3 The UV-V spectra of the deposition of Pc*SA←Cu(——),Pc*SA(---) and ready-made CuPc(-·-)

*SA ←Cu is not clear compared with that of Pc*SA.The little difference in UV spectrum between Pc*SA←Cu and Pc*SA seems to support the results in XPS spectra, that is,the possibility of the formation of CuPc complex.The similar profile of the UV-V spectrum of Pc ←Cu and the pure Pc film,omitting the figure,support this possibility. The possibility could be affirmed from the FT-IR spctra,though we could not have clear data because the present samples were too thin.In the case of Pc*SA←Ni,both XPS UV-V pectra indicated no formation of complexs under the present condition.

References

1) Y.Izumi,F.Hosoi,et.al,Abstracts of The First TIARA Research Review Meeting.,p.27(1992)
2) M.Ashida,Bull.Chem.Soc.Japan.,39,p.2625&2632(1963)
3) K.Nouchi,K.Tsuchiya,K.Orihara,et.al, JSAP Extended Abstracts.,3,p.1114 (The 54th Autumn Meeting,1993)
4) K.Tsuchiya,K.Nouchi,K.Aoki,K.Orihara JSAP Extended Abstracts.,3,p.1115 (The 54th Autumn Meeting,1993)
5) K.Tsuchiya,K,Nouchi,K.Aoki,K.Orihara contributing to other journal.
6) Y.Niwa,H.Kobayashi,T.Tsuchiya,et.al, The Journal of Chemical Physics., 60,p.799(1974)

5. Inorganic Materials

5.1 METASTABLE PHASE FORMATION BY ION IMPLANTATION (II)

Hidefumi TAKESHITA, Syunya YAMAMOTO, Yasushi AOKI and Hiroshi NARAMOTO

Department of Materials Development, JAERI Takasaki

1. Introdution

Ion implantation has been proved to be valuable both for new material development and understanding of basic principles underlying the formation of metastable phases that , by definition, do not appear in equilibrium phase diagrams. Ion implantation has enabled extention of equilibrium solid solubilities in a large number of systems. The solid solubility extention is applicable not only to subsitutional solutions but also to interstitial solutions. These metastable supersaturated solid solutions have formed the basis of alloy development through ion implantation. Ion implantation has been also used to make metastable crystalline intermediate phases. It is well known that some of metastable intermediate phases show interesting properties such as Nb_3Ge, which exhibits higher superconducting transition temperature by conforming to the stoichiometry compared to the corresponding equilibrium nonstochiometric phase. Thus, understanding of the process of metastable phase formation through ion implantation can be scientifically challenging and technologically useful.

As a first step we have started to investigate the metastable phase formation in the silicon and noble metal binary systems. In the Si-Au system, mutual solubilities are quite low and no equilibrium intermediate phases exist in the diagram.This is the case also for the Si-Ag system. The mutual solubilities of Si and Ag are negliligible. Thus, our interests for these systems are the metastable silicide formation as well as extended solid solubilities.

2. Experiment

Ion implantation was carried out using the 400kV Ion Implanter in a dynamic vacuum better than 10^{-4} Pa. Si wafers were implanted at room temperature with Au or Ag ions. The beam energy and current were 0.4MeV and about 1 uA/cm^2, respectively. To avoid channeling of implanted ions, the samples were tilted by 5 degree from the position normal to the beam. The implantation doses of Au and Ag were evaluated on the basis of the RBS(Rutherford backscattering spectroscopy) measurements. After the implantation, the samples were annealed in a argon atmosphere to allow a direct reaction between implanted metal atoms and amorphized silicon matrix. RBS was used to determine the depth profile of the Au or Ag concentration in the implanted and annealed samples. The parameters for RBS were 2.0 MeV He ion, a 165 degree scattering angle and a silicon solid detector with 14keV energy resolution.

3. Results

3.1 Au-Si system

As expected, the surface of silicon matrix was fully amorphized by ion implantation in the range from the surface to the ion range. The

supersaturated solid solution was formed around the ion range, where Au atoms were randomly located with the gaussian curve of distribution. The Au-implanted sample was annealed at 400 C for 1 hr. In the equilibrium phase diagram for the Au-Si system, there is the eutectic point at 363 C. Thus, at the above annealing temperature, a part of the supersaturated solid solution would be expected to form a liquid solution with the composition determined by the sample tempperature. However, the RBS spectra did not show any change of the distribution of Au and the state of amorphous silicon.

3.2 Ag-Si system

The RBS spectra for the as-implanted sample were shown in fig.1. At first, this implanted sample was annealed at 400 C for 2hr. This annealing temperature was chosen so that crystallization of the amorphized silicon matrix beneath the surface was not detected to a noticable extent. It was found from the RBS spectra for the as-implanted and annealed samples that there were no changes in the state of implanted Ag and amorphous silicon after the annealing. This annealing treatment was made with the hope for a reaction between implanted Ag and amorphous silicon, because, from the thermodynamic point of view, both of Ag and silicon in the implanted region might have higher activities compared to those for their equilibrium states. There would be, however, a possibility of metastable phase formation if a prolonged annealing was adopted.

For the next preliminary step, the implanted samples were annealed at 800 C and 860 C, respectively. These temperatures were selected to be located at lower and upper positions compared to the eutectic temperature(835 C) of the Ag-Si systems. The RBS spectrum for the sample annealed at 800 C for 30min was shown in fig.2 with that for the as-implanted sample. The corresponding result for the sample anneald at 860 C was not different from that for the sample annealed at 800 C. It is seen form the figure that the peak concentration of Ag decreased remarkably and resulted in the spread of Ag into the inside direction of the bulk silicon. As well as the diffusion of Ag into the inside, this annealing treatment induced some crystallization of the amorpous silicon matrix and slight alignment of Ag atoms within the recoverd silicon matrix.

4. Discussion

So far ion beam mixing has been used to synthesize metastable intermetallic compounds. The formation of metastable phases in the Au-Si system have been confirmed by means of this method. Normally a thin film bilayer of binary systems is formed by sputtering or vapor deposition and subsequent bombardment by energetic ions, which penetrate through the interface of the bilayer, causes intermixing of each sub-layer because of the atomic displacement produced by the passage of ions through the solid. There have also been several observations of metastable Au gold silicides in gold-silicon alloys under nonequilibrium conditions from, e.g., very rapid quenching.

For the Ag-Si system, the occurence of two metastable phases was reported on the Ag-rich side of the diagram. These phases were obtained in rapidly solidified alloys by melt spinning on Cu substrates and started decomposing to the equilibrium phases above 100 C or higher temperatures.

Our results have shown in fig.2 and fig.3 that there is some possibility for the metastable crystalline phase formation in the Ag-Si system by using the combined treatment of ion implantation and thermal annealing at higher temperatures.

Fig. 1

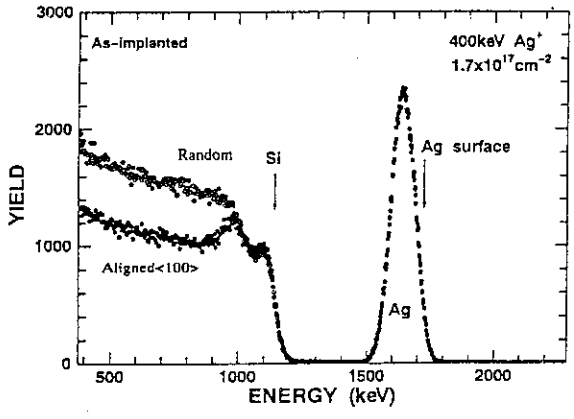

Fig. 2

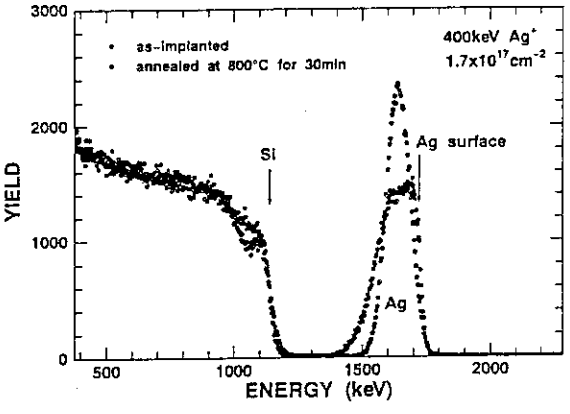

Fig. 3

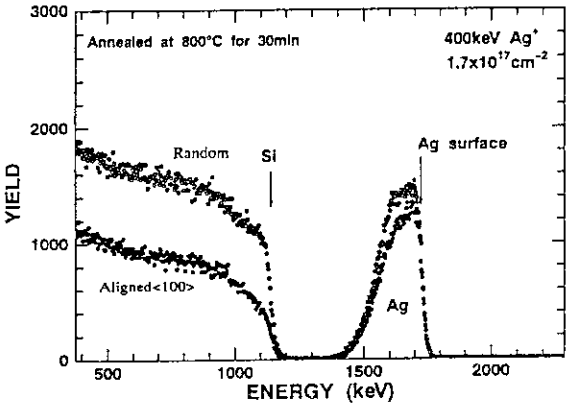

5.2 Electrical Conductivity of MgO and Al_2O_3 Irradiated with High Energy He ions

T. Nakazawa, T. Tanifuji, D. Yamaki, K. Noda
JAERI, Tokai, Material Innovation Lab.

Magnesium oxide (MgO) and Aluminum oxide (Al_2O_3) are attractive materials as insulators for fusion reactors[1]. In fusion reactor environment, helium (He) is introduced in the materials due to nuclear transmutation as well as severe displacement damage. The synergistic effects of introduction of He and displacement damage in though to have very large influence on the insulating properties. In this study, the electrical conductivities of MgO and Al_2O_3 were measured as function of temperature after He-ion irradiation. The results are discussed in term of the behavior of the He atoms on radiation damage.

The materials used in this study were single crystal MgO (10mmx10mmx0.5mm) and single crystal Al_2O_3 (10mmϕx0.5mm, 10mmx 5mmx1mm). He-ion irradiation was carried out with an AVF cyclotron accelerator at Japan Atomic Energy Research Institute (JAERI). The specimens were irradiated with 50 MeV He ions up to the fluence of 4.5×10^{15} ions/cm^2 (5×10^{-3}dpa) at the ambient temperature in a vacuum of better than 10^{-6} torr, and then He concentration in the implanted region was about 25appm for both of MgO and Al_2O_3. After irradiation, the electrical conductivities in the temperature range 298 to 1073K were measured for the irradiated samples with Keithley source measure unit (Model 238) under vacuum (~10^{-5} torr). The He gas release was also measured with the quadrupole mass spectrometer (ULVAC, Model MSQ-150A) in the temperature range 298 to 1453K, by heating at a constant temperature rising rate of 5 K/min.

The electrical conductivity of MgO and Al_2O_3 before and after irradiation were shown versus the reciprocal of temperature in figure 1. For MgO, the values of electrical conductivity at various temperature after irradiation were almost the same as these before irradiation (Fig. 1-A). On the other hand, by comparing the values of electrical conductivity before irradiation with these after irradiation for Al_2O_3, the decrease of electrical conductivity due to the irradiation was formed in the temperature range 298 to 600K (Fig. 1-B). It is also recognized for Al_2O_3 that the temperature dependence of electrical conductivity after irradiation shifts to low temperature side.

He gas release rate of Al_2O_3 irradiated is presented in the temperature range 298 to 1453 K in figure 2. The release rates measured with the quadropole mass spectrometer were not almost changed in the range 298 to 1073K. this suggests that the He gas was not virtually released in the examined temperature range. For the irradiated MgO, He gas release was not also observed in the same temperature range.

Displacement threshold energies of Mg atom (60eV) is nearly equal to these of O atom (64eV) in MgO. However, Displacement threshold energies of Al atom (18eV) is about a quarter of these of O atom (76eV) in Al_2O_3[1]. Accordingly, the microstructural evolution is thought to be different between MgO and Al_2O_3. The microstructural evolution in Al_2O_3 due to irradiation is supposed to be larger than them in MgO. Such difference in microstructural evolution is assumed to be origin of difference of radiation influence on electrical properties between MgO and Al_2O_3. In order to confirm this assumption, it is necessary to observe the microstructure (defect cluster, point defect) of these materials irradiated with transmission electron microscopy and optical absorption spectroscopy.

The studies on electrical conductivity and gas release for various ceramics will be systematically carried out in the near future.

Reference

[1] G.P. Pells, J. Nucl. Mater. 155-157(1988)67.

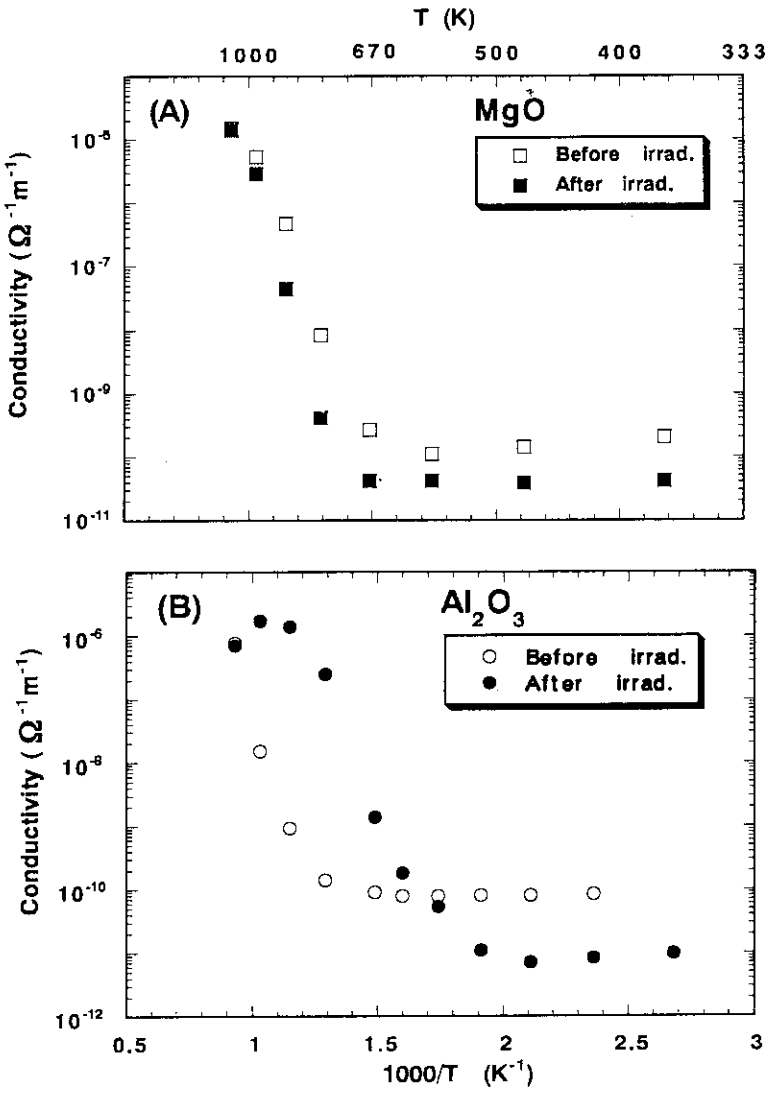

Fig. 1 Electrical conductivities of MgO(A) and Al_2O_3(B) before and after irradiation

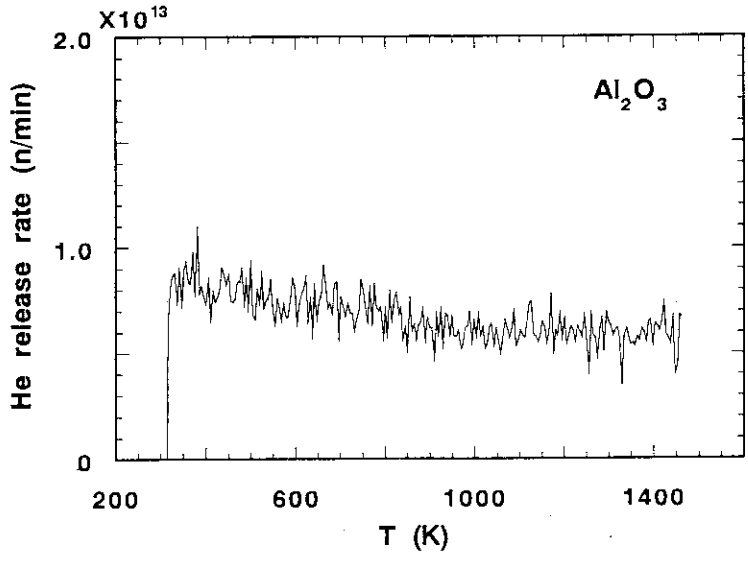

Fig. 2 He gas release rate of Al_2O_3 irradiated

5.3 Proton Irradiation Effect on Mechanical Strength of Carbon/Carbon Composite

S.Baba, M.Ishihara, M.Eto
JAERI, Tokai, Energy Materials Development Lab.

Introduction

Carbon/Carbon (C/C) composites are used for plasma-facing component (pfc) applications in magnet-confinement plasma-fusion devices such as International Thermonuclear Experimental Reactor (ITER), JAERI Tokamak 60U (JT-60U) and Fusion Experimental Reactor (FER). The C/C composites show high thermal conductivity and excellent thermal shock resistance compared with an isotropic graphite IG-110. In the fusion reactor PFCs are damaged under the fast neutron irradiation condition. The neutron energy is 14 MeV ($D+T \rightarrow {}^4He(3.52MeV) + n(14.06MeV)$). Recently some C/C composite data for neutron irradiation condition have been reported. However, these data are obtained under the thermal neutron irradiation condition. Therefore a simulation test was performed under a high energy proton irradiation condition.

Experiment

Four kinds of C/C composite specimens (MFC-1, MCI-felt, CX-2002U, PCC-2S) were irradiated by the 10 MeV protons at a current of 500 nA at room temperature in a vacuum. The specimens were irradiated through a wedge shown in Fig.1. The mechanical properties of these C/C composites are summarized in Table 1. The E-DEP-1ex code[1] was employed to estimate the irradiation damage. The maximum estimated damage in these specimens was about 3×10^{-3}dpa at a depth of 580 μm from the surface.

After the irradiation dynamic hardness was measured using a micro-indentation test machine with a triangular pyramid indentor. The indentation loads were 5g and 1g for 50 μm and 10 μm indentation intervals, respectively. The dynamic hardness, DH, for this type of indentor is defined as

$$DH=37.838Lmax/dmax^2 \quad (1)$$

where, Lmax, dmax are maximum indentation load and indentation depth, respectively.

Results and Discussion

It is said that slopes in Fig.2, which are the coefficient B at loading process and coefficient D at unloading process, are correlated to tensile strength, σ_t, and Young's modulus, E, as follows[2,3]:

$$\left.\begin{aligned}\sigma_t &= k_1 B \\ E &= k_2 D\end{aligned}\right\} \quad (2)$$

Hence, the coefficient B and D are determined applying the least square method to the experimental data on these C/C composite materials which are shown in Fig.3. Consequently, the following correlations are obtained:

$$\left.\begin{aligned}B &= -0.0241+0.0217DH \\ D &= 1.228+0.0781DH\end{aligned}\right\} \quad (3)$$

From Eq.(2) and (3), We can estimate, therefore, the relative tensile strength and Young's modulus from the measured dynamic hardness. The change of dynamic hardness as a function of the distance from the surface is shown in Fig.4. We can see a damage peak at about 530 μm from the surface; this damage peak depth is almost in good accordance with the one

calculated using the E-DEP-1ex code.

From the measured dynamic hardness, ratios of tensile strength and Young's modulus at the peak damage position to those at undamaged position for these C/C composites are estimated and listed in Table 2. It is found that the tensile strength is 1.3 to 1.9 times and the Young's modulus is 1.1 to 1.5 times greater than those of unirradiated ones at 3×10^{-3}dpa.

Now proton irradiations with different fluences are planned to clarify the irradiation fluence effect on the properties.

Reference

1)Manning,I. and Muller,G.P., Comp. Phys.Commun.7,85(1974)
2)T.Oku et al., TANSO,No.156,15(1993)
3)T.Suzuki,et al.,Seisan kenkyu Vol.42,No.5(1990)

Table 1 Mechanical properties of C/C composites.

	MFC-1	MCI-felt	CX-2002U	PCC-2S
Tensile strength* (MPa)	25.6	29.0	29.7	7.5
Young's modulus* (GPa)	20.8	19.3	5.1	8.7

*Property for with fiber direction

Table 2 Ratios of the value at the damage peak to the mean value for C/C composites.

	MFC-1	MCI-felt	CX-2002U	PCC-2S
Tensile strength	1.7	1.3	1.8	1.9
Young's modulus	1.3	1.1	1.5	1.4

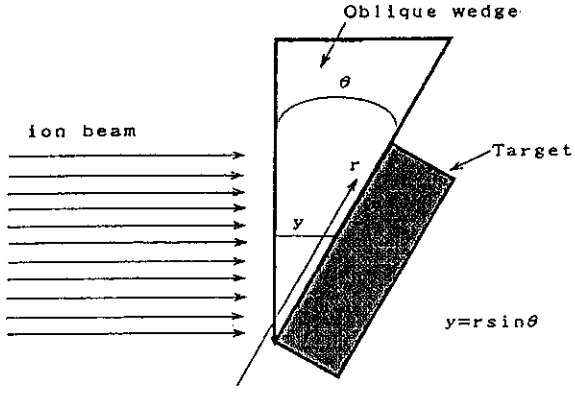

Fig.1 Proton bombardment method.

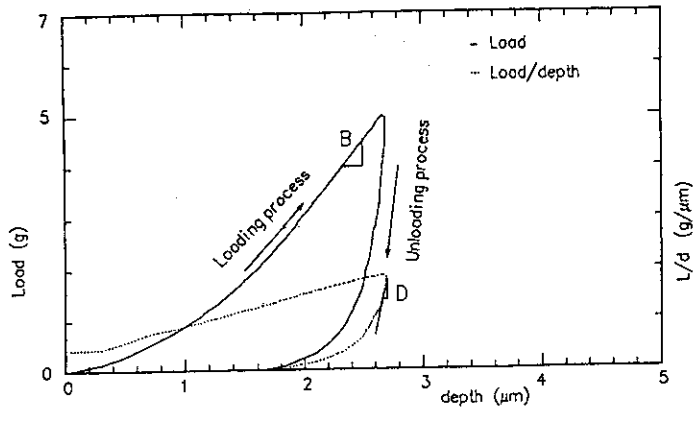

Fig.2 Load vs. depth relationship by a micro hardness testing.

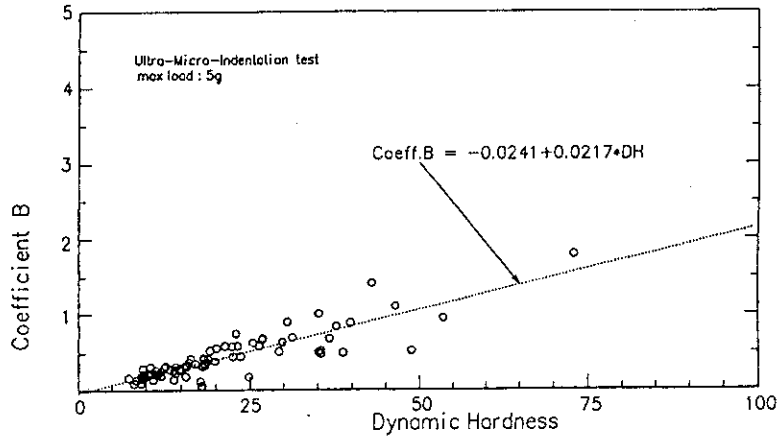

(1) Coefficient B

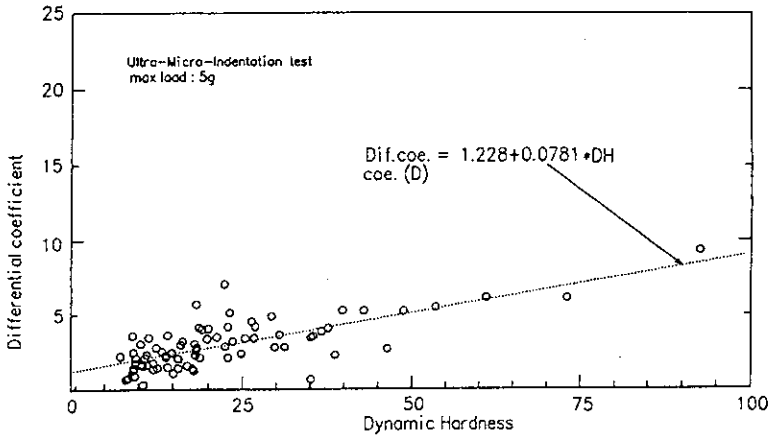

(2) Coefficient D

Fig.3 Relationship between coefficient B and dynamic hardness.

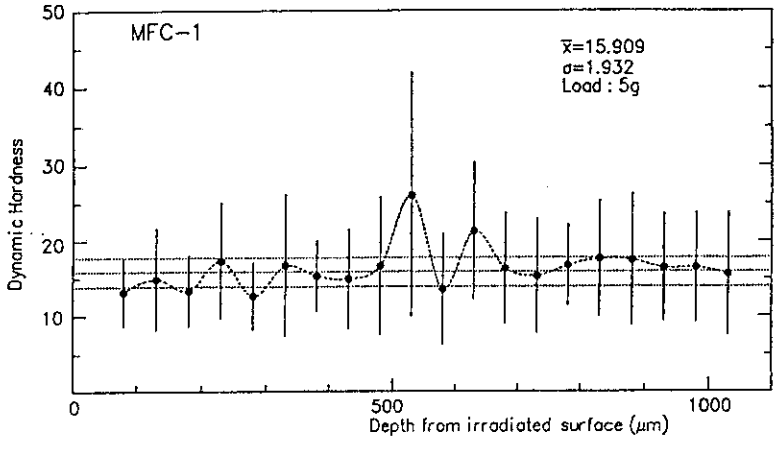

Fig.4 Change of the dynamic hardness from irradiation surface.

5.4 Defect Formation in Ceramics Irradiated with High Energy ions.

Y. Aoki, S. Yamamoto, H. Takeshita, H. Naramoto, A. Osa*, N. Shigeta*, M. Koizumi*, H. Matsuoka*, T. Sekine*

Department of Materials Development, JAERI. *Department of Radioisotopes, JAERI

Ion irradiation introduces various kinds of defects in materials and in many cases electrical and optical properties of irradiated materials are dominated by the defects produced. Thus, in order to control electrical, electronical or optical properties by means of ion irradiation, precise and detailed knowledge is necesary about the kind of ion-induced defects and the efficiency of its formation. On the other hand, observing changes in optical properties in irradiated sample make the energy loss process in materials by high energy ions visualized. Furthermore, appearace of the overlapping effects can be estimated from the results of the dose dependence in such observation.

The depth profiles of damege in some ion irradiated alkali halides have been investigated by microscope-photometric methods, microhardness etc. on LiF[1-3], KCl[4] and NaF[5]. The depth profiles of anodic defects centers, F-centers for lighter ion irradiation and F_2-centers for heavy ion irradiation, have been found to give good correspondence to the electronic energy loss profiles for LiF. However, any proof for overlaps of ion tracks has not been found up to 10^{14} ion/cm^2. In the case of KCl irradiated with about 2 MeV protons or He ion, F-center profile did not follow the dE/dx.

In this paper, we have examined the observation of defect profile in LiF and attempted to expand this investigation to ionic crystals of oxide ceramics MgO.

Samples were single crystals of LiF(Harshaw Chemical Company) and highly pure MgO(99.9999%). LiF was irradiated by γ-ray to be hardened and it was cleaved into pieces of appropriate size (ca. 5mm x 10mm), then thermal annealing was done for preparing samples. Ion irradiation wsa performed at LA-1 beam port of AVF cyclotron in TIARA facility. Samples were irradiated with 175 MeV $^{40}Ar^{8+}$ under vacuum. The current and diameter of ion beam were 40nA and about 1cm^2, respectively. After irradiation, samples were reserved in a refrigrator for more than 4 weeks for cooling the radioactivity. Photoabsorption of the samples was measured in a selected small aerea and as a function of depth by a microscope photometer(MPM800, Zeiss) at room temperature.

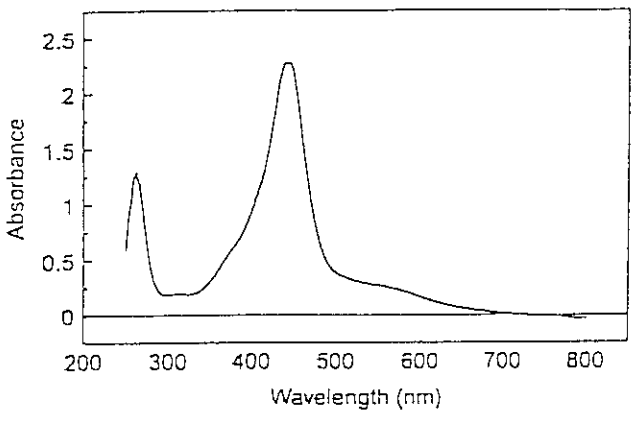

Fig. 1 Optical Absorption spectrum of LiF irradiated with 175 MeV $^{40}Ar^{8+}$ at the dose of 1 x 10^{13} ions/cm^2.

Fig. 1 shows optical absorption spectrum for LiF single crystal irradiated with 175 MeV $^{40}Ar^{8+}$ at the dose of 1 x 10^{13} ions/cm^2. Clear absorption peaks can be observed around 260 nm and 450 nm. These seem to be ascribed to anionic vacancies, F-center and F_2-center[1-3]. In addition, small peak at 310 nm and shoulders around 380 nm and 550 nm can be seen, they seems to be due to two kinds of F_3-centers and F_4-center[1-3]. Since intense absorption of F_2-center and absorption of higher aggregation states, such as F_3- and F_4-centers, are observed, high dense defects were produced by irradiation of 175 MeV Ar ions and its aggregation might proceed during irradiation and in the period of cooling.

In Fig. 2, the depth profile of absorbance measured at the wavelength of 450 nm is shown. In this measurement, the magnification of object lens was 40 and area-defining diaphram located behind the object lens was 0.1 mm in diameter, so that the depth resolution of this measurement is about 2.5μm. Absorption intensity is almost constant between the irradiarion surface and the projected range of 175 MeV Ar ion (36μm), and it decreases

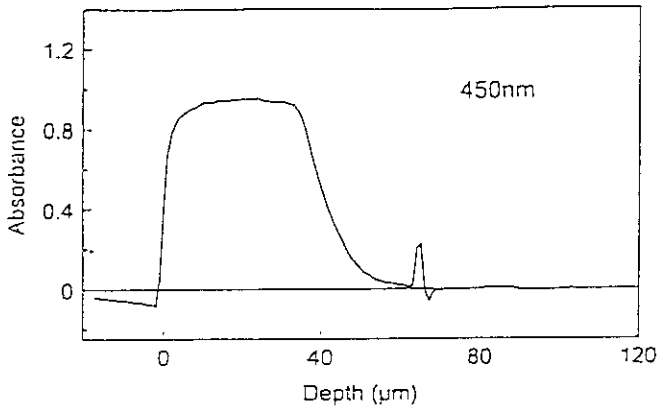

Fig. 2 The depth profile of absorbance measured at 450nm for LiF irradiated with 175 MeV $^{40}Ar^{8+}$ at the dose of 1 x 10^{13} ions/cm^2.

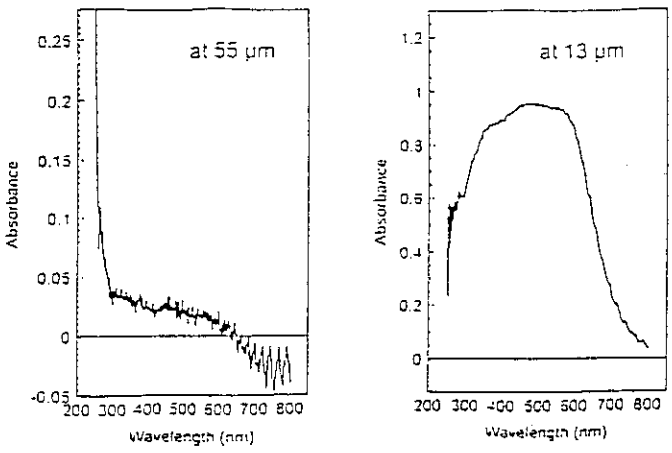

Fig. 3 The optical absorption spectra for LiF irradaiated with 175 MeV 40Ar8+ at the dose of 1 x 1013 ions/cm^2 measured at the depths of 13μm and 55μm.

slowly towards the deeper region. It suggests a large contribution of secondary enectrons to formation of defects in this case. Fig. 3 shows photoabsorption spectra measured at the depths of 13μm and 55μm are shown, which correspond to the depths for the saturated region of F_2-center absorption and for the deeper region than the ion range, respectively. Within the ion range(at 13 μm), not only F_2-center but F_3- and F_4-centers show significant absorption intensities. On the other hand, in the region over the ion range(at 55 μm), the intensity of F-center absorption is much higher than the others. These results show that, in this irradiation condition, high dense electronic energy loss formed various kinds of F-aggregate states in the irradiation region and over the ion range F-center are dominantly formed by secondary radiation. Furthermore, through the irradiation region, F_2-centers are formed with constant cocentration but F_3- and F_4-centers have some distributions. MgO sample irradiated with 175 MeV Ar at the dose of 5 x 10^{13} ions/cm^2 showed weak absorption, so that we failed to

measure depth profiles of any defect absorption at this stage.

In the near future, we will investigate the dose dependence of spectrum and depth distributions for alkali halides and oxide ceramics.

References

(1) A. Kikuchi, H. Naramoto, K. Kozawa and Y. azumata, Nucl. Instr. and Meth. B39 (1989) 724.

(2) L.L. Regel, V.R. Regel, S.E. Boriskin, G.G. Knab, A.A. Urusovskaya, L.I. Alekseeva and V.V. Klechkovskaya, Phys. Stat. Sol. 73 (1982) 255.

(3) A. Perez, J.Davenas and C.H.S. Dupuy, Nucl. Instr. and Meth. 132 (1976) 219.

(4) M. Luntz, P.E. Thompson, R.B. Murray and D.J. Whittle, Radiat. eff. 31 (1977) 89.

(5) K. Kubo, J. Phys. Soc. Jpn. 35 (1973) 125.

5.5 Studies on Radiation Effects in Solids Using Low-Temperature Electron Irradiation Facility

A. Iwase, M. Watanabe, N. Ishikawa and T. Iwata

Group for Low-Temperature Irradiation Effects
Advanced Science Research Center JAERI

Electron irradiation can produce isolated Frenkel defects (vacancy and interstitial) homogeneously in bulk specimens and is indispensable for the research in radiation effects. As Frenkel defects are thermally unstable in most of solids, irradiation must be performed below 4.2K to freeze a thermal motion of defects.

In March 1994, we assembled a low-temperature electron irradiation facility at SX beam line of a single-end accelerator and started a low-temperature electron irradiation in July. This facility (Fig.1) is designed for 0.4-3MeV electron irradiation below 4.2K. It consists of efficient electron beam guide system and two cryostats for calorimetric measurements and for measurements of electrical properties. Change in physical properties (specific heat, release of stored energy, electrical resistivity and so on) by electron irradiation can be measured *in situ* without warm up specimens.

The present research themes are as follows; (1) selective displacement and flux pinning in electron-irradiated high-Tc superconductors, (2) resonance mode caused by irradiation-produced interstitials in copper and graphite and (3) behavior of interstitials below 4K in electron-irradiated BCC metals.

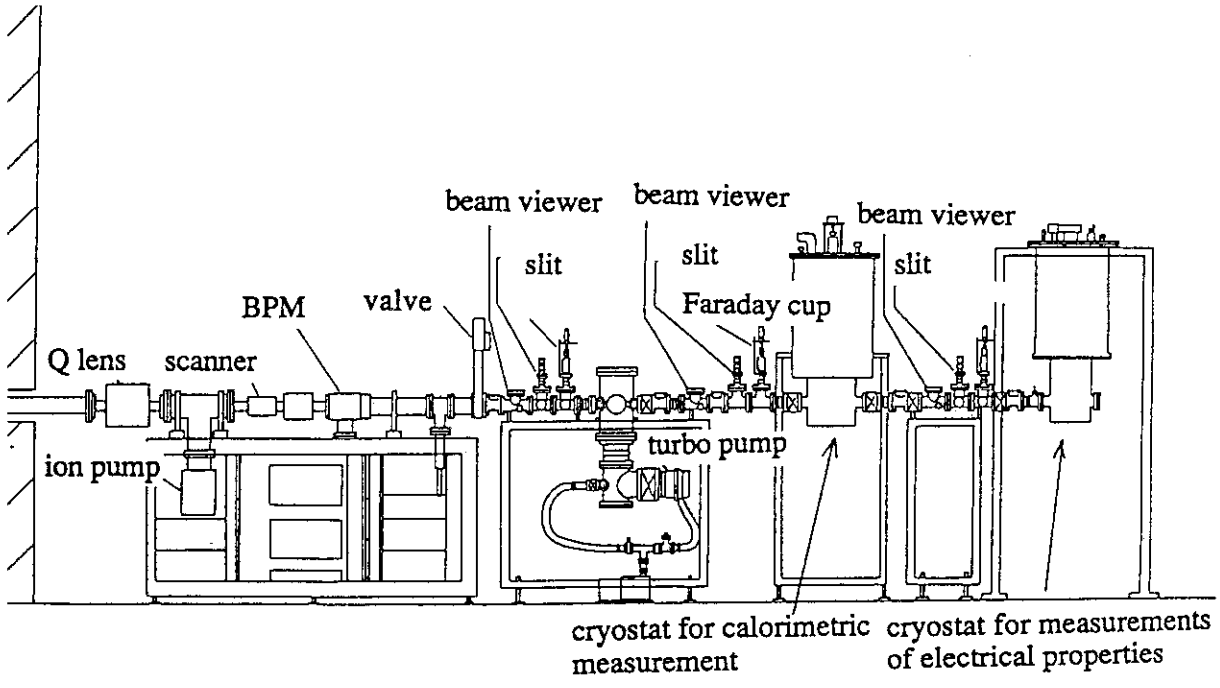

Fig.1 Low-temperature electron irradiation facility at SX line of a single-end accelerator.

5.6 Development of Triple Ion Beam Irradiation Facility

S. Hamada, Y. Miwa, Y. Katano, T. Nakazawa, K. Noda

Materials for a fusion reactor, which include structural materials, solid tritium breeder materials and ceramics materials as insulators, will be exposured under too severe irradiation circumstance of heavy displacement damage and a great deal of helium and hydrogen atoms including tritium, which produce by transmutation reaction of (n, α) and (n, p), respectively. In order to develop materials for a fusion reactor, it is important to study the overlapped effects of both these displacement damage and transmutation reaction gas products as helium and hydrogen on properties and degradation of durability of fusion materials. Therefore, to simulate the irradiation circumstance of a fusion reactor, triple ion beam irradiation facility [1,2], which can simultaneously irradiate three species of ions on a target, has been developed and completed. The abstract and status of this facility are reported below.

This facility was installed in the second target room of the multiple beam building in Takasaki site of JAERI at the end of January in 1994 and beam alignment tests have been performed. Fig.1 shows the appearance of the triple ion beam irradiation facility. This facility mainly consists of two components : one is a chamber for irradiation experiments and another is incident ports to induce ion beams from accelerators. The incident ports have three beamlines : One is used to lead heavy ions such as nickel and oxygen to provide displacement damages to materials. other two lines are to do light ions as hydrogen and helium to inject into materials. The beamline for heavy ions connects with a 3-MV tandem accelerator, those for hydrogen and helium ions with a 0.4-MV ion implanter and a 3-MV single-ended accelerator, respectively. Fig. 2 shows a two dimensional plan view of the chamber and the beamlines in fig.1. The beamline from the ion implanter is essentially normal to the actual target, whereas the beamlines from the remaining accelerators are about 15° on each side of the 0.4-MV ion implanter. These beamlines are almost same level from the floor.

The chamber is manufactured by 304 stainless steel. The dimensions are about 50 cm in diameter and 60cm in height. the vacuum of the chamber was below 2 x 10^{-8} torr without heating and below 1 x 10^{-7} torr during heating of 500℃.

In the chamber, a sample stage to irradiate and degraders to inject light ions relatively uniformly in the depth direction of materials are set up. There are two kinds sample stages : one is a cold stage available to irradiation in the temperature range from liquid nitrogen temperature to 400℃, another is a hot one for high temperature irradiation, which is available from room temperature to 1200℃. Each sample stage has three sample holders and three micro faraday cups in a row in vertical direction. Fig.3 shows the hot stage. All sample holders are normal to the beamline of the ion implanter. Each sample holder is capable of loading either seven specimens (3mm in diameter) at maximum for a transmission electron microscope (TEM) or one specimen (10 mm in diameter) at one time by replacing the cover of a sample holder. Each micro Faraday cup is essentially normal to each beamline and the position and the diameter of each hole on it corresponds to those of each specimen of a sample holder, by which the beam current of each beamline is measured. A sample stage is capable of shifting in the vertical direction to irradiate materials and measure beam currents. Therefore, the beam current can not be estimate during beam irradiation. The irradiation is available in the area 15 mm x 15 mm at minimum using scanners, which are described below. Each degrader is located on the beamline of the ion implanter and the single-ended machine, and at the position of about 20 cm toward each accelerator apart from the target. The nickel foils is supplied to the degraders and its thickness is 1 μ m and 4 μ m for each beamline of the ion implanter and the single-ended accelerator, respectively. The dimension of a nickel foil is 68 mm x 50 mm. The degrader can be anticlockwise rotated to the angle of 45° from the plane normal to the beamline.

In order to obtain more uniform and wider irradiation area, scanners available to the horizontal (X) and vertical (Y) direction are installed to all beamlines and its polarized wave is triangle. The frequency of a scanner is changeable in three stages : the stages in the X and Y direction are 10kHz, 1kHz and 100Hz, and 1kHz, 100Hz and 10Hz, respectively. Furthermore, the scanner also possesses the function

maximum in the X and Y direction.

This facility, furthermore, is designed to be able to carry out ion beam analysis in the beamlines of the tandem and the single-ended accelerator. A sample stage attached with a six axes goniometer has already been prepared and some additional apparatuses such as detectors and amplifiers will be installed for ion beam analysis in the near future. A high-resolution quadrupole mass analyzer is also attached to the chamber, which can analyze the mass of He-3 and He-4. Most of performance as described above can be remote-controlled in the control room for electrostatic accelerators.

The results achieved during beam alignment tests at the end of 1993 fiscal year were as follows :
(1) All ion beams from three were focussed on the same position on a target.
(2)The irradiation temperature was controlled in the temperature range from room temperature to 800℃ and the accuracy of temperature was ±2℃ at 800℃.
(3)The scanners and the degraders worked as designed.
(4)Each micro Faraday cup was able to measure ion beam current and the beam profile on a sample holder was confirmed to be relatively uniform.

Resultantly, triple ion beam experiments can be carried out at high temperature in the present time. The irradiation experiments under lower temperature and ion beam analysis will be completed in the near future.

References

(1) K. Farrell, M. B. Lewis and N. H. Packan, Scripta Metallurgica., Vol.12, (1978) 1121.
(2) M. B. Lewis, N. H. Packan, G. F. Wells and R. A. Buhl, J. Nucl. Instru. and Methods, 167 (1979) 233

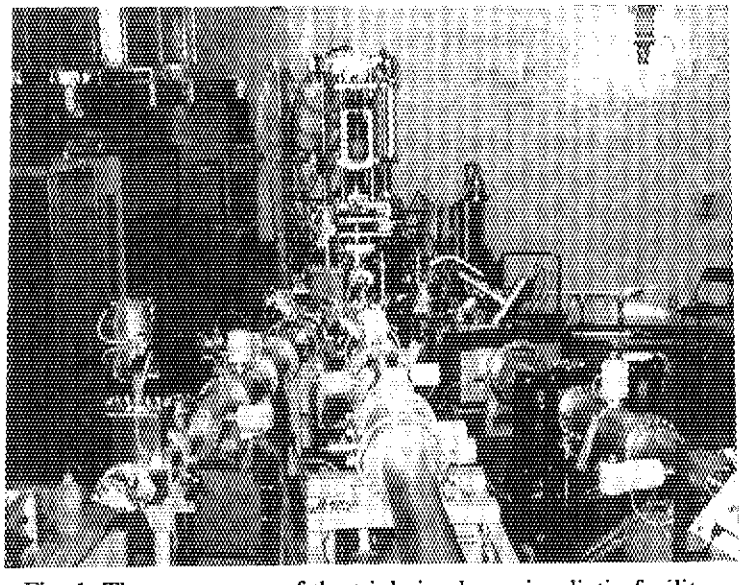

Fig. 1 The appearance of the triple ion beam irradiatin facility

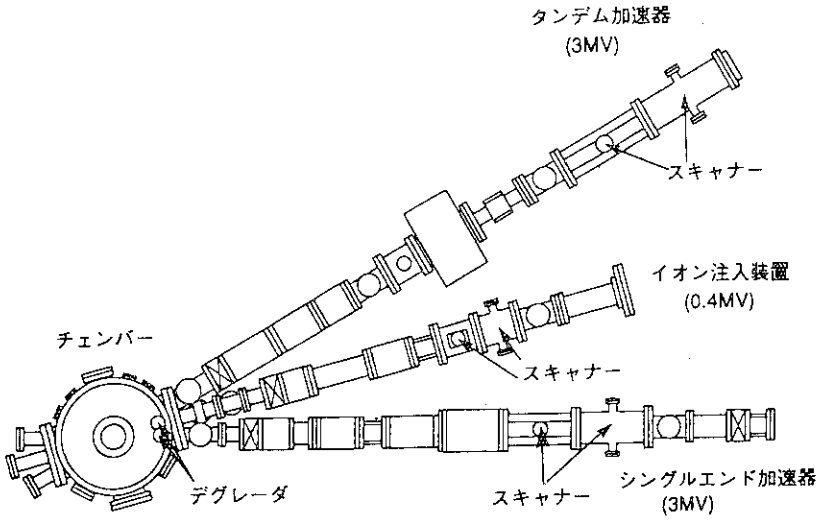

Fig.2 A two dimentional plane view of the chamber and beamlines in fig. 1

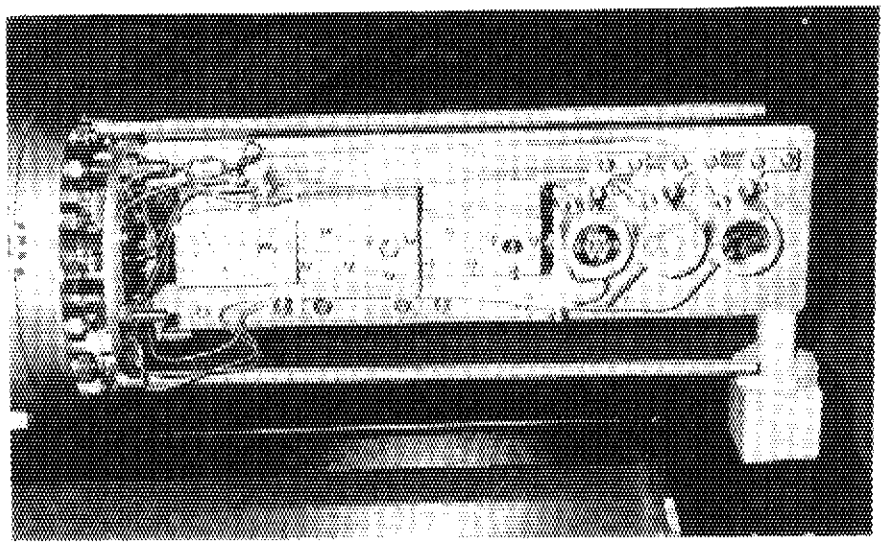

Fig.3 The sample stage for high temperature irradiation (a)The left three boxes with rectangular shape are micro Faraday cups (b) The right three cylinders are sample holders. The third one is for TEM samples and the second is for a sample of 10 ϕ in diameter from the right.

5.7 A Study of Cascade Damage Analysis Method based on PKA Energy Spectrum

Jun Saeki,Seiji Okada,Naoto Sekimura and Shiori Isino
Faculty of Enigneering, Univ. of Tokyo

Abstract

Self-ion irradiation was performed to investigate PKA energy dependence of defect cluster formation and cascade damage structure. Thin foils of gold were irradiated at room temperature using the 3 MV tandem accelerator in TIARA facilities. Groups of defect clusters, i.e., subcascade structure produced by high energy PKAs, are observed by a 200kV transmission electron microscope (TEM). Since self-interstitial atoms in gold have high probability to escape to the foil surface, all the observed clusters were considered to be of vacancy type. The number density and size distribution of the clusters and number of defect clusters in a group are measured. PKA energy dependence of energetic effect that was caused by cascade is also estimated.

Introduction

The structure of cascade damage in metals produced by high energy particles is dependent on energy of PKAs (Primary Knock-on Atoms). To establish correlations between various irradiation data, microstructural changes in irradiated materials should be analyzed based on the PKA energy spectrum. In the case of gold that was irradiated by energetic neutron using RTNS-II or YAYOI reactor, the fluence dependence of cluster number density varies from linear relation to almost the square relation with increase of fluence. The reason for this is considered to be attributed to the conversion of the TEM-invisible clusters to visible ones by the energetic influence from nearby cascades.

In the present study, thin foils of gold were irradeated with high energy self-ions to examine PKA energy spectrum dependence of defect cluster formation and the conversion of invisible clusters to visible ones.

Experimental

Thin foils of 99.99% pure gold were prepared by electro-polishing after annealing in a high vacuum (10^{-7} torr) for one hour at 973K. These specimens were irradiated with 21MeV self-ions at room temperature. Ion fluence is ranging from $5x10^{13}$ to $5x10^{14}$ ions/m^2.

Post-irradiation observation was performed for all specimens using a JEM-2000FX transmission electron microscope operated at 200kV.

Result and discussion

The fluence dependence of defect cluster number density is shown in Fig1. Though the defect density increases in propotion to fluence (ϕt) up to $5x10^{14}$ ions m^{-2}, for the higher fluence it increase with $(\phi t)^n$ where $n>1$. At the fluence where the number density was deviated from the linearity, the density and group density of defect clusters are $1.96x10^{21}$ m^{-3} and $1.13x10^{21}$ m^{-3}, respectively . Assuming that defect cluster groups are formed uniformly in the matrix, the average distance

L_{21} between the groups is evaluated to be about 55nm. In the other hand, those, i.e., L_Y and L_{14} are 57 and 90 nm for YAYOI reactor and RTNS-II irradiation, respectively.

It is considered to be reasonable that the influence of cascade to the conversion of invisible clusters to visible ones is larger for higher PKA energy , because larger energy is dispersed from the cascades with a higher PKA energy through the matrix. If we assume the following two points:

(1) The volume affected by cascade formation is propotional to Lindhard's damage energy.

(2) Only when the PKA energy is greater than E_{im} , the PKA event converts invisible clusters into visible ones.

The value of <E> is defined as follows.

$$<E> = \int_{E_{im}}^{E_{max}} E_D(E_p) W(E_p) N \phi t \, dE_p$$

where $W(E_p)$ is the PKA energy spectrum, N is atom number density of gold ,and E_D is the damage energy . $<E_Y>$, $<E_{21}>$ and $<E_{14}>$ can be defined under the above irradiation cases (YAYOI, Tandem and RTNS-II, respectively). <E> represents the averaged damage energy corresponding to each irradiation case. then the following equation should be satisfied.

$$Ly : L21 : L14 = \sqrt[3]{\langle Ey \rangle} : \sqrt[3]{\langle E21 \rangle} : \sqrt[3]{\langle E14 \rangle}$$

From this equation , the energy Eim is successfully evaluated to be 165 keV.

Pablications

1) Okada,A study of Cascade Damage Analysis Method based on PKA Energy Spectrum by Higy Energy Particle Irraddiation, M.thesis of Engineering, Univ. of Tokyo (in Japanese).

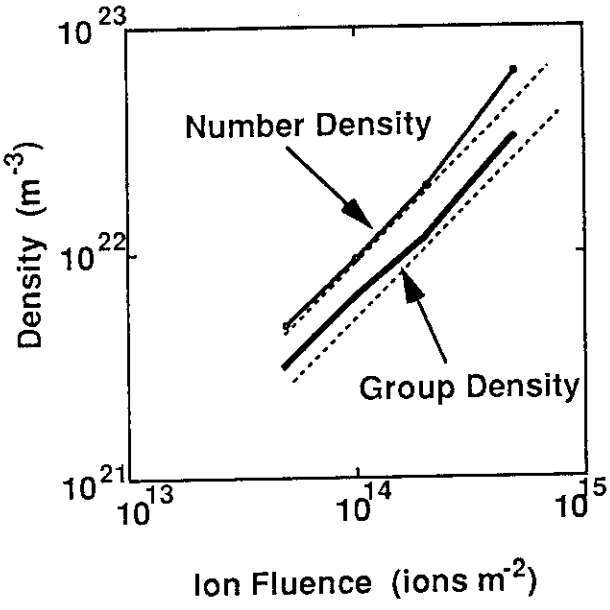

Fig.1 Ion fluence dependence of defect cluster density in irradiated gold to 5.0x 10^{15} ions m^{-2} at room emperature.

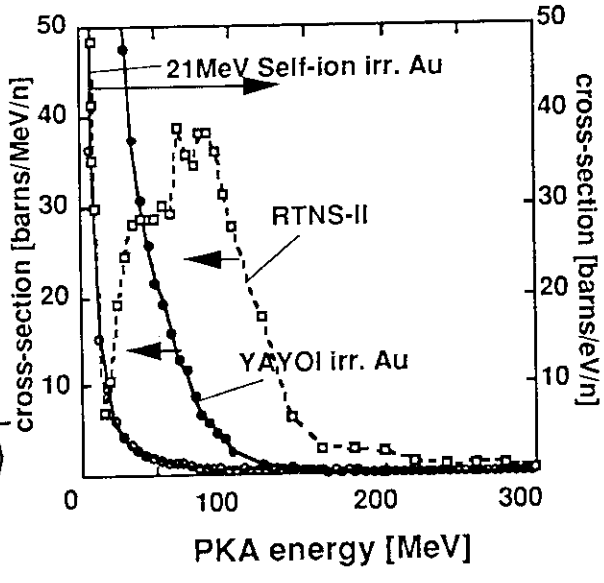

Fig.2 PKA energy spectrum in each irradiation case.

5.8 Application of Ion- or Electron-Beam Irradiation to Promote Nitrogen Compound Layer Formation in Iron

T.Okada, M.Ikeya*. M.Nunogaki, S.Nishijima, H.Kohno*,
H.Takeshita**, Y.Aoki**, S.Yamamoto** and H.Naramoto**
ISIR, Osaka University
* Faculty of Science, Osaka University
** Takasaki Establishment, JAERI

1. Introduction

For the purpose of decreasing the erosion of plasma facing materials in the experimental fusion devices due to high thermal shock and energetic particle bombardment, a new process of surface improvement composed with the preceding processing such as an ion or electron beam irradiation and the main processing such as surface nitridation or coating of light-Z elements has been developed by authors. In the process, the ion or electron beam irradiation has worked positively or negatively on the main processing relating to ion species and beam fluence.

In the experiment, the effects of 1MeV-Ni-ion pre-irradiation on changes in hardness and thickness of nitrogen compound layer in pure iron were examined in comparison with that of 20MeV-electron beam pre-irradiation.

This experiment is a part of experiments to research the mechanism of the effects caused by the preceding ion or electron beam irradiation on the main processing and to develop the new process for surface improvement such as nitridation, silicification, coating films, bonding of dissimilar metals and so forth.

2. Experimental procedure

The experimental procedure was presented in table 1. The experiment was consisted of two processes; the first was the irradiation with a MeV-order ion or electron beam irradiation, and the second was the surface nitridation with use of plasma processing. The specimens of pure iron (99.99%, purity) were 10x10 mm^2 in area and 2 mm in thickness. The surface was polished mechanically to optical quality, and the specimens were annealed in vacuum for 2hrs at 500C.The ion irradiation was performed at ambient temperature using a tandem accelerator installed in Takasaki establishment,JAERI.The mean projectile of injected ions was estimated to be 0.33um by calculation. The irradiated samples were deposited in air for weeks. The 20MeV-electron beam irradiation was made to the specimens cooled with pure water in air.

Nitridation was carried out in the plasma mixture of nitrogen and hydrogen by applying the negative bias of 1kV to samples against plasma.

Hardness was detected with Vicker's hardness tester. The modified surface was analyzed with XRD(X-Ray Diffraction), EPMA(Electron Photon Mass Spectroscopy) and AES(Auger Electron Spectroscopy). The effects of electron beam irradiation were checked with use of PAS(energy-spread Positron Annihilation Spectroscopy). The experimental conditions were tabulated in table 2.

3. Results and Discussion

3.1. Hardness and Thickness

The relative hardnesses plotted in Fig. 1 and 2 were expressed as the ratios of the nitrided hardness with or without beam irradiation to the hardness of raw iron. The sharp rise and fall of curve coresponded well to the phase change in e-phase, r'-phase and pure iron, which were identified from the data of component analysis described later and the phase diagram.

Figure 1 showed the relative hardnesses nitrided for 1 hour after 1 MeV-Ni^+-ion pre-irradiation at a fluence range of $5x10^{15}$ to $5x10^{16}$ cm^{-2}. Hardness and thickness (a sum of e-phase $Fe_{2-3}N$ and r'-phase Fe_4N layer) varied with fluence and had the optimum value at $2x10^{16}$ cm^{-2}. The increasing ratios of the maximum hardness and thickness were about 1.3 and 1.7 ,respectively. These fluence effcts may be caused by some changes in the surface state such as formation of lattice defects, amorphousation and the resultant variation of potential distribution. When the mechanism of enhancement of nitrogen adhesion due to the pre-irradiation was made clear by piling up the data of the correlations among ion species,

Table 1 Experimental proccdurc

Sample	Preparative processing	Main processing	Measurement
Polishing Annealing	1MeV $-Ni^+$ ion irrad or 20 MeV $- e^-$ irrad	Nitriding	Hardness XRD AES, EPMA

Table 2
Experimental conditions

Annealing		Preparative irradiation				Plasma source nitriding			
Temp. (°C)	Time (h)	Temp.	Particle species	Fluence (cm^{-2})	Energy (MeV)	Gas (Pa)	N:H	Temp. (°C)	Time (h)
500	2	R.T.	Ni^+	$1x10^{16}$	1	$6x10^{-2}$	5:2	400	1, 4,
		Water T.	e^-	$1x10^{19}$	20				

fluence and materials, the new type of surface processing will be developed reasonably for direct surface improvement, coating films, bonding of dissimilar metals and so on.

The relative hardness distributions with 20MeV-electron pre-irradiation were represented in Fig.2. The real and dotted lines showed hardness changes with and without the pre-irradiation, respectively. The nitriding time for the curves (a) and (b) were 1 and 4 hrs, respectively. The fluence of electron beam was approximately $1x10^{19}cm^{-2}$. In the figure, the increasing ratio of thicknesses of both the compound layers were about 1.2 by the pre-irradiation. Hardnesses at the outermost surfaces were not decreased like as ones with the ion pre-irradiation in Fig. 1. This difference was explainable from the nitrogen concentration at the outermost surface as shown in Fig.4 & 5, since e-phase layer was formed under the conditions of abundant concentration of nitrogen and its hardness was lower than r'-layer.

3.2. Abundance ratio of nitrogen

The surfaces of nitrided specimens were analyzed with XRD, EPMA and AES. The typical X-ray diffraction pattern of the specimen nitrided after the pre-irradiation was shown in Fig.3. It indicated that the nitrided layers in pure iron were the mixture of the solid solution composed of Fe, N, $Fe_{2\sim3}N$(b.c.c.) and Fe_4Nf(f.c.c.). In the outermost surface, O and C were sometimes contained.

The specimen nitrided after 1MeV-Ni-ion pre-irradiation was analyzed with EPMA as in Fig.4. In the figure, the relative nitrogen concentration was extremely high at the outermost surface over about 8um. The specimens nitrided without any pre-irradiation as shown in the curve (a) in Fig.5 also had the higher nitrogen concentration at the surface. However, its thickness and volume was small. The formation of this intense and thick nitrogen concentration layer appeared to be one of the distinctive features induced by the 1MeV-Ni-ion pre-irradiation.

Figure 5 shows the cross-sectional nitrogen concentration profiles in the surfaces nitrided without (a) and with (b) 20MeV-electron beam pre-irradiation. The average nitrogen concentration shown in the curve (b) was decreased to about one half to the curve (a). This decreased nitrogen concentration was brought about by an increase of nitrogen diffusion length due to the irradiation-induced lattice defects and was still enough to form r'-phase layer.

The decrease of the abundance ratio of nitrogen at the outermost surface in the curve (b) suggested that e-phase layer was hardly composed with 20MeV-electron beam pre-irradiation, in spite of that a cosidarably thick e-phase layer was always produced in the case of nitriding iron with ion- or gas-soft-nitridation used commonly. This means that the MeV-order electron beam pre-irradiation was advantageous to form thick r'-layer, which was superior to toughness and had various advantages for the industrial use, directly on the surface of iron.

For the purpose to understand the reasen why 20MeV-electron irradiation was effective on increasing the thickness of nitrogen compound layer, the positron annihilation method was utilized to obtain some informations of lattice defects in the specimens before and after nitridation. The life time spectra were decomposed into three components; the matrix component(τ_1, I_1), vacancy component(τ_2, I_2) and another larger one(τ_3, I_3), where τ and I were lifetime and the relative intensity, respectively. However, the last one were neglected here due to the low time resolution of the electrical circuits used. The obtained results were shown in Fig. 6. From the figure, it was ascertained that the annealing was surely effective to reduce the size and concentration of defects, and that the vacancy-type defects and clusters created by the pre-irradiation were disappeared by nitridation to the level of annealed state, and that the interstitial-type atomic clusters and the grain boundaries were increased by nitridation.

4. Conclusion

Hardness and thickness of nitrogen compound layer in pure iron was varied with the fluence of 1MeV-Ni-ion irradiation. Implanted Ni-ions worked to enhance the adhesion of N-atoms through the plasma-solid interface to the surface of iron. Further investigation is required to clarify the mechanism.

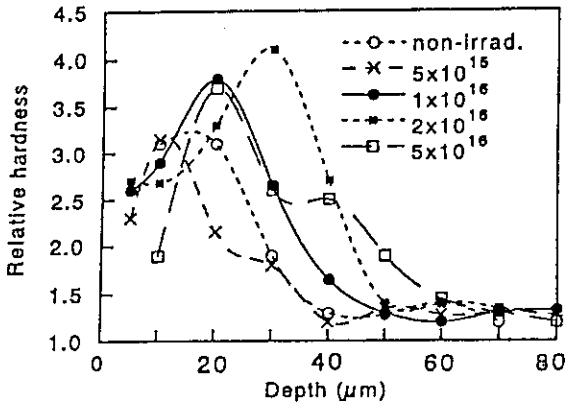

Fig. 1

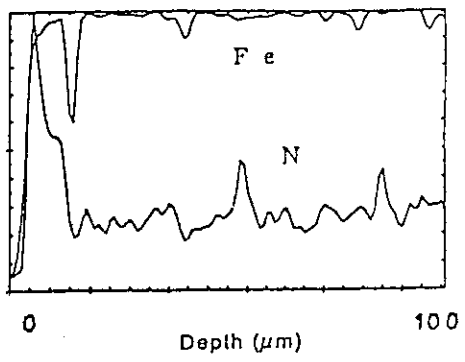

Fig. 4

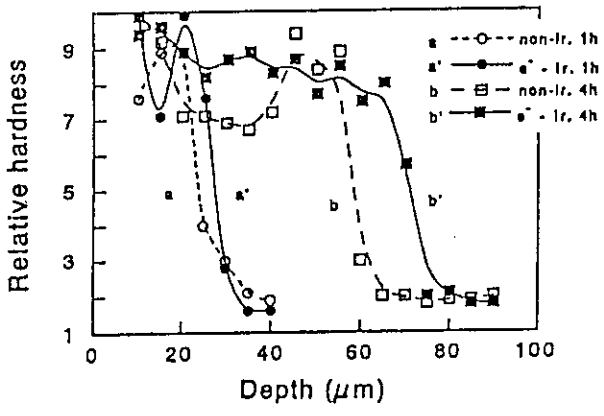

Fig. 2

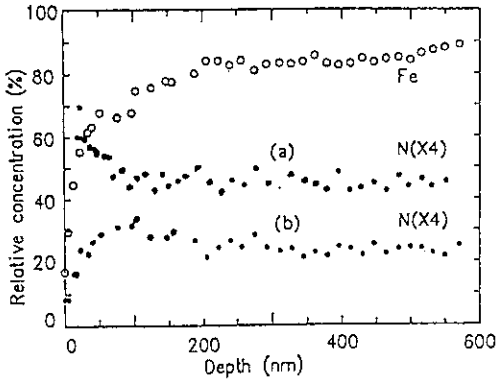

Fig. 5

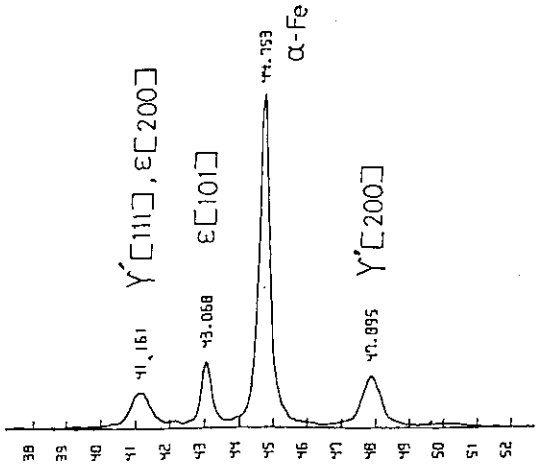

Fig. 3

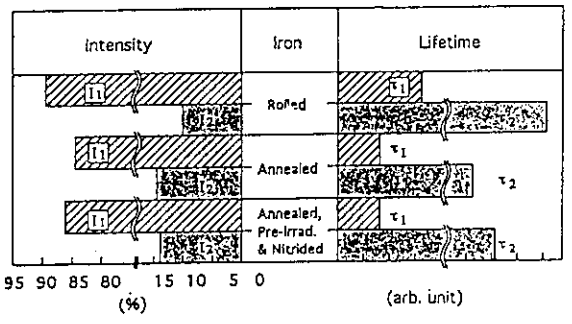

Fig. 6

5.9 Luminescent properties of Cr doped Al_2O_3 under Ion Bombardment

Yasushi Aoki, Nguyen. T. My, Hidefumi Takeshita,
Shunya Yamamoto, Peter Goppelt-Langer
and Hiroshi Naramoto

Functional Materials Lab. II, Department of Materials
Development, TRCRE, JAERI

Cr doped poly-crystalline Al_2O_3 (Al_2O_3:Cr) is a luminescent materials which is often used for beam positioning, beam focusing and defocusing etc. in accelerators facilities like TIARA facility, because it emits intense red light on being exposed to radiation. However, the intensity depends strongly on the irradiation parameters such as kind of ion beam, energy of the ion and irradiation dose. Especially, the dose dependence is important for practical use of this materials. We have just started to study the luminescent properties of Al_2O_3:Cr under ion bombardment on basis of the correlation with changes in surface states.

Cr doped single-crystalline α-Al_2O_3 (Ruby) has been examined about its absorption and emission of R-lines[1], and laser and maser actions[2-3]. In the present study, luminescence from doped Cr^{3+} in poly-crystalline Al_2O_3 was mesured during ion bombardment of 200 keV Ar^+ and He^+ ions.

Samples used here were a commercial sintered Al_2O_3 doped with Cr (AF995F, Demarquest) and a single crystal of Al_2O_3:Cr. Ion irradiation was performed with a 200 keV ion implanter (Takasaki Ion Beam Implanter). Samples were irradiated with 200 keV Ar^+ and He^+ and luminescence spectra of the samples were maesured by a combination of a spectrograph (HR250, Jobin-Yvon) and an optical multichannel Detector (MHD-42, Atago-Bussan). Measured spectral range was limited between 630nm and 830nm. Complementary data were obtained with a fluorometer (F-4500, Hitachi), for exmple cooresponding luminescence spectra induced by light excitation and excitation spectra for irradiated and unirradiated samples. In addition, RBS-Chaneling analysis was also done for single crystal samples.

Fig. 1 shows a typical luminescence spectrum of sintered Al_2O_3:Cr sample measured during 200 keV Ar^+ bombardment. An intense luminescence peak is observed at 695 nm. This peak is similar to taht observed from single crystal sample (Ruby) excited with a tungsten lamp[1]. Furthermore, the same luminescence peak was observed from the poly-crystalline samples in our photoexcitation experiment and the excitation spectra reflected the

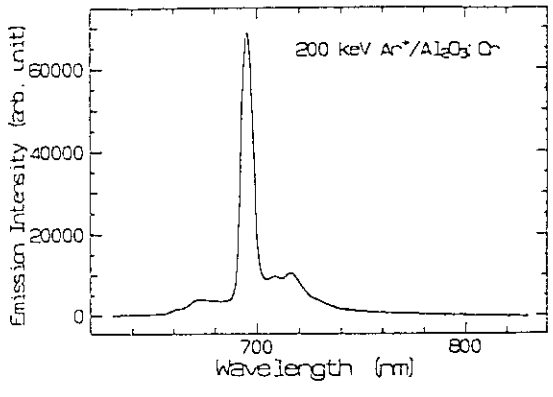

Fig. 1 The luminescence spectra of sintered Al_2O_3:Cr during 200 keV Ar^+ Bombardment.

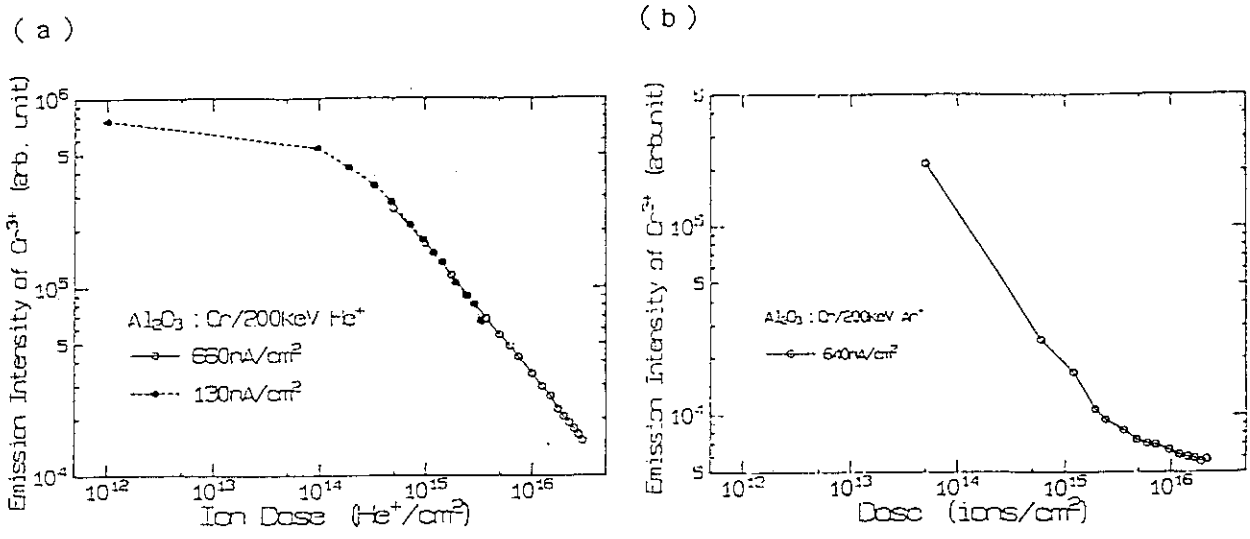

Fig. 2 The change in intensity of R-line from Cr^{3+} observed in ion bombardment. (a) 200 keV He^+, (b) 200 keV Ar^+.

electronic energy levels of Cr^{3+}[1,2]. The lifetime of this luminescence was measured about 3.4 msec which agrees with that measured for ^2E levels of Ruby at room temperature[1]. Therefore, it is concluded that the luminescnece observed at 695 nm for the ion bombarded poly-crystalline Al_2O_3:Cr should be due to the electronic transition from ^2E states (first excied states) to ^4A states (ground states) of the doped Cr^{3+}, so-called R-line.

Fig 2(a) and (b) show the dose dependences of intensity of 695 nm luminescence in ion bombardment experiments with 200 keV He^+ and Ar^+, respectively. Although much more intense luminescence can be obtained in He ion bombardment than that in Ar ion bombardment, in both cases luminescence yield of R-line decraeses with irradiation dose and the dgree of decrease is more than one and half order of magnitude. This phenomenum is important for the practical use of the material as a luminescent material in beam experiments.

The shift of luminescence spectra was observed in continuous irradiation experiment and in the experiments with different current densities, as seen in Fig. 3. The higher dose was irradiated or the higher current density was used, the lower enegy of luminescence was obtained. It indicates that the irradiated sample was heated by energetic ions. When sample is heated, the peak position moves to longer wavelength and at the same time the intensity is decreased[1]. However, only this temperature dependence cannot explaine the decrease in intensity observed in Fig. 2. It suggests that other mechanism should work for the decrease in intensity of R-line in ion bombardment experiment.

In the experiments for single crystalline samples, faster decrease of the intensity

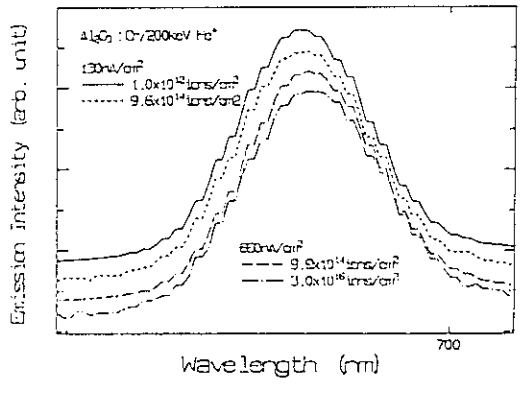

Fig. 3 The luminescence spectra of Cr^{3+} (R-line) during 200keV He^+ bombardment.

with dose than taht for polycrystal was observed, but the tendency of the results was the same as described above for polycrystals. In RBS-Channeling analysis, the damage created in the sample evolved with the irradiation dose up to 2×10^{16} ions/cm^2. It can be related to the decrease of luminescence yield. Further investigation is needed to clarify the degradation mechanism of luminescent efficiency of Al_2O_3:Cr and the excitation mechanism for luminescence of doped impurities under ion irradiation.

References

(1) D.F. Nelson and M.D. Sturge, Phys. Rev. 137 (1965) 1117.

(2) T.H. Mainman, R.H. Hoskins, I.J. D'Haenens, C.. Asawa and V. Evtuhov, Phys. Rev. 123 (1961) 1151.

(3) F.J. McClung, S.E. Schuwarz and F.J. Meyer, J. Appl. Phys. 33 (1962) 3139.

(4) D.F. Nelson and J.P. Remeika, J. Appl. Phys. 35 (1964) 522.

5.10 Formation of Silicide Film by means of Ion-Mixing

S. OHNUKI, T. HATAKEYAMA, H. TAKAHASHI,
S. YAMAMOTO*, H. TAKESHITA*, H. NARAMOTO*
Faculty of Engineering, Hokkaido University
*Takasaki Institute, JAERI

Ion-mixing can modify the material properties through two processes; one is production of large amount of point defects, which enhances lattice diffusion, and the other is the direct atomistic collision, which causes atom movement even at low temperature. For the formation of silicides during fabricating LSI, heat-treatment at relatively high temperature has been needed. Therefore, ion-mixing has currently application as a method of silicide formation at low temperature. The objectives of this study are to clarify the condition of silicide formation by means of ion-mixing, to identify microstructures of formed phases and to evaluate diffusion constant during irradiation.

Si wafer with (100) was used for experiment, after Mo vapor deposition with thickness of 600 A. Irradiation with Ar^+ ion of 180 keV was carried out in 300 kV accelerator of Hokkaido University, at where the temperature were -100 - 300 C, and irradiation doses were $1x10^{16}$ - $1x10^{17}$ ion/cm^2. Si^+ ion irradiation of 1000 keV was carried out in TIARA at only ambient temperature. After irradiation, specimens for transmission electron microscopy (TEM) were prepared by the cross-cut method, which means the observed direction was <110>, perpendicular to irradiation beams. Depth distribution of concentration of Mo and Si was determined by using a energy dispersive X-ray spectroscopy (EDS) equipped with 200 kV TEM.

Ar^+ ion Irradiation in Hokkaido university

Crossectional TEM observation and electron diffraction were carried out the specimen after the irradiation of 180 keV Ar^+ ion. At lower irradiation dose, $1x10^{16}$ /cm^2, the irradiation affected to the thickness of 200 nm of Si substrate, and the middle of the layer turned to amorphous. Crystalline Mo remained, and a layer between Mo and amorphous Si was confirmed as amorphous stricture. With increasing of dose, the amorphous of mixture of Mo and Si was increased in thickness. This means that ion-mixing process occurred in this condition. In the case of higher dose, $1x10^{17}$ /cm^2, gas bubbles were observed at amorphous layer.

Ar^+ irradiation was continued to higher doses of $1x10^{17}$ /cm^2 at various temperature. At lower temperature, -100C, almost all of mixed layer was crystalline, and Mo rich layer can be defined as a dark contrast. After the irradiation at 100 C, crystalline $MoSi_2$ was formed between amorphous Mo/Si mixture and amorphous Si layers. At 200 C, the thickness of $MoSi_2$ increased, and amorphous Si layer turned to crystalline Si layer which included large amount of irradiation-produced damages. At higher temperature, 300C, only $MoSi_2$ and damaged Si layers were observed. This results indicate that by ion-mixing method crystalline $MoSi_2$ can be formed over 100 C, which temperature is quite lower comparing to thermal treatment. It

can be suggested that the stability of each amorphous layers is the order of $MoSi_2$ < Mo/Si mixture < Si. It has been reported that amorphous Si is stable under 240 C.

Figure 3 shows the concentration profiles of Si in specimens irradiated to $1x10^{17}$ /cm^{-2} at various temperatures. At lower temperatures, Si diffused to the direction of the surface and formed concentration gradient, though data points have large scattering. At higher temperatures, the gradient of Si concentration became to flat, which can be suggested to occur more progressive diffusion.

Si$^+$ ion Irradiation in TIARA

Crossectional TEM observation and RBS measurement were carried out in TIARA in which 1000 keV Si$^+$ and He$^+$ ions were used at room temperature to different ion doses. At lower irradiation dose, $1x10^{16}$ /cm^2, the irradiation affected to the thickness of 200 nm of Si substrate, and Si layer until 1000 nm in thickness turned to be amorphous. Crystalline Mo remained, and a layer between Mo and amorphous Si was confirmed as amorphous stricture. With increasing of dose, the amorphous of mixture of Mo and Si was increased in thickness, which means that ion-mixing process occurred clearly in this condition. In the case of higher dose, $5x10^{16}$ /cm^2, gas bubbles were not confirmed at this irradiation condition. EDS analysis also applied for these specimens, and showed that Si diffused to the direction of the surface and formed concentration gradient. At higher dose, the gradient of Si concentration became to flat, which showed that a enough diffusion occurred at this condition. Those profiles detected from EDS consisted with the RBS spectrum.

The data can be summarized as follows: Ion beam mixing of 180 keV Ar$^+$ and 1000 keV Si$^+$ ion irradiation were applied for the formation of silicide of Mo/Si system. The objective silicide $MoSi_2$ was formed by the irradiation

relatively low temperatures, over 100 C. The estimation of diffusion constant indicates that atomistic collision and radiation enhanced diffusion processes are predominate in this phenomenon. The ion-mixing is strongly dependent on ion species, especially gaseous elements has a possibility to reduce the amount of ion-mixing during gas bubble formation.

5.11 Influences of Ion Implantation on the Structure and Properties of C_{60} Thin Films

T.Asakawa, M.Yoshimoto, M.Sasaki[2], H.Koyama[2], H.Takeshita[3], Y.Aoki[3], S.Yamamoto[3], P.Gopperlt-Langer[3], H.Naramoto[3] and H.Koinuma

Res. Lab. of Eng. Mater., Tokyo Inst. of Tech.

[2]Faculty of Eng., Dept. of Commun., Tokai Univ.

[3]Dept. of Mater. Develop., JAERI/Takasaki

1.INTRODUCTION

C_{60} is expected to have novel functional properties based on its unique soccer ball structures (dia. of 7Å). Superconductivity was discovered in carrier-doped C_{60} with alkaline metal, such as K_3C_{60} and $RbCs_2C_{60}$[1].

It has been reported that addition reactions to C_{60} molecules occurred with such reagents as hydrogen and fluorine in liquid or vapor phase. For instance, C_{60} was converted to $C_{60}H_{36}$, $C_{60}F_{36}$ and $C_{60}H$ by Birch reduction[2], fluorination[3] and ionic reaction with CH_5^+ or $C_2H_5^+$[4], respectively. Chemical modification of C_{60} by ion implantation was also attempted. Isoda et al. reported that p/n type control was achieved by P or B ion implantation into C_{60} thin films[5]. However, there remains some ambiguity in this result in view of plausible difficulty in substitutional doping in π-conjugated compound. Here, we have investigated the implantation of various ions into C_{60} thin films and the physical and electrical properties of implanted films.

2. EXPERIMENTAL

C_{60} thin films were deposited at 120°C on various substrates by the conventional vacuum evaporation ($5x10^{-6}$Torr) of C_{60} powders (purity>99.5%) from an alumina crucible heated at 500°C and their films thicknesses were between 100nm and 2μm. The substrates used were fused silica glass, cleaved NaCl(100) and Si(111).

Ion implantation into the films was performed with Ag, Mn and H ions at the energies between 30 and 100keV. The ion dose was varied from 10^{13} to 10^{16} ions/cm^2 to examine the radiation and chemical effects.

Structures and optical properties of the films were characterized by X-ray diffractometry (XRD), Raman scattering spectroscopy, and UV-visible (UV-VS) absorption spectroscopy. The film component was analyzed by laser desorption time-of-flight mass spectrometer (TOF-MS) and a secondary ion mass spectrometer (SIMS) using Cs^+ ion beam. Electric conductivity was measured by a conventional two probe method in the temperature range between room temperature (20°C) and 150°C under a vacuum ($5x10^{-6}$Torr) condition.

3. RESULTS AND DISCUSSION

The intensities of XRD peaks and UV-VS absorptions of C_{60} films decreased by the 100keV Ag and Mn-implantation (>10^{13} ions/cm^2), indicating the formation of amorphous phase in the film. Figure 1 shows Raman scattering spectra of the ion-implanted films. It is reinforced that C_{60} molecules were decomposed and changed into amorphous-like carbon by the ion implantations. The conductivity at room temperature of the Ag-implanted film increased by about 11 orders of magnitude

as compared with that of non-implanted C_{60} film.

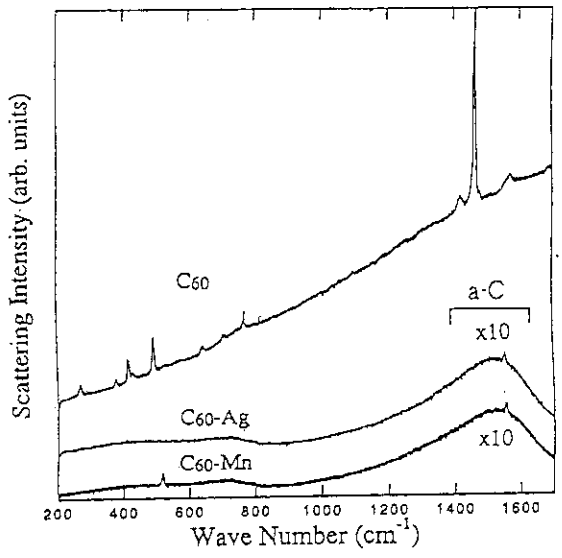

Fig.1. Ramann scattering spectra of the 100keV Ag or Mn-implanted films and the non-implanted C_{60} film. The ion dose is 10^{13} ions/cm^2.

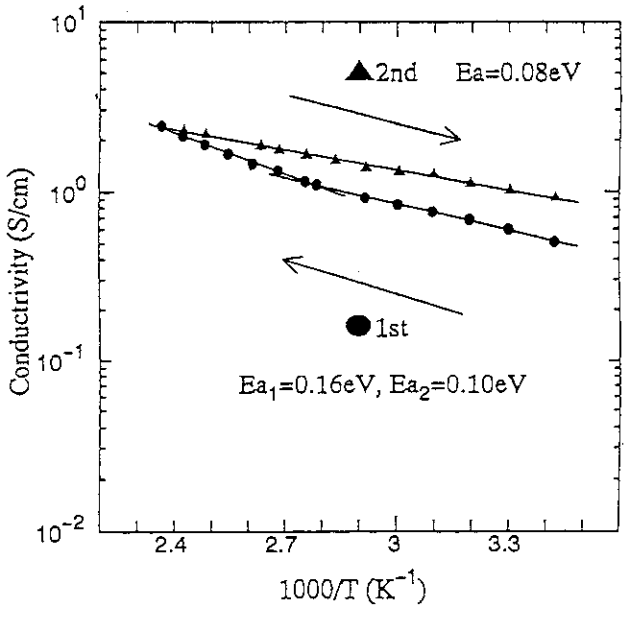

Fig.2. Temperature dependences of the electric conductivity of the 100keV Ag-implanted film. The ion dose is 10^{13} ions/cm^2.

Figure 2 shows a semiconductive behavior in the Ag-implanted film with an activation energy of 0.1eV. In the SIMS depth profile of the Ag-implanted film, Ag atoms distributed deeper than the boundary between the film and the substrate (Fig.3). The 100keV Mn-implanted C_{60} film gave the results very close to those of the Ag-implanted films.

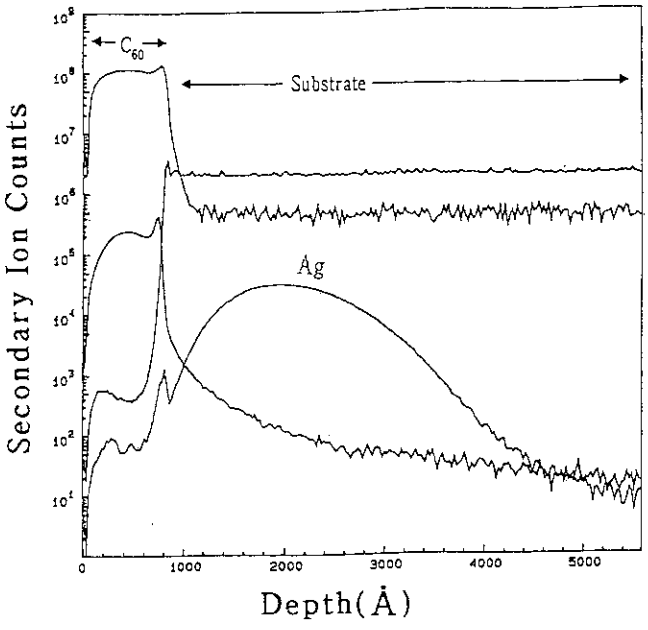

Fig.3. SIMS depth profile of the 100keV Ag-implanted film. The ion dose is 10^{13} ions/cm^2.

Then, H^+-implantation was performed by an acceleration energy of 30keV. The XRD, UV-VS and Raman scattering spectra of films implanted with less than 10^{14} ions/cm^2 did not change from those of the non-implanted C_{60} films. Figure 4 shows TOF-MS spectra of 10^{13} H-ions/cm^2 implanted film. A drastic change occurred in the peak profile; new peaks appeared at 721, 730, 732 and 736m/z. These peaks are assignable to $C_{60}H$, $C_{60}H_{10}$, $C_{60}H_{12}$ and $C_{60}H_{16}$, respectively. The implantation of more than 10^{13} H-ions/cm^2 decomposed the C_{60} molecules into amorphous-like carbon as well as the case of Ag and Mn-implantations. H atoms were

found from SIMS depth profile to be distributed uniformly in the H-implanted films. The presence of $C_{60}H$ molecule attracts our interest since it can be endohedral $H@C_{60}$ produced by the implantation of H^+ ion with the diameter smaller than the inner size of a benzene ring in the C_{60} molecule.

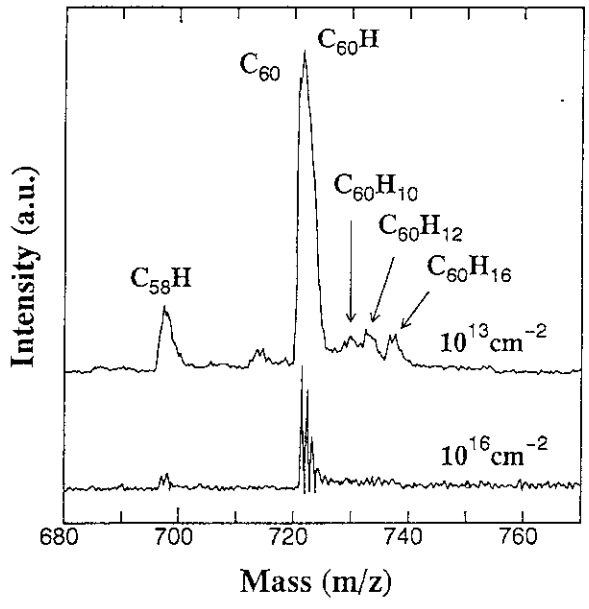

Fig.4. TOF-MS spectrum of the 30keV H-implanted film. The ion doses are 10^{13} and 10^{16} ions/cm^2.

4.SUMMARY

100keV Ag or Mn implantations increased the conductivity C_{60} films remarkably, but those induced simultaneously the decomposition of C_{60} molecules and changed to amorphous-like carbon. In the TOF-MS spectrum of film implanted with 10^{13} H-ions/cm^2 at 30keV, new peaks appeared at mass numbers of 721, 730, 732 and 736m/z, corresponding respectively to $C_{60}H$, $C_{60}H_{10}$, $C_{60}H_{12}$ and $C_{60}H_{16}$. The location of H in $C_{60}H$ attracts our interest and is under further investigation.

ACKNOWLEDGMENT

The authors thank Prof. O.Odawara (Tokyo Inst. of Tech.) for his SIMS measurements. This work was supported in part by a Grant-in-Aid for Scientific Research from the Ministry of Education, Science and Culture of Japan and was performed under JAERI/TIARA Collaboration Program.

REFERENCES

1) A.F.Hebard, M.J.Rosseinsky, R.C.Haddon, D.W.Murphy, S.H.Glarum, T.T.M.Palstra, A.P.Ramirez and A.R.Kortan: Nature 350(1991)600
2) R.E.Haufler, J.Conceicaio, S.Flanagan, M.M.Haley, S.C.O'Brien, C.Pan, Z.Xiao, W.E.Billups, M.A.Ciufolini, R.H.Hauge, J.L.Margrave, L.J.Wilson, R.F.Curl and R.E.Smalley: J. Phys. Chem. 94(1990)8634
3) H.Selig, C.Lifshitz, T.Peres, J.E.Fischer, A.R.McGhie, W.J.Romanow, J.P.McCauley Jr. and A.B.Smith: J. Am. Chem. Soc. 113(1991)5475
4) S.W.McElvany and J.H.Callahan: J. Phys. Chem. 95(1991)6186
5) S.Isoda, Y.Hanasato, M.Miyamoto, K,Akiyama and O.Wada: Abstracts of the 4th C_{60} Symposium 4(1993)95

5.12 Radiation Damages in Vitreous Silicas Induced by High Energy Fe^{+2} Ions Irradiation

S.Nasu, S.Oonishi, H.Nanto, R.Yamamoto,
H.Takeshita[2], Y.Aoki[2], S.Yamamoto[2], H.Naramoto[2],
T.Igarashi[3]
Kanazawa Institute of Technology, JAERI, Takasaki[2], Ushio Inc.[3]

The purposes of this study are (1) to clarify the effect of hydroxyl contents on radiation damages in vitreous silicas induced by high energy Fe^{+2} ions irradiation and (2) to examine photostimulated luminescence phenomenon due to ultraviolet light induced color centers and implanted transition elements.

Samples used were different types of vitreous silicas, GE214 (type I, electric fusion; below 1 wppm OH), VITREOSIL (type II, flame fusion; ~200 wppm OH), SK1300 (type III, synthetic; ~200 wppm OH), SK1310 (type IV, synthetic; below 1 wppm OH), and their dimensions are 10mmϕ x 1mmt for GE214 and VITREOSIL and 10x10x1mm^2 for SK1300 and SK1310 respectively.

The samples were irradiated at room temperature with 6MeV Fe^{+2} ions using the TIARA 3MV tandem accelerator to fluences of 4×10^{15} to 9×10^{16} atoms/cm^2.

Table 1 shows samples used for the experiment, together with the irradiation conditions.

Table 1 Sample list

	GE214	VITREOSIL	SK1300	SK1310
TYPE	I	II	III	IV
	ELECTRIC FUSION	FLAME FUSION	SYNTHESIS	SYNTHESIS
OH	–	~200wppm	~1200wppm	–
FLUENCE ions/cm^2	Nov. 10, 1993 3.6x10^{15} 3.9x10^{15} 1.8x10^{16}	Sept. 14, 1993 4.1x10^{15} 3.6x10^{16} 3.7x10^{15}	Mar. 1-2, 1994 3.6x10^{16} 6.4x10^{15} Apr. 9, 1994 1.8x10^{16} 1.8x10^{16}	Mar. 2, 1994 3.3x10^{16} 7.4x10^{15} Apr. 8~9, 1994 8.5x10^{16} 1.8x10^{15} 1.8x10^{16}
	~6MeV	~6MeV	~5.5MeV	~5.5MeV

All optical measurements were made at room temperature.

(1)Optical Absorption

Before irradiation, any optical absorption peaks were not observed in a wavelength range of 190 ~ 800nm for SK1300 and SK1310 samples, while a small peak at about 240nm was observed for GE214 and VITREOSIL samples.

After irradiation of 6MeV Fe^{+2} ions to 10^{15} atoms/cm^2, an absorption peak at 245nm (5.06eV) and a shoulder at 215nm (5.77eV) were observed in this wavelength range for GE214, VITREOSIL, SK1300 and SK1310 samples.

In fig.1 we show the optical absorption spectra of SK1300 and SK1310 samples by way of example.

The optical density at 245nm for dry silica glasses (GE214 and SK 1310) was higher than that for wet silica glasses (SK1300 and VITREOSIL).

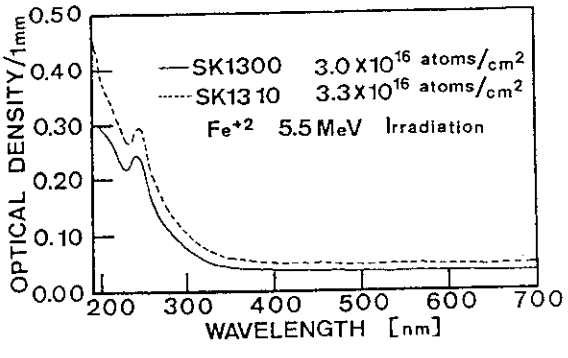

Fig.1 Optical absorption spectra of SK1300 and SK1310 after irradiation.

(2) Photoluminescence

In fig.2 we show the PL spectra and the PL excitation (PLE) spectra of SK1310 sample after irradiation.

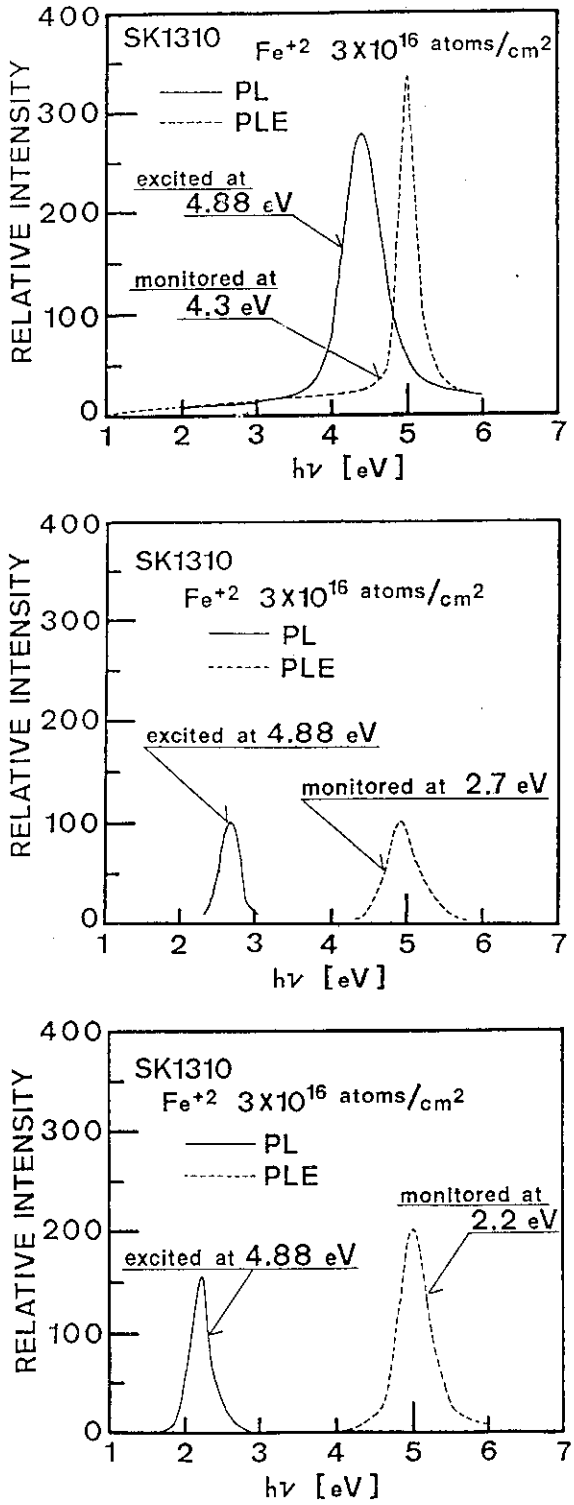

Fig.2 PL and PLE spectra of SK1310 after irradiation. monitored at (a)4.3eV, (b)2.7eV and (c) 2.2eV.

Annealing behavior of the PL and the PLE was observed as a function of annealing temperature with stepwise rise from 100 ~ 600℃, that is, the sample was maintained for 30min, in air, and then the PL and the PLE spectra were measured at room temperature for each sample. These results are shown in fig.3 for SK1300 and SK1310 samples.

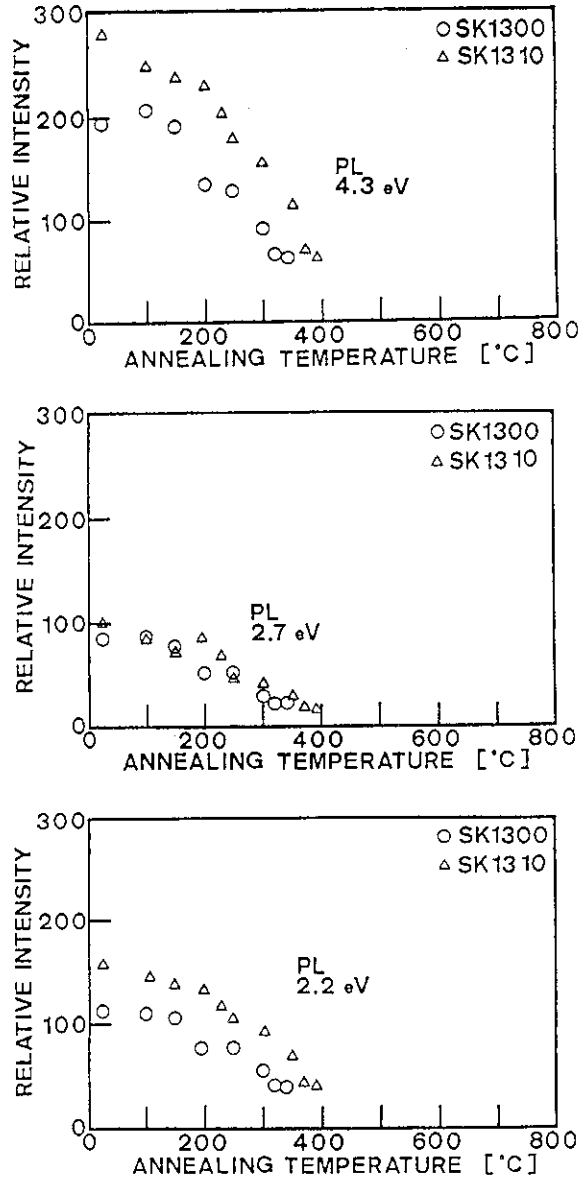

Fig.3 Annealing behavior of PL of SK1300 and SK1310 (a)4.3eV PL, (b)2.7eV PL and (c)2.2eV PL.

Before irradiation any steady atate photoluminescence (PL) peaks were not obsreved for SK1300 and SK1310 samples, while three PL peaks at 290nm (4.3eV), 400nm (3.1eV) and 560nm (2.2eV) were observed for GE214 and VITREOSIL samples.

After irradiation, three steady state PL peaks at 4.3eV, 2.7eV (460nm) and 2.2eV were observed for SK1300 and SK1310 samples. For GE214 and VITREOSIL samples, in addition to three peaks, a PL peak at 2.7eV was observed.

It is interesting to note that the maximum of the PLE peaks were located at 5.05eV for the 4.3eV and 2.2eV peaks, and at 4.95eV for the 2.7eV peak. This suggests that there are two different excited states in the iron irradiated silica glass.

The PL intensities at 4.3eV and 2.2eV were higher for SK1310 (the OH band is not detected) sample than those for SK1300 (OH content: 1200 wppm) sample as shown in Fig.3. This suggests that the OH content plays an important role in the formation of the PL bands.

Several authors have reported that the absorption peak at 5.77eV and the luminescence peak at 4.3eV are attributed to the E'center[1], while the absorption peak at 5.6eV and the luminescence peak at 4.3eV are attributed to the $B_2\alpha$ band[2,3].

Therefor, it is preliminaryly concluded that high energy ion irradiation can form the E'center and the $B_2\alpha$ band.

(3)Strain

Any strains were not observed near the surface of each sample after irradiation.

(4)Conclusions

From the optical absorption, the PL and the PLE measurements, we noticed the following points.

1. High energy iron irradiation forms an optical absorption band at 215nm (5.77eV, the E'center and, a the $B_2\alpha$ band, and the PL bands at 4.3eV (the E'center and, a the $B_2\alpha$ band), 2.7eV and 2.2eV.

2. The OH content seemed to play an important role in the formation rate of radiation damages. The larger the OH content, lower the intensities of the optical absorption and the PL.

3. The PLE measurements showed a maximum at 5.05eV for the 4.3eV and the 2.2eV peaks and that at 4.95eV for the 2.7eV peak. This suggests the existence of two different excited states.

References

(1) N.Kuzuu, Y.Komatsu and M.Murahara, Phys.Rev.B44, (1991) 9265.

(2) M.Kohketsu, K.Awazu, H.Kawazoe and M.Yamane, J.Appl.Phys.28, (1989) 615.

(3) R.Tohomon, H.Mizuno, Y.Ohki, K.Sasagane, K.Nagasawa and Y.Hama, Phys.Rev.B39, (1989) 1337.

5.13 Photoquenching of hopping conduction in carbon- ions irradiated semi-insulating GaAs

K. Kuriyama, K. Tomizawa, T. Kato
H. Naramoto [2], H. Takeshita [2], S. Yamamoto [2], Y. Aoki [2]

College of Engineering and Research Center of Ion Beam Technology, Hosei University
Department of Materials Development, JAERI / Takasaki [2]

GaAs has been widely used as a functional material to form high speed devices such as n-p-n bipolar transistors. The diffusion coefficient of carbon in GaAs is known to be lower than those of the traditional p-type dopants such as Be, Zn, Mg, Cd. Therefore, the fabrication of the shallow p-type layer[1] due to carbon doping has been expected. The carbon doping by ion irradiation, however, introduces various defects, and the thermal annealing above 600 ℃ activates the doped carbon[2]. These defects would influence the electrical properties of GaAs.

The photoquenching phenomenon in the *variable range hopping* conduction below 125 K was observed in fast neutron irradiated semi-insulating GaAs[3]; the neutron irradiation decomposes completely the atomic arrangement of the native EL2 defect that forms a midgap level but thermal annealing above 250 ℃ generates the EL2-like defects contributing to the photoquenchable hopping conduction.

In this work, we evaluate the defects introduced in the carbon-ion irradiated semi-insulating GaAs through the electrical method. The sample used here were obtained from undoped (100)-oriented semi-insulating GaAs (ρ= ~10^7 Ωcm) grown by As pressure-controlled Czochralski (PCZ) technique. The conductivity was n-type and the concentration of EL2 was ~10^{16} cm^{-3}. 1.0-MeV carbon ions were irradiated at around 270 K. The carbon dose was $1x10^{14}$ cm^{-2}. In order to avoid the ion-channeling effects, irradiations were carried out in the 7 °-off <100> direction. A carbon depth profile in GaAs evaluated by TRIM simulation has a peak at about 1.2 μm. The irradiated samples were confirmed to be crystalline by Rutherford Backscattering channeling experiments. Irradiated samples were isochronally annealed for 15 min at 200, 400, 450 and 500 ℃, respectively.

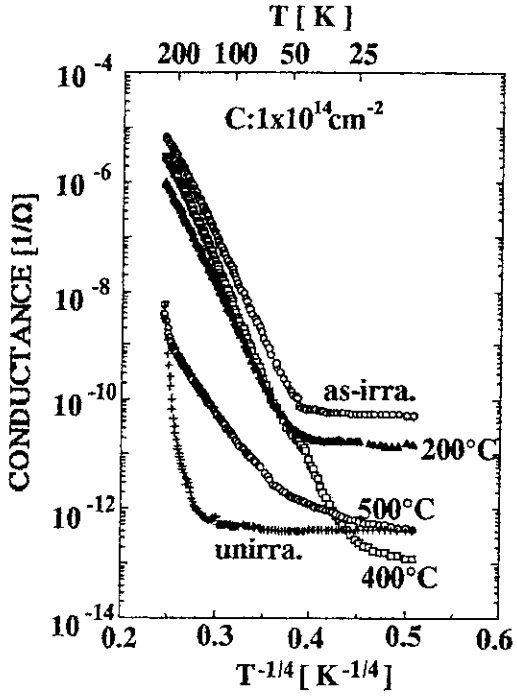

Fig.1 Temperature dependence of conductance for semi-insulating GaAs irradiated with carbon-ions and followed by thermal annealing . The carbon dose is $1x10^{14}$ cm^{-2}.

Figure 1 shows the temperature dependence of conductance at various annealing temperatures. After irradiation, samples annealed below 500 ℃, showed a hopping conduction [$G \propto T^{-1/4}$] at a temperature ranging from 50 to 200 K. This behavior is known as *variable range hopping*[4] that electrons hop between defect levels introduced by the irradiation. The defect concentration associated with the hopping conduction was estimated to be ~$10^{17}$$cm^{-3}$ by Mott's theory[4]. The temperature independent conduction was observed at a temperature range below 50 K, which is attributed to the conduction of electrons trapped at irradiation-induced defected in the surface region. The deviation from $T^{-1/4}$ law was observed at a temperature

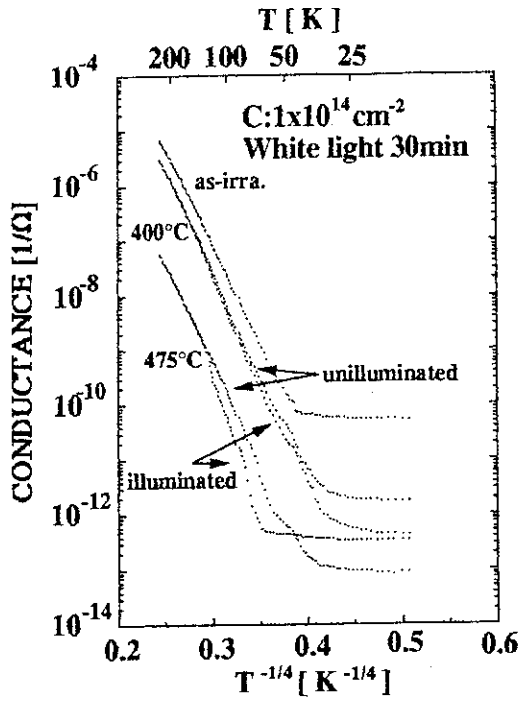

Fig.2 Influence of illumination on temperature dependence of conductance for carbon-ion irradiated and annealed semi-insulating GaAs.

range above 200 K which arises from the band condution.

In order to survey the relationship between EL2 defect and hopping sites, the conductance was measured after illumination. Figure 2 shows the temperature dependence of conductance before and after illumination on sample annealed at various temperatures. The conduction change was not observed by annealing below 200 ℃. However, for annealing above 400 ℃ the conductance after illumination was decreased before one. This indicates the photoquenching of compared with that EL2 defect. Table 1 shows the defect concentration associated with the hopping conduction. These values were estimated using slope of conductance curve. The concentration of quenchable component in samples annealed above 400 ℃ is much larger than that of the native EL2 defects($\sim 10^{16}cm^{-3}$). This indicates that EL2-like defects are generated as a quenching component by annealing. The high quenching rate by white light illumination suggests the defect-level formation relating to the hopping conduction near the midgap level.

Table 1 The site concentration for hopping conduction in GaAs samples unannealed and annealed at 200, 400, 450 and 475 ℃ after carbon ion irradiation.

	concentration of hopping sites N_{HP} [cm^{-3}]	concentration of non-quenchable sites N_{NQ}[cm^{-3}]	concentration of quenchable sites N_Q [cm^{-3}]
as-irradiated	9.5×10^{17}	9.5×10^{17}	0
200°C	5.9×10^{17}	5.9×10^{17}	0
400°C	5.2×10^{17}	4.8×10^{17}	4.0×10^{16}
450°C	7.9×10^{17}	4.1×10^{17}	3.8×10^{17}
475°C	7.9×10^{17}	3.3×10^{17}	4.6×10^{17}

$N_{HP} = N_{NQ} + N_Q$

References

1) P. M. Enquist, Appl. Phys. Lett.57, 2348 (1990)
2) J. D. Sansbury et al , Radiat. Eff. 6, 269 (1970)
3) M. Satoh, K. Kuriyama, Phys. Rev. B40, 3473 (1989)
4) N. F. Mott, J. Noncryst. Solid 1, 1 (1968)

5.14 Annealing Behavior of α-SiC Implanted with 1 MeV Ni Ions

K.Kawatsura, N.Shimatani, T.Nakae, A.Nishihata, R.Takahashi, S.Arai, Y.Horino[2], Y.Mokuno[2], K.Fujii[2], H.Takeshita[3], Y.Aoki[3], S.Yamamoto[3], P.Goppelt-Langer[3], and H.Naramoto[3]
Faculty of Engineering and Design, Kyoto Institute of Technology, Osaka National Research Institute, AIST[2], JAERI, Takasaki Dept. Mater. Development[3].

Introduction

Recently, MeV ion implantation into semiconductors has attracted more and more attention since it can provide very promising methods for material property modification and three dimensional device fabrication. However , the extension of the ion energy to the MeV range also raises many interesting questions about the mechanisms of radiation damage and radiation-induced phase transition and their relation to the implant distribution in crystalline solids. An understanding of associated physical processes involved in MeV ion implantation, as well as in the subsequent annealing, is crucial before it can be applied universally in device technology. Therefore, we have investigated the annealing of implantation damage and redistribution of implanted ions in α-SiC by MeV heavy ion implantation[1-3]. In this report, we present the annealing behavior of α-SiC(0001) single crystal by 1.0 MeV Ni ion implantation with dose of 5.4×10^{13} and 1.8×10^{17} cm^{-2}.

Experimental

The α-SiC single crystals used in the present investigation were synthesized by the Acheson method at Taiheiyo-rumdum Co.. The polytype was confirmed to be predominantly 6H form by Raman scattering spectroscopy. The 1.0 MeV Ni^+ ions implantation was performed at RT with a dose of 5.4×10^{13} and 1.8×10^{17} cm^{-2} using a 3 MV tandem accelerator at the TIARA facility of JAERI, Takasaki. Thermal annealing of implanted α-SiC was carried out at 500, 1000 and 1500 ℃ for 2 h in Ar ambient at Kyoto Inst. Technology. Rutherford backscattering spectrometry with channeling (RBS-C) was performed using 1.6 and 1.8 MeV He^+ ions from a 2 MV Van de Graaff accelerator in Osaka National Research Institute of Ikeda, and 3.0 MeV He^{2+} ions from the 3 MV tandem accelerator at the TIARA facility of JAERI, Takasaki.

Results and discussion

The RBS-C measurements show that the as-implanted α-SiC crystals were amorphized with more than 5.4×10^{14} cm^{-2} Ni implantation. Fig. 1 shows the values of χ_{min} as a function of depth from the SiC surface with different doses. It can be seen for the 1.8×10^{17} cm^{-2} Ni implanted sample that it has a minimum yield χ_{min}=1.0 from the surface to a depth of 900 nm. From the RBS-C using 3 MeV He ions, it can be also found that implanted Ni atoms distribute nearly Gaussian with a maximum Ni concentration of 6 at.% at a depth of 540 nm, which is identical at aligned and random orientation.

After thermal annealing of this sample at 500 and 1000 ℃ for 2 h in Ar ambient, the RBS-C spectra did not change from those

of the as-implanted one and, therefore, neither recrystallization of SiC nor redistribution of Ni occurred. During the 1500 ℃ annealing, a drastic recrystallization and an intensive Ni diffusion occurs simultaneously. Fig. 2 shows random and aligned backscattering spectra of the Ni implanted SiC after the 1500 ℃ annealing measured by 3.0 MeV He^{2+} ions, and Fig. 3 shows depth dependence of χ_{min} for annealed SiC together with those of as-implanted and unimplanted ones. It is found that χ_{min} decreased to 0.2 at the surface due to the recrystallization. The values of χ_{min} are as small as those for the unimplanted region of SiC. However, a small step is observed at a depth of 500 nm in the χ_{min} curve of the 1500 ℃ annealed sample. This suggests that a layer with a high defect concentration exists at the depth in the recrystallized layer. It has been pointed out that recrystallizaion of amorphous SiC layers introduced by ion implantations occurs epitaxially from the remaining crystal layers[4,5]. If the surface is amorphized, the epitaxial regrowth can proceed only from the bulk crystal to the surface. In the present experiment, the recrystallization occurred only from the bulk crystal, not from the surface. Even if the annealing time was insufficient, remaining damages should have been found near the surface. Any residual defect layer was not observed in the 1500 ℃ annealed SiC of 1.8×10^{15} cm^{-2} Ni implantation[1]. Therefore, the defect layer observed seems to be related to the implanted Ni concentration. The average range of implanted Ni ions was 540 nm, and the FWHM was 320 nm, and the peak concentration was as high as 6 at.% for the 1.8×10^{17} cm^{-2} implantation, which agree well with the E-DEP-1 calculation. The implanted Ni atoms did not diffuse during the annealing below 1000 ℃. But a drastic change occurred on the Ni profile during the 1500 ℃ annealing. The Ni atoms diffused to both directions of the surface and the bulk during the recrystallization of amorphous SiC. A total number of the redistributed Ni atoms in the depth region from the surface to 900 nm was decreased to 1.1×10^{17} cm^{-2}, which is about 60 % of the as-implanted ones. The new distribution for Ni atoms was like a trapezoid except a small peak at 540 nm as observed in the case of defect profile. This indicates that a region with an abnormally high Ni concentration exists inside SiC. The aligned spectrum of these Ni atoms was the same as the random one and, therefore, the redistributed Ni atoms do not occupy the SiC substitutional lattice sites.

References

1) K.Kawatsura et al., JAERI-M 93-241 (1994) p.105
2) N.Shimatani, K.Kawatsura, S.Arai, T.Shiono, Y.Horino, Y.Mokuno, K.Fujii, H.Takeshita, S.Yamamoto, Y.Aoki, and H.Naramoto, Nucl. Instrum. Methods, B91 (1994) 529.
3) N.Simatani et al., in preparation.
4) R.R.Hart, H.L.Dunlap, and O.J.Marsh, Radiat. Eff. 9, (1971) 261.
5) H.G.Bohn, J.M.Williams, C.J.Mchargue, and G.M.Begun, J. Mater. Res. 2, (1987) 107.

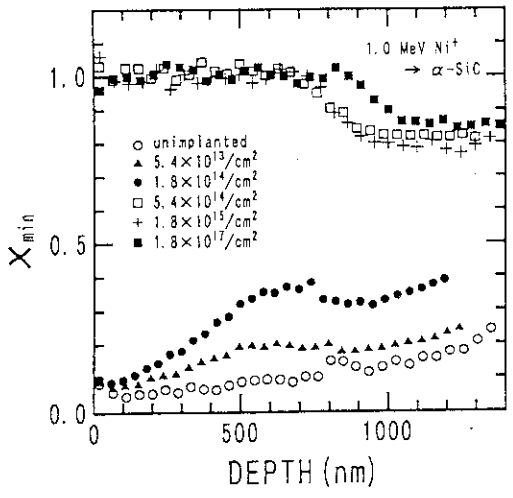

Fig.1 Depth dependence of χ_{min} for 1.0 MeV Ni implanted α-SiC (0001) single crystal with doses of 5.4×10^{13} and 1.8×10^{17} cm^{-2}. The values of χ_{min} for the unimplanted region are also given as a reference.

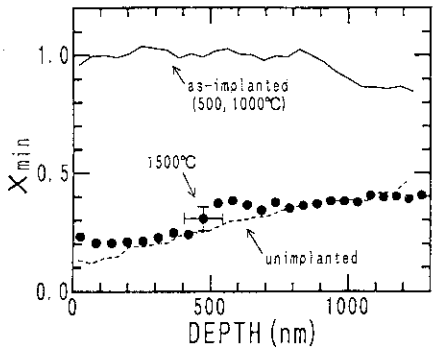

Fig.3 Depth dependence of χ_{min} for the annealed SiC sample together with those of as-implanted and unimplanted ones.

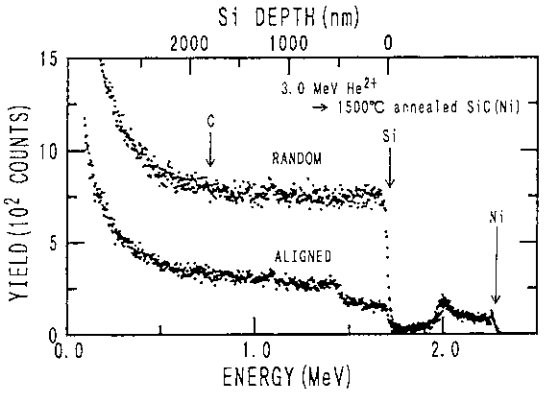

Fig.2 RBS-C spectra from the 1500 ℃ annealed SiC implanted with a dose of 1.8×10^{17} cm^{-2}. Spectra were measure using 3.0 MeV He^{2+} ions.

5.15 Heavy Ion Implantation into Single Crystal MgO

R.Takahashi, T.Nakae, N.Shimatani, A.Nishihata, K.Shiono, K.Kawatsura, S.Arai, H.Takeshita[2], Y.Aoki[2], S.Yamamoto[2], P.Goppelt-Langer[2], H.Naramoto[2], Y.Horino[3], Y.Mokuno[3], K.Fujii[3], and N.Masuda[4]
Faculty of Enginnering and Design, Kyoto Inst. Technology, JAERI, Takasaki, Dept. Mater. Development[2], Osaka National Research Institute, AIST[3], Tateho Chem. Indus. Co. Ltd[4]

Introduction

Recently the heavy ion implantation is used for ceramics materials to change the characteristics of near surface, i.e. hardness, conductivity, and absorbance. Not only could it be to improve from surface to a few nm depth with low energy ions[1], but it has been possible to improve a few μm depth with high energy ions. However the stopping of energetic ions in solids leads to radiation-induced damage due to atomic collisions and electronic excitations. Observation of the recovery process of radiation-induced damage and the redistribution of implanted atoms after thermal annealing is necessary to improve ceramics materials with high-energy and heavy-ion implantation.

We performed ion implantation into MgO(100) single crystal with 1.0 MeV Ni^+ that attracted attention for nuclear reactor materials. At the first we investigated the dose effects on radiation-induced damage. At the surface the radiation damage was not formed very much, but increased slowly with dose. While it increased sharply and saturated with dose from 2×10^{16} cm^{-2} at the depth of 500 nm. Next we performed thermal annealing on the as-implanted sample to investigate the annealing behavior with radiation-induced damage and implanted ions. As a result the radiation-induced damage is recovered and implanted ions diffused to the whole of crystal and occupied substitutional positions after 1400 ℃ annealing treatment.

Experimental

The cleaved MgO(100) single crystals employed in the present study were obtained from Tateho Chemical Industries Co. Ltd. Ion implantations were carried out at room temperature in a vacuum of about 1×10^{-5} Pa using the 3 MV tandem accelerator at the TIARA facilities of JAERI Takasaki. The current density was about 1 μA cm^{-2} in order to restrict thermal effects during ion implantation. The 1.0 MeV Ni^+ ions were implanted in the range from 1×10^{15} to 1×10^{17} cm^{-2}. The radiation-induced damage and the location of implanted ions were measured by Rutherford backscattering spectrometry of 1.6 and 1.8 MeV He^+ ions using the 2 MV Van de Graaff accelerator at Osaka National Research Institute of Ikeda, and 3.0 MeV He^+ ions using the 3 MV single ended accelerator or 3.0 MeV He^{2+} using the 3 MV tandem accelerator at the TIARA facilities of JAERI Takasaki. The thermal treatment was performed only for the 1×10^{17} cm^{-2} sample from 500 to 1400 ℃, for 1 h in a gas flow of Ar.

Results and Discussion

Fig. 1 shows the random and aligned RBS spectra of 3.0 MeV He^{2+} for the as-implanted MgO(100) with a dose of 1×10^{17} cm^{-2} of 1.0 MeV Ni^+ together with the

aligned RBS spectrum for the unimplanted region of the same sample. As seen from the figure, it can be found that little radiation damage is induced from the surface to about 250 nm, but there is much more from 250 nm to 1 μm. It can be also found that the Ni depth profile is nearly Gaussian with a maximum concentration of 4 at.% at a depth of 500 nm, which agrees well with the E-DEP-1 calculation. The Ni spectra show that the percentage of the as-implanted Ni ions occupied interstitial positions at the implanted region is 73 % and especially at the depth of 500 nm is 80 %. Thus using the minimum yield χ_{min} for Mg or Ni at the each depth, we can obtain the information with radiation-induced damage in MgO and the location of implanted Ni ions.

1. Dose dependence

Fig. 2 shows the dependence of radiation-induced damage on dose at the depth of 100 and 500 nm. The depth of 500 nm is the average range of implanted Ni ions. The value of χ_{min} at the unimplanted region is 0.03. The value of χ_{min} at the 100 nm is linearly increases from 0.05 to 0.11 in the dose of 1×10^{15} and 1×10^{17} cm^{-2}. While at 500 nm it increased sharply with dose and saturated with dose at 2×10^{16} cm^{-2}. To analyze dose dependence at different depths quantitatively, we should investigate the incident energy dependence of radiation-induced damage, and the ion implantation at low temperatures to quench the defects produced and to observe the effects of the recombination of the displaced atoms and vacancies[2,3]. Moreover we should carry out the experiments of high energy electron or high-energy light ion irradiation in order to observe the primary process of the radiation damage[2,3].

2. Annealing behavior

We investigated the thermal annealing behavior of radiation-induced damage and implanted Ni ions. Fig. 3 shows the degree of disorder in the Mg sublattice at the depth of 100 and 500 nm, and the rearrangement of Ni ions at the depth of 500 nm after the thermal annealing treatments for 1×10^{17} cm^{-2} Ni implanted sample. The χ_{min} for the Mg sublattice as implanted at the depth of 100 and 500 nm is 0.11 and 0.49, respectively. The value of χ_{min} for Mg at 100 nm decreases slowly with annealing temperature, and reaches to 0.03 which is the same as that for the unimplanted region. While, after annealing at 500 ℃, the χ_{min} for Mg at 500 nm does not change, but it decreases slowly, during 500 to 1000 ℃ annealing, and then decreases sharply after annealing at 1100 ℃. Thus the Mg sublattice is rapidly ordering due to redistribution of displaced Mg atoms in the cation vacancies at 1100 ℃. After annealing at 1400 ℃, the value of χ_{min} for Mg at 500 nm approaches that of the unimplanted region.

To compare the thermal annealing behavior for Mg at 500 nm with that for the implanted Ni ions, we analyze the implanted Ni ions at 500 nm. As implanted, 80 % of the implanted Ni ions occupy interstitial positions. During 500 to 800 ℃ annealing treatments, the tendency of the χ_{min} for the Ni ions is similar to that for Mg at 500 nm. But after annealing at 1000 ℃, it increases in contrast to Mg atoms, and 90 % of the implanted Ni ions occupy interstitial positions. Perez et al.[1] also obtained the similar results as our results. And after annealing at 1100 ℃, χ_{min} for the Ni ions decreases

atoms at 500 nm. Thus at the same time the displaced Mg atoms are ordering, the Ni ions occupied interstitial positions also start to transfer to substitutional positions from 1100℃ annealing. After annealing at 1400 ℃, most of the implanted Ni ions diffused to the whole of the crystal and occupied substitutional positions.

References

1) A.Perez, G.Marest, B.D.Sawicka, J.A.Sawicki and T.Tyliszczak, Phys. Rev. B28 (1983) 1227.
2) W.A.Sibley and Y.Chen, Phys. Rev. 160 (1967) 712.
3) K.J.Caulfield, R.Cooper and J.F.Boas, J. Chem. Phys. 92 (1990) 6441.

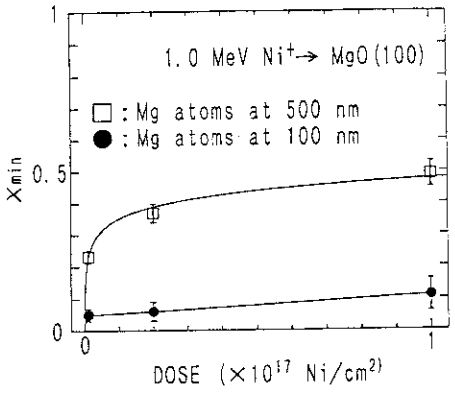

Fig.2 The dependence of radiation-induced damage on dose at the depth of 100 and 500 nm.

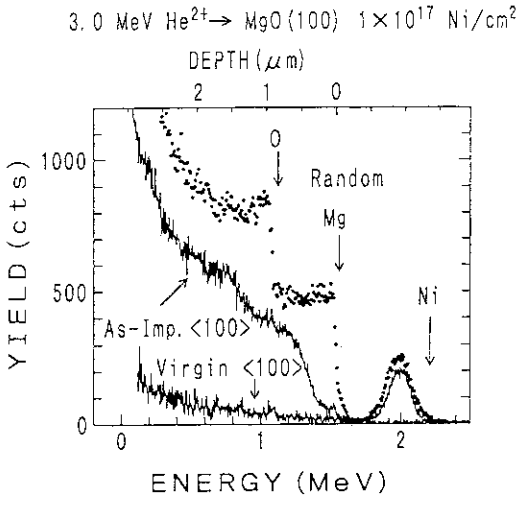

Fig.1 Random and aligned RBS-C spectra for the as-implanted region with a dose of 1×10^{17} cm^{-2} of 1.0 MeV Ni^{+} together with the aligned spectra for the unimplanted region. Spectra were measured using 3.0 MeV He^{2+}.

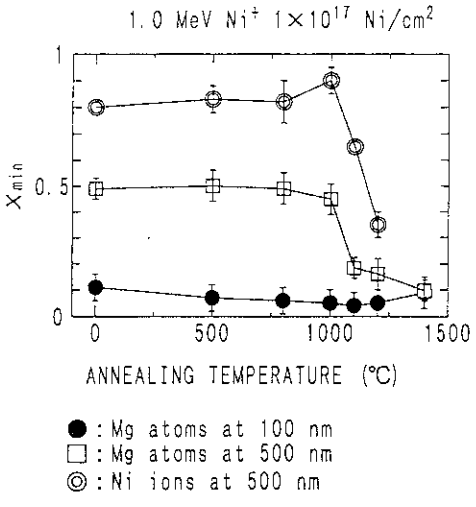

Fig.3 The degree of disorder in the Mg sublattice at the depth of 100 and 500 nm, and the rearrangement of Ni ions at the depth of 500 nm after the annealing treatments for 1×10^{17} cm^{-2} Ni implanted sample.

5.16 Precipitation Behavior of Ag and Au Atoms implanted into Al Single Crystalline Films

S. Yamaguchi[1], K. Takahiro[1], S. Nagata[1], M. Sugawara[1]
H. Naramoto[2], H. Takeshita[2], Y. Aoki[2], S. Yamamoto[2]
Institute for Materials Reaearch, Tohoku Univ.[1]
Japan Atomic Energy Institute, Takasaki[2]

Ion implantation is a non-equilibrium process which often leads to a metasable situation[1]. In the previous work[2], the precipitation behavior in Cu-implanted Al films at concentration of 1-5 at.% Cu has been studied by means of transmission electron microscopy and selected area electron diffraction. The results showed that the sequence of precipitation in the Cu-implanted Al was modified from that in the supersaturated solid solution; high temperature ageing (about 300℃) produced a large precipitate with a Ni_4Mo-type structure, while ageing at low temperature (about 130℃) gave a precipitate with a modulated Pt_2Mo-type structure.

In the precent work, we have studied the precipitation behavior of Ag and Au atoms implanted in Al single crystalline films as a part of systematic investigation on the precipitation phenomena of the implanted solute atoms in Al matrix.

The specimens used were single crystalline Al films prepared by a vacuum evaporation onto a cleavage surface of rocksalt maintained at 400℃. The vacuum in the evaporation chamber was brought to 5×10^{-8} Torr prior to evaporation. The thickness of the Al films was about 100 nm. Ag and Au ions of 200 and 300 keV energy, respectively, were implanted into the specimens to doses of $1\text{-}5\times10^{16}$ ion cm^{-2} at room temperature. The concentration of the implanted atoms determined from Rutherford backscattering was ranged 1.4-7.0 at.% depending on the implantation doses. The specimens were examined by a 200 kV electron microscope. In some cases, the specimens were studied directly inside the electron microscope using a high temperature specimen stage.

The structure and type of precipitate or zone can be determined from an electron micrograph and an electron diffraction pattern both taken from the same area. Photo 1 is a typical transmission electron micrograph obtained from the Ag-implanted specimens after ageing for 30 minute at 300℃. In this micrograph, large precipitates of about 100 nm in diameter are recognized. The corresponding diffraction pattern of Photo 2 suggests that the precipitates is different from that for the δ (Ag_2Al) phase, but it can be interpreted by assuming the Ni_4Mo-type structure, as illustrated in Fig. 1. This type of precipitates are also formed in the Cu-implanted Al by the high temperature aging. The Ni_4Mo-type precipitate is thought to be ordered alloy phase which has a definite orientation relationshipe and good coherency with the Al matrix.

Typical exampless of electron micrographes and corresponding electron diffraction patterns from the Au-implanted specimen after aging for 30 minute at 300℃ are shown in Photo 3 and 4, respectively. Irregular precipitates of 2-30 nm in diameter are appearent, as seen in Photo 3. The corresponding diffraction pattern of Photo 4 consistent with that for Al_2Au phase of CaF_2-type structure. This phase has neither any orientation relationships nor coherency with the Al matrix.

The nucleation of the new precipitates may be associated with the special feature of the ion-implanted materials; a large number of defects are introduced by the implantation, so the kinetics of phase transformation as well as the stability of the relevant possible phase should be modified[3]. Systematic studies concerning the precipitation of the ion-implanted alloys are now in progress.

References

[1] J.A. Borders, Ann. Rev. Mater. Sci., 9(1979)313.
[2] S. Yamaguchi et al., Surface Coating Technol., 66(1994)255.
[3] K. C. Russell, Prog. Mater. Sci., 28 (1984)229.

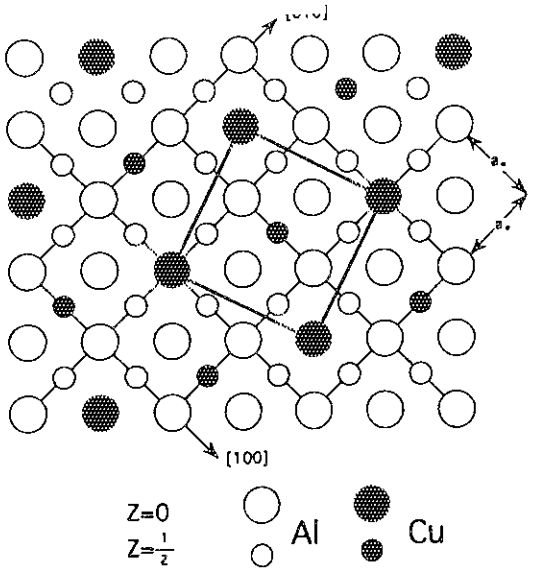

Fig. 1 Atomic arrengement of the Ni_4Mo-type structure projected along [100].

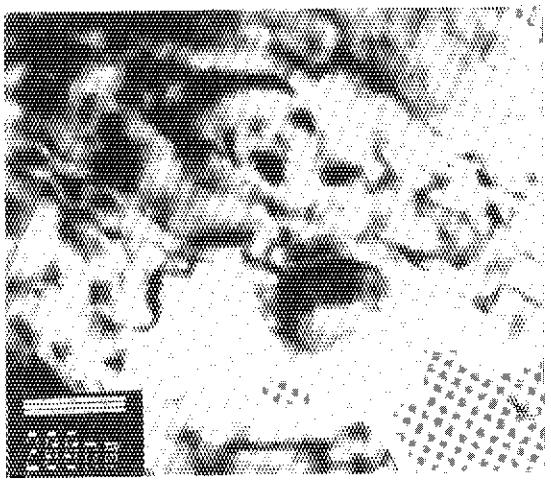

Photo 1 Electron micrograph from Ag-implanted specimen aged for 30 min at 300 ℃.

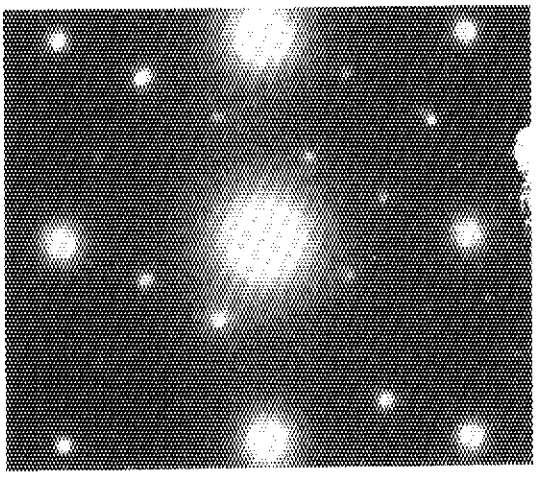

Photo 2 Electron diffraction pattern corresponding to Photo 1.

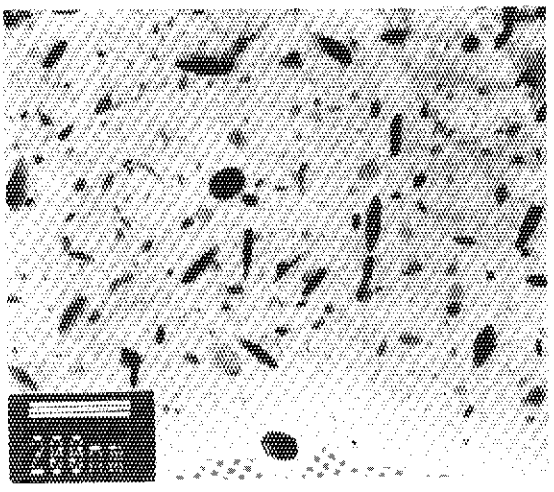

Photo 3 Electron micrograph from Au-implanted specimen aged for 30 min at 300 ℃.

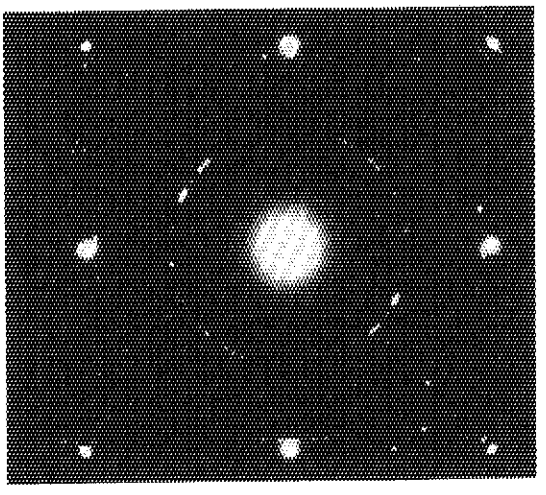

Photo 4 Electron diffraction pattern corresponding to Photo 3.

6. Materials Analysis

6 . 1 Light Element Profiling Using Heavy Ion Beams

P. Goppelt-Langer, S. Yamamoto, Y. Aoki, H. Takeshita, H. Naramoto
Dept. of Materials Development, JAERI/Takasaki

The analysis of thin layers in a surface near region with high resolution is an important problem in ion beam analysis. Here an elastic recoil detection technique (HE- ERD) has been developed and optimized for analysis of light elements as H, D, He, but has also proven its suitability for medium light elements up to B and C. The use of high energetic heavy incident ions, 8 - 16 MeV ^{16}O or 30 MeV ^{58}Ni ions, from a tandem accelerator increased the resolution for H analysis by a factor of 3, compared with standard ERD using 2 MeV ^{4}He. Additionally, the sensitivity of the method was increased by up to one order of magnitude, when the heaviest ion, was used. The experimental setup for the HE-ERD is sketched in Fig. 1. Size and emittance of the incident beam is limited by two circular apertures of 1 mm diameter in a distance of 350 mm. The samples are fitted on a sample stage for up to 6 samples which can be rotated and moved in all 3 directions. The detector is set preferably at 30° scattering angle, while the sample is rotated to 15° relative to the beam. This symmetric geometry yields to the best overall results. Primary ions, scattered into forward direction into the detector, are suppressed using 6.5 and 12.5 μm Mylar absorber foils. The signals are amplified and data are taken using a MCA. The beam current is measured on the sample and integrated using a current integrator and fast counter.

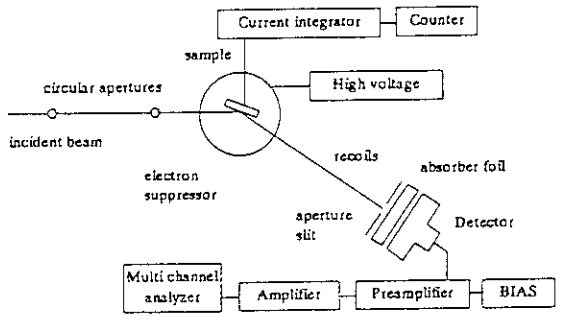

Fig.1: Experimental setup for HE-ERD experiments using absorber foil.

Results of the HE-ERD investigations of H in thin Cu/Nb multilayer samples are shown in Fig. 2. The sample consisted of thin Nb layers of 50, 100, 200 and 300 Å thickness separated by Cu spacers of 200 Å each. As incident beam first 16 MeV ^{16}O was used and a Mylar absorber foil of 12.5 μm thickness. Then the incident energy was reduced to 8 MeV and the absorber foil thickness to 6.5 μm. This increased the resolution due to smaller straggling in the absorber foil and smaller kinematic broadening, while the energy loss of the incident ion was nearly unchanged. The sensitivity was increased by a factor of 4. When using 30 MeV ^{58}Ni incident ions and the same absorber thickness, primary ions transmitted through the foil overlap the H spectrum. The shown spectrum has therefore been subtracted from this contribution using a H free pure Cu target.

When heavy ions are used, not only H recoils can transmit through the absorber foil, but also light to medium heavy recoils, and in some cases, as shown above, the forward scattered primary ions, too. Fig. 3 shows the result of an investigation of a thin boron layer on an iron substrate, which was a sample of first wall material of the JT-60U tokamak device and contained H, D and He. When using a 16 MeV ^{16}O incident beam, the H spectrum is overlapped by the B recoil spectrum. D and He are well separated. When the Energy is reduced to 8 MeV the spectra of H, D and He are separated, but the B recoil spectrum is partly lost. Using 30 MeV ^{58}Ni all spectra can be measured from H to C. The heavier recoils undergo a large energy loss and straggling in the absorber foil. Therefore, the measured energy for C is lower than for B

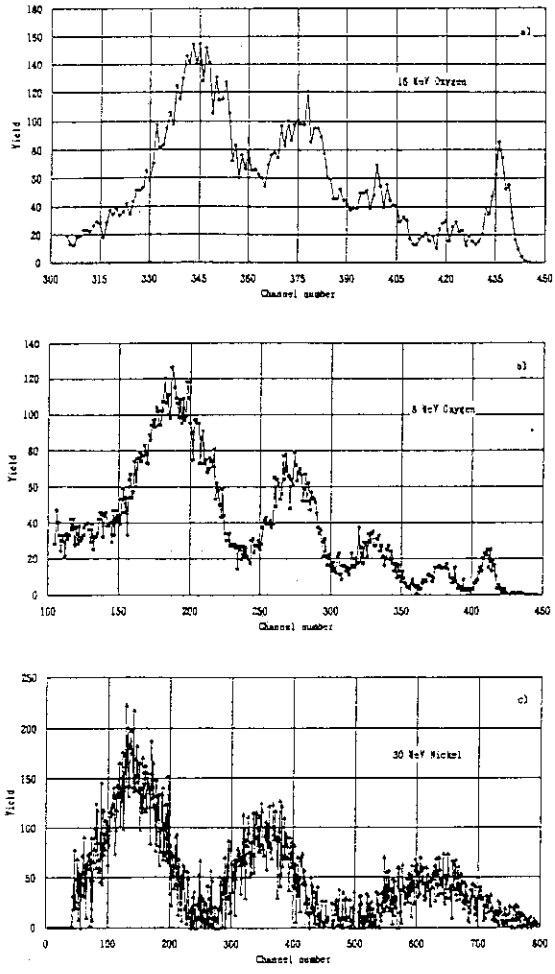

Fig. 2: HE-ERD spectra of a H charged multilayer sample consisting of 4 Nb layers with thicknesses 50, 100, 200 and 300 Å and 5 Cu spacer layers of 200 Å each. The first peak at the high energy side of the spectra is hydrogen adsorbed at the surface. Incident beam and absorber foil for a) 16 MeV ^{16}O + 12.5 μm Mylar, b) 8 MeV ^{16}O + 6.5 μm Mylar and c) 30 MeV ^{58}Ni + 6.5 μm Mylar. The spectrum for 30 MeV Ni beam has been subtracted from the Cu(Ni, Ni) background. Incident angle 15°, detection angle 30°, aperture slit 1 mm.

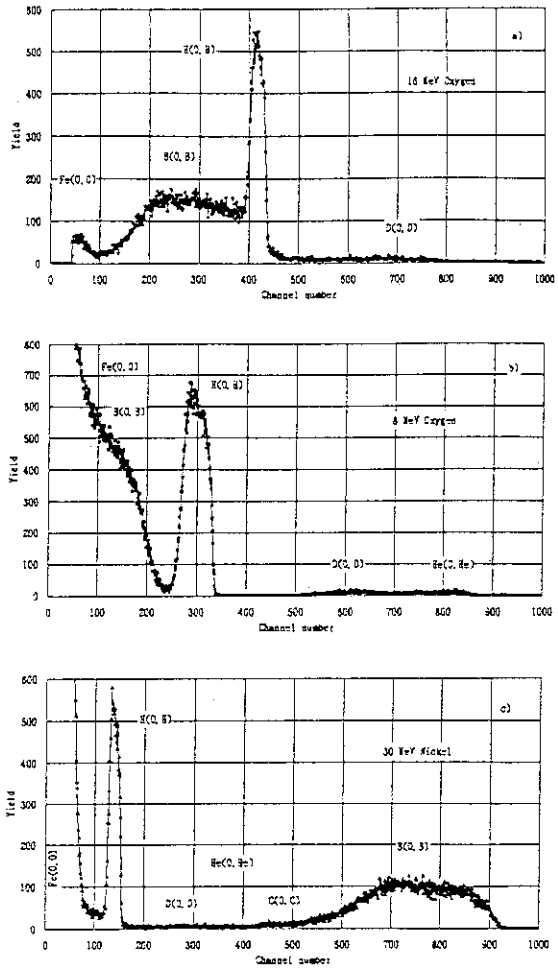

Fig. 3: Thin boron layer (2100 Å) on iron containing H, D and He. Incident beam and absorber foil for a) 16 MeV ^{16}O + 12.5 μm Mylar, b) 8 MeV ^{16}O + 6.5 μm Mylar and c) 30 MeV ^{58}Ni + 6.5 μm Mylar. Incident angle 15°, detection angle 30°, aperture slit 1 mm.

[1]. The energy loss in the foil can be accurately calculated using the wellknown TRIM code [2]. In this measurement a relatively low resolution of 200 – 300 Å was obtained, because of the low stopping power of the target material. Employing an ERD system without absorber foil using time-of-flight and energy measurement (TOF-ERD), the limitation due to spectrum overlap for different recoil masses can be omitted and the resolution can be increased to about 50 –100 Å.

References:

1. P. Goppelt- Langer, S. Yamamoto, Y. Aoki, H. Takeshita, H. Naramoto, M. Saidoh, J. Yagyu, N. Ogiwara, submitted to Nucl. Instr. and Meth. B (1994)

2. J.F. Ziegler, J.P. Biersack, U. Littmark, The Stopping and Ranges of Ions in Matter, Vol 1. Pergamon Press, N.Y. (1985)

6.2 ION BEAM ANALYSYS ON SAPPHIRE IMPLANTED WITH VANADIUM IONS

Hiroshi NARAMOTO, Hidefumi TAKESHITA, Yasushi AOKI
and Shunya YAMAMOTO

Department of Materials Development, JAERI/Takasaki

1. Introduction

Transition elements are known to have various kinds of charge states in the host matrix with generation of lattice defects, which influences on the electronic structure of its matrix. The introduction of these elements into chemically inert oxides like sapphire can be realized using ion implantation technique in a well controlled manner[1]. Some vanadium oxides are expected to experience the phase transition under the changes of temperature, hydrostatic pressure and impurity incorporation[2]. These phenomena can be utilized for the synthesis of thin layer with electric function. In this course of study, it is examined how to realize the thin oxide layer with high pressure phase by ion implantation and subsequent annealing.

In the study of 1993 JPY, the recovery behavior of sapphire samples implanted at low temperature(100K) was analysed using RBS/Channeling method.

2.Experimentals

(0001) sapphire platelets were polished and annealed to remove the induced lattice strain. Typical size of sapphire samples was 5x10X0.3 mm^3 and the implantation of 150keV ^{51}V was made at 100K along the direction 5 degrees off from <0001> direction to avoid the channeling effect. The implanted doses(10^{15}-10^{17} /cm^2) were chosen so as to trace the amorphization process. During the ion implantation, a sample was covered partly to leave the virgin region for <0001> axis reorientation after annealing.

Samples were annealed in air for 1 hour up to 1273K. RBS/Channeling analysis was made to observe the substitution of Al sublattice by V atoms and the recovery of lattice defects using 2 MeV ^4He ions mainly.

3. Results and Discussion

Different from the results of RT implantation, the low temperature implantation induces the quite different features in RBS/Channeling spectra. Three kinds of spectra are shown; two from virgin and implanted under <0001 > aligned condition and one from implanted under random condition.

Figs. 1 and 2 show the as-implanted spectra after the implantation to the doses of 2.19x10^{15} and 1.06x10^{17} /cm^2, respectively. From a comparison between aligned and random spectra of Fig. 1, it is concluded that sapphire is easilly turned into amorphous by the low temperature implantation. At this dose level, it is not reasonable to expect the contribution of implanted species to the amorphization. The critical dose to that is two orders of magnitude lower in low temperature implantation. Further implantation up to 1.06x10^{17}/cm^2 makes the amorphous layer thicker but there is no indication of the substitution of Al sublattice by V atoms as can be seen in Fig. 2. At this dose, the average concentration of V atoms amounts to about 10% and the implanted layer can be assumed to be oxygen-defficient.

Annealing of these samples results in the considerable recovery of lattice defects after 800C. One can see the big difference in the spectra of Figs 3 and 4. The defects in Al sublattice still remain in the low dose sample and there is no indication of substitution of Al lattice by V. On the contrary, the high dose sample exibits almost the complete recovery of Al sublattice with about 90% loss of implanted V, and remaining V atoms in the deeper region occupy Al sub-

lattice. These unexpected results can be tentatively explained by referring to the gamma phase formation of amorphized layer after thermal annealing. It is reasonably considered that the blocking of gamma phase formation by high dense V impurities facilitates the solid state epitaxial growth in the high dose sample.

References

1)H. Naramoto, C. W. White, J. M. Williams, C. J. McHargue, O. W. Holland, M. M. Abraham and B. R. Appleton, J. Appl. Phys. 54(1984) 683.
2)D. B. McWhan, A. Menth, J. P. Remeika, W. F. Brinkman, T. M. Rice: Phys. Rev. B7(1973)1920.

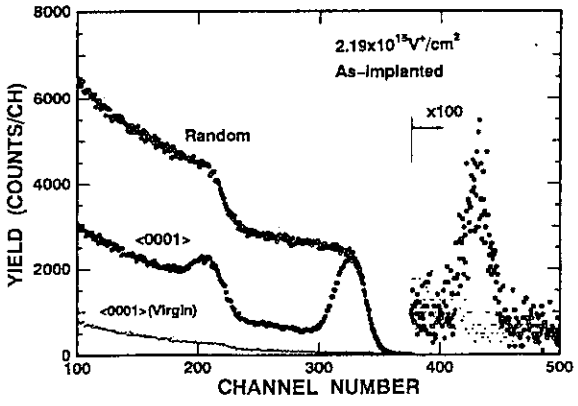

Fig. 1: 2MeV ^{4}He RBS/Channeling spectra from as-implanted sapphire. 150keV ^{51}V ions were implanted lightly to 2.19x $10^{15}/cm^{2}$ at 100K.

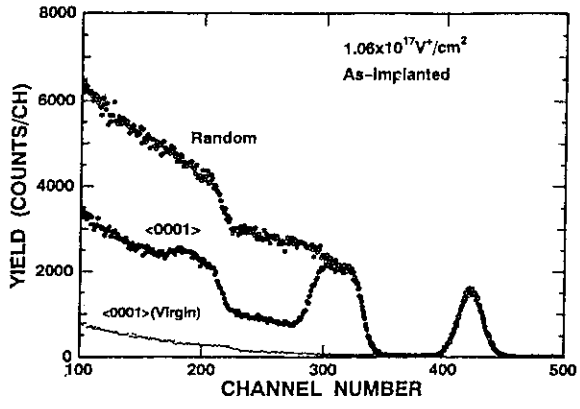

Fig. 2: 2MeV ^{4}He RBS/Channeling spectra after 800C-annealing of the same sample as in Fig. 1.

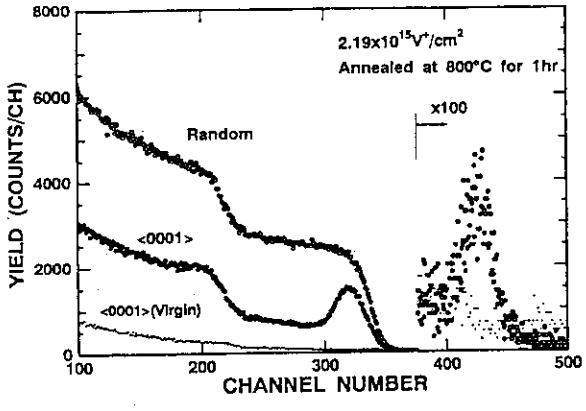

Fig. 3: 2MeV ^{4}He RBS/Channeling spectra from as-implanted sapphire. 150keV ^{51}V ions were implanted heavily up to 1.06x$10^{17}/cm^{2}$ at 100K.

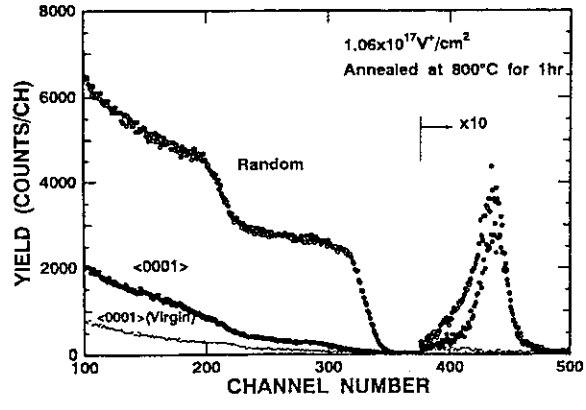

Fig. 4: 2MeV ^{4}He RBS/Channeling spectra after 800C annealing of the same sample as in Fig. 3.

6.3 Analysis of Hydrogen in Nb/Cu Multilayers Using ^{15}N NRA

S. Yamamoto, P. Goppelt-Langer, Y. Aoki, H.Takeshita and H. Naramoto

Functional Materials Laboratory 2, Department of Materials Development, Japan Atomic Energy Research Institute, Takasaki Radiation Chemistry Research Establishment, 1233 Watanuki, Takasaki, Gunma, 370 -12 JAPAN

Introduction

The Nb/Cu multilayer structure is expected to show novel physical properties. The distribution of hydrogen atoms will be influenced far beyond the thermal equilibrium by this structure. This system is also interesting in its electromagnetic properties at low temperature [1,2]. It is needed to do detailed structural analysis with good depth resolution. The depth distribution of copper and niobium atoms of the matrix are obtained by Rutherford backscattering spectrometry (RBS) [3] and that of hydrogen atoms is accomplished by employing nuclear reaction analysis (NRA). The $^{1}H(^{15}N,\alpha\gamma)^{12}C$ resonant nuclear reaction (6.385 MeV) has a very narrow resonance of about 2 keV [4] and a low off-resonance cross-section, and the depth resolution of less than 5 nm in this technique is sufficient to measure the H concentration at each layer. Thus, hydrogen profiling with ^{15}N-NRA can be applicable to analyze the multilayered structure of matrix elements with smaller mass-difference as e.g. niobium and molybdenum atoms where a standard RBS is not effective.

Experiment

Nb/Cu multilayer samples were prepared on MgO substrates using the electron beam evaporation technique under UHV conditions. Our system is equipped with three EB guns and liquid nitrogen shrouds covers the heated part to keep the vacuum in the 10^{-8} Torr range even during evaporation. Deposition rates and thicknesses were controlled by quartz monitors located near the substrate. The samples were charged by hydrogen using a $Ar(H_2)$ gas mixture under atmospheric pressure and heated up to 150°C for 30 min. The H charging was performed without exposing samples to open air.

^{15}N ion beams were available from the 3 MV tandem accelerator of the TIARA facility at JAERI Takasaki. Fig. 1 shows the experimental setup for ^{15}N-NRA measure-

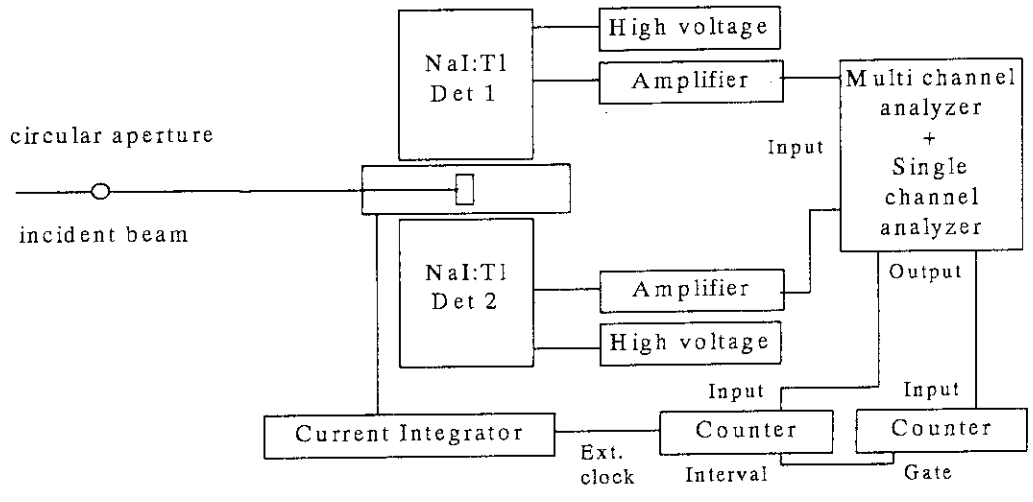

Fig. 1: Experimental setup for ^{15}N NRA measurements.

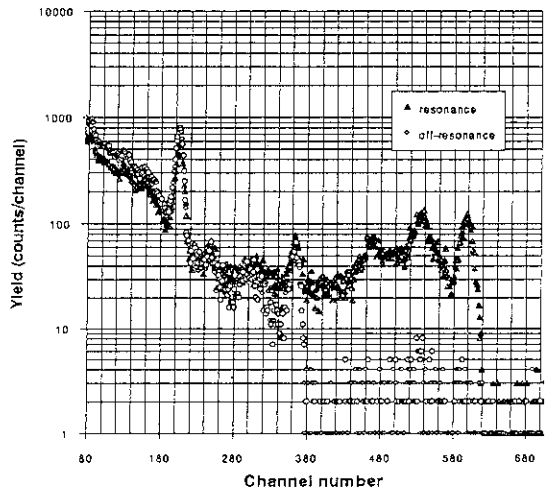

Fig.2: γ-ray spectra measured with the NaI detectors during ^{15}N NRA.

ments. A sample holder for up to 6 samples was used. The beam size was limited to 3 mm diameter and γ-rays were detected with two 3" by 3" NaI(Tl) detectors, on both sides of the small NRA chamber. In this case the total detection angle is enlarged to about 8sr. The detector signals were amplified using ORTEC 571 amplifiers and the 4.43 γ-signals, single and
double escape peaks were selected by setting appropriate energy windows in a portable Dual MCA/SCA. The SCA outputs were connected to fast counters. The whole chamber was insulated and served as Faraday cup. The beam current was integrated using an current integrator and a fast counter. The signal counter was gated by the integrated current. Data points were taken in steps of 10 to 20 keV. To avoid H loss due to beam bombardment, the measurements were done with increasing and decreasing energy. For H calibration a hydrogenated amorphous Si layer with 17 at.% of H on crystalline silicon was used.

Results

Fig.2 shows a typical γ-ray energy spectrum of the NaI(Tl) detector. Two spectra are shown, one with higher energy (6.60 MeV) and the other with off resonance energy (6.37 MeV). The yield of the 4.43 MeV γ-rays is proportional to the hydrogen concentration of target. The characteristic γ-ray energy region has low-background and the contribution of off-resonance reaction is small. Fig.3 shows the γ-ray yield (4.43 MeV) of a-Si detected as a function of the incident energy of the ^{15}N ions. This spectrum corresponds to the depth profile of the hydrogen concentration. A strong hydrogen peak appears at the resonance energy (6.385 MeV). It is due to contamination (water, hydrocarbons) adsorbed at the surface of the sample.

In order to study the influence of beam irradiation on the hydrogen concentration of the sample, we compared an amorphous silicon layer (1μm) with 17 at.% of H on crystalline silicon and a Kapton film (14 μm). The hydrogen in the Kapton film decreased rapidly with ^{15}N ion dose, while the a-Si sample was stable. The experimental results show that the hydrogen in a-Si is stable and homogeneous along the depth. This result assures us use a-Si sample for hydrogen calibration.

Fig .4 shows the depth profile of hydrogen in a Cu/Nb multilayered sample with thicknesses of 10, 20, 40 and 80 nm. This sample was high charged with hydrogen by heating at 150°C for 30 min under 1 atm $Ar:H_2$(3

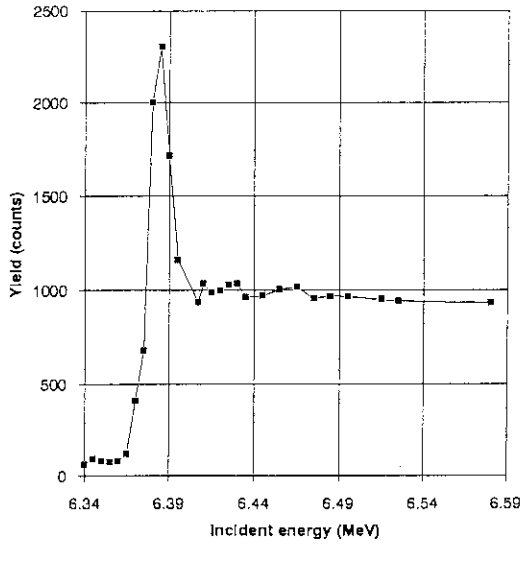

Fig.3: Depth profile of hydrogen in a-Si.

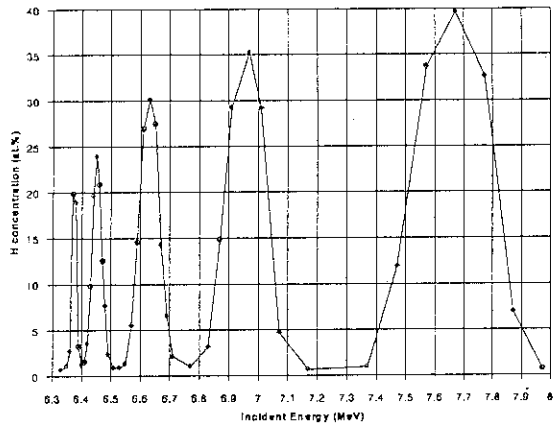

Fig 4: H concentration profile of a Nb/Cu multilayer sample.

at.%). The hydrogen concentration of the Nb layers increases with layer thickness and reaches about 40 at.% at 80 nm thickness. Also, the measurement of an uncharged sample with less than 5 at.% at the Nb layers showed the same behavior. These hydrogen atoms were absorbed during evaporation from the remaining hydrogen molecules in the vacuum chamber.

Summary

In this report we have shown the hydrogen concentration profile in amorphous silicon and Cu/Nb multilayered samples using ^{15}N resonant nuclear reactions at 6.385 MeV. The hydrogen of a-Si was stable for ^{15}N ion bombardment and kept to be homogeneous along the depth. It is clear that this ion beam analysis method is a more direct way to know the hydrogen concentration near the surface compared with other spectroscopic methods. This technique of hydrogen profiling can be applicable to analyze multilayered structures with thicknesses of about 5 nm. We found that the hydrogen concentration in thin Nb layers increases with the increase of layer thickness.

Acknowledgment:

We like to thank the TIARA accelerator team for kind operation of frequent energy tuning.

References:

1. C.M. Falco, and I.K. Schuller in *Synthetic Modulated Structures* , Eds: L.L. Chang, B.C. Gicssen, (Academic Press 1985) 339.
2. T. Ruggiero, and M.R. Beasley in *Synthetic Modulated Structures* , Eds: L.L. Chang, B.C. Gicssen, (Academic Press 1985) 365.
3. S. Yamamoto, H. Takeshita, Y. Aoki, and H. Naramoto, TIARA Report 1992.
4. W.A. Lanford, Nucl.Instr. and Meth. B66 (1992) 62.

6.4
Studies on the Processes of Atomic Adsorption and Desorption at the Solid-Liquid Interface by In-situ RBS Technique

K.Morita, J.Yuhara, R.Ishigami, B.Tsuchiya, S.Yamamoto[2],
Y.Aoki[2], H.Takeshita[2], and H.Naramoto[2]
Dept.Cryst.Sci., Nagoya University, Takasaki Establishment, JAERI[2]

The aim of this study is to develop the experimental system for measuring, by in-situ RBS technique, the depth distribution of heavy impurity atoms adsorbed at the inner surface of a thin film wall of a liquid container which are dilutely dissolved in a liquid specimen, and for determining the rate constants of their adsorption and desorption at the solid-liquid interface. In order to achieve the aim of this study, it is necessary to prepare a stable thin film specimen which can isolate the vacuum system for the RBS measurement from the impurity-dissolved liquid. Moreover, it is necessary to determine the energy range of probing He^+ ion beam enabling the detection of adsorbed species which depends on their mass and thickness of the thin film wall.

In this experiment, we have confirmed the possibility of detecting using gold atoms, of 2ML in thickness, deposited on the silicon self-supporting film of 2.6μm in thickness. The two different RBS spectra are shown in Fig.1, which were obtained for the cases of 6MeV He^+ ion beam incident on the specimen, of which a gold layer was deposited on the front surface (a) and on the back surface (b). It is seen from Fig.1 (a) that the RBS peaks from the Au atom and the Ar atom, of which masses are larger than that of Si, appears clearly at energies higher than the Si peak, and the RBS peaks from C and B atoms, of which masses are small, appears at energies lower than the Si peak.

It is seen clearly from Fig.1 (b) that the RBS peak from the Au layer located at the back surface of the Si film is observed, which indicates that the impurities such as Cs or Ce adsorbed on films of SiO_2 or Ai_2O_3 can be detected with 6MeV He^+ ion beam when their thickness is a few μm.

Now we are preparing a thin self-supporting film of 3mm in diameter in a thick silicon wafer for practical purposes.

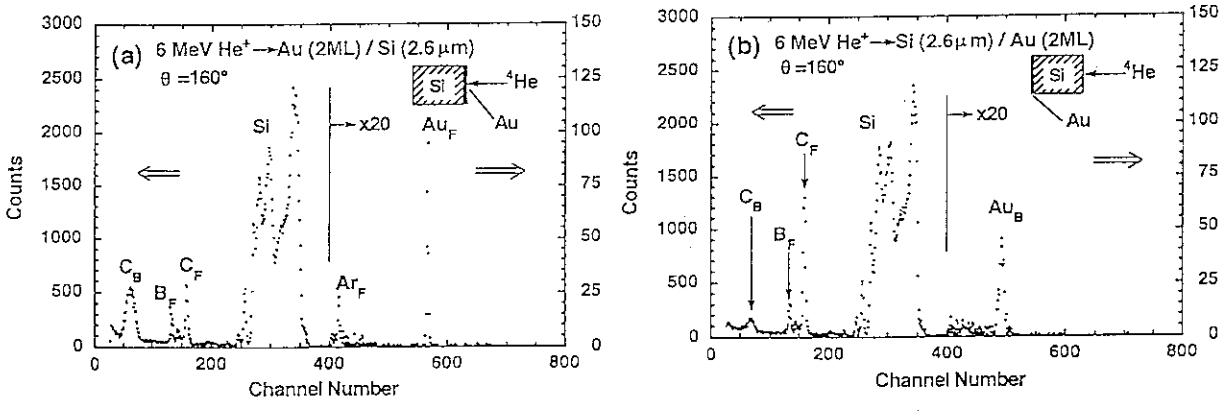

6.5 Ion Beam Analysis of Materials by Using Ion-Induced Secondary Electrons

H. Kudo, T. Fukusho, A. Tanabe, T. Ishihara,
H. Takeshita[2], Y. Aoki[2], S. Yamamoto[2], P. Goppelt-Langer[2], H. Naramoto[2]
Instutute of Applied Physics, University of Tsukuba, JAERI, Takasaki[2]

This joint research program has been continued through the past year to pioneer a new field of ion beam applications in solid state physics and material analyses. The experiments have been based on our original analysis system for ion-induced secondary electrons emitted at a backward angle of 180° with respect to the beam direction by using parallel-plate electrostatic spectrometer of the mirror-symmetry type. Measurements of high-energy (keV) secondary electrons allow detailed analysis of the initial stage of ion channeling, i.e., the high-energy shadowing effect which is difficult to observe by other methods. The main research includes: (i) Determination of charge states of ions in glancing collisions with aligned atoms in single crystals, (ii) Ion beam analysis of bond electron distribution in solids, and (iii) Characterization of crystalline materials by using shadowing pattern imaging with secondary electrons.

We have collected secondary electron data for 1.5- to 3.5-MeV/u energy range of various ions incident on Si by joint use of the TIARA tandem, the TIARA single-ended accelerators and the UTTAC tandem accelerator.

In this fyscal year, we have collected fundumental data on the effective target thickness for generating secondary electrons that are emitted at keV energies. These data are to be fully used in the reserches (i)-(iii) as a physical basis of analysis.

I. *High-energy shadowing effect*

The high-energy shadowing effect can be measured as a ratio of channeling to random (nonchanneling) yield at a fixed electron energy. For an electron energy between the loss-peak energy and the binary-peak energy (E_B), all the target electrons (inner-, outer-shell, and valence electrons) contribute to the observed electron yield. It should be noted that above the loss-peak energy ($=E_B/4$) the electron yield consists of pure binary-encounter electrons. The electron yield below the loss peak energy partly results from loss electrons and convoy electrons which have a somewhat complicated character compared with the binary encounter electrons, so that it is inadequate to measure the shadowing effect. Since the energy spectrum of electrons that stem from binary encounter processes has a well known Z_1^2-scaling character if the ions are fully stripped, the shadowing effect for fully-stripped different ions can be compared in terms of the ratio of channeling to random yield at a fixed electron energy.

II. *Effective target thickness for electron yield*

The measured ratios of channeling to random yield at electron energies in the

middle of the loss-peak and binary-peak energies are shown in Fig. 1 for the case of protons and alpha particles under Si<100> and Si<110> channeling incidence conditions. We see that the ratio decreases with increasing the ion velocity, and becomes constant above 6 MeV/u. These curves indicate that for high-energy ions the effective target thickness for the channeling case is approximately proportional to the ion velocity. Measurements for wider energy range of ions and for various target materials are needed for more general understanding of the effective target thickness, which is a key concept for applied use of the high-energy shadowing effect.

The data shown in Fig. 1 have been used to determine the charge states of the 2.5- and 3.5-MeV/u ions in Si. They also provide useful knowledge on the effective target thickness in the analysis of bond electron distribution in solids. To aquire more high-quality data, highly stabilized ion beams are neccesary .

Related publication

1) Kudo et al., *High-energy Shadowing Effect and Its Application to Atomic and Solid State Physics*, Proc. 15th Int.Conf. Atomic Collisions in Solids (Ontario, Canada,1993), and Nucl. Instrum. Methods **B90**, 533 -536(1994).

III. *Concluding Remarks*

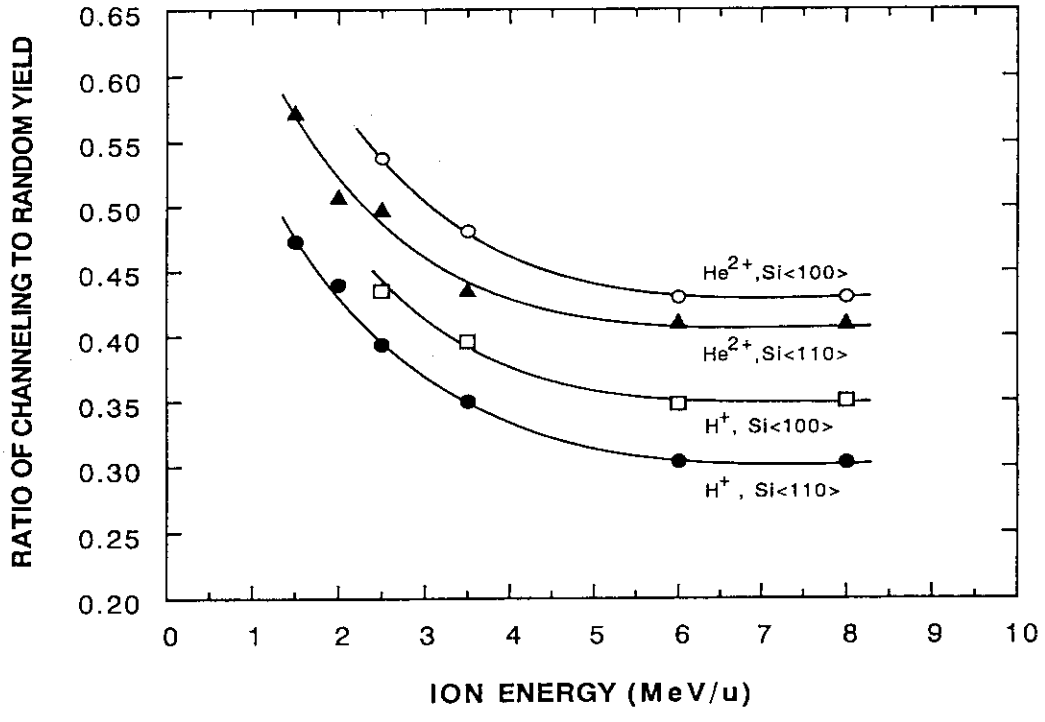

Fig. 1 Dependence of the ratio of channeling to random yield at $E_B/2$ on the ion energy in MeV/u.

6.6 Positron Annihilation Study of Irradiation-Induced Defects in Silicon-Related Materials : Silica Glass

M. Hasegawa[1], M. Tabata[1], T. Miyamoto[1], M. Fujinami[2], H. Sunaga[3], S. Okada[3], A. Kawasuso[1], M. Suezawa[1] and S. Yamaguchi[1]

[1] *Institute for Materials Research, Tohoku University, Sendai 980-77,*
[2] *Advanced Materials and Technology Research Laboratories, Nippon Steel Corporation, 1618 Ida, Nakahara-ku, Kawasaki 211,*
[3] *Takasaki Establishment, Japan Atomic Research Institute, Takasaki 370-12*

1. Introduction

One of fundamental properties of vacancy in semiconductors and their compounds is its formation energy. To obtain the formation energy it is very necessary to carry out high temperature experiments. Further in order to study interfaces and vacancy-type defects induced by phase change, such as glass transition of silicon dioxide, positron annihilation measurements at high temperature have to be done. It is, however, very difficult to carry out the high-temperature experiments, because usual positron source ^{22}NaCl melts at temperatures above 800°C. Internal source method is free from such a restriction and is very necessary for these high temperature experiments. For silicon related materials we can use the nuclear reaction ^{28}Si(p, ^{7}Be) ^{22}Na of high energy protons. Further it is also interesting to study defects introduced by proton irradiation for production of the internal source. In the present work we have studied irradiation-induced defects in silica glass by electron or neutron bombardment as a preliminary experiments for high-energy (70 -90 MeV) proton irradiation which will be employed for introducing the internal source in samples in the current project.

Study of irradiation damage in silica glass is related to important technological problem of optical fibers in nuclear power plants and long-term behavior of radioactive waste storage materials [1]. It is also of particular interest because silica glass is a prototype for many glassy materials and its defect structure is of intrinsic scientific interest.

2. Experimental

Specimens of about 8x8x1 mm^3 were cut from two kind of silica glass plates (Nippon Silica Glass Corp., Japan): HRP and ED. The HRP glass was produced from natural quartz by electrical fusion. The ED glass, synthetic silica, was produced by the vapor phase axial deposition (VAD) method [2,3]. These were bombarded with 3 MeV electrons up to a dose of 1.0 x 10^{18} e/cm^2 below 50°C using Dynamitron accelerator at Takasaki Institute, JEARI or fast neutrons up to a dose of 8.3x10^{18} n/cm^2 below 150°C in the Irradiation Facility of Hydraulic Rabbit II in Japan Materials Testing Reactor. The samples irradiated to 8.6x10^{17} were isochronally annealed for 30 min up to 900°C in air. Positron lifetime measurements were carried out with a usual apparatus having time resolution of about 180 ps (FWHM).

3. Results and Discussion

The lifetime spectra for silica glass are well decomposed into three lifetime components with the time constants τ_i and the relative intensities I_i (i=1,2,3) ($I_1 + I_2 + I_3 = 1$) before irradiation; τ_1 is about 0.12 ns, τ_2 is 0.8ns and 1.1 ns for HRP and ED respectively, and τ_3 is about 1.7 ns[2,3]. The longer lifetime τ_3 is nearly independent of the samples and due to pick-off annihilation of ortho-positronium (o-Ps) formed in 3 dimensional open space, "intrinsic" structural voids, with radius of about 0.3nm and τ_1 is mostly arising from self-annihilation of para-Ps (p-Ps) formed in the voids [2,3]. The lifetime τ_2 is strongly dependent on the sample, which may be closely related to the starting materials and the preparation method. Possible way to explain this component is positron (or Ps) compound formed around impurities, or free positrons, without forming Ps, trapped in the voids.

Figure 1 presents these lifetime parameters against displacement per atom (dpa) ratio of oxygen atoms where the threshold energy for displacement is assumed to be 10eV [1]. The lifetime τ_2 decreases from 0.88ns to about 0.50 ns even for the lowest dpa of 6.9x10^{-5}, followed by a small decrease at 1.4x10^{-4} dpa, but shows no change for the higher dpa; τ_2 is about 0.47 ns for dpa higher than 1.4 x10^{-4}. This clearly provides evidence that positrons are trapped at irradiation-induced defects and annihilates there with the observed lifetime of about 0.47 ns. The intensity I_2 increases with dpa and attains as high as about 80%, which shows accumulation of the irradiation-induced defects responsible for the lifetime of

about 0.47ns. We have, however, observed this component only after irradiation and call them the first type irradiation-induced defects, which are sensitively introduced by irradiation as seen after electron irradiation.

The lifetime τ_3 is slightly shortened by irradiation with doses up to 4.6×10^{-3} dpa, which is due to small change in the size of the void in which Ps is formed. The intensity I_3, however, decreases rapidly with dpa, which indicates that positrons are trapped by the first type defects. This trapping reduces Ps formation and hence the intensity I_3.

Before irradiation the τ_1 component mostly come from p-Ps annihilation [2,3]. However slight increase in τ_1 is observed after irradiation. This suggests that some irradiation-induced defects, the second type irradiation-induced defects, with positron lifetime of about 0.3 ns contribute positron trapping and that the observed τ_1 is given by an average between p-Ps lifetime of 0.125ps and the lifetime at the second type defects [2,3].

Figure 2 shows the isothermal annealing behavior of the lifetime parameter for HRP irradiated with 3MeV electrons to 1.4×10^{-4} dpa. The τ_2 lifetime gradually recovers with annealing temperature and exhibits rapid annealing around 800°C. This suggest that the first type defects are stable up to 700°C. The annealing behavior of the lifetime parameters for HRP and ED after neutron irradiation of 4.6×10^{-3} dpa are shown in Fig.3. In HRP τ_1 shows a small increase at about 150°C and then gradually decreases with annealing temperature up to about 500°C, but shows little change for further annealing up to 800°C. The lifetime τ_2 shows sluggish increase with temperature up to about 700°C and rapid recovery around 800°C. In contrast to these small changes in the lifetimes, the intensities I_2 and I_3 recover successively with temperature; I_2 decreases but I_3 increases in a compensatory way with annealing temperature, and they attain their intensities of unirradiated state after annealing at about 800°C. It should be emphasized that I_2 and I_3 exhibit enhanced recover around 450°C which corresponds to the stage for τ_1. In ED the recovery of the lifetime parameters is very close to that in HRP. However, τ_2 for ED recovers much faster than that for HRP with annealing temperature above 500°C.

Fundamental irradiation-induced point defects in silica glass are oxygen vacancies, peroxy bridges (globally equivalent to Frenkel defects), peroxy radicals (POR) , silicon vacancies and interstitials [1]. Because of its small displacement energy we can assume major defect species are associated with oxygen. These defects usually trap holes or electrons and sometimes relax with small atomic displacement. The resulting defects are the E' center, peroxy radi-

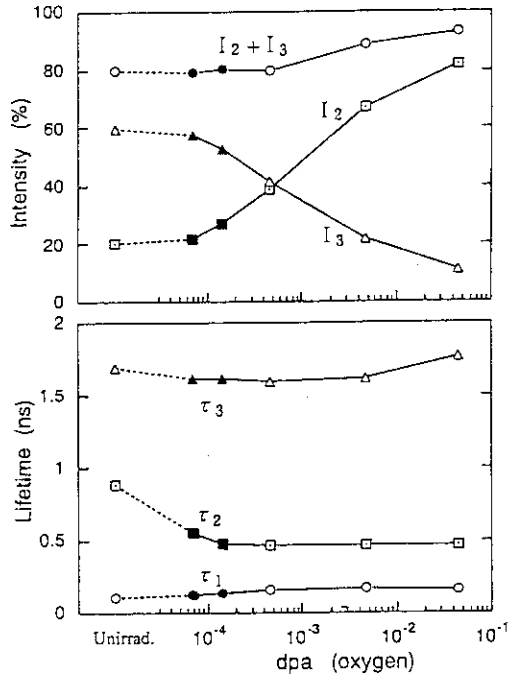

Fig. 1. Changes in the lifetimes and their intensities in the HRP glass with the dpa ration for oxygen. 2. The shaded symbols stand for 3MeV electron irradiation, and open ones for neutron irradiation.

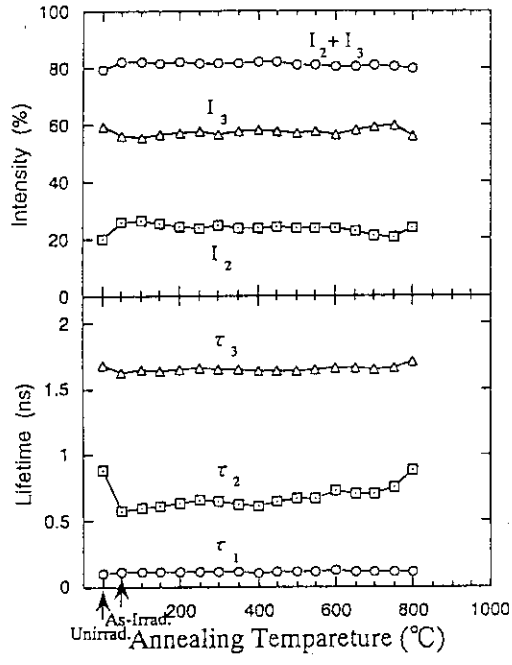

Fig. 2. Isochronal annealing behavior of the positron lifetime parameters for the HRP glass irradiated with 3 MeV electrons to a dose of 1×10^{18} e/cm^2 (1.4×10^{-4} dpa).

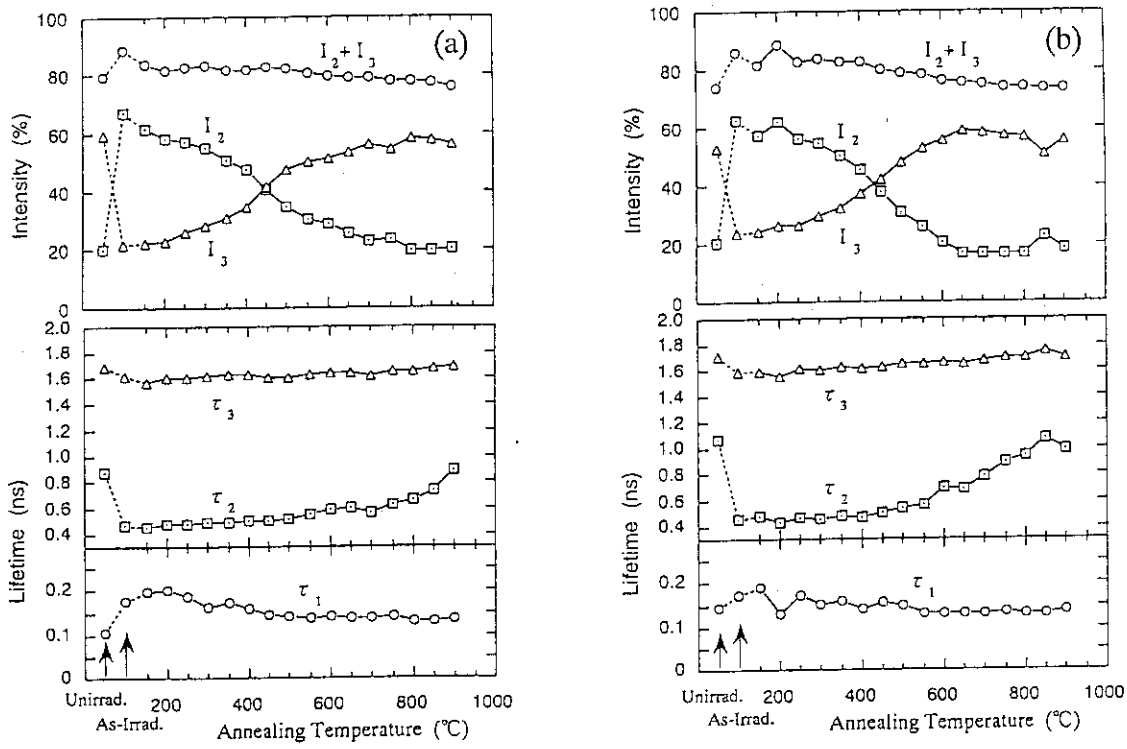

Fig. 3. Isochronal annealing behavior of the positron lifetime parameters after neutron irradiation to a dose of 8.6×10^{17} n/cm^2 (4.6×10^{-3} dpa): (a) HRP and (b) ED glass.

cals, non-bridging oxygen hole center (NBOHC) and so on. These have been extensively studied by ESR and optical absorption measurements [1,4,5]. Griscom showed that after gamma-ray irradiation the E' centers recovers completely at about 300°C in low-OH silica glass while at about 400°C in high-OH silica glass, and that POR in low-OH silica glass are stable and their complete recovery occurs 700°C [4,5]. Nagasawa et al. showed recovery of the E' centers (below 300°C), NBOHC (below 400°C) and POR (below 600°) [24]. Considering these previous studies, we can explain the present results of isochronal annealing as follows. Firstly the recovery in I_2, the first type defects, can be attributed to POR which is known to anneal out around 700°C. As stated above the lifetime τ_2 increases rapidly with annealing temperature above 500°C in ED, while very slowly in HRP. This difference may be due to OH group or metallic impurities. Secondly the small increase by annealing at 150°C and successive recovery up to about 450°C in τ_1 are due to the E' centers which will trap positrons and gives positron lifetime of about 0.30 ns. Then we can ascribe the second type defects as the E' centers.

Defects in silica glass have been studied mostly by ESR method which is a very sensitive tool for paramagnetic defects but gives no signals for diamagnetic defects. On the contrary positron annihilation method has no such restriction. Then ESR and optical absorption experiments on the same samples for positron annihilation will be very useful to studies of defects in silica glass. Such experiments are now in progress.

References

1)C. H. de Novin and A. Barbu: Solid State Phenom. **30&31** (1993) 277.
3)M.Hasegawa, M.Tabata, T.Miyamoto, M.Fujinami H. Sunaga, S. Okada and S. Yamaguchi: Sci. Rep. Res. Inst. Tohoku Univ. (RITU) **40A** (1994) 203.
4)M.Hasegawa, M.Tabata, T.Miyamoto, Y.Nagashia, T.Hyodo, M.Fujinami and S. Yamaguchi: Mater. Sci. Forum (in press).
4)D.L. Griscom: J. Ceram. Soc. Jpn. **99** (1991) 923.
5)G.L. Griscom: Rev. Solid State Sci. **4** (1990) 565.
6)K. Nagasawa, Y. Hoshi, Y. Ohki and K. Yahagi: Jpn. J. Appl. Phys. **25** (1986) 468.

6.7 Dynamic Observation of Laser Ablated Carbon Particles Using Time-Resolved X-ray Absorption Spectroscopy

A.Miyashita, T.Ohyanagi*, O.Yoda and K.Murakami*
Department of Materials Development, JAERI Takasaki
*Institute of Materials Science, University of Tsukuba

Recently, laser ablation is recognized to be well suited for formation of new materials such as carbon cluster[1-2] which properties are very hot topics in the physical field. It is important to understand how they are formed in clusters. However, behaviors of the laser ablated species are not clear yet. We have measured ablated carbon particles by a time-resolved X-ray absorption spectroscopy using laser produced plasma X-ray (LPX) as an X-ray source.

CONSTITUTION OF THE APPARATUS

The time-resolved X-ray absorption spectroscopy apparatus is composed mainly of two parts: the laser system and the spectrometer. Figure 1 shows a schematic drawing of our spectrometer. A 20J Q-switched Nd:YAG/glass laser is used both to produce soft X-rays and to irradiate samples. The FWHM of the laser pulse is about 12ns. The fundamental laser pulse of 1064nm is frequency-doubled with the use of second harmonics generators (SHGs). The first SHG generate 7J, 532nm beam. The 7J beam is focused on the cylindrical target, 40mm in diameter and 25mm long, with condenser lens. The focus size on the target is about 100μm in diameter, in this case, target irradiance power density reaches 7×10^{12}W/cm^2, and hot and dense laser plasma generates soft X-rays on the target. A part of the fundamental wave passes through the first SHG, which is again frequency-doubled with another SHG. A 1J, 532nm beam is generated and converged on the sample with a lens. A delay circuit (10~120ns) is installed in the 7J beam path to adjust the timing between sample irradiation and probing.

Our spectrometer has two sets of X-ray optical systems[3], one for lower energy region, from 90eV to 1000eV, and the other for higher energy region, from 1keV to 3keV. For both energy regions, toroidal mirrors are used to collect and converge X-rays on the sample. X-rays are absorbed by the sample, and then arrive at the polychromator. In the lower energy region, we use a grazing incident flat field grating as an energy analyzer, and a 1024 channel MCP-PCD as an X-ray detector. In the higher energy region, convex curved KAP crystal and MCP-PCD are used.

For the energy calibration and the determination of the energy resolution of the spectrometer, an observed spectrum was compared with a simulated spectrum[4]. Thus, energy resolutions of our spectrometer were found to be 0.8eV, 2.0eV, 10eV and 8eV in energy ranges of 100~200eV,

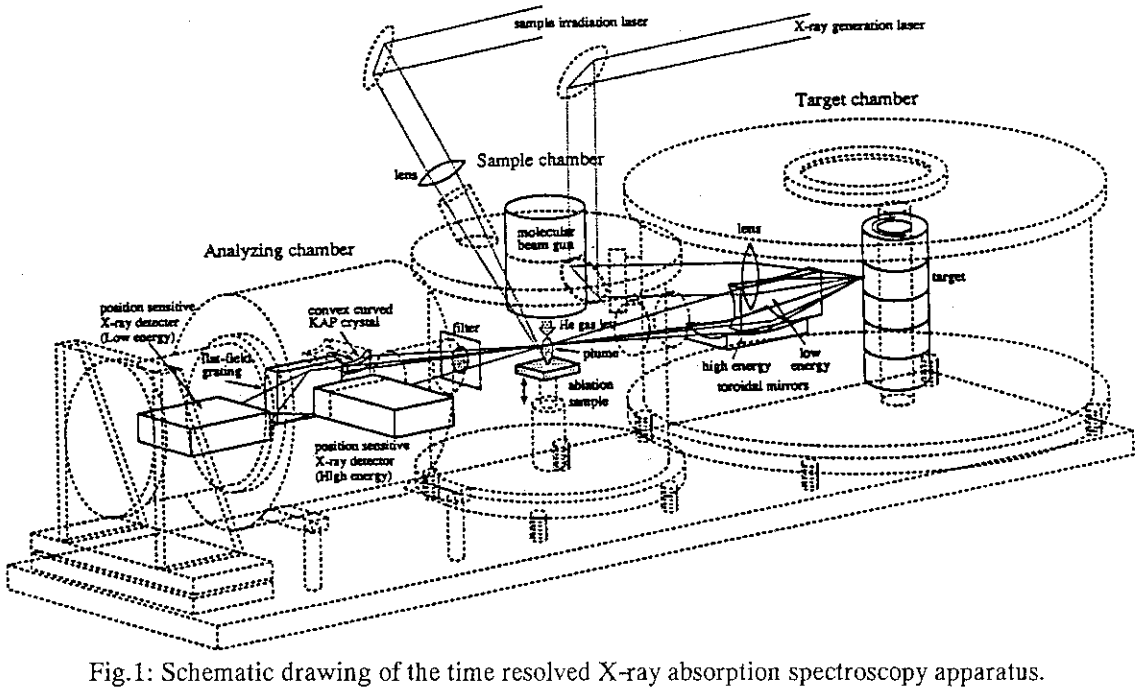

Fig.1: Schematic drawing of the time resolved X-ray absorption spectroscopy apparatus.

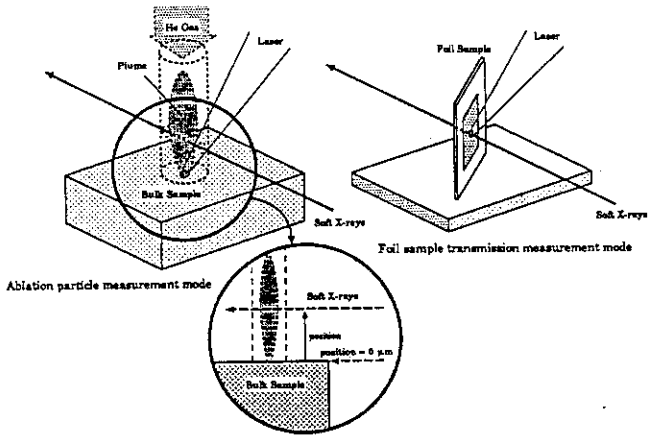

Fig.2: Schematic drawings of the sample measurement mode.

200~500eV, 500~1000eV, 1~3keV, respectively.

We have measured carbon near K-edge X-ray absorption spectra in two modes, the ablated particle measurement mode and the foil sample transmission measurement mode. Figure 2 shows schematic drawings of the sample measurement mode. In the ablated particle measurement mode, soft X-rays passes through the ablation plume which is generated by laser irradiation. The X-ray probing position is adjusted by sample surface. We have decided the probing position at which half X-rays are blocked by sample to be 0. We have also performed the X-ray absorption measurement in the helium gas environment. Helium gas jet has been synchronized with laser ablation to make a localized helium gas environment on the sample. An accumulation tube is attached on the sample to generate a localized helium environment effectively. In the foil sample measurement mode, irradiation laser is adjusted to the X-ray probe position to get dynamic behavior of the foil sample after laser irradiation.

RESULTS AND DISCUSSION

The properties of ablation process of carbon

Figure 3 shows spatial dependence of the ablated carbon species. The energy density of the irradiation laser on the sample is about 20J/cm^2 and the delay times between laser irradiation and X-ray probing are 120ns. The spectra exhibit a main absorption edge and peaks. The absorption edge at 296.5eV is from 1s→vacuum level transition, and the absorption peaks, 284.3eV, 288eV and 293eV are originated from 1s→2p transition of neutral carbon atom(C^0), C^+ and C^{2+} ions, respectively[5]. The absorption peak, 281eV is also observed. This peak energy is lower than C^0, thus it is considered to be a peak originated from negative charged ions(C^-).

Figure 4 shows the spatial distribution of the ablated carbon particles. The absorption peak originated from neutral carbon is stronger as the probing position is closer to the sample surface and remains strong near the surface even when X-ray probing delay time extends to 120ns. On the contrary, C^{2+} peak is observed more than 2mm from the surface when delay time is 120ns. Therefore, at the initial stage, the speed of C^{2+} ion is more than 1.5×10^6cm/s. The absorption peak of the neutral carbon decreases in inverse proportion to the distance from the surface. On the other hand, the absorption peak of C^- decreases rapidly and the peak of C^+ decreases gradually more than that of the neutral carbon. This situation suggests: 1) Lowly ionized and neutral carbons are emitted from the sample surface even after laser irradiation. 2) Two distinct effects exist in the acceleration of the particles. One is the Coulomb repulsion effect by the transient electric field. This effect accelerates charged particles in

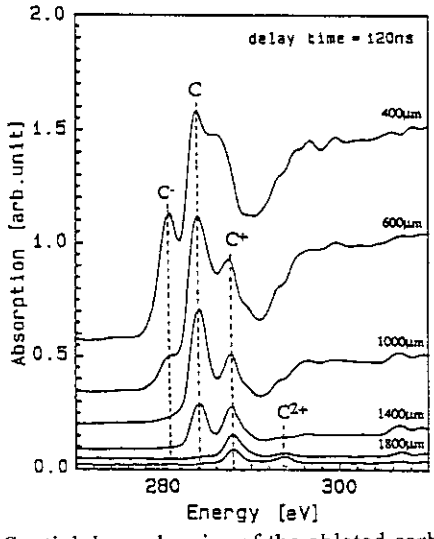

Fig.3: Spatial dependencies of the ablated carbon species.(laser energy density: 20J/cm^2, delay time: 120 ns)

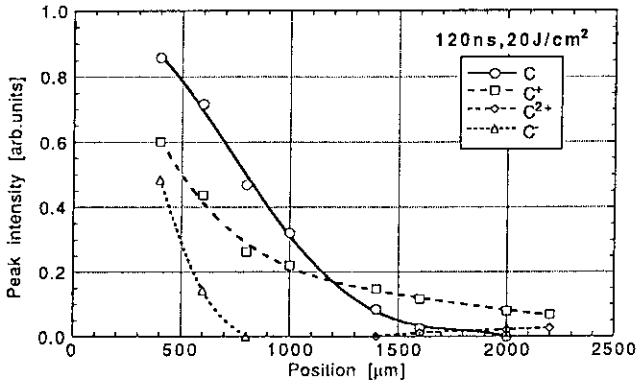

Fig.4: Spatial distribution of the ablated carbon species.(laser energy density: 20J/cm^2, delay time: 120 ns)

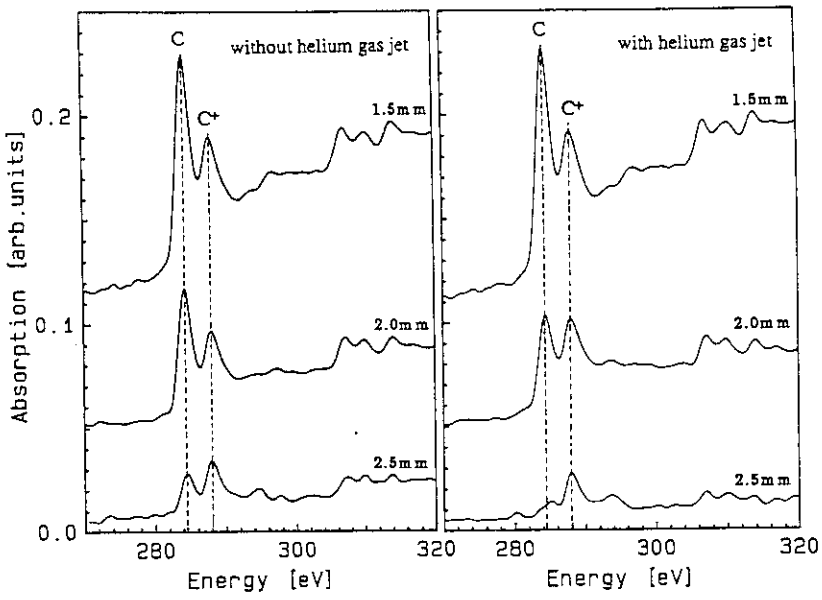

Fig.5: The depression effect of the helium gas environment. X-ray absorption spectra of the laser ablated carbon. (laser energy density: 5J/cm^2, delay time: 120ns.)

proportion to the ionization level. The other is a hydrodynamic expansion from the sample surface to vacuum. This effect continues even after the laser irradiation, and accelerates neutral atoms and ions equivalently.

Ablated carbon particles in the helium gas environment

In the rare gas environment, it is expected that ablated particles are cooled by collision with rare gas atoms and clustering is promoted. Helium gas jet is synchronized with laser ablation to make a localized helium gas environment on the sample. Figure 7 shows the X-ray absorption spectra with and without helium gas. In the region close to the sample surface, the neutral carbon (C^0) peak in the helium gas environment is equivalent to that in vacuum. However, at the top of the ablation plume, the C^0 peak height reduces with helium. The C^+ peak in the helium gas environment remains almost equivalent to the peak in vacuum. Even at the top of ablation plume, there are no additional absorption peaks originated from small carbon clusters, such as C_2 or C_3. These results suggest following possibilities. In the helium gas environment, the expansion of the ablation plume brings about compression of the helium gas, and makes a dense helium region at the top of ablation plume. The dense helium cloud depresses the free expansion of the ablation plume. Thus, what can be seen at 2.5mm above the sample surface in vacuum appears at about 2.2mm in the helium environment. The helium cloud effect has been observed at longer delay time experiments before[6]. Although w have observe a depression effect even when the delay time is 40ns, up to 120ns delay time range, we could not observed absorption peaks assigned to small clusters.

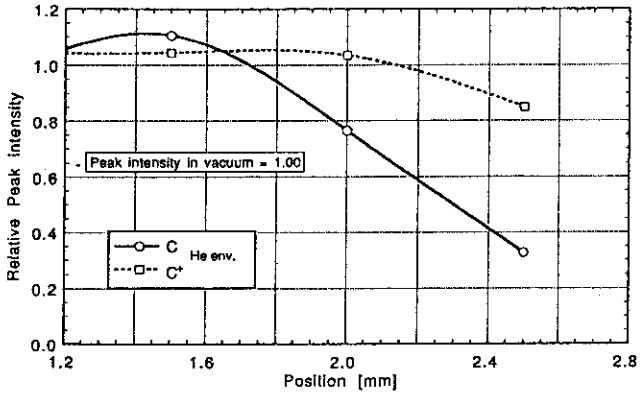

Fig.6: The depression effect of the helium gas environment. Spatial distribution of the ablated carbon species. (laser energy density: 5J/cm^2, delay time: 120ns).

REFERENCES

1) H.W.Kroto, J.R.Heath, S.C.O'Brien, R.F.Curl and R.E.Smalley, Nature 314, 162 (1985).
2) H.S.Carman,Jr. and R.N.Compton, Proc.2nd Inter.Conf. Laser Ablation, (1993).
3) A.Miyashita and O.Yoda, JAERI-M Report 88-212 (1988).
4) A.Miyashita, O.Yoda, K.Murakami, T.Ohyanagi, S.Aoki and N.Yamaguchi, Proc.Laser Advanced Materials Processing '92, 1029 (1992).
5) E.Jannitti, P.Nicolosi and G.Tondello, Physica Scripta 41, 458 (1990).
6) D.B.Geohegan, Appl.Phys.Lett. 60, 2732 (1992).

6.8 Dynamics of Laser-Ablated Si Particles

T. Ohyanagi, A. Miyashita†, K. Murakami and O. Yoda†
Inst. of Materials Science, University of Tsukuba,
† JAERI Takasaki, Functional Material Lab. II

1.Introduction

Laser ablation is known as the technique to produce various-sized clusters, but the process of cluster formation is not made clear. Understanding the process of cluster formation is important to synthesize new functional materials efficiently. In order to make clear the dynamics of cluster formation, we performed time-and-space resolved X-ray absorption spectroscopy measurements of laser-ablated Si particles along with supersonic He gas bombardment with a time range from 0 ns to 120ns after a laser-irradiation on a Si sample.

2.Experimental Setup

Figure 1 shows the scheme of the apparatus. The laser is a pulsed Nd:YAG/glass system. The frequency-doubled output of the laser is split into two beams. One of the beams is focused on a cylindrical target to produce hot plasma and hence X-rays. The other beam is used to irradiate samples. The delay time between the ablation and the X-ray generation is controlled from 0 ns to 120 ns by changing the optical path length. Generated X-rays are collected by a toroidal mirror and focused at the position of the sample. A grazing incident flat field grating with 2400 lines/mm is used to analyze X-rays. X-rays are detected with a 1024 channel microchannel plate (MCP). The energy resolution of the present experimental region (80 eV – 180 eV) is 0.8 eV. A more detailed description of the apparatus has been given in a previous paper.[1,2]

3.Results and Discussions

Figure 2 shows typical X-ray absorption spectra of ablated Si particles measured at different distances. The spectra in Fig. 2(a) have been taken with an ablation energy density of 20 J/cm^2 and a delay time of 0 ns. For Fig. 2(b), the conditions are 10 J/cm^2 and 120 ns. In order to analyze the absorption spectra, we first made the assignments of the absorption peaks. We have observed transitions from a core configuration $2s^22p^6$, which has 0 to 4 additional valence electrons, to $2s^22p^5nl$ or $2s^12p^6nl$ with n=3 up to n=∞ in our energy window, i.e., from 80 eV to 180 eV. The term 'nl' represents $3s, 3p, 3d, 4s, 4p, 4d, \cdots$. Peaks have been grouped into those for the neutral Si atom (Si^0) and Si ions with charges of +1 up to +4.[3,4]

Figure 3 shows spatial distributions of Si atom and ions, which are obtained from peak heights of their $2s \rightarrow 3p$ transitions at 120 ns delay. Although the X-ray absorption cross sections are expected to show various values for the Si atom and ions, we assume for simplicity that the cross sections are almost identical. It is noted that each species in the ablation plume is divided into two components, a fast component and a slow one. The fast component is a result of an acceleration by repulsive Coulomb force, which has been shown by the transient electric field, or due to the negatively charged sheath. The higher the charge state, the faster the ions move. The slow component includes both particles showing hydrodynamic expansion and particles of Si atoms and ions with lower charges ejected after laser irradiation. Accordingly, spatial distributions are significantly different for each charged ion.

We have utilized pulsed supersonic helium gas jet and have performed X-ray absorption measurements of laser-ablated Si particles with pulsed supersonic helium gas bombardment. The results are shown in Fig. 4. The spectra in Figs. 4(a) and 4(b) have been taken at 15 J/cm^2 and at the position of 2.5 mm, and

at 15 J/cm^2 and 3 mm, respectively. In both cases, helium backing pressure is 9 kgf/cm^2. In Fig. 4(a), peaks of Si^{2+} ions produced by laser ablation with pulsed helium gas bombardment are higher than those without helium, whereas peak heights of Si^{+} ions produced with helium are lower than those without helium. This is clearly seen if we compare the $2s \rightarrow 3p$ transition of Si^{2+} at 155.6 eV. In Fig. 4(b), peaks of both Si^{+} and Si^{2+} ions with helium become smaller than those without helium. Particles produced without helium reach as high as 3.5 mm, while those produced with helium do not reach. Some changes between with and without helium are observed only at the positions more distant than 2.5 mm. At positions nearer than 2.5 mm, no changes are observed. Similar changes are also seen at 8 J/cm^2, but not at 4 J/cm^2.

This suggests that a higher-density region of helium gas is formed at the top of the plume of ablated particles, and free expansion of laser-ablated p articles is restrained by this helium cloud. This helium cloud is not formed in the case of lower energy densities. We believe that at lower energy densities, helium gas is pushed aside and no higher-density regions are formed.

Laser-ablated particles are considered to collide with helium, because the spatial distributions of laser ablated particles are changed between with and without supersonic helium gas. However, no remarkable absorption peaks of clusters have been measured. This indicates that the formation of clusters or growth of clusters occurs at times later than 120 ns.

References

1) A. Miyashita et.al., Time-Resolved Soft X-Ray Absorption Spectroscopy Apparatus Using Laser Produced Plasma X-ray, Proc. LAMP '92 1029-1034 (1992)

2) O. Yoda et.al., A Laboratory Scale Apparatus for the Time-Resolved X-ray Absorption Spectroscopy Using Laser Plasmas as an X-ray Source, Jpn. J. Appl. Phys. **32** Suppl.2 255-257 (1993)

3) K. Murakami et.al., LASER-PLASMA SOFT X-RAY ABSORPTION SPECTROSCOPY OF LASER-ABLATED Si AND C PARTICLES, AIP Conf. Proc. Vol.288 375-384 (1994)

4) T. Ohyanagi et.al., Time-and-Space Resolved X-ray Absorption Spectroscopy of Laser-Ablated Si Particles, Jpn. J. Appl. Phys. **33** 2586-2592 (1994)

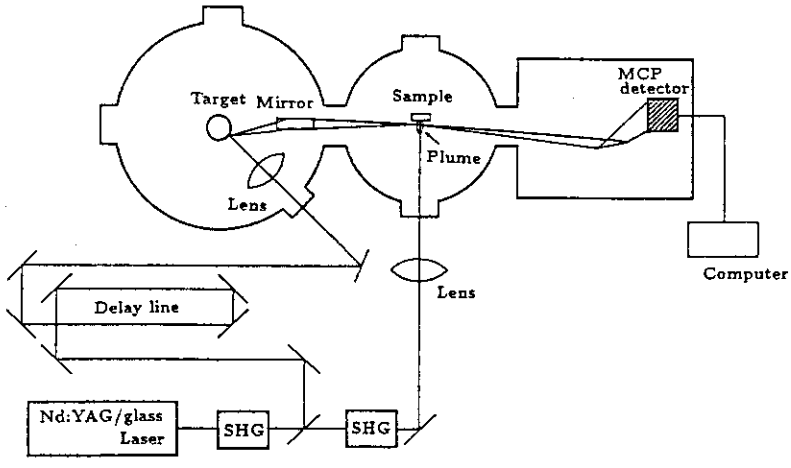

Fig. 1. Schematic diagram of the time-and-space resolved X-ray absorption spectroscopy apparatus.

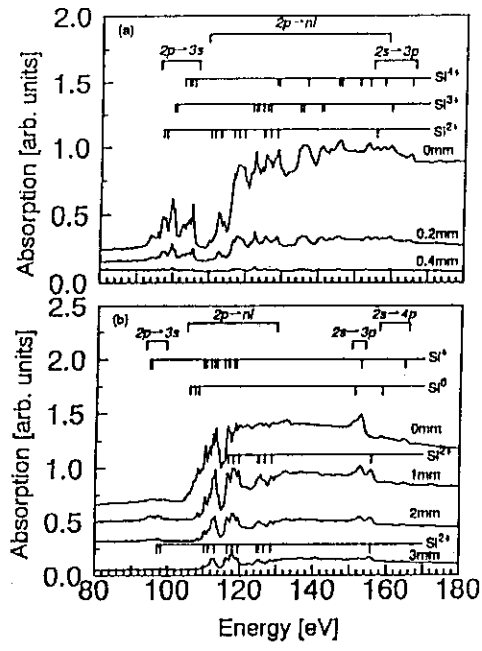

Fig. 2. Typical X-ray absorption spectra at an energy density of 20 J/cm^2 and a delay time of 0 ns (a), and at 10 J/cm^2 and a delay time of 120 ns (b).

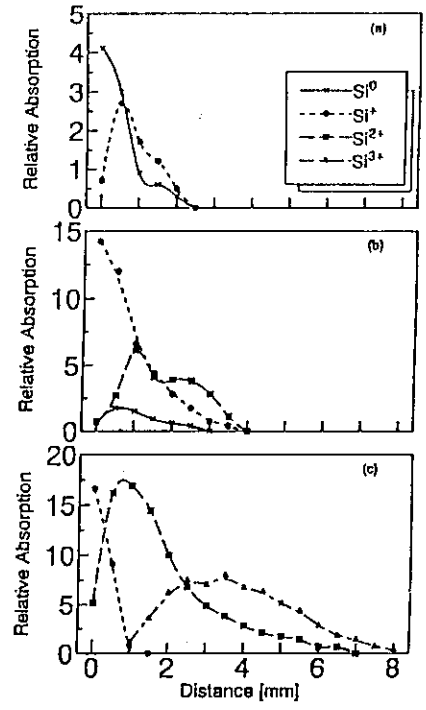

Fig. 3. Spatial distribution of ablated particles obtained from the peak heights of $2s \rightarrow 3p$ transitions of Si atom and ions. The energy density is 5 J/cm^2 and delay time is 120 ns (a), 10 J/cm^2 and 120 ns (b), and 20 J/cm^2 and 120 ns (c).

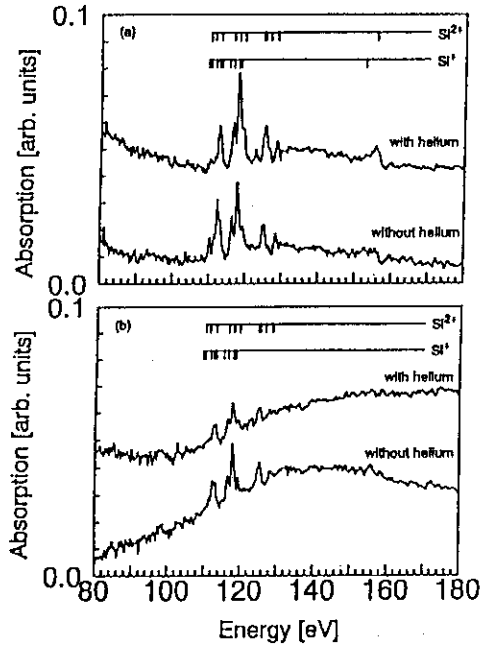

Fig. 4. X-ray absorption spectra of laser-ablated particles by supersonic helium gas bombardment. The energy density is 15 J/cm^2, the delay time is 120 ns. The measured positions are at 2.5 mm (a) and 3.0 mm (b).

6.9 CARBON THIN FILM GROWTH BY ION BEAM DEPOSITION

Hideki OHNO*, Yasushi AOKI and Siro NAGAI
Takasaki Radiation Chemistry Research Establishment, JAERI
*Department of Physics, Meisei University

INTRODUCTION

Much attention has recently been paid to ion beam deposition (IBD) of thin films employing low energy ($\leq$ 100 eV), mass and energy selected ion beam due to the fact that this technique may produce defect - and impurity - free crystalline films[1,2]. Although IBD is expected to be one of the promising techniques which allow us to control film growing process on atomic scale, our understanding is quite poor for the effects of various experimental parameters such as ion energy and current density, and temperature of substrate surface on the growing process of thin films. This report describes our study on the effect of ion energy on carbon film growth by in-situ Auger electron spectroscopy.

EXPERIMENT

The low energy ion beam deposition apparatus used in this study has been described in detail elsewhere[3]. Briefly, it consists of a Freeman-type ion source, a magnet for ion mass selection, and differentially pumped ion beam line attached to a UHV target chamber. The chamber is equipped with instrumentation for Auger electron spectroscopy (AES), ion scattering spectroscopy (ISS), secondary ion mass spectrometry (SIMS), and reflection high energy electron diffraction (RHEED). Efficient differential pumping of the beam line allows maintenance of the target chamber pressure in the order of 10^{-10} Torr.

Carbon ions (C^+) deposition with energy of 10 and 100 eV was carried out on Si(111) surface at room temperature in ca. 10^{-9} Torr. Ion current density was 1.1 ~1.3 $\mu A/cm^2$ at both energies. C^+ ions were extracted from the ion source using high purity CO_2 gas as the source material. The substrates used were 1.5×1.5 cm^2 samples of commercially prepared p-type Si(111) wafer. The samples were then cleaned by 3 keV Ar^+ ion bombardment.

The deposition and in-situ AES measurement were repeated in order to observe the growing process of deposited film. In the AES measurement, the energy of probing electrons was 3 keV and the observed energy range of secondary electrons was from 40 to 600 eV.

RESULTS AND DISCUSSION

Figure 1 shows a series of AES spectra for the 10 eV C^+ ion deposition on Si(111). Before deposition an intense Si_{LVV} peak at 92 eV is clearly observed in addition to a weak signal at 214 eV due to Ar atoms implanted during sputter cleaning. As the deposition dose is increased, the intensity of the Si peak is decreased and at the same time C_{KLL} peak at 273 eV appears and then increases in intensity, indicating carbon atoms deposition in the substrate surface. The line shapes of the carbon Auger electrons observed at dose of 6.9×10^{16}

and 2.8×10^{17} ions/cm^2 show the formation of carbidic and graphitic layers[4], respectively. Similar change in AES spectrum was observed in the deposition with 100 eV C^+ ions. The C_{KLL} line shape observed at dose of ~10^{15} ions/cm^2 showed the formation of a carbidic layer. For a rough estimation of the depositing rate, the carbon atomic concentration calculated with the AES spectra is plotted as a function of ion fluence for 10 eV and 100 eV C^+ ion beam deposition in Figure 2. This plot shows that the deposition rate with 10 eV ions is twice that with 100 eV C^+ ions. Depth profiling was performed on both the carbon films deposited with 10 and 100 eV C^+ ions, by repeated AES measurement after 3 keV Ar^+ ions sputtering. Throughout the measurement oxygen was not detected. As shown in Figure 3, although both the carbon films deposited by 10 eV and 100 eV C^+ ions have carbidic structure in the interface region and subsurface region, the carbon film deposited by 10 eV C^+ ions has a sharper interface with the substrate compared to the film by 100 eV C^+ ions. There results show that difference in C^+ energy gives rise to the difference in deposition rate and interface structure which may influence the growing process and structure of carbon films.

References

1) Kevin G. Orrman-Rossiter, Amir H. Al-bayati, D.G. Armour, S.E. Donnelly and J.A. van den Berg, Nucl. Instr. and Meth., B59/60, 197(1991).

2) Y.Lifshitz, S.R. Kasi and J.W. Rabalais, Phys. Rev., B41, 10468(1990).

3) H.Ohno and S. Nagai, Proc. Symposium on Beam Engineering of Advanced Material Syntheses, Tokyo, Nov. 24-26,(1992), 261.

4) For instance, see Haas, T.W., Grant, J.T. and Dooley, G.J., J. Appl. Phys., 43, 1853(1972).

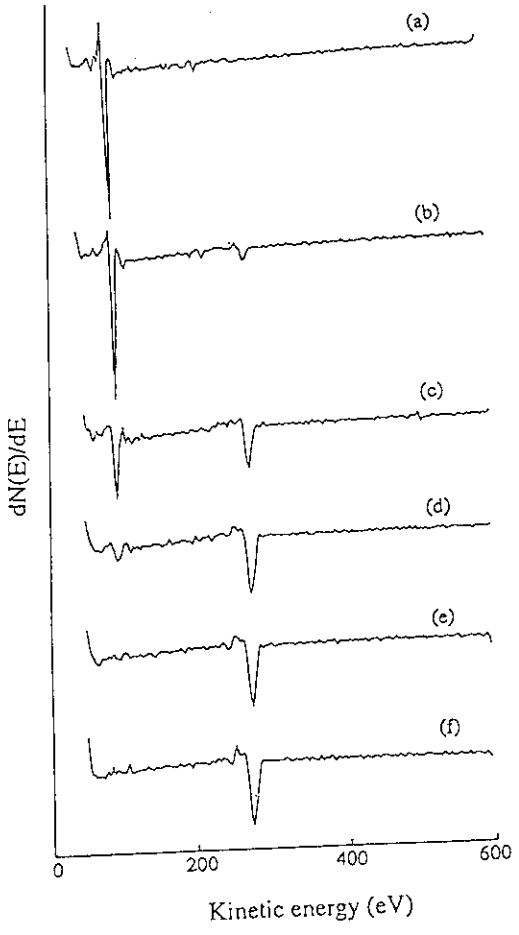

Fig. 1 Change of AES spectra for 10 eV C^+ deposition on Si(111). The fluences in ions/cm^2 are (a) 0 (clean surface), (b) 3.3×10^{16}, (c) 1.3×10^{16}, (d) 6.9×10^{16}, (e) 1.2×10^{17}, (f) 2.8×10^{17}.

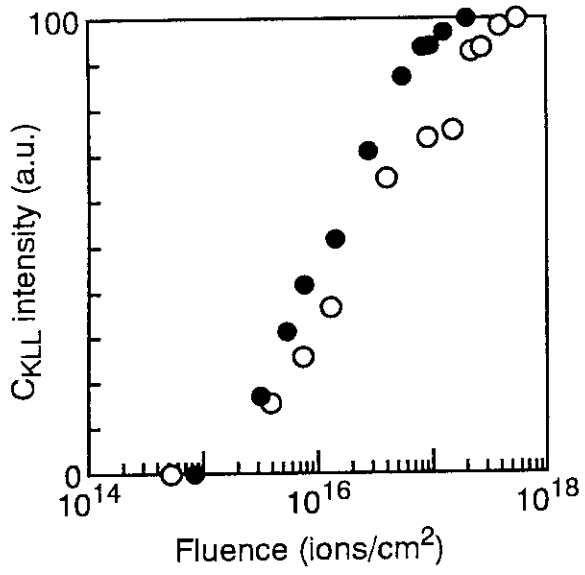

Fig. 2 Intensity of C_{KLL} as a function of C^+ fluence of 10 eV (○) and 100 eV (●) C^+ ions on Si(111).

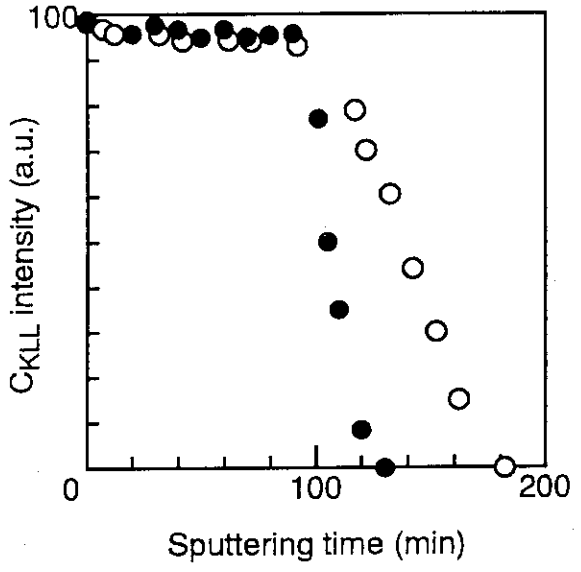

Fig.3 The depth profiles of carbon deposited by 10 eV (○) and 100 eV (●) C^+ ions on Si(111) measured by 3 keV Ar^+ sputtering and AES.

6.10 The charge states of metals implanted into oxide ceramics

Y. Aoki, T.Futagami*, O. Yoda and S. Nagai

Department of Materials Development,Takasaki Radiation Chemistry Research Establishment, JAERI. *Institute for Cosmic Ray Research, the University of Tokyo

Ion Implantation in ceramic materials has been studied in order to modify the near-surface properties, such as hardness, whose changes are considered to be correlated with the micro-structure of damage created by ion implantation[1-3]. On the other hand, the charge state of the implanted ions can be associated with the latticedefectscreated near the end of ion range, since the implaned ions can interact the lattice defects. Charge states of ^{57}Fe and ^{119}Sn implanted in α-Al_2O_3 and MgO were measured by conversion electron Mössbauer spectroscopy(CEMS)[4-8], while charge states of Zr and Cu ions implanted in α-Al_2O_3 were investigated by XPS[9-11]. We have studied the charge states of Cu and Cr ions implanted in MgO and α-Al_2O_3 by XPS[12-13]. In this report, consideration about the dependence of charge state on concentration of implanted ions using the simple statistical model proposed by Perez et al. is described.

Single crystals of (100) MgO and (0001) α-Al_2O_3 with an optical polish were used as implantation substrates. Ion implantation was performed at room temperature with an ion implanter (Danphysik). Irradiation energy and current density were 200 keV and 1.5-3.0 $\mu A/cm^2$, respectively. During the implantation, normals to sample surfaces were inclined by about 5° from a direction in a beam in order to avoid channeling effects. Ion beams were scanned to get uniform implantation doses over the sample surfaces(10mm X 5mm).

The XPS measurements were performed by an ESCA LAB-MKII (VG, Scientific Co.). An etching method with a 4 keV Ar ion gun was used under the pressure of 1 X 10^{-7} Torr, and the depth dependence of XPS spectra was obtained. The charge state of implanted Cr ions were determined using chemical shift (2.2 eV) of the Cr^{3+} $2p_{3/2}$ photoelectrons from the Cr^0 $2p_{3/2}$ photoelectrons.

From our previous work[12], Cr ions implanted in α-Al_2O_3 and MgO were trapped as Cr^0 and Cr^{3+}. The fractions of Cr^{3+} and Cr^0 at each depth were calculated by separation of the Cr $2p_{3/2}$ XPS peak into two peaks of Cr^0 and Cr^{3+}. The fractions of Cr^0 and Cr^{3+} were plotted agaist $(Cr^{3+} + Cr^0)$/Al or $(Cr^{3+} + Cr^0)$/Mg in Figs. 1(a) and 1(b). The fraction of Cr^0 monotonically increased with the Cr/Al or Cr/Mg ratio, while the Cr^{3+} fraction monotonically decreased. The trend was similar to the case of Fe ion implantation in MgO and α-Al_2O_3[4,14]. The fraction of Fe^0 increase with the concentration of Fe, while the fraction of Fe^{2+} or Fe^{3+} decreased.

The simple statistical model by Perez et al.[4] was applied to our experimental results. The curves in Fig.1(a) and (b) represent the probability fuction $P_N(n, x)$, where x denoted Cr/Al or Cr/Mg. The fit in α-Al_2O_3 was obtained for N=13, where N=13 is the number of nearest cation

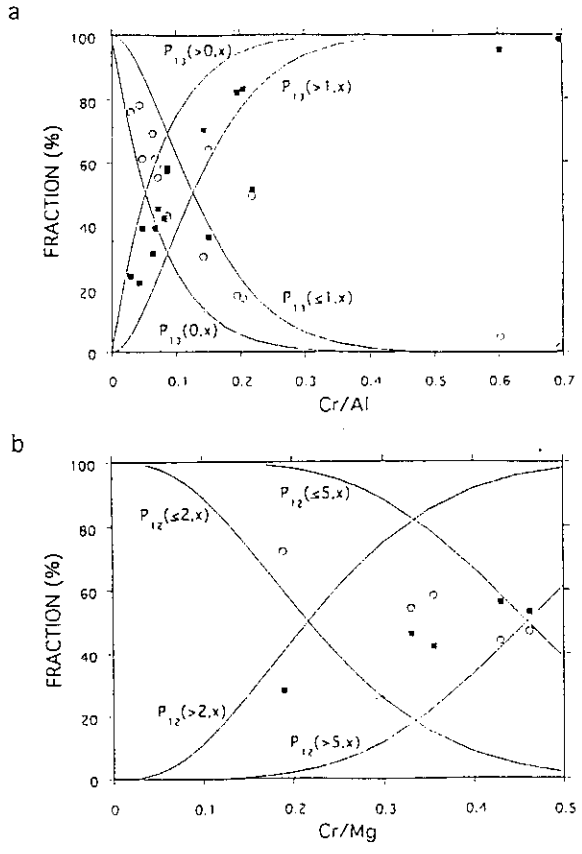

Fig. 1 Fraction of Cr^0 and Cr^{3+} vs. the concentration of implanted Cr ions in (a)α-Al_2O_3 and (b) MgO. The symbols of open circles and filled squares represent data points for Cr^{3+} and Cr^0, respectively. The curves represent the probability function $P_N(n, x)$ defined by Perez et al.(4).

neighbors in four coordination shells for one cation atom in α-Al_2O_3 lattice[14]. As seen in Fig.1(a), most of data for Cr^{3+} in α -Al_2O_3 are included in a region separated by the two curves $P_{13}(0, x)$ and $P_{13}(1, x)$. It is implied that isolated atoms and a portion of dimers were trapped as Cr^{3+}, while the rest dimers, timers and other polymers were trapped as Cr^0. On the other hand, the fit for data of Cr in MgO was obtained for N=12, where N=12 is the number of nearest cation neighbors in MgO structure[4]. The data of Cr^{3+} in MgO are included in a region separated by the two curves $P_{12}(2, x)$ and $P_{12}(5, x)$. This implies the isolated atoms, dimers, and trimers were trapped as Cr^{3+}, although the results coud not be simply interpreted.

References

(1) H. Naramoto, C.J. McHargue, C.W. White, J.M. Williams, O.W. Holland, .M. M. Abraham and B.R. Appleton, Nucl. Instr. and Meth. 209/210 (1983) 1159.

(2) P.J. Burnett and T.F. Page, J. Matter. Sci. 19 (1984) 3524.

(3) T. Hioki, A. Itoh, S. Noda, H. Doi, J. Kawamoto and O. Kamigaito, Nucl. Instr. and Meth. B7/8 (1985) 521.

(4) A. Perez, G. Marest, B.D. Sawicka, J.A. Sawicki and T. Tyliszczak, Phys. Rev. B28 (1983) 1227.

(5) C.J. McHargue, G.C. Farlow, P.S. Sklad, C.W. White, A. Perez, N. Kornilios and G. Marest, Nucl. nstr. and Meth. B19/20 (1987) 813.

(6) J.A. Sawicki, G. Marest, B. Cox and S.R. Julian, Nucl. Instr. and Meth B32 (1988) 79.

(7) J. Kowalski, J. Stanek and T. Tyliszszak, Nucl. Instr. and Meth. 209/210 (1983) 1145.

(8) C.J. McHargue, P.S. Sklad, J.C. McCallum, C.W. White, A. Perez, E. Abonneau and G. Marest, Nucl. Instr. and Meth. B46 (1990) 74.

(9) C. Donnet, H. Jaffrezic, N. Moncoffre, J. Tousset and G. Fuchs, Nucl. Instr. and Meth. 46 (1990) 89.

(10) C. Donnet, G. Marest, N. Moncoffre, J. Tousset, A. Rahioui, C. Esnouf and M. Brunel, Nucl. Instr. and Meth. B59/60 (1991) 1205.

(11) T. Miyano, T. Matsumae, H. Yoko-o, Y. Andoh, M. Kiuchi and M. Satou, Nucl. Instr. and Meth. B59/60 (1991) 1167.

(12) T. Futagami, Y. Aoki, O. Yoda, S. Nagai and D.M. Rück, Nucl. Instr. and Meth. B80/81 (1993) 1168.

(13) T. Futagami, Y. Aoki, O. Yoda and S. Nagai, Nucl. Instr. and Meth. B88 (1994) 261.

(14) C.J. McHargue, P.S.Sklad, C.W. White, G.C. Farlow, A. Perez, N. Kornilios and G. Marest, in: Materials Modification by High-Fluence Iob Beams, eds. R. Kelly and M.F.Silva (Kluwer Academic, 1989) p.245.

7. Nuclear Chemistry and Radioisotope Production

7 . 1 Development of Radioisotopes: Production of Carrier-Free ^{186}Re and Aqueous ^{18}F

N. Shigeta, H. Matsuoka, A. Osa, M. Koizumi, M. Izumo, K. Kobayashi, K. Hashimoto and T. Sekine
Department of Radioisotopes, JAERI

1 Introduction

Rhenium-186(^{186}Re), which is chemically an element of the group of manganase in the periodic table, is expected to behave physiologically like ^{99m}Tc. In addition, ^{186}Re is considered to be useful for various applications in radioimmunotherapy due to its attractive properties which include emission of high-energy β-rays ($E_{\beta,max}$ = 1.07 MeV), an appropriate half-life ($T_{1/2}$ = 3.8 d) and decay to stable daughter. Previous investigations of production of ^{186}Re have dealt almost exclusively with a neutron capture reaction in a reactor.[1),2)]

The present investigation was undertaken to produce a carrier-free ^{186}Re with the ^{186}W(p,n)reaction at the AVF cyclotoron in TIARA, and the excitation function was measured for this reaction.

The radionuclide ^{18}F($T_{1/2}$ = 110 min) has been widely used for diagnosis of various diseases by positron emission tomography (PET). Typical methods of ^{18}F production are the ^{20}Ne(d,α)^{18}F and ^{18}O(p,n)^{18}F reactions. We have developed a method of production of high-purity ^{18}F in water by the ^{16}O(α,pn)^{18}F reaction, taking advantage of a high-energy α beam available from the AVF cyclotron. The production of ^{18}F in water was initiated in order to study material transfer inside plants.

2 Production of ^{186}Re

2.1 Excitation function of the ^{186}W(p,n)^{186}Re reaction

In order to estimate the yield of ^{186}Re, the excitation function of the ^{186}W(p,n)^{186}Re reaction were measured up to 20 MeV using the stacked-foil technique. Targets were irradiated with proton beams of 0.1-0.5 μA for 10-30 minutes. The foil's activities were assayed by γ-ray spectrometry using a calibrated Ge detector. Figure 1 shows the experimental excitation function of the ^{186}W(p,n)^{186}Re reaction. It was found that the excitation function peaks at 10 MeV with a pronounced tailing on the high-energy side.

2.2 Production of ^{186}Re from an enriched [^{186}W]WO_3 target

A 99.79%-enriched [^{186}W]WO_3 powder was used as a target. It was pressed at 680 kg/cm^2 into a disk-shaped pellet, which was 1 mm thick by 10 mm diameter with a thickness of 580 g/cm^2, and then baked at 900°C for 24h.

The target was irradiated with 13.6 MeV protons at a beam current of approximately 3μA. The irradiation continued for a period of 5h. After irradiation the target was removed from the irradiation port and transported on a truck to the hot cell.

The chemical separation method used in this work is shown schematically in Fig.2. The WO_3 disk was dissolved in 30 mℓ of 1M NaOH, after being heated to 98°C. The ^{186}Re separation was accomplished by an anion exchange method with the resin DIAION SA‡100 (100-200 mesh). The

resin was contained in a 10 mm-diameter column. The solution was loaded on the column which was then washed with 70 mℓ of 0.5M NaOH : 0.5 M NaCl solution and then 25 mℓ of 1.5M HCl at a typical flow rate of 1.5 mℓ/min. This served to remove ^{187}W and ^{183}Ta as well as the stable tungsten, as shown in Fig.3. The ^{186}Re was eluted from the column with 80 mℓ of 4 M HNO_3 and was recovered in approximately 90% yield.

The ^{186}Re solution was concentrated on a hot plate near to dryness and dissolved in 5 mℓ of water. The addition of 5 mℓ of water and the evaporation of the solution to dryness was repeated once more. Finally, the rhenium activity was dissolved in 5 mℓ of saline and an aliquot of the solution was taken for γ-ray analysis with a Ge detector.

The final solution was obtained under the yield of 6.51 MBq at the end of bombardment and the radiochemical purity was more than 99%. On the basis of these results, the next step is to study production of ^{186}Re on a large scale and synthesis of labelled compounds with carrier-free ^{186}Re.

3 Production of aqueous ^{18}F

^{18}F was produced by the ^{16}O(α,pn)^{18}F reaction in a 6 ml ultra-pure water using the irradiation system, as shown in Fig.4. The target water was irradiated with a 46 MeV α beam of a current of 1 μA for 40 min.

The irradiated target was transferred on a truck to the hot laboratory and taken out by the syringe for a plant experiment. The yield of ^{18}F in water was found to be 88 MBq at the end of bombardment. No other radioactivity was detected in the final solution. No damage ascribable to the α-beam irradiation was found on the window of the target holder.

We may claim that the irradiation system is not difficult to operate and the product can be treated in safety at subsequent experiments. Another merit of this method is that there is no loss of the radioactivity through the transfer from the irradiation port to the hot laboratory.

1) J. M. H. de Klerk, et.al., J. Nucl. Med., 33, 646(1992).
2)Breiz H. B., et.al., J. Nucl. Med., 33, 1099(1992).

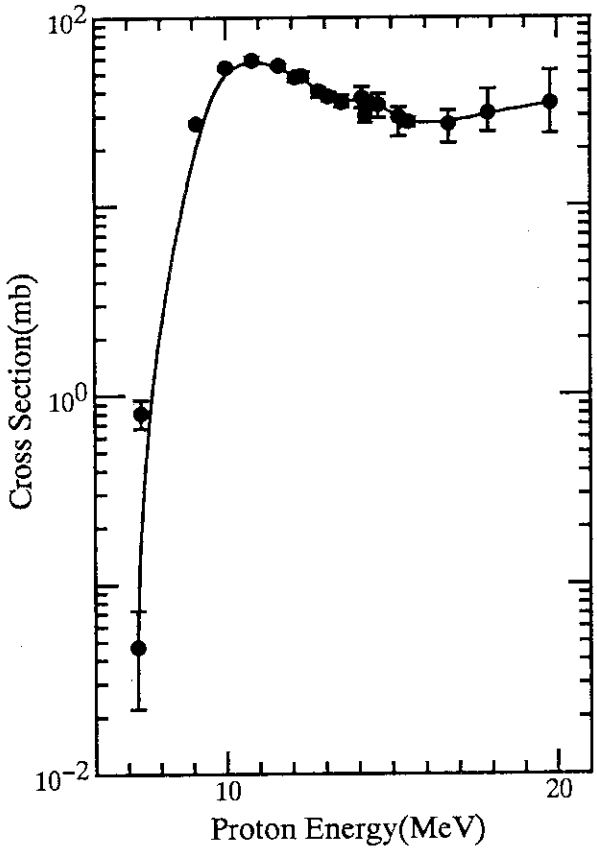

Fig.1 Excitation function for the ^{186}W(p,n)^{186}Re reaction.

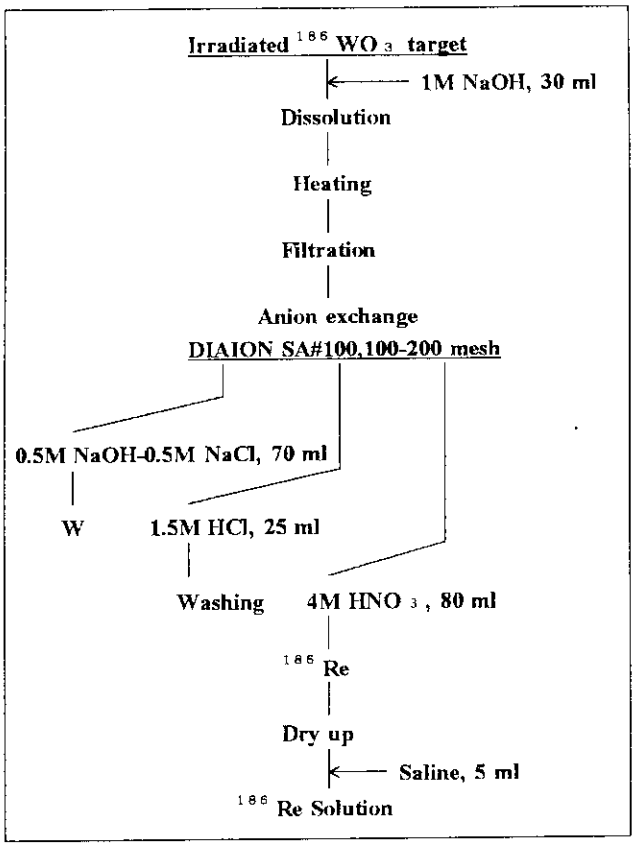

Fig.2 Chemical procedure of the separation of ^{186}Re from a WO_3 target.

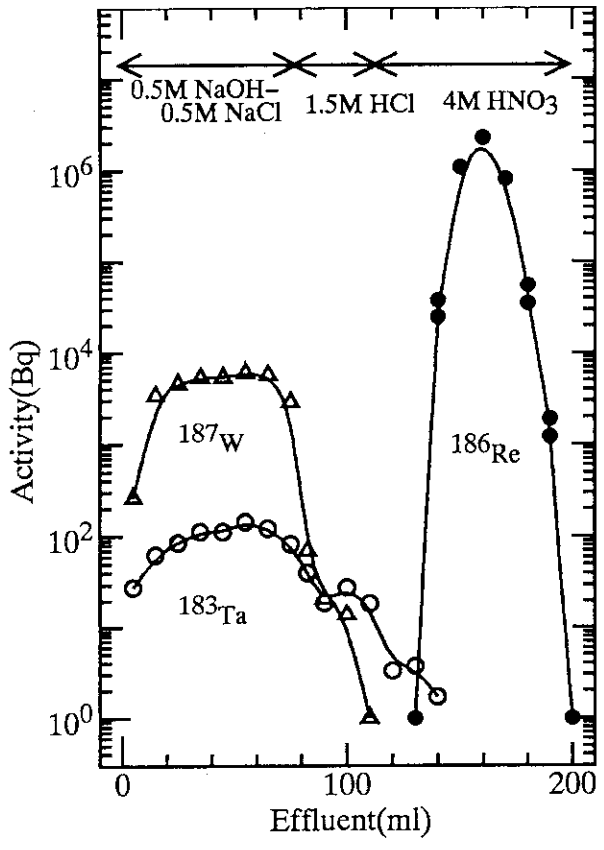

Fig.3 Elution curve of ^{186}Re by anion exchange.

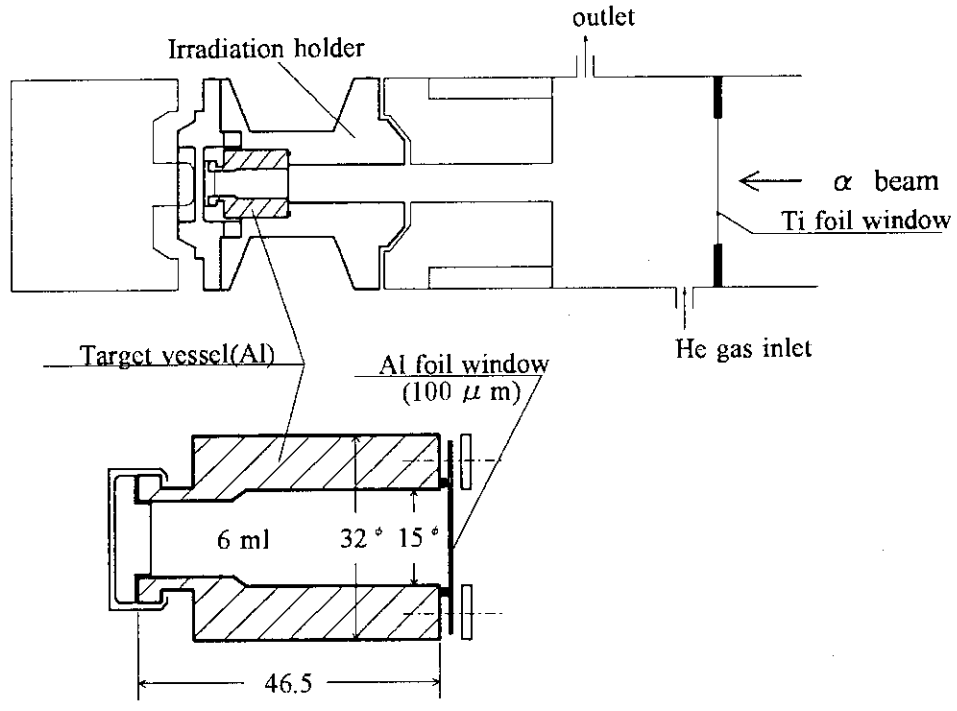

Fig.4 Irradiation system for the production of aqueous ^{18}F.

7.2 Identification of the new isotope ^{127}Pr

Toshiaki SEKINE, Akihiko OSA, Mitsuo KOIZUMI,
Shin-ichi ICHIKAWA, Masato ASAI,* Hiroshi YAMAMOTO*
and Kiyoshi KAWADE*
Department of Radioisotopes, JAERI and
*School of Engineering, Nagoya University

Introduction

The isotope separator connected on line to the AVF cyclotron accelerator has been used for the decay study of neutron deficient praseodymium isotopes. The decay properties of ^{127}Pr are not reported in literature, although the isotope is considered to be within the proton drip line and its precursor ^{127}Nd is identified by detecting β-delayed protons [1]. It is partly because the β-delayed proton emission of ^{127}Pr is not strong enough to detect a weak radioactivity [2].

The present work aims at identifying the ^{127}Pr isotope and investigating the level structure of ^{127}Ce by means of γ-ray measurements on mass-separated sources.

Hold-up time measurement

For ionization of praseodymium isotopes, a surface ionization type ion source was used [3, 4]. It is important for an isotope separator on-line that the time interval between production of radioisotope and radioactivity measurement is kept as short as possible. We measured the intensity of a mass-separated beam before and after the accelerator beam stopped. It was confirmed that the intensity of a mass-separated beam decreased exponentially after the accelerator beam was switched off and production of the nuclide of interest stopped. As a result, a delay half-time of the radioactivity after switching off the accelerator beam was obtained; the value of $T_{1/2}^{del}/\ln 2$ should be considered as a mean hold-up time in the ion source.

In an experiment, the accelerator beam bombearded the target during 64 s. The accelerator beam was switched on and off by using a movable Faraday cup. Before and after the accelerator beam stopped, the mass-separated beam was collected at an aluminized Mylar tape and transferred to a detection port equipped with a coaxtial n-type germanium detector. In a cycle, a γ-ray spectrum measurement was repeated sixteen times. Events were accumulated by repeating the cycle several ten times.

Figure 1 shows a profile of a mass-separated beam of ^{130}Pr at 2600 K. Two components of delay half-times $T_{1/2}^{del}$ were observed: 4.3 s and 22 s. The existence of the fast component suggested a possible separation of the praseodymium isotope ^{127}Pr whose half-life is predicted to be 15.1 [5, 6], 6.29, 15.5 and 9.27 s [7].

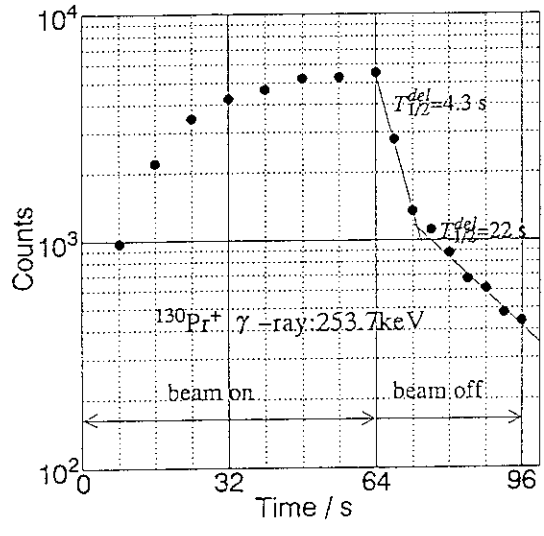

Fig. 1. A release profile of the ^{130}Pr$^+$ ion at an ion source temperature of 2600 K.

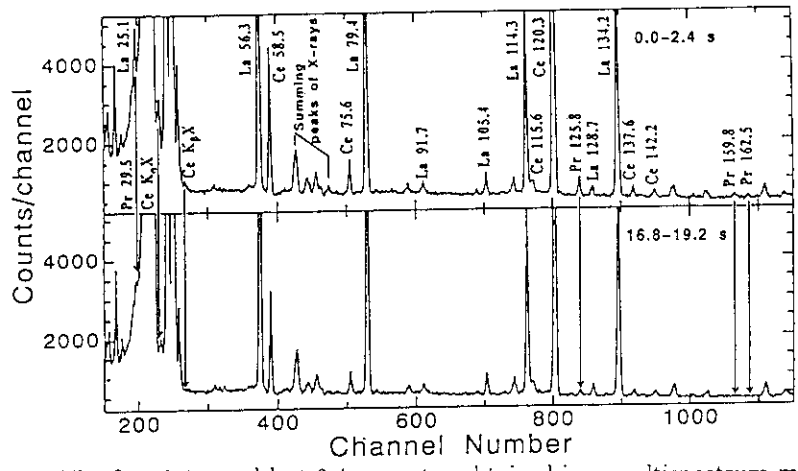

Fig. 2. The first 2.4-s and last 2.4-s spectra obtained in a multispectrum-mode measurement of the oxide-ion beam for A=127.

Identification of ^{127}Pr

The ^{94}Mo(^{36}Ar,p2n)^{127}Pr reaction was used to produce ^{127}Pr. A 5.4 MeV/u ^{36}Ar beam from the AVF cyclotron was directed through a 2.2 μm thick Harvar-foil window onto a 3.08 mg/cm^2 thick molybdenum foil, enriched in ^{94}Mo to 93.9 %. The recoiling products passing through an ion source window made of 1.5 mm thick tantalum were caught into 0.1 mm thick tantalum catcher. The products ionized as metallic or oxide ions [3] were mass-separated in a magnetic field as 40 keV beam.

In order to investigate β-, γ- and X-rays, the mass 127 (metallic ion) or 143 (oxide ion) beam was directed onto an aluminized Mylar tape in a tape-transport system. After collecting for a preselected time period, the radioactivity was transported to a canal made of thin stainless steel into the counting position. The counting position was equipped with a plastic scintillator for β-detection, and a planar germanium detector and a coaxial n-type germanium detector for γ- and X-ray detection. Using the detectors, γ-singles, β-gated γ and $\gamma\gamma$-coincidence measurements were performed. For the planar detector, the γ-singles data were taken also in a multispectrum mode in which the 19.2 s counting time was divided into sixteen 1.2 s intervals. The data were accumulated 10 h for the oxide-ion beam and 0.5 h for the metallic-ion beam.

Figure 2 shows γ-ray spectra of the oxide-ion beam, obtained with the planar detector; the first 2.4 s and last 2.4 s spectra recorded in the multispectrum mode are compared for energies up to 200 keV. From the spectra, short-lived γ-rays were found at 30, 126, 160 and 162 keV. These γ-rays are not attributed to the decay of ^{127}La and ^{127}Ce, which were included in the oxide-ion beam. The energies and intensities of the new γ-rays are listed in Table 1. The observation of the cerium X-rays indicates that the new γ-rays are associated with the β^+/EC decay of ^{127}Pr and/or the isomeric transition of ^{127}Ce.

The time decay curves of the new γ-rays were plotted in Fig. 3 together with that of the cerium K_αX-ray. It is seen that the γ-rays and cerium X-ray decayed with almost the same half-lifves. The mean half-life value of the γ- and X-ray was found to be 7.7$\pm$0.6 s.

Table 1 γ-rays associated with the decay of ^{127}Pr and their coincidence relationship

Energy (keV)	Relative intensity	Coincidence relation
29.53(5)	1.02(12)	
125.82(5)	1.00(12)	162.49, $\gamma^{\pm}$, Ce X-ray
159.81(7)	0.50(7)	$\gamma^{\pm}$, Ce X-ray
162.49(5)	0.32(6)	125.82, $\gamma^{\pm}$, Ce X-ray

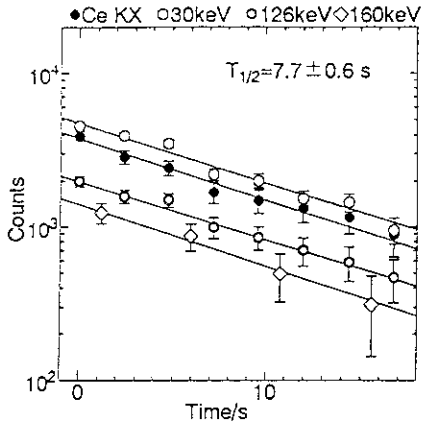

Fig. 3. The time decay curves of new γ-rays and the K_αX-ray, obtained from the measurement of the oxide-ion beam for A=127.

The coincidence relations obtained were summarized also in Table 1. It was confirmed that the new γ-rays, except for the 30 keV line, the cerium X-rays and β-ray were coincident with each other. This fact excludes the possibility that the radiations with the 7.7 s half-life were ascribable to the isomeric transition of ^{127}Ce.

On the basis of the experimental results, we propose the partial decay scheme of ^{127}Pr as shown in Fig. 4. The possible spins of the levels in ^{127}Ce were given by assuming that the three levels are members of the rotational band with K=5/2 and the inertial parameter $\hbar^2/2\Im$ = 18.01±0.04 keV.

The half-life of ^{127}Pr obtained can be compared with theoretically predicted values. One can see that the theoretical half-lives are in agreement with the experimental value within a factor of two.

Table 2 Experimental and theoretical β-decay half-lives of ^{127}Pr

Half-life/s		Mass-formula
Present work	Theory	
7.7(6)	15.1	Tachibana *et al.*[a]
	6.29	Hilf *et al.*[b]
	15.5	Groote *et al.*[b]
	9.27	Möller and Nix[b]

[a]Calculated with the revised gross theory [5, 6].

[b]Calculated with a proton-neutron quasiparticle random-phase approximation (pn-QRPA) model[7].

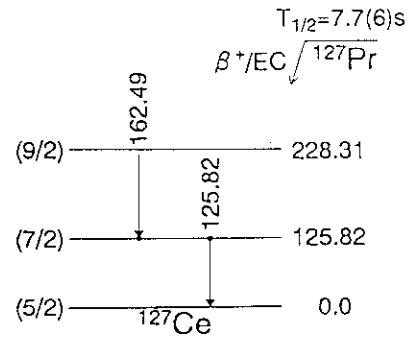

Fig. 4. The proposed partial decay scheme of ^{127}Pr.

References

[1] P.A. Wilmarth, J.M. Nitschke, R.B. Firestone and J. Gilat, Z. Phys., **A325**, 485 (1986).

[2] J.M. Nitschke, M.D. Cable and W.-D Zeitz, Z. Phys., **A312**, 265 (1983).

[3] S. Ichikawa, T. Sekine, H. Iimura and M. Oshima, Nucl. Instr. Meth. **A274**, 259 (1989).

[4] S. Ichikawa, T. Sekine, H. Iimura and M. Oshima, Nucl. Instr. Meth. **B70**, 156 (1992).

[5] T. Tachibana, M. Yamada and K. Nakata, Report of Science and Engineering Research Laboratory, Waseda University, No.88-3 (1988); No.88-4 (1988).

[6] T. Tachibana, M. Yamada and Y. Yoshida, Prog. Theor. Phys. **84**, 641 (1990).

[7] M. Hirsch, A. Stdaut, K. Muto and H.V. Klapdor-Kleingrothaus, At. Data Nucl. Data Tables, **53**, 165 (1993).

7.3 Determination of the Change of the Nuclear Charge Radius in the 81 keV Transition of ^{133}Cs by Conversion-Electron and Mössbauer Spectroscopy

H.Muramatsu, H.Ito, M.Misawa, T.Miura[2], T.Sekine[3], M.Koizumi[3], A.Osa[3], M.Yanaga[4], K.Endo,[5], H.Nakahara[6], M.Fujioka[7]

Faculty of Education, Shinshu University, National Laboratory for High Energy Physics[2], Takasaki Establishment, JAERI[3], Jikei University School of Medicine[4], Showa College of Pharmaceutical Sciences[5], Faculty of Science, Tokyo Metropolitan University[6], CYRIC, Tohoku University[7]

Since there exist Mössbauer nuclei in typical elements of the fifth period (Sn, Sb, Te, I, Xe), it is possible to systematically study chemical bindings and electronic states of these different elements. The Mössbauer isomer shift arises from the Coulomb interaction between the nuclear and electronic charge distributions. If it is assumed that a nucleus is a sphere of charge with a radius of R in the ground state, and the electron density at the nuclear origin $\rho(0)$ over the nuclear volume is constant, the isomer shift δ can be written as

$$\delta = (4/5)\pi Ze^2R^2(\Delta R/R)\Delta\rho(0),$$

where Z is the nuclear charge, e the electronic charge, $\Delta R/R$ the relative difference of the nuclear charge radius between the excited and ground states, $\Delta\rho(0)$ the difference of the total electron density at the nucleus between the absorber and the source materials, respectively. Thus, an exact knowledge of $\Delta R/R$ is essential for a quantitative interpretation of the isomer-shift data in terms of a change of the electron density. During the last decade, the determination of the $\Delta R/R$ values for ^{119}Sn, ^{125}Te and ^{121}Sb has been carried out by the present authors.[1-3] In this report, the preliminary observation for the determination of $\Delta R/R$ in the 81 keV transition of ^{133}Cs is described while focusing on a measurement of the internal-conversion electrons.

Experimental

The implantations of ^{133}Xe($T_{1/2}$=5.25 d) were carried out at a terminal voltage of 20 kV using the electro-magnetic isotope separator of JAERI at Takasaki. Radioactive ^{133}Xe gas was purchased from LMRI(France) with a carrier gas of nitrogen. The target materials were an aluminium foil of 250 μm thickness with a purity of 99.999% and a zinc foil of 250 μm thickness with a purity of 99.99%. The Mössbauer spectrum was measured while keeping both the source and absorber at liquid-helium temperature, using a single-line absorber, CsCl with 360 mg/cm^2 Cs thickness. The 81keV γ-rays of ^{133}Cs from the implanted source were detected with a pure germanium low-energy photon spectrometer (LEPS). A constant acceleration drive with a triangular velocity shape was used at ± 4 mm/s.

The internal-conversion electron spectra of ^{133}Cs were measured with a 75 cm radius, double-focusing, $\pi\sqrt{2}$ iron-free β-ray spectrometer at INS(the University of Tokyo). For measurements of the internal-conversion electrons in the region of the K-line, L-lines and M-,N-,O- and P-lines of the 81 keV transition, a single wire proportional counter with a front side window of 1 μm-thick Al coated propylene film was used as a focal plane detector. The central wire was a carbon coated silica filament which has 8 kΩ/mm.[4,5] A momentum range of about 4% could be measured simultaneously. The gas pressure was controlled using an automatic gas flow and pressure control system, and isobutane was flowed as a counter gas. The source was covered with two aluminium slits for defining the source dimensions to 1.0 X 20 mm^2.

Results

The source strengths of the implanted samples were determined to be 27 μCi for Al and 9.6 μCi for Zn, respectively, by measuring 81-keV γ-rays with a LEPS. They were not enough to measure a Mössbauer spectrum strong. Fig.1 shows the conversion-electron spectra in the region of L-lines and M-,N-,

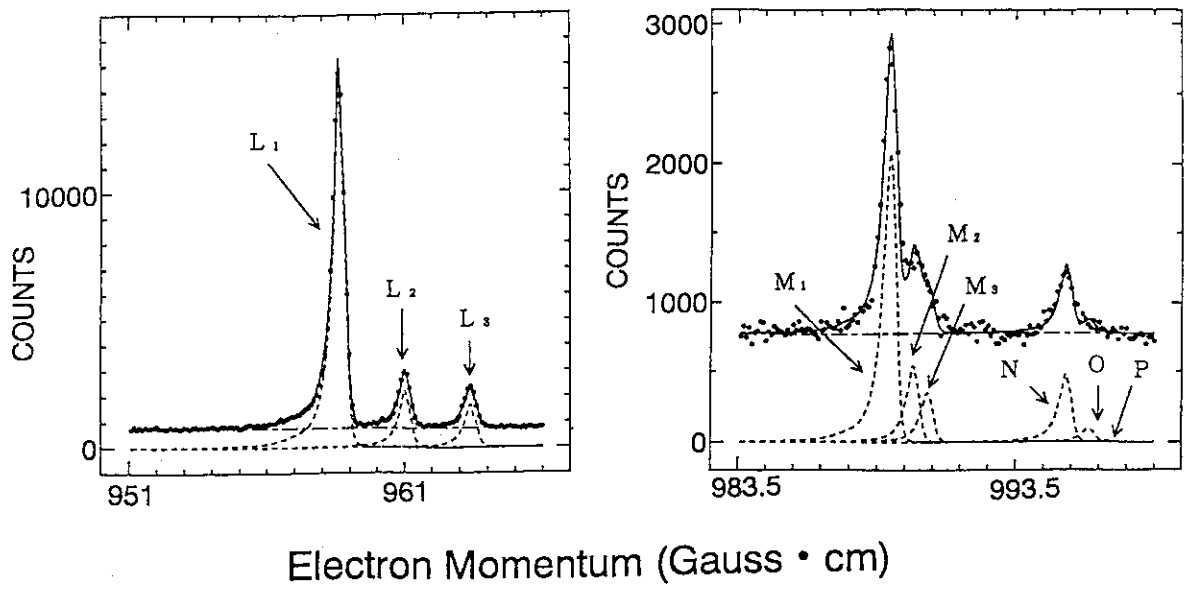

Fig.1 Conversion electron spectra of the 81 keV(M1+2.8%E2) transition in ^{133}Cs implanted into Al. The points are the observed counts which include β−continuum and background rates.

O+P−lines of the 81 keV transition in ^{133}Cs. The momentum resolution was 0.05%, though the spectrometer resolution was set at 0.03% momentum resolution. The conversion spectra were analyzed by a least−squares fitting using the computer code ACSEMP[6], which employs numerical line shapes and adjusts them in the process of peak fitting following the rule of constant tail−fraction, in addition to the adjustment of line positions. Comparison with the theoretical conversion coefficients of Rösel et al.[7] and with the experimental line intensities by Siegbahn et al.[8] indicated that the present values for the inner shells are almost in agreement with them. Due to the poor resolution, O− and P−lines, which should be the most important part to examine the chemical effect on the conversion electron intensities, could not be resolved at all. Judging from the fact that the energy difference between the O_I− and P_I−lines is only 23 eV, more than 0.03% momentum resolution must be achieved in order to measure these conversion electrons separately.

The research and development for a new−type focal−plane detector are in progress to realize over 0.03% momentum resolution around an electron energy of about 80 keV. Furthermore, in order to obtain a strong radioactive source (more than 100 μCi), we are planning to use a ^{133}Xe gas with higher specific activity.

References

1) H.Muramatsu, T.Miura, H.Nakahara, M.Fujioka, E.Tanaka and A.Hashizume, Hyp. Int.**20**(1984)305
2) T.Miura, Y.Hatsukawa, M.Yanaga, K.Endo, H.Nakahara, M.Fujioka, E.Tanaka and A.Hashizume, Hyp. Int. **30**(1986)371
3) M.Yanaga, K.Endo, H.Nakahara, S.Ikuta, T.Miura, M.Takahashi and M.Takeda, Hyp. Int. **62**(1990)359
4) Y.Fujita, H.Kawakami and M.Hosoda, Genshikaku Kenkyu, **24**(1979)66
5) Y.Fujita, H.Kawakami and M.Hosoda, Nucl. Instr. Methods, **196**(1982)271
6)M.Fujioka and M.Takashima, J. Phys.**40**(1979)C2,32
7)F.Rösel, H.M.Fries, K.Alder and C.Pauli, Atom. Data and Nucl. Data Tables, **21**(1978)91
8)K.Siegbahn, C.Nordling, S.−E.Karlsson, S.Hagström, A.Fahlman and I.Andersson, Nucl. Instr. and Methods, **27**(1964)173

7.4 Decay Spectroscopy of Neutron-Deficient ^{125}Ce and ^{126}Ce Isotopes

M. Asai, Y. Kojima, A. Osa[1], M. Koizumi[1], T. Sekine[1],
H. Yamamoto and K. Kawade
School of Engineering, Nagoya University and
[1]Department of Radioisotopes, JAERI

Introducton

Neutron-deficient nuclei in the mass region of A=120∼130 exhibit various interesting behaviours on both collective motion and particle excitation, which have been revealed from their high-spin level structures systematically studied with in-beam γ-ray spectroscopy. However, there is less information about low-energy low-spin states for these nuclei, which is essential to refine theoretical calculations and to understand their nuclear structures.

Previously, we performed a series of spectroscopic studies on the decay of neutron-deficient Cs, Ba and La isotopes by using the on-line isotope separator, JAERI-ISOL[1]. This study was extended to Ce and Pr isotopes by using the TIARA-ISOL[2] connected to the JAERI AVF cyclotron.

In the present work, decay spectroscopy of ^{125}Ce and ^{126}Ce was performed to study low-lying states of ^{125}La and ^{126}La. Level schemes of ^{125}La and ^{126}La were partly constructed by Leigh et al.[3] and Nyakó et al.[4] with in-beam spectroscopy. In the decay of ^{125}Ce and ^{126}Ce, a few γ-rays were identified by Gilat et al.[5] and Genevey et al.[6], but the decay schemes were not reported.

Experimental

^{125}Ce and ^{126}Ce were produced by the reactions ^{92}Mo(^{36}Ar,2pn) and ^{94}Mo(^{36}Ar,2p2n), respectively, at a beam energy of 195 MeV. Isotopically enriched targets with a thickness of 3 mg/cm^2 were used. Reaction products were ionized in a surface ionization ion source and mass-separated as a monoxide ion[7]. Mass-separated products were collected on an aluminum-coated Mylar tape in a tape transport system and periodically transported to a measuring position, at a time interval of 7.4 s for ^{125}Ce and 49 s for ^{126}Ce.

At the measuring position, γ-ray singles, γ-γ coincidence and β-γ delayed coincidence measurements were simultaneously performed with a 33% n-type coaxial HPGe detector, a low energy photon HPGe detector (LEPS) with a diameter of 25 mm and a thickness of 15 mm, and a thin (1 mm thick) plastic scintillator. γ-ray singles spectra were also taken in a multi-spectrum scaling mode. In addition, γ-ray singles and γ-γ coincidence measurements were also performed at the collection position equipped with another two n-type coaxial HPGe detectors with relative efficiencies of 33% and 29%.

Results

Many γ-rays were identified to the decay of ^{125}Ce and ^{126}Ce from their half-lives and coincidence relations with La KX-rays. Figure 1 shows γ-ray singles spectra measured by the LEPS for A=125+16 and A=126+16, in which γ-rays assigned to the ^{125}Ce and ^{126}Ce decay are indicated with their energies.

The partial decay scheme of ^{125}Ce presented in Fig. 2 was constructed from γ-γ coincidence, γ-ray intensities and energy relationships. There are two distinct bands in this decay scheme. The first band on the right side of the Fig. 2 was unambiguosly

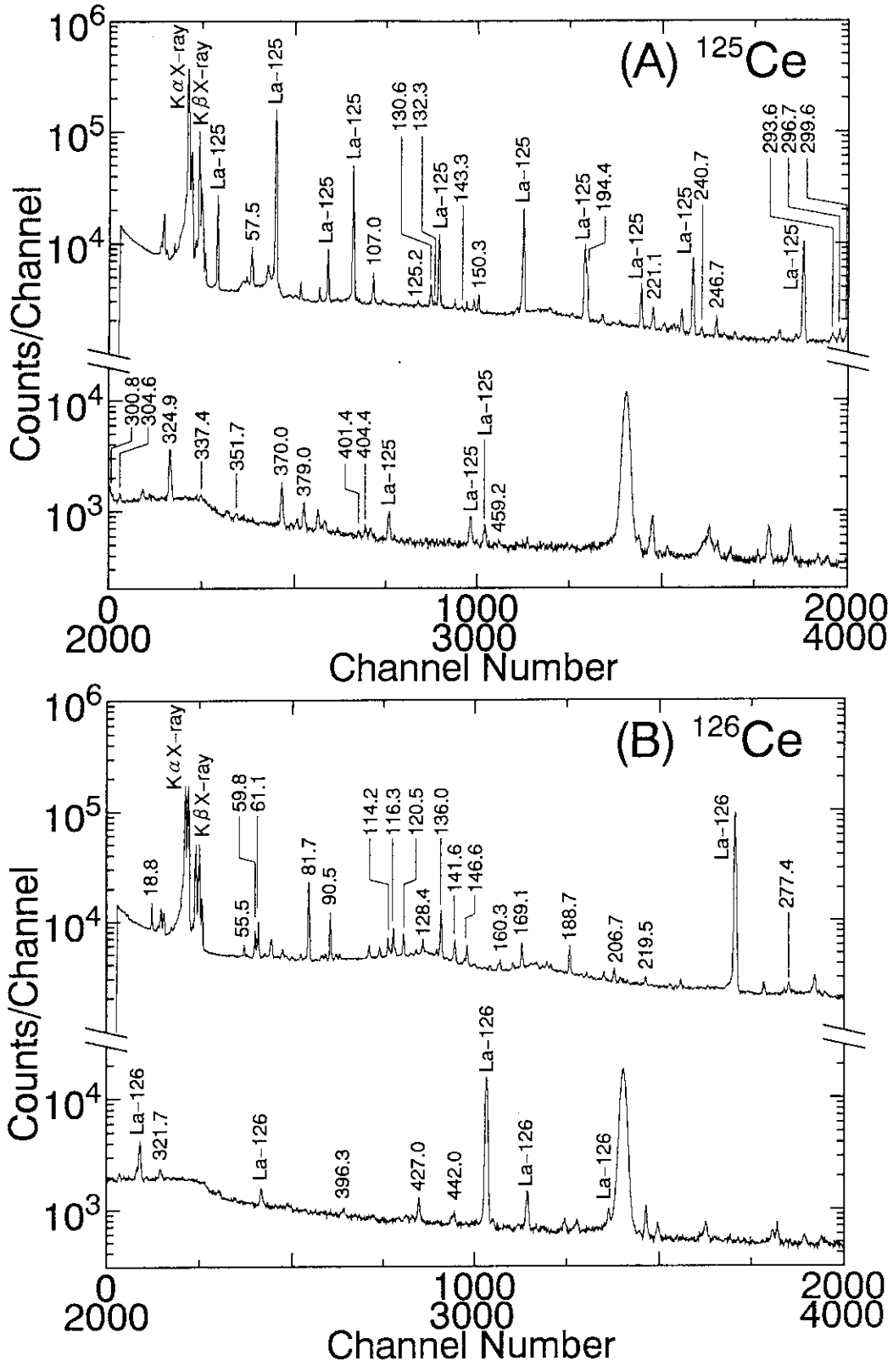

Fig. 1. Gamma-ray singles spectra measured by a LEPS. (A) and (B) were obtained at A=125+16 and A=126+16, respectively. Gamma-rays assigned to the ^{125}Ce and ^{126}Ce decay are indicated in the spectra with their energies in keV.

constructed since the γ-rays of 194.4, 324.9, 370.0 and 379.0 keV were efficiently strong. The 9.0 keV transition to the ground state was not observed in this experiment because of its low energy. The second band was constructed based on coincident γ-rays with the relatively strong 57.5 keV transition. γ-rays crossing between these two bands were not observed, so that the level energies of the second band from the ground state were not determined. A strong γ-ray of 107.0 keV was also identified to the ^{125}Ce decay mainly due to the analysis of half-life. However, this γ-ray is not coincident with the other γ-rays and β-rays. It indicates that the 107.0 keV transition has a long life-time, estimated to be more than 10 μs.

A more detailed analysis for ^{125}Ce and ^{126}Ce is now in progress.

Summary

The decay spectroscopy of ^{125}Ce and ^{126}Ce was performed. Many γ-rays were identified to the decay of ^{125}Ce and ^{126}Ce, and a partial decay scheme of ^{125}Ce was constructed. In future, systematic measurements of γ-γ angular correlation and β-ray maximum energy will be performed, based on these detailed decay studies.

References

1) S. Ichikawa, T. Sekine, M. Oshima, H. Iimura and Y. Nakahara, Nucl. Instr. and Meth. B70 (1992) 93.
2) T. Sekine, S. Ichikawa and Y. Hatsukawa, JAERI-M93-047 (1993) p.169.
3) J. R. Leigh, K. Nakai, K. H. Maier, F. Pühlhofer, F. S. Stephens and R. M. Diamond, Nucl. Phys. A213 (1973) 1.
4) B. M. Nyakó, J. Gizon, D. Barnéoud, A. Gizon, M. Józsa, W. Klamra, F. A. Beck and J. C. Merdinger, Z. Phys. A-Atomic Nuclei 332 (1989) 235.
5) J. Gilat, J. M. Nitschke, P. A. Wilmarth, K. Vierinen and R. B. Firestone, Proc. of the 5th Int. Conf. on Nuclei far from Stability, Rosseau Lake, Canada, (1987) p.463.
6) J. Genevey, A. Gizon, N. Idrissi, B. Weiss, R. Béraud, A. Charvet, R. Duffait, A. Emsallem, M. Meyer, T. Ollivier and N. Redon, Proc. of the 5th Int. Conf. on Nuclei far from Stability, Rosseau Lake, Canada, (1987) p.419.
7) S. Ichikawa, T. Sekine, H. Iimura and M. Oshima, Nucl. Instr. and Meth. A274 (1989) 259.

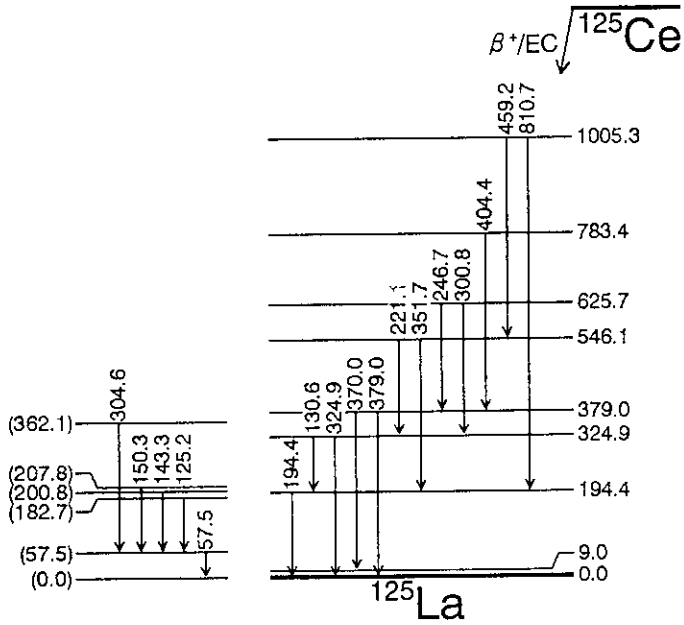

Fig. 2. Partial decay scheme of ^{125}Ce. It is uncertain if the base level of the left side band is the ground state of ^{125}La.

7.5 Production of Fluorine 18 Nuclide via 018(p,n)F18 Reaction in Crystallized Oxalic Acid

N.Ishiwatari JAERI, Tokai, Nucl.Safety Res. Cent.

Objective To make experimentally small amounts of F-18 nuclide via 018(p,n)F18 reaction in laboratory, not in the BWR facility.

Method Fifty ml of 3.0 w/o oxalic acid aqueous soln. were removed into a plastic petri dish(90 mm.dia.) and dried the soln. by warming from the upper side by using an infrared rays radiation heater, little by little. Then, the dish was covered closely by a plastic sheet(8.5 micro meter in nominal thickness, Cupton, Toray Dupont). The dish was fixed on the sample holder to irradiate the proton beam from 3 MV Tandem type accelerator(NEC Corp. Model 9SDH-2) for 30 minutes under the atmosphere. The energy added to the proton beam in the accelerator system was 3.0 Mev. The proton beam current value from the same system above was 158 nA in average for the irradiation period. After the proton beam irradiation to the dish finished, the gamma ray activity in the sample in the dish was measured by gamma ray spectrometry (counting efficiency, 1.34 o/o).

Result In Fig.1 and Table 1, the results of measurement by the gamma ray spectrometry were shown. The 1st measurement data in the table was eliminated because of containing the effect by the gamma ray at 0.51 MeV from the short lived radioactive nuclide on the determination of the produced amounts of the F-18 nuclides. And in the same table, the 5th data was evaluated to be equal to the back ground value on the detector in the gamma ray spectrometer system. From the 2nd~4th data in the table, the amounts of F-18 nuclide at the end of irradiation period was determined (61.3 Bq).

Discussion The result of the preliminary calculation by using IRAC computer code showed that the amounts of F-18 nuclides to be produced were 144 Bq. at the end point of irradiation under the conditions of the process as described above (proton activation cross section, 30 mb). Further, in the above calculation, the proton beam flux in the end part of vacuum system in the accelerator was selected for the input data of the same code, not the sample part under the atmosphere. When F-18 nuclide may be utilized as the tracer without the accurate estimation on the amounts to be produced and the need to eliminate the coexistent oxalic acid in the aqueous soln., the suitable amounts of the nuclides can be produced by way of the process described above to make use of these tracer in laboratory. But when F-18 nuclides in carrier-free state are required for the same purpose as described above, the oxalic acid in the aqueous soln. has to be eliminated by separating. In the Boiling Water Reactor type plant during the power operation, the formation and the release of gas by radiolysis of coolant water occur in the reactor vessel(1). And so, the formation reaction of proton with the water radiolysis can be inferred, and then the reactions of 018 (p,n) F18 and 016 (p,a) N13 in the reactor core zone will be able to occur. As a matter of fact, in the JPDR plant during the power operation, the author had measured F-18 nuclides in the reactor water and N-13 nuclides in the reactor off gas system, respectively(2). On this experimentation, the oxalic acid was made use of instead of light water as the oxygen element supplier, and the mostly positive proof on the formation of F-18 nuclide by way of 018 (p,n) F18 reaction was given in the author's prediction.

References

(1) "Initial Critical and Power Test of the Japan power Demonstra-tion Reactor Plant",JPDR Division; JAERI-1067(1965)123~137(Japan.)
(2) "Water Chemistry of JPDR", Ishiwatari, Nasumi ; JAERI -1135 (1967) (Eng.)

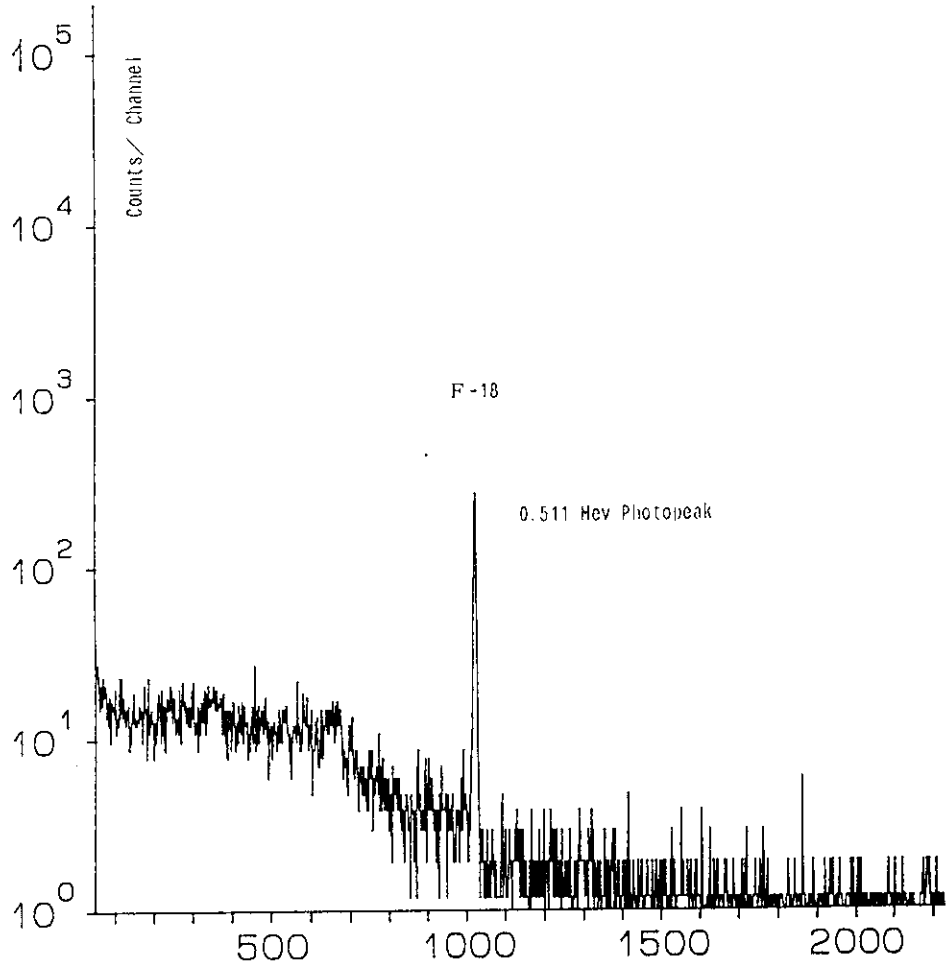

Fig. 1 Gamma ray spectrum of oxalic acid after proton beam flux irradiation

Table 1 Measurement of gamma ray activity of F-18 nuclide in oxalic acid after proton beam flux irradiation

No.	Count starting (0'clock time) Jan.18,'94	Counted (sec)	Count
1	16 21' 34''	2,000	1661.8 ±43.0
2	18 10' 00''	2,000	626.3 ±27.1
3	19 51' 09''	2,000	352.0 ±19.9
4	22 58' 53''	2,000	112.2 ±12.6
5	11 19' 01''(Jan.20, '94)	50,000	736.1 ±37.9

8. Accelerator Shielding

8.1 Measurement of Benchmark Data for Radiation Streaming through Labyrinth (I)

Su. Tanaka, H. Nakashima[2], Y. Nakane[2], Y. Sakamoto[2], S. Tanaka[2], S. Meigo[3], N. Nakao[4], M. Takada[4], T. Nakamura[4], H. Hirayama[5], Y. Uwamino[6], M. Imamura[6], E. Tanabe[7], K. Shin[7]
Ion Beam Develop. Lab., JAERI/Takasaki, Shielding. Lab., JAERI/Tokai [2], Thermal Reactor Phys. Lab., JAERI/Tokai[3], Cyclo. R. I. Center, Tohoku Univ.[4], Radia. Safety Cont. Center, KEK[5], Insti. for Nucl. Study, Univ. Tokyo[6], Faculty of Eng., Kyoto Univ.[7]

I. Introduction

It is important to estimate radiation streaming through a labyrinth as well as to treat radiation transmission through a bulk shielding throughout shielding design. The intensity of emerging radiations from the labyrinth depends on the geometry of the labyrinth and the characteristic of incident radiations.

In high-energy accelerator facilities, a lot of labyrinths are designed for entrance way and utilities. High-energy neutrons which are produced at irradiated targets and beam loss points along beam transport lines are the most crucial radiations for the labyrinth design.

Hence, a labyrinth experiment was carried out to obtain benchmark experimental data using the labyrinth of Light Ion Room 2(LIR2) at TIARA.[1] The measured benchmark data in this experiment are divided into three categories: a characteristic of neutron source, radiation distribution in the target room, and radiation distribution along the labyrinth.

II. Experimental facility and environment

A plain view of the LIR2 is presented in Fig.1 with the location of the neutron source and the measurement points. The labyrinth has three legs of which the cross section is 1.5 m width and 3.5 m height for 1st and 2nd legs, 3.0 m height for 3rd one. The dimension of the target room is 8.5 m x 7.5 m in floor area and 4.8 m in height. The design of the labyrinth was decided based on the calculation of streaming neutron dose H_d by Tesch's formula[2] assuming a neutron source which produced by 10 μA protons of 90 MeV stopped by thick-Cu target.[3]

In this experiment, protons of 67 MeV accelerated by the AVF cyclotron were vertically transported along the beam transport line from the ceiling of target room, and stopped fully by a Faraday cup of thick-Cu target placed 108 cm above the floor to produce a white neutron source. The maximum intensity of the proton beam was controlled below 2 μA for the experiments. The neutrons emitted in a direction of 90 degrees from the target entered the mouth of the 1st leg.

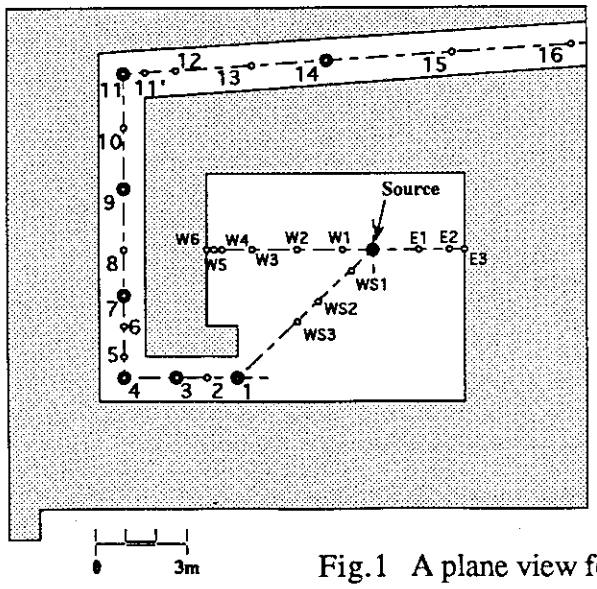

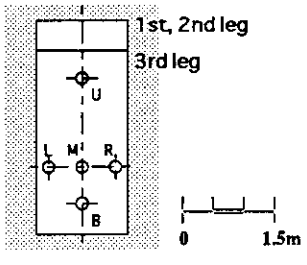

Sectional view of labyrinth

● : points for measurement of all quantities
◊ : points for measurement of neutron dose

Fig.1 A plane view for labyrinth experiment

III. Measurement quantities and instruments

During the experiment, the neutron source intensity was monitored with two fission detectors placed near the Cu target and with the Farady cup. Both energy spectrum and angular distribution of the neutron source were measured by plural kinds of activation detectors, where $^{209}Bi(n,xn)$ reactions were used to measure neutrons above 20 MeV together with conventional activation detectors. Distributions of fission rates, thermal neutrons and gamma-ray exposure in the target room were measured using ^{232}Th fission counter (Centronic FC-480) and TLDs (Harshaw TLD100, TLD700). Besides, energy spectrum by a BC501A (BICRON) scintillator, neutron doses by a rem-counter (Studsvik 2202D), a solid state nuclear track detector(Nagase Landauer Ltd.) and a bonner ball detector, and gamma-ray exposure by TLDs were measured along the labyrinth from the mouth.

IV. Results and discussion

The angular distribution of the neutron source was measured from 0 to 150 degrees at intervals of 30 degrees. In the target room, the distribution of thermal neutrons and gamma-ray exposure were measured at the points indicated by the symbols $E_{i,j}$(East), $W_{i,j}$(West) and $WS_{i,j}$ (Southwest) in Fig.1. The double circles along the labyrinth represent that the measurements have been made using all the detectors, while the single ones indicate the points of the neutron dose equivalent rate H_m measured by the rem-counter.

Fig. 2 demonstrates the distribution of H_m along the labyrinth, which is compared with a calculated neutron dose H_C. The H_C was obtained by multiplying a ratio of Y_{67} to Y_{90} by the design data H_d, where Y_{67} (0.068 neutrons/proton) and Y_{90} (0.12 neutrons/proton) were the neutron yield produced by protons of 67 MeV and 90 MeV, respectively. As shown in Fig.2, the H_c agrees with the H_m within a factor of three, so that the design data is expected to satisfy the specified design criteria. The detailed analyses of other measurement data are in progress.

References

1. S. Tanaka and T. Nakamura, "Shielding Experiments and Analysis at 90 MV AVF Cyclotron Facility, TIARA," Proc. OECD/NEA Specialists' Meeting on Shielding Aspects of Accelerators, Arlington, Texas, USA 28-29 April 1994
2. K. Tesch, Particle Accel., 12, 169(1982)
3. H. Watanabe, Su. Tanaka et al., "Design and Construction of TIARA Facility", JAERI TIARA Annual Report(Vol.2), (1993)

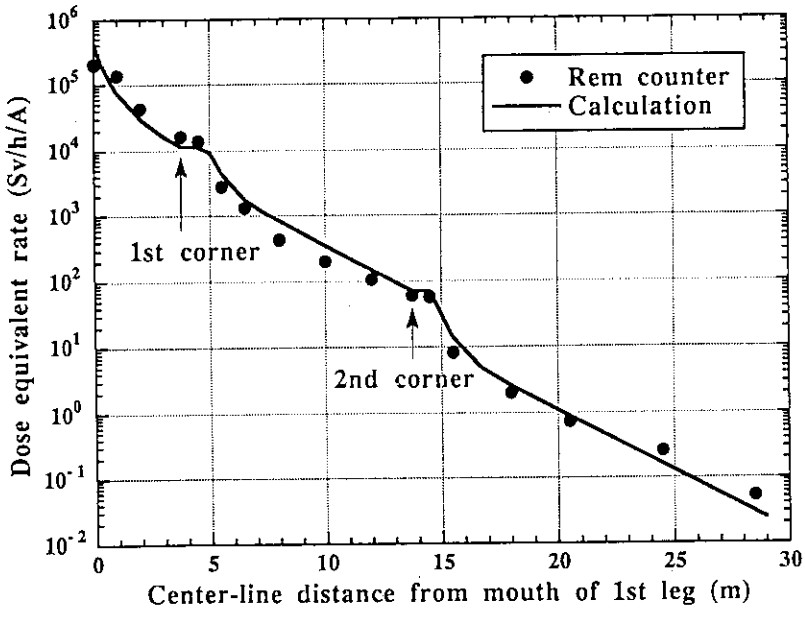

Fig.2 Comparison between the measured and the calculated neutron dose equivalent rate through labyrinth

8.2 Measurements of Differential Thick Target Neutron Yields for 220 MeV C^{5+} Ions

K. Shin, E. Tanabe, H. Takada[2],S. Meigo[2], T. Sasa[2], H. Nakasima[2], S. Tanaka[3]
Dept. Nucl. Eng., Kyoto Univ. JAERI, Tokai, Dept. React. Eng.[2]
JAERI, Takasaki, Adv. Radn. Technol. Center[3]

Introduction

Differential thick target neutron yields are basic data for the estimation of source term in accelerator shielding designs. However, the number of measurements of the data is very small, especially for heavy ions. The objectives of the present series of works are (1) to measure systematic data of the differential thick target yields for variety of ions, (2) make benchmark test of theoretical calculation methods of the data for proton and heavy ions by the measured data, (3) clarify the systematics in the thick target neutron yields regarding the projectile, the target and the projectile energy, and (4) develope a practical source term estimation mathod for accelerator shielding designs. This paper reports results of the first trial experiment of the series in the TIARA facility.

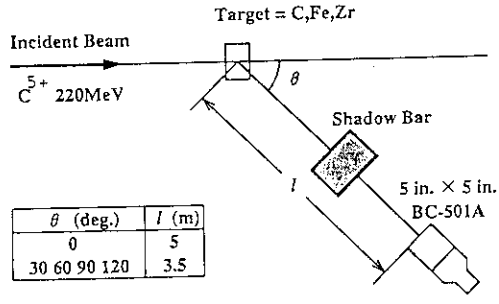

θ (deg.)	l (m)
0	5
30 60 90 120	3.5

Figure 1: Experimental arrangement

Experiment

The measurement was made at the HB-1 beam course at the AVF-cyclotron in the TIARA facility. The experimental arrangement is showed in Fig.1. Targets of C, Fe and Zr, which were thick enough to stop the ion, were irradiated by 220-MeV C^{5+} ions from the cyclotron and generated neutrons were measured by a 5in.×5in. BC-501A detector at 0°, 30°, 60°, 90° and 120° from the beam incident direction. The background owing to the room scattering was measured by placing a 40-cm long iron shadow bar between the detector and the target. The obtained pulse height spectra were unfolded to neutron energy spectra by the FERDO-U[1] code, and then converted to the differential neutron yields using the number of incident ions.

Results

An example of the obtained differential thick target neutron yields for the Zr target is showed in Fig.2. The neutron spectrum becomes softer and the cross section becomes smaller with increasing the angle.

The obtained differential yields were analyzed by the two-component moving source model,[2] and the yields of the equilibrium neutron(EN) and the nonequilibrium neutron(NEN) components, and the nuclear temperatures of the both neutron components were obtained. Results of the EN and NEN yields were consistent with those previously obtained at INS, University of Tokyo

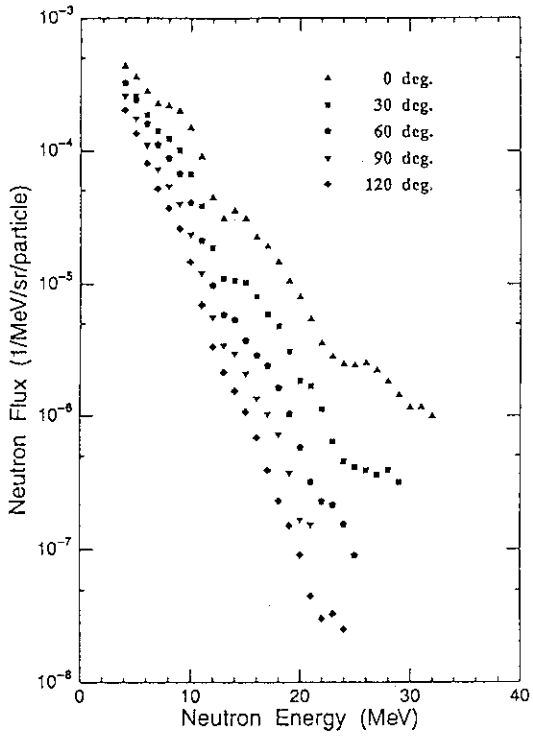

Figure 2: Differential thick target neutron yields for Zr

for 120 MeV and 75 MeV C^{5+} ions[2]. This is demonstrated in Fig.3, for the EN component. The present results are compared with those of the previous measurements and also with the model calculation which describes the systematics of the previous data. From this analysis we confirmed that the measurement in the TIARA facility with even the higher ion energy of about twice the previous one was possible.

However the nuclear temperature of both the EN and the NEN of the present work was too small, suggesting the calibration of the pulse height might be slightly doubtful. So we need some improvements in the measurement. We are planning to use the time-of-flight(TOF) method, by which we do not need to use the pulse height to measure the neutron energy.

The obtained differential yield data were also used tentatively to test the accuracy of the quantum molecular dynamics(QMD) method, which has nbot been tested yet at such a lower ion energy of the present case. The QMD reproduced the relative variations of the yields with the neutron energy and the angle, but gave larger absolute values. The reason of the discrepancy is now being investigated. Although the measured data

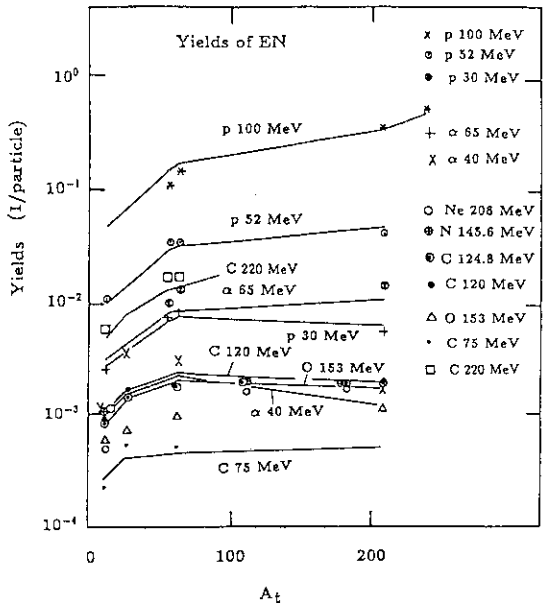

Figure 3: EN yields for variety of ions.

are rather tentative at this moment, this kind of analysis will enable the benchmark test of the theoretical calculation method in future when better data are obtained.

Similar measurements for 220-MeV C^{5+} are planned to be made again this year by the TOF method. Measurements of the differential neutron yields for 100-MeV α, 70-MeV p and 460-MeV Ar are also planned.

REFERENCES

1) K. Shin, Y. Uwamino and T. Hyodo, *Nucl. Technol.*, **53**, 783 (1981).

2) K. Shin, K. Miyahara and Y. Uwamino, "Thick Target Neutron Yield for Charged Particles", Proc. New Horizons Radn. Protec. Shield., April 26-May 1, 1992 Pasco, Washington, pp.528-536.

8.3 Study of ^{7}Li(p,n) Source Spectra and Double-differential Charged-particle Emission Cross Sections of Carbon

M.Baba, T.Kiyosumi, T.Iwasaki, S.Matsuyama, N.Hirakawa,
T.Nakamura[2], N.Nakao[2], Su.Tanaka[3], Sh.Tanaka[4], H.Nakashima[4], S.Meigo[4]
Nuclear Engineering, Tohoku University, CYRIC, Tohoku University[2],
JAERI Takasaki[3], JAERI, Tokai[4]

1. Introduction

As a part of the project research on accelerator shielding using the mono-energetic neutron source facility of TIARA[1], experiments have been conducted on the 1)spectrum of the ^{7}Li(p,n) neutron source, and 2)double-differential charged-particle emission cross sections using a specially developed counter-telescope[2,3].

The spectrum and intensity data of source neutrons are indispensable for the analyses of experiments. In tens MeV region, neutron spectrum measurement with a conventional organic scintillator is difficult because of efficiency uncertainty[2]. Therefore, we have developed a proton-recoil telescope (PRT) with high efficiency and signal-to-background ratio.

Energy-angular double-differential charged-particle emission cross sections for fast neutrons are of great importance in various applied fields, i.e., medical application, radiation damage, and neutron detectors. However, experimental data are very scanty because of very limited mono-energy neuron sources and of experimental difficulty.

During the last year, experiments[2,3] were performed for the 1)source characterization for Ep=43 and 67 MeV, and 2)C(n,xp), (n,xd), (n,xt) reactions for the sources (En=40 and 64 MeV).

2. Experimental

Neutrons were produced by bombarding a ^{7}Li(99% ^{7}Li) metal target with the proton beams from the AVF cyclotron. The targets were ~2 MeV thick (3.6 mm and 5.2 mm for Ep=43 and 67 MeV, respectively). Neutrons to 0° are guided to the Light-Ion-Room III through a ~3-m thick iron and concrete collimator.

Figure 1 illustrates experimental setup.

In the spectrum measurement, upper "annular" geometry was employed. Neutrons coming from left side irradiate the polyethylene radiator and emit recoil-protons. Recoil-protons are detected with a ΔE-E telescope consisting of an E-detector, 5-cm diam by 3-cm thick NaI(Tl), and a ΔE-detector, 900 mm^2 PIPS. The telescope is shielded from the neutron beam by a shadow bar (50-cm long brass). The polyethylene radiator was 1.0-0.12-mm thick and 8x9 cm, with a 6-cm-diam hole in the center. It was placed in the air supported by thin nylon strings. By use of this "annular" geometry, good signal-to-background ratio and energy resolution are achieved with minimal loss of the efficiency, compared with conventional designs. The radiator-telescope distance was taken around 40 cm to obtain good energy resolution by reducing the angular spread of recoil-protons.

Three signals, ΔE and E and the TOF between the E-detector and cyclotron RF, were accumulated by a three-parameter data acquisition system.

Charged-particle emission cross sections of carbon were measured at seven angles from 7° to 120° by use of the counter telescope. The arrangement was the "annular" geometry at forward angles than 20°, and the lower "inclined" geometry at backward angles. In the "annular" geometry, the emission angle was varied by changing the sample-telescope distance. This enabled measurements at extremely forward angles like 7° which is not allowed in the latter

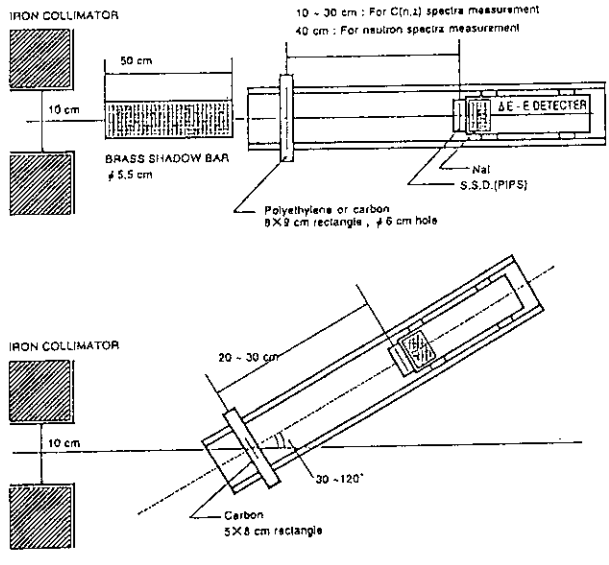

Fig.1: Experimental setup.

geometry.

The carbon sample was a 0.5-mm thick plate.

The neutron production rate was monitored by beam current in the Faraday cup, and ^{238}U and ^{232}Th fission-chambers placed around the target.

The average beam current was 1 to 3 μA.

3. Data Analysis

Firstly, particles were identified using the ΔE-E two dimensional spectra, and then the energy spectrum for each particle was deduced. The energy scale was determined from the linear response of a NaI(Tl) scintillator[4] and the peak neutron energy determined by a TOF measurement with an NE213 or a BC501A scintillator.

The source spectrum was deduced by correcting the proton spectrum for 1)sample-out backgrounds, 2)C(n,xp) backgrounds, 3)energy loss, 4)efficiency, and for 5)inelastic-scattering in the detectors[5]. The efficiency and response of the PRT were calculated by the analytic and Monte Carlo method using recent data for differential n-p scattering cross sections[6].

The carbon data were analyzed similarly, but the events induced by the peak neutrons of the $^{7}Li(p,n)$ source were selected by use of TOF signal. Their absolute values were determined using the neutron flux obtained by the PRT.

4. Results and Discussion

Figure 2 shows the $^{7}Li(p,n)$ spectra for 67 MeV (upper) and 43 MeV protons (lower) measured at ~5.5-m from the target. The neutron spectra show clear peaks due to the $^{7}Li(p,n_{0,1})^{7}Be$ reactions but include continuum neutrons due to breakup reactions. The peak neutron fluences at 5.5-m were 1.5×10^{4} and 1.1×10^{4} (n/cm^2/μCoulomb), and the fraction of peak neutrons to total (En>15 MeV) neutrons were 57 % and 40 % for Ep=43 and 67 MeV, respectively.

The spectrum of these breakup neutrons should be known quantitatively, since these neutrons introduce backgrounds in the experiments using the sources. Therefore, we have analyzed the spectrum of the breakup neutrons and found, as shown by the lines in Figs.2, they were reproduced consistently with the three-body phase-space distribution for the $^{7}Li(p, n^{3}He)\alpha$. This model will be useful to estimate the lower energy part which is difficult to measure. The present results were in fair agreement with those by TOF measurement with a BC501 scintillator whose efficiency was determined on the basis of experimental response function[7].

The cross sections for the $^{7}Li(p,n_{0,1})^{7}B$ were also deduced. As shown in Fig.3, the present values are in agreement with previous ones[8,9]. (Recent result at Ep=58 MeV is also shown.)

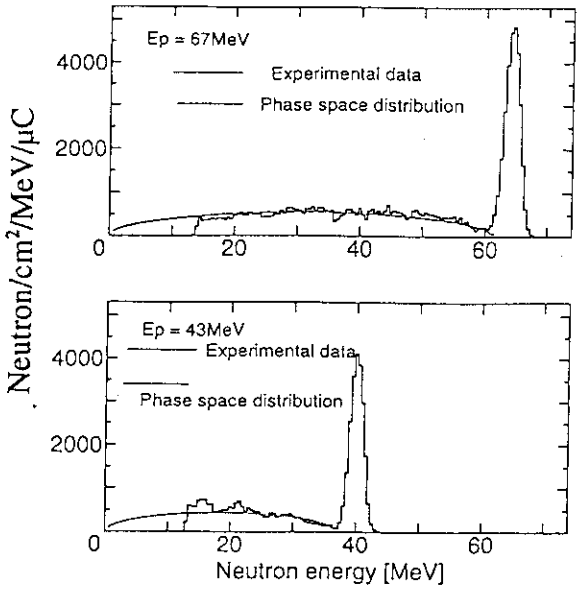

Fig.2: $^{7}Li(p,n)$ source spectrum for 67 MeV (upper) and 43 MeV (lower) protons; the lines show phase-space distributions for the $^{7}Li(p,n^{3}He)\alpha$ reaction.

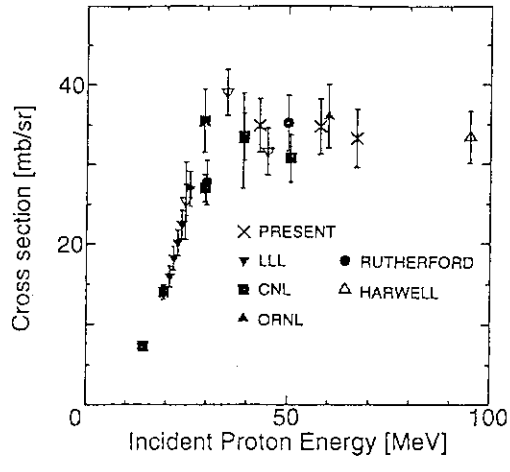

Fig.3: $^{7}Li(p,n_{0,1})^{7}Be$ cross section. (This figure is an extension of Fig.12 in Ref.8.)

Figure 4 illustrates the results of C(n,xp) and (n,xd) emission spectra at 64 MeV. These spectra show strong angle-dependence and peak structures characteristic for each particle. The lower energy parts, on the other hand, are almost continuous and have milder angular dependencies. Similar features were reported by UC Davis group[10,11].

Therefore, to calculate KERMA factors, damage parameters and scintillator response function, double-differential data for charged-particles are very important. The analyses of the data are now in progress.

Experiment will be extended to other energies and elements by upgrading detectors for higher efficiency and dynamic ranges to get the data for α-particles and lower energy particles.

References

1.Su.Tanaka et al.: *Proc.2-nd Int.Symp.on Advanced Nuclear Energy Research - Evolution by Accelerators-*", (1992, Mito,) p.342
2.M.Baba et al.: *JAERI-M* 94-019 200 (1994)
3.M.Baba et al.: *Proc.Int.Conf. on Nucl. Data for Sci. Technol.*, (1994, Gatlinburg) to be published
4.J.L.Romero et al.: *Nucl.Instr.Methods*, **A301** 241 (1991)
5.D.F.Measday.: *ibid.*, **76**, 45(1969)
6.G.Fink et al.: *Nucl.Phys.*, **A518**, 561(1990)
7.N.Nakao et al.: 8-th Int.Conf. on Rad. Shielding, (1994 Arlington) to be published
8.J.W.Watson et al.: *Nucl.Instrum.Methods*, **215**, 413 (1983)
9.T.N.Taddeuchi et al.: *Nucl.Phys.*, **A469**, 125 (1987)
10.T.S.Subramanian et al.: *Phys.Rev.*, **C28(2)**, 521 (1983)
11.F.P.Brady et al.: *ibid.*,., **C43(5)**, 2284 (1991)

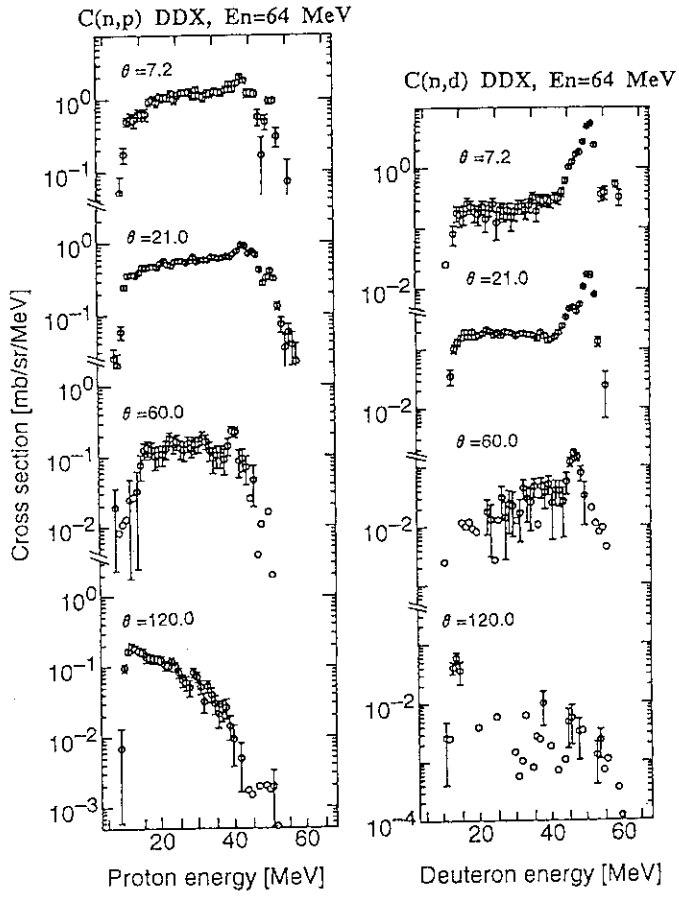

Fig.4: C(n,px), C(n,dx) emission spectra for 64 MeV neutrons.

8.4 Measurements of Neutron-induced Activation Cross Sections at En=41.5 and 64.3 MeV

M. Imamura, T. Shibata, S. Shibata, Y. Uwamino, T. Ohkubo, S. Satoh, T. Nakamura[2], A. Konno[2], Susumu Tanaka [3] and Shun-ichi Tanaka [4]
Institute for Nuclear Study, University of Tokyo、Cyclotron Radioisotope Center, Tohoku University[2]、JAERI- Takasaki[3]、JAERI- Tokai[4]

Neutron-induced activation cross sections have been measured using the p-Li quasi-monoenergetic neutron sources at JAERI-Takasaki. We report on the results of the experiments performed in fiscal year 1993 at En=41.5 and 64.3 MeV.

Leakage neutrons up to about 100 MeV are the main source responsible for activation of materials in accelerator facilities. In order to evaluate radioactivity production, neutron-activation cross sections are required for various elements comprising accelerator equipments and shielding materials. The leakage neutron flux can be evaluated by irradiating various monitor targets of known activation cross sections with different threshold energies. Neutron-induced activation cross sections are also important as basic data for nuclear physics and astrophysics. However, experimental data exceeding 20 MeV are quite scarce at present, mainly because of experimental complexity and very few facilities available for activation experiments. The 90-MeV AVF cyclotron of the TIARA accelerator facility provides a quasi- monoenergetic neutron source from 20 to 90 MeV using the (p,n) reaction on Li targets. In a 5-year research program that we started last year, it is aimed to acquire neutron-induced activation cross sections as basic data for accelerator shielding studies using the quasi-monoenergetic neutron source facility at TIARA-JAERI.

During fiscal year 1993 we performed two activation experiments at En=41.5 and 64.3 MeV. In the expriments targets were first irradiated with neutrons for one hour or for about 24 hours. Short-time irradiations(1 hour) were performed to measure short-lived nuclides, and extended irradiations (ca. 24 hours) to measure longer-lived nuclides. The neutron intensities (peak energy) were of the order of 10^5 n/cm^2/sec at the irradiation position, which was located 400 cm down-stream from the neutron source (Li target). The energy dispersion of the neutron energy (peak energy) was approximately 2 MeV for both irradiations, the most of which come from the energy loss of incident protons in the Li target.

Since the neutron intensity was weak and the available experimental time was limitted, we used large-sized targets of several to 50 g in weight (approximately 30x30x2mm in size) and of many kinds that are important for shielding studies : C, SiO_2(as an O target), Si_3N_4(asN), Na_2CO_3(as Na), Mg, Al, Si, K_2CO_3(as K), $CaCO_3$(as Ca), Cr, Fe, Ni, Cu, Au and Bi. Except for Au and Bi, these are the important constituents of accelerator

equipments, shielding materals and the air. C, Al, Cu and Au have been used as neutron monitors. In the course of our experiment, it was found that Bi is a new excellent monitor target for determining a neutron spectrum up to 100 MeV.

Shortly after irradiation, γ-ray activities produced in the targets were measured with a Ge detector (relative efficiency 36%) at TIARA. For some targets weak γ-rays were measured using the well-shielded Ge detectors at INS(the Institue for Nuclear Study , University of Tokyo). Radioactivities with half-lives of 10min. to 30 years were detemined for more than 50 reactions.

Neutrons from the $^{7}Li(p,n)^{7}Be$ reaction has a lower energy component with a broad and almost continuous spectrum in addition to the peak component. In order to calculate activation cross sections, therefore, it is necessary to correct for the production contributed by this lower energy part of neutrons. In principle, cross section data for the lower energy must be known for this purpose. Cross-section measurements below 38 MeV have been carried out for natural C, N(Si_3N_4), O(SiO_2), Na(Na_2CO_3), Mg, Al, Si, Ca($CaCO_3$), Cr, Fe, Ni, Cu, Au and Bi targets using the p-Be and p-Li quasi-neutron sources at the SF cyclotron of INS[3-6]. The neutron energies in the above two experiments are too coarse at least to evaluate the cross sections at En=64.3 MeV. Expriments in every 5-MeV interval are required to evaluate activation cross sections in confidence.

The $^{209}Bi(n,xn)^{210-x}Bi$ reactions were found to be very useful for neutron dosimetry up to ca.100MeV. Theoretical calculations for these reaction cross sections have been given in ENDF/VI. Using the INS experiment data[6] and assuming the calculated data of ENDF/VI between 45 and 60 MeV we evaluated the cross sections at 41.5 and 64.3 MeV, and are shown in Fig.1 as preliminary data.

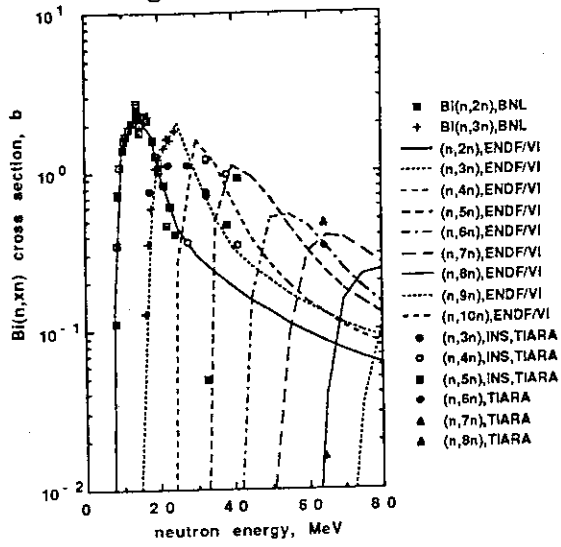

Fig.1 Preliminary results on the $^{209}Bi(n,xn)^{210-x}Bi(x=3-8)$ reactions. Errors are not indicated.

References

1)Shun-ichi Tanaka et al..Proc. OECD/NEA Specialists' Meeting on Shielding Aspects of Accelerators, Targets and Irradiation Facilities (Arlington, Texas, Apr. 1994) (to be published).

2) Susumu Tanaka et al., Proc. 2nd Int. Symp. on Advanced Nuclear Energy Research- Evolution by Accelerators- (Mito, Nov., 1992) p.342.

3) Y. Uwamino et al., Nucl. Sci. Eng.111,391-403(1992).

4) Y. Uwamino et al., J. Nucl. Sci. Tech. 31, 1-11(1994).

5) M. Imamura, unpublished data

6) Y. Uwamino et al. Ann. Report 1993, INS(in press).

8.5 SPECTROMETRY OF SEVERAL TENS MeV NEUTRONS WHICH PENETRATED SHIELDS

T. Nakamura[1], N. Nakao[1], M. Takada[1]
Shun. Tanaka[2], H. Nakashima[2], Y. Sakamoto[2], Y. Nakane[2]
Su. Tanaka[3], K. Shin[4], E. Tanabe[4], M. Baba[5]

1. Cyclotron and Radioisotope Center, Tohoku University
2. Tokai Establishment, Japan Atomic Energy Research Institute
3. Takasaki Establishment, Japan Atomic Energy Research Institute
4. Department of Nuclear Engineering, Kyoto University
5. Department of Nuclear Engineering, Tohoku University

I. INTRODUCTION

This study is a part of a research programme running as a cooperative project between JAERI and several universities to acquire the cross section and shielding data for several tens of MeV neutrons using a p-^{7}Li quasi-monoenergetic neutron field at the TIARA. In this work, we provide the experimental benchmark data for neutrons which penetrated concrete and iron shields.

II. EXPERIMENT

We measured the spectra of neutrons which penetrated concrete and iron shields using BC501A and Bonner ball with 40.5 and 64.0 MeV quasi-monoenergetic neutrons in the AVF cyclotron of the TIARA. The neutron beam was injected into 120cm by 120cm concrete slab of 25 to 200cm thickness or iron slab of 10cm to 130cm thickness, which were fixed in contact with the 10cm diam collimator exit located at 4m from the target. The experimental arrangement at TIARA is shown in Fig.1.

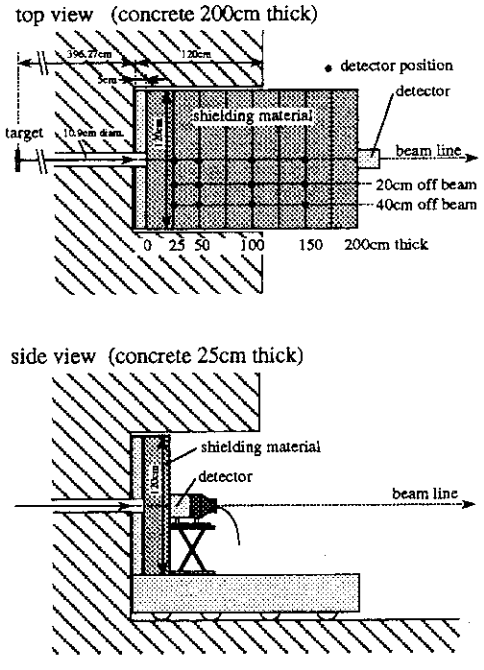

Fig. 1. Experimental arrangement at TIARA

A. Source neutron spectra

The source neutrons were produced from 3.6 mm and 5.2 mm thick ^{7}Li targets bombarded by 43 and 67MeV protons, respectively. The absolute fluences of source neutrons in the monoenergetic peak per proton beam current were obtained from the PRT(proton recoil counter telescope) [1]. The counts of fluence monitors (^{238}U and ^{232}Th fission chambers) which were placed near the target were normalized to this absolute fluence values, then the source neutron fluence during each experiment was given from the fluence monitor counts. The source neutron spectra were measured with the 12.7-cm-diam by 12.7-cm-long BC501A organic liquid scintillator (BICRON Co. Ltd.) coupled to a R4144 photomultiplier (Hamamatsu Photonics. Co. Ltd.) using the TOF method. Finally the source neutron energy spectra per unit current were obtained and are shown in Fig.2

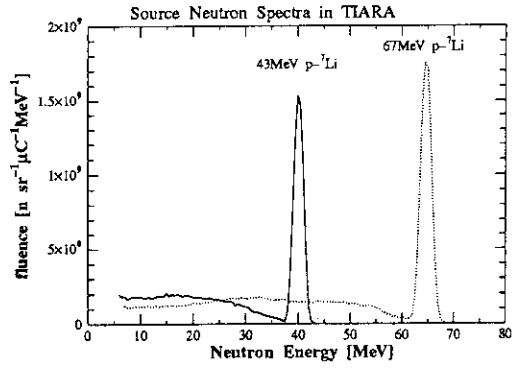

Fig. 2. 43 and 67MeV p-^{7}Li neutron spectrua

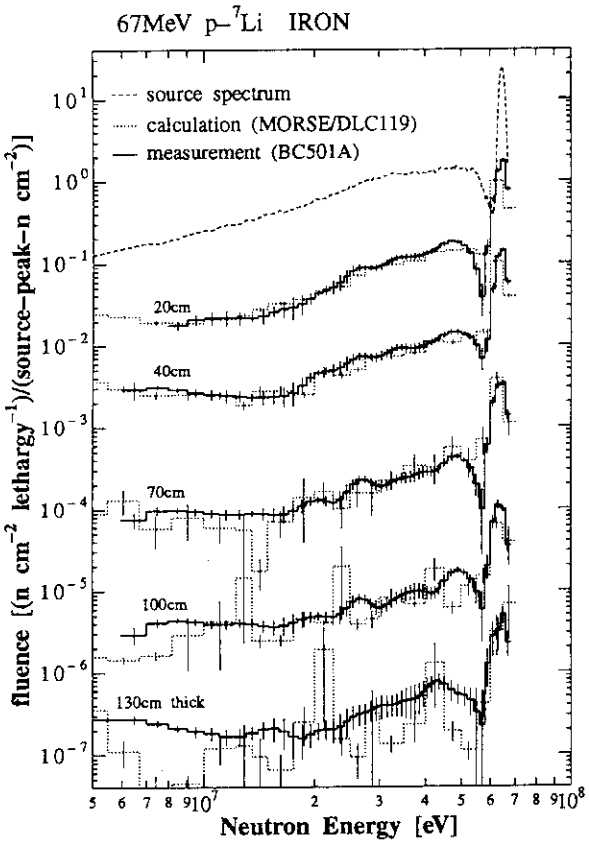

Fig. 3. Energy spectra of neutrons penetrating iron using 67.0 MeV p-^{7}Li using BC501A

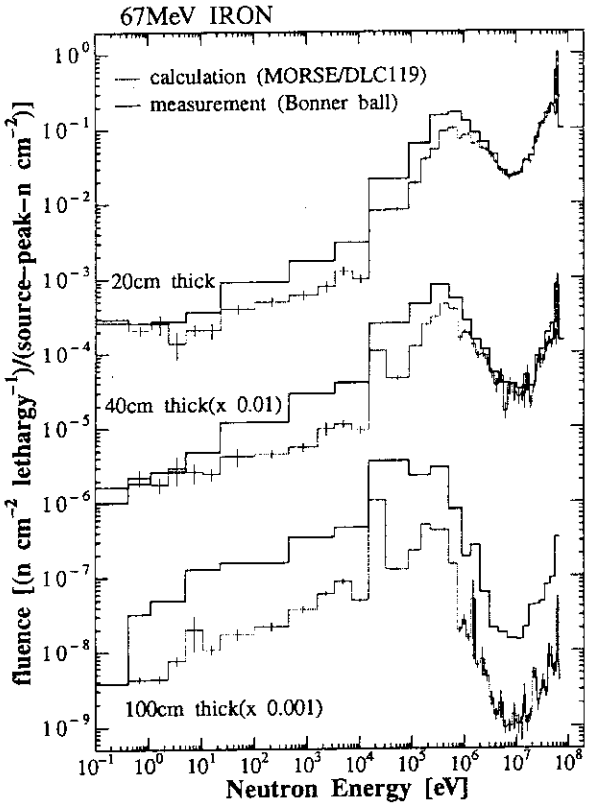

Fig. 4. Energy spectra of neutrons penetrating iron using 67.0 MeV p-^{7}Li using Bonner Ball

B. Measurement of neutrons penetrated shields

The neutrons which penetrated shields were measured with the BC501A. The detector was located in contact with the shield surface on the beam axis and also on the surface at 20cm and 40cm distance off the beam axis to investigate the surface distribution of neutrons scattered at a large angle. The pulse-height and the rise-time of the detector light outputs were recorded in dual mode.

Multi-moderator spectrometer(Bonner Ball) with four spherical polyethylene moderators of 1.5, 3.0, 5.0 and 9.0cm thickness and without moderator was also used in some cases only on the beam axis. The thermal neutron detector inserted in the center of the moderator is a 5.08 cm diam spherical proportional counter, made by LND Inc., filled with 10 atm(at 22 ℃) ^{3}He gas. We recorded the pulse hight spectra for five different moderators of Bonner ball.

C. Spectral analysis

The γ-ray pulses were eliminated from the two dimensional data measured with BC501A, and we converted the light output distributions induced by neutrons into the neutron energy spectrum using the FERDOU [2] unfolding code and the measured response matrix. The energy range was above several MeV.

The five pulse height data measured with Bonner ball in one case of experiment were summed up to get counts above the γ-ray discrimination level, and these five counts were unfolded by using SAND-2 code [3] and the response matrix given by Uwamino et al. [4] Initial guess spectra used in unfolding were obtained from the calculations described later. We then obtained the spectra of neutrons in the energy range from 10^{-4}eV to the maximum energy.

III. CALCULATION

The calculations of the neutron spectra transmitted through concrete and iron shields were made with the MORSE Monte Carlo code [5] using the DLC-119/HILO86 [6] multi-group cross sec-

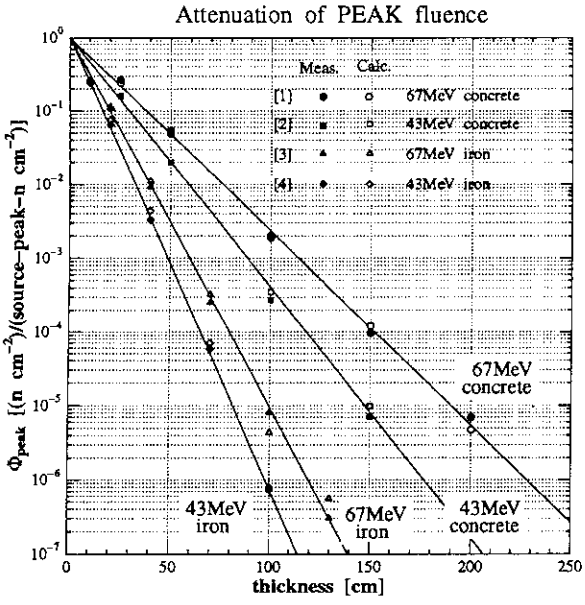

Fig. 5. Attenuation of peak fluence through shields

tion library. The source neutron spectra measured with BC501A by TOF meathod were used in the calculations, and source neutrons were assumed to be emitted only in a very sharp cone of 5.94×10^{-4}sr along the beam line, considering the geometry of the neutron beam collimator as seen in Fig.1 The concrete and iron shielding materials were located at 4m away from the target, and the concrete walls surrounding the shield materials were considered to be 40cm thick.

IV. RESULT AND DISCUSSION

The neutron energy spectra measured and calculated on the beam axis for varius shield thicknesses are exemplified in Figs.3 and 4. The figures show the spectra for iron shield experiment using 67MeV p-^{7}Li neutron source. Fig.3 compares the BC501A measurement in the energy range from 5 MeV to 100 MeV, and Fig.4 compares the Bonner Ball measurement in the energy range from 0.1 eV to 100 MeV with the Monte Carlo Calculation. The measured results for 0cm thick shield which are the neutron spectra incident on the shield surface in contact with the collimator exit were obtained through the distance correction from the source neutron spectra measured with the telescope and BC501A. The spectra are shown as lethargy fluence per peak fluence for 0cm thickness (source peak neutron).

We can see in Fig.3 the very good agreement between measurement and calculation both in peak region and continuum region. On the other hand, discrepancy around broad peak in the energy below 1 MeV is found in Fig.4, and this discrepancy becomes larger with thicker iron shield.

Fig.5 shows the peak fluence attenuation profiles in concrete and iron shields. The calculated and measured peak fluences obtained by summing up monoenergetic peak fluxes showed good agreement as seen in the figure. The attenuation lengths of concrete were obtained to be 28.8 g/cm^2(for 43MeV), 38.1 g/cm^2(for 67MeV), and those of iron were 55.9 g/cm^2(for 43MeV), 67.6 g/cm^2(for 67MeV) by fitting the measured and calculated results.

V. CONCLUSION

Neutrons which penetrated shields were measured for concrete shield from 25 to 200cm thickness and for iron shield from 10cm to 130 cm using quasi-monoenergetic neutrons of energy 40.5 and 64.0 MeV.

The data provided a good prediction for the absolute value of neutron spectra behind concrete and iron shields and will be useful as the integral benchmark experimental data. The attenuations of peak fluence were also well reproduced by the calculation using MORSE Monte Carlo code and DLC119/HILO86 cross section library.

REFERENCES

1) M. Baba et al., JAERI-M, 94-019, 200 (1994)

2) K. Shin, Y. Uwamino, T. Hyodo, *Nucl. Technol.*, **53**, 78 (1981).

3) W. N. McElroy et al., AFWL-TR-67-41, Air Force Weapons Laboratory (1967).

4) Y. Uwamino, T. Nkamura, A. Hara, *Nucl. Instr. and Meth.*, **A239**, 299 (1985)

5) G. R. Straker, P. N. Stevens, D. C.Irving, and V. R. Cain,ORNL-4585 (1970)

6) R. G. Alsmiller Jr., J. M. Barnes and J. D. Drischler, ORNL/TM-9801 (1986)

9. Accelerator Technology

9.1 Beam Positioning and Single Ion Hit for Heavy Ion Microbeam

Tomihiro KAMIYA, Tamotsu SUDA, Toshio HIRAO*,
Isamu NASHIYAMA*, and Ryuichi TANAKA
Advanced Radiation Technology Center
and Department of Material Development*, JAERI

I. INTRODUCTION

The heavy ion microbeam apparatus connected to the 15 degree beam line (TB) of the 3 MV tandem accelerator was designed to analyze microscopic process of single event upset (SEU) with a single ion hit system under development[1-4].

The SEU phenomena depends not only on the mass and energy of the incident ions, but also on the hit position on the integrated circuit. Therefore the exact microbeam positioning is required[1,5], as well as microbeam focusing and single ion hitting, for the SEU experiment using the heavy ion microbeam apparatus. We already achieved the beam size of 1 μm for 15 MeV nickel ions. The development of single ion hit system is in good progress for single-ion detection and the hit control.

For more accurate beam positioning, the original target chamber was replaced with a new chamber specially designed for SEU analysis which is equipped with target stages with higher spatial resolution. A new single ion detection system will be also installed in the new chamber.

II. BEAM POSITIONING

Precision of beam positioning has been examined through secondary electron imaging of a target specimen obtained by two-dimensional scan of a microbeam. It is required that the image be an exact copy of the specimen in the detailed geometric structure. However oscillatory distortion in the horizontal direction as shown in Fig. 1 was observed in the secondary electron images of a Cu mesh (1000 lines/inch) mapped by a microbeam scanning of 15 MeV $^{58}Ni^{4+}$ ions. The beam scanning area was about $100 \times 100\ \mu m^2$ with horizontal sweeping. If scanning is done with vertical sweeping, the oscillatory distortion disappears, while the image of the vertical line blurs because the direction of beam sweep is at right angle to that of image oscillation.

The oscillatory image does notr change even when stopping operation of all the pumps or motors and replacing power suppliers is done. Therefore it appeared that neither mechanical vibration nor electrical instability affects this phenomenon. However the situation was changed when (1) the beam objective aperture, (2) the field of the quadrupole magnets, and (3) the sweep direction of scanning were rotated by 90 degree simultaneously. It has not been made clear yet why the oscillatory distortion in the horizontal direction is observed in a secondary electron image as shown in Fig. 2.

One of unidentified factors may be or alternating magnetic field around the beam line. Some power supplier may emit the weak alternating magnetic field. Although the field may be very low, the integration of the field along the long beam path may give rise to appreciabel distortion in the target image by bending high-energy heavy ion beam trajectory. We are planning to check these factors in the following experiments.

III. SINGLE ION HIT SYSTEM

The single ion detector for the single ion hit consists of a pair of microchannel plates (MCP); the one detects secondary electrons emitted from an ultra-thin carbon foil through which a single ion passed, and the the other one detects secondary electrons emitted from the target. Considering a small space between the exit of the doublet quadrupole magnet and the target, we preferred to use the annular type MCP, in spite of its disadvantage that the signal to noise ratio is higher than that of normal type. The MCP noises can be eliminated from the single ion detection signals by using coincidence-signals from two MCPs. Figure 3 illustrates the single ion detector in the target chamber. The detector can be removed by a rotational stage in normal microbeam mode. The circuit diagram of the single ion detector is shown in Fig. 4. The outer diameter of assembled double-stack MCP is 30 mm and the diameter of the center hole is 4 mm. The total current gain is 1×10^{-6} when the bias voltage between input and output side of the double-stack MCP is 2 kV. A fast timing signal is obtained through the capacitor C. In order to correct electrons efficiently, a holed correction electrode is set in front of the MCP. Various parameters such as the high voltages for those electrodes will be optimized in order to obtain the maximum detection efficiency by the measurement with a α-source and heavy ion beams from the accelerator

IV. SUMMARY

In the heavy ion microbeam apparatus, the original target chamber was replaced by the new one for SEU analysis with high-precision target stages. However the oscillation phenomena were observed in the horizontal or vertical direction of the secondary electron image. The frequency of oscillation is around 100 Hz, and the amplitude is much larger than 1 μm, the precision required in the beam positioning. We have tried to identify this phenomena with checking mechanic and electric factors, and now we are running down the real cause of it. A compact single ion detector for the single ion hit system was designed to fit the new target chamber which will be used for detailed SEU analysis in well-controlled hitting conditions. Parameter optimization and performance tests will be followed to establish the single ion hit system.

REFERENCES

[1] T.Kamiya et al., Nucl. Instrum. Methods. B64, 362 (1992)
[2] T.Kamiya et al., Proc. of 3rd Int. Conf. on Evolution in Beam Applications, Takasaki, Japan, 286 (1991).
[3] T.Kamiya et al., Proc. of 1st. Meeting on The Ion Engineering Society of Japan, Tokyo, Japan, 105 (1992).
[4] T. Kamiya et al., Proc. of 3rd Symp. on Beam Engineering of Advanced Material Syntheses, Tokyo, Japan, 453 (1992).
[5] I.Ohdomari et al., Nucl. Instrum. Methods. B54, 71 (1991).
[6] I.Nashiyama et al., IEEE Trans. Nucl. Sci. NS-40, No.6, 1935 (1993).
[7] T.Hirao et al., to be published in JAERI TIARA Ann. Rep. (1994).

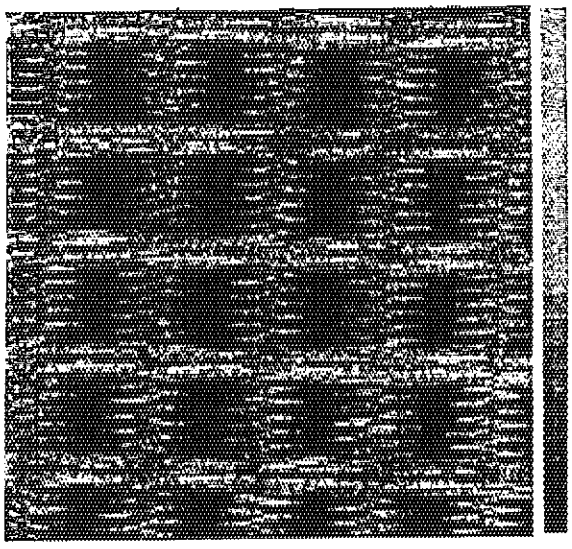

Fig. 1 A secondary electron image of a Cu mesh (1000 lines/inch)with 15 MeV Ni^{4+} before 90-degree rotation.

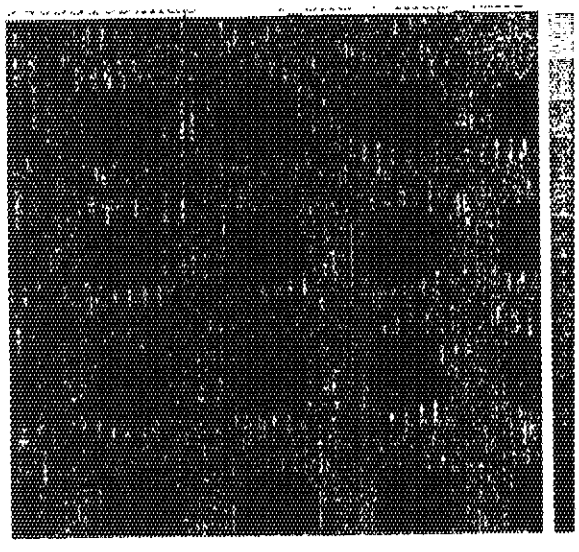

Fig. 2 A secondary electron image of a Cu mesh (1000 lines/inch)with 15 MeV Ni^{4+} after 90-degree rotation.

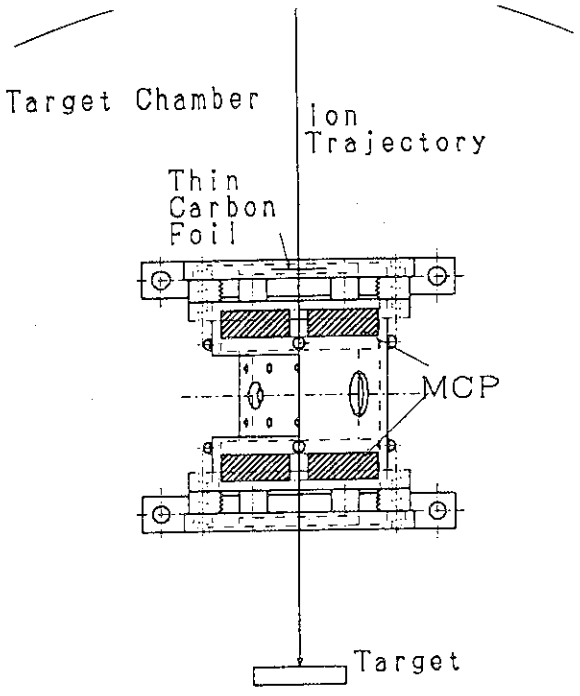

Fig. 3 A schematic view of the single ion detector

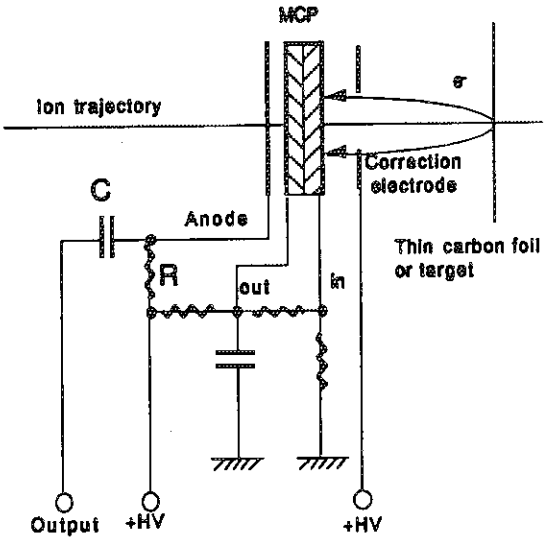

Fig. 4 A circuit diagram of the single ion detector

9.2 Development of High-Intensity Submicron Microprobe

Tomihiro KAMIYA, Tamotsu SUDA, and Ryuichi TANAKA
Advanced Radiation Technology Center, JAERI

I. INTRODUCTION

High-energy ion microbeam is a powerful tool not only for element analysis such as PIXE, RBS or NRA[1-3] but also for studies of irradiation effects on local areas of semiconductor devices[4-6]. In the Advanced Radiation Technology project in TIARA, an emphasis is put on application of ion microbeams for these multiple purpose.

In the first phase we constructed the heavy ion microbeam apparatus[7,8] connected with the 3 MV tandem accelerator, now being mainly used for studying microscopic process of single event upsets (SEU) of semiconductor devices in space environment. In the second-phase we constructed a light-ion microbeam apparatus, connected with the 3 MV single-ended accelerator, and are now developing submicron beam technique with higher beam current. The combination of two different microbeam lines is quite effective.

We are aiming to achieve a beam spot size of 0.25 μm or less with a beam current of 100 pA or more in the light-ion microbeam apparatus. Although we have to consider thermal damage of specimen caused by high fluence rate ion beams in actual applications, we intend to expand further possibility of microbeam applications such as not only ion beam analysis, but also high-energy, microbeam processing. However the chromatic aberration is the most important factors dominating the beam size and current of the high energy microbeam[9]. In order to decrease the chromatic aberration, we combined the microbeam apparatus with the single-ended accelerator with an extremely high voltage stability of within electrostatic accelerator and a high resolution beam analyzing system.

This paper describes the outline of the light-ion microbeam apparatus, the ion beam optical design for the system including the accelerator, and the beam size measurement using 2 MeV Helium ion.

II. LIGHT ION MICROBEAM LINE

Figure 1 is a photograph of the light-ion microbeam line in a target room for the single-ended machine.. The lens system has the demagnification factors of 12 and 60 for the horizontal and vertical directions, respectively. These are relatively large, while those of the heavy ion microbeam line are 4.6 and 28. To control the objective beam size more accurately, the microslit for each direction has a wedge-shape jaw with a couple of tungsten carbide cylinders, as shown in Fig. 2. The microslit gaps are controlled by longitudinal motions of the jaws driven by stepping motors.

III. ION BEAM OPTICAL DESIGN

The 3 MV single-ended accelerator has a balanced type Schenkel DC high-voltage generator providing a maximum voltage of 3 MV with a stability of $\pm 1 \times 10^{-5}$ [10,11]. In order to verify the energy stability of the beams for the final lens system, a 1.5 m 90 degree analyzer magnet was installed in the beam transport system. The magnet has a bending radius of 1.5 m and a pole shape for double focusing. The magnetic field is stabilized within $\pm 1 \times 10^{-5}$

by a feed-back system with a nuclear magnetic resonance teslameter. There are an objective slit and an image slit at a distance of 3 m from the entrance and the exit pole edge of the magnet, respectively. When the horizontal gap of the objective slit is 0.1 mm, the energy resolution is evaluate at $\pm 1.4 \times 10^{-5}$ for this analyzing system.

The chromatic aberration coefficients $\langle x|\theta\delta\rangle$ and $\langle y|\phi\delta\rangle$, fixed by the geometry of the final lens system, are 175.5 and 164.5 μm/mrad%, respectively, where q and f are the maximum beam divergence in mrad for X and Y direction, respectively, and d is the momentum spread in % and is half as much as the energy spread. Since the maximum beam divergence of our system is 0.18 mrad for each direction, the chromatic aberrations are 0.032 and 0.030 μm, respectively, much smaller than the beam size of 0.25 μm that is our goal, if the beam energy spread is the same as the voltage stability of the accelerator, $\pm 1 \times 10^{-5}$.

The target beam current depends on the brightness, which may be reduced by a analyzing system. Figure 4 shows energy dispersion of a beam by analyzer magnet. An original beam which has an energy variation of $\pm \Delta E/E$ at the objective slit, is transferred to the microslits as a dispersed beam. Only if the absolute value of $\Delta E/E$ for the original beam is smaller than 1.4×10^{-5}, larger $\Delta E/E$ component of the beam is not cut at the microslits for X direction and then the brightness will keep. Therefore the brightness of the beam in the final lens system only depends on that of an ion source and also on the energy variation of the source, which is rf type.

The target beam current also depends on the acceptance of the final lens system, which is uniquely defined by the geometry of the system and by the target beam sizes required. Then the brightness required for the beam collimated by the microslit can be evaluated at 27.8 pA/μm^{2}mrad^2, to obtain the target beam current of 100 pA in simple calculation.

III. MICROBEAM OBSERVATION

In a preliminary experiment, a clear secondary electron image was obtained by the target system as shown in Fig.4, where the ion beam is 2 MeV He^+, the target is a Cu mesh (600 lines/inch). The scanning area is about 300×300 μm^2, and the resolution of the image is of 150×150 pixels. The beam size estimated roughly was 4 μm as compared with the resolution of the image.

IV. SUMMARY

The light-ion microbeam apparatus was constructed and installed on a beam line of the 3 MV single-ended electrostatic accelerator with high-stability mainly for ion beam analysis. A clear secondary electron image was obtained with 2 MeV helium ion beam so far in the system. We are now aiming to measure the beam size precisely using the target system, to improve the performance of the system, to advance practical ion beam analyses, and also to develop new applications.

REFERENCES

1) F.Watt and G.W.Grime, Principles & Applications of High-energy Ion Microbeams (Adam Hiller, Bristol, 1987).
2) K.Traxel, Nucl. Instrum. Methods. B50, 177 (1990).
3) M.Takai, Nucl. Instrum. Methods. B85, 664 (1994).
4) B.E.Fischer, Nucl. Instrum. Methods. B54, 401 (1991).
5) T.Matsukawa et al, Nucl. Instrum. Methods. B77, 239 (1993).
6) K.H.Horn et al, Nucl. Instrum. Methods. B77, 355 (1993).
7) T.Kamiya et al., Nucl. Instrum.Methods. B64, 362 (1992)
8) T.Kamiya et al., Proc. of 3rd Int. Conf.

on Evolution in Beam Applications, Takasaki, Japan, 286 (1991).
9) G.J.F.Legge et al, Nucl. Instrum.Methods. B77, 153 (1993).
10) Y.Saitoh et al., Nucl. Instrum. Methods. B89, 23 (1994).
11) Y.Ishii et al., Proc. of 4th Symp. on Beam Engineering of Advanced Material Syntheses, Tokyo, Japan, 105 (1993).

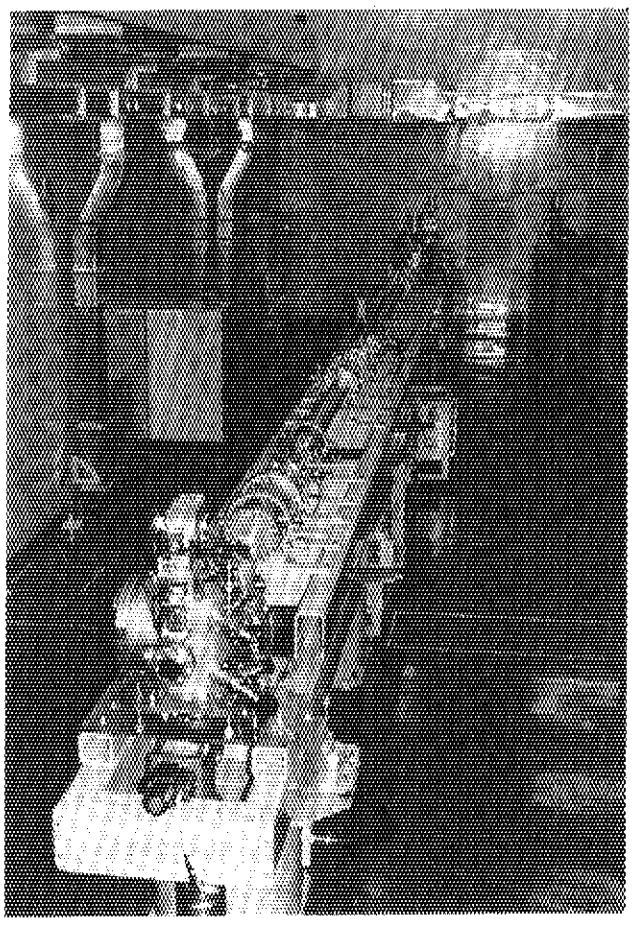

Fig. 1 Photograph of the submicron microbeam line.

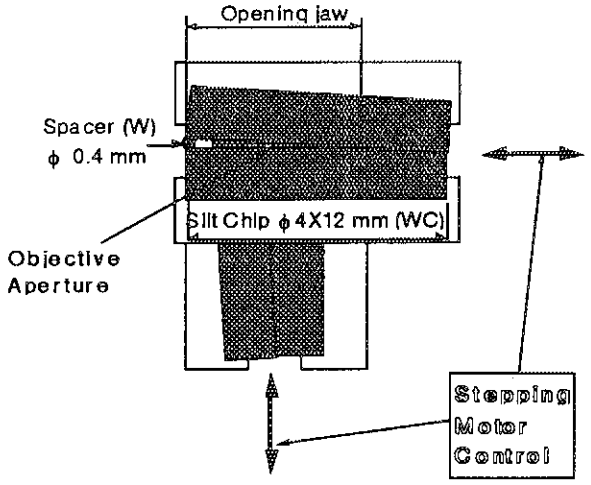

Fig. 2 Schematic diagram of the microslit for the vertical (Y) direction.

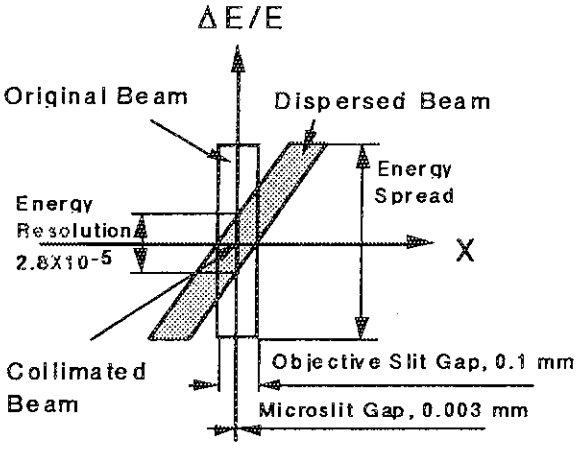

Fig. 4 Energy dispersion by the analyzer magnet, displayed as projections of beams to a (x, ΔE/E) phase plane. A beam at the objective slit of the analyzer magnet which is indicated by a upright square is transformed to one at the microslit indicated by parallelogram. A center bold line indicates a beam collimated by the microslit gap (X).

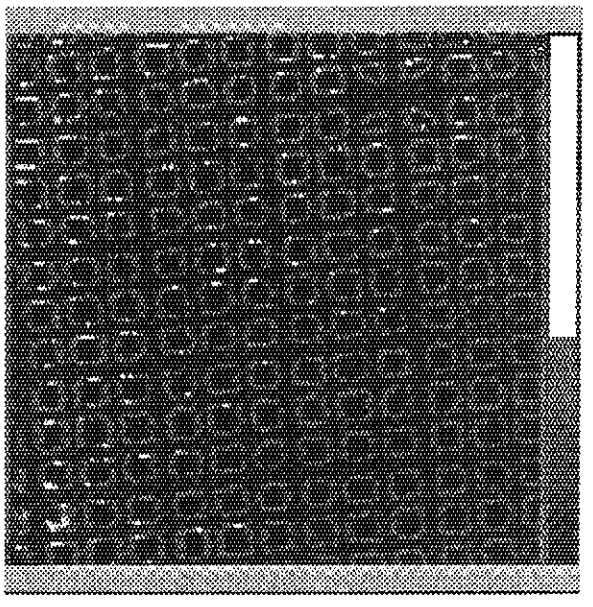

Fig. 3 Secondary electron image of a Cu mesh.

9.3 DEVELOPMENT OF VISUAL BEAM ADJUSTMENT METHOD FOR CYCLOTRON

Takashi AGEMATSU, Kazuo ARAKAWA, Susumu OKUMURA, Yoshiteru NAKAMURA, Watalu YOKOTA, Mitsuhiro FUKUDA, Takayuki NARA, Ikuo ISHIBORI, Tetsuya OKAMURA* and Toshiki TACHIKAWA*

Advanced Radiation Technology Center, JAERI
* Sumitomo Heavy Industries, Ltd.

I. INTRODUCTION

A cyclotron design requires a large number of physical theories, calculation codes and analysis of the beam trajectory. These codes and analysis results are helpful but have not been used in actual operation. For development of new cyclotron control techniques, we have developed a computer-based visual assistance system[1] for JAERI AVF cyclotron[2] by using above the codes. To examine reliability of this system, it is needed to compare the result of the simulation with that of the actual operation.

II. HUMAN INTERFACES

This system provides three kinds of visual human interfaces for beam parameter adjustment; (a) Beam trajectory is rapidly calculated and graphically displayed whenever the operators change the cyclotron parameters, (b) Feasible setting regions (FRS's) of the parameters which satisfy beam acceptance criteria of the cyclotron's are indicated, (c) Search traces, being a historical visual map of beam current values represented by various colored dots, are superimposed on the FRS's.

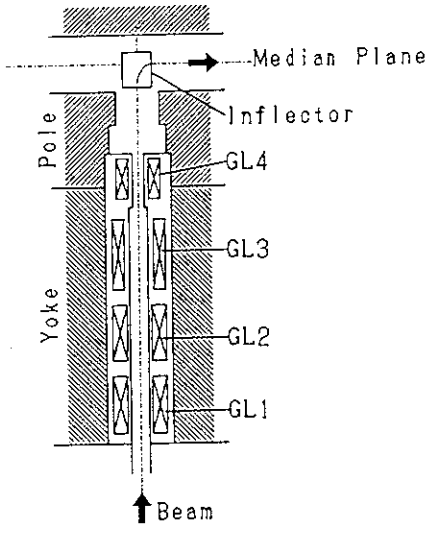

Fig. 1 Cross section of the axial injection block.

The system treats three blocks divided for the cyclotron control: the axial injection, the central region and the extraction. This system is constructed by the language of C and works on workstation of VAX-3100 connected through Ethernet with computers controlling[3] the cyclotron.

III. EVALUATION OF SIMULATION

(1) Axial Injection Block

The axial injection block treats a region between the bottom of the cyclotron yoke and the inflector as shown in Fig. 1. There are four Glaser lenses (GL1,2,3,4) with adjustable focal lengths. The beam is led into the cyclotron through a small gap of the inflector entrance by adjusting these lenses. A typical simulated beam envelope is shown in Fig. 2. The FSR's are limited mainly by the geometry of the inflector entrance.

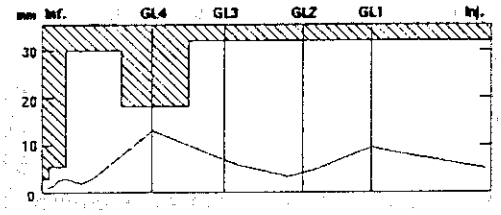

Fig. 2 Typical beam envelope of the axial injection.

We have compared the human interfaces with the results of actual operation in the accelerating conditions of H^+10MeV etc. It is realized that there is discrepancy between the simulated FSR's and the search traces obtained in actual operation. To identify the main reason of the discrepancy, we searched a condition to make a good agreement between the FSR's and the result of actual operation. The simulated beam trajectories deviated from the search trace just after GL4. By correcting the leakage magnetic field from main magnet, the FSR's agree with the search trace, as shown in Fig. 3. More accurate measurement of the leakage magnetic field from the main magnet is required for the better agreement.

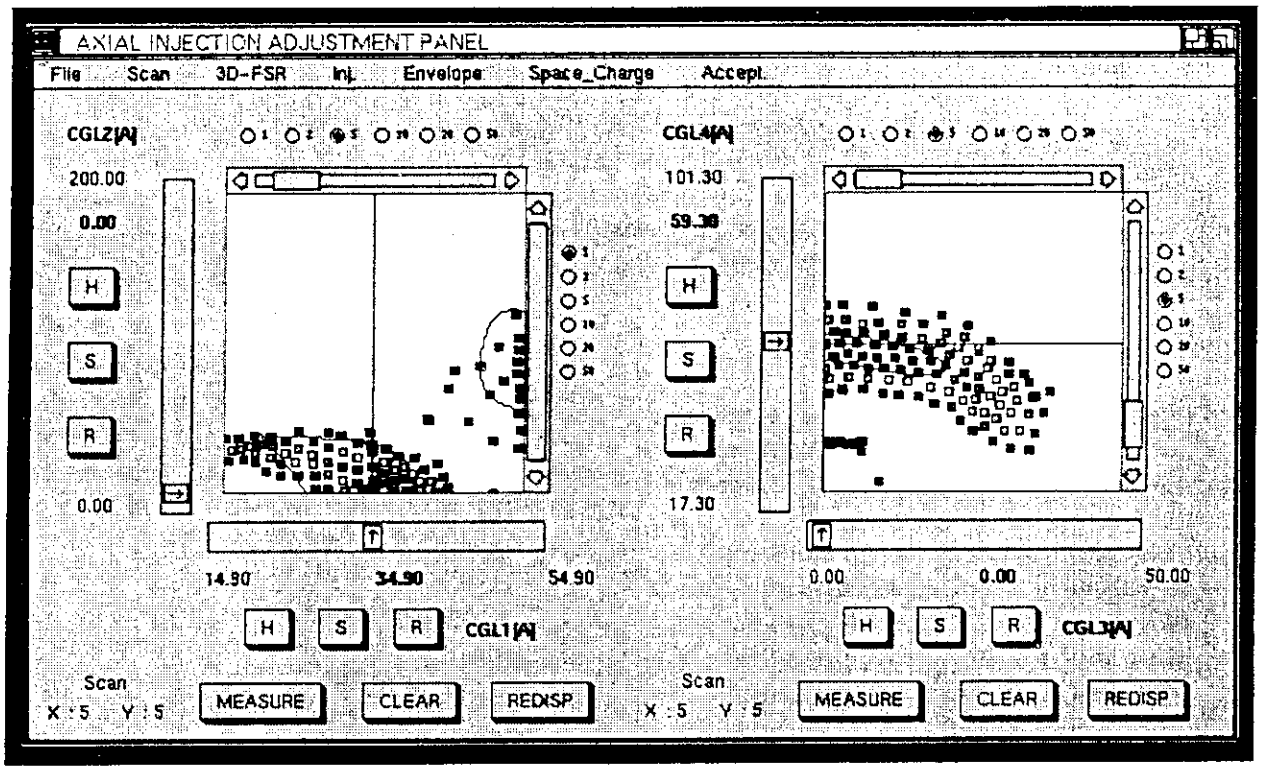

Fig. 3 The feasible setting regions (FSR's) and measured data at the injection block.
Search trace display showing colored dots of the measured beam current values.
The beam condition of H^+ 3.10kV, 1μA at the injection line.

(2) Central Region Block

The central region block, which follows the axial injection block, determines the first turn of the beam trajectory after the inflector. The adjustable parameters in this region are dee voltages, trim coil currents and the phase of beam buncher voltage. These parameters are adjusted so that the beam passes through two sets of phase slits. The beam trajectory and FSR's are calculated from these parameters and magnetic and electric field data. The FSR's are determined by the geometrical condition of the phase slits.

At the first place, we compared the simulated beam trajectory with the results of actual operation. The actual beam positions were measured by the following methods: (a) Searching a beam position of the maximum beam current monitored at the main cyclotron beam probe by moving the phase slit, (b) Searching a beam position by measuring turn patterns using the main probe. Figure 4 shows the top view of a cross section of this block and a simulated trajectory in a solid line and actual slit positions. The trajectory passes through the actual slit positions. The simulation is in good agreement with the actual condition. We will test the system for different values of the magnetic field of the central region, the dee voltage and the phase of beam buncher voltage.

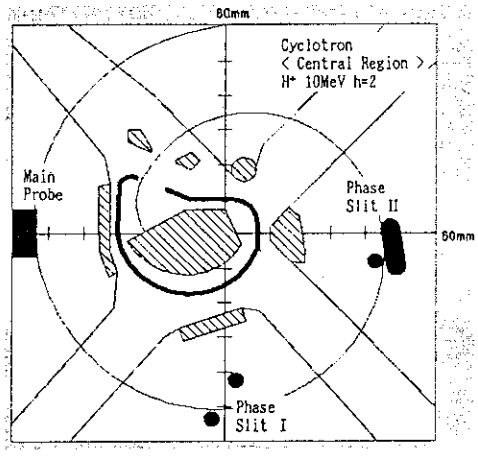

Fig. 4 The central region block.
Simulated beam trajectory and measured beam positions for H^+10MeV in 2nd harmonic mode.

(3) Extraction Block

The beam in the final turn is led into the deflector and the magnetic channel, deflected from the circular orbit, and finally extracted from the cyclotron. In this block, the system simulates the deflected beam

trajectory. At the first step, the beam trajectory entering the deflector is calculated on the basis of the magnetic field data and two beam positions detected by the main and the deflector probes. At the second step, the beam trajectory in the deflector and the magnetic channel is simulated on the basis of the deflector position, the deflecting field and the magnetic channel field. The FSR's were calculated from the above parameters and clearance of the deflector and from the magnetic channel.

An example of simulated beam trajectories for nominal 50MeV, $^{4}He^{+2}$ beam trajectory is shown in Fig. 5. We have executed simulations to get the beam trajectories for several beam energies. The most suitable energy for the trajectory in actual operation condition is in a range from 49.85 to 50.00MeV. Since the actual beam position detected by the main probe is located outside of the standard orbit, the incident angle at the deflector and at the magnetic channel is too large for the standard orbit. So, path of the simulated trajectory is agreement with angle of the deflector and the magnetic channel.

IV. FUTURE ACTIVITY

Precise comparison of the simulated beam trajectory and the actual beam trajectory is planned for the three blocks of the cyclotron under various accelerating conditions. We will upgrade this system to execute simulations for all the available particles and energies. For the extraction block, the extracted beam energy will be measured accurately by the method based on scattering kinematics. It is expected that the result will be fed back to improvement of the system.

REFERENCE

1) T.Okamura and T.Murakami, "An Operator Assistance System for Beam Adjustment of a Cyclotron", IEEE Trans. on Nucl. Sci., Vol.39, No.1, pp.13-20(1992).
2) K.Arakawa, Y.Nakamura, W.Yokota, M.Fukuda, T.Nara, T.Agematsu, S.Okumura, I.Ishibori, T.Karasawa and R.Tanaka "Construction and First Year's Operation of the JAERI AVF Cyclotron", Proc. 13th Int. Conf. on Cyclotron and their Applications, Vancouver, Canada, pp.119-122(1992).
3) S.Okumura, T.Agematsu, W.Yokota, T.Kamiya, M.Fukuda, Y.Nakamura, T.Nara, I.Ishibori, K.Arakawa, M.Maruyama, K.Iso, K.Hoshika and M.Tachibana, "Control System for JAERI AVF Cyclotron", Proc. 13th Int. Conf. on Cyclotron and their Applications, Vancouver, Canada, pp.648-651(1992).

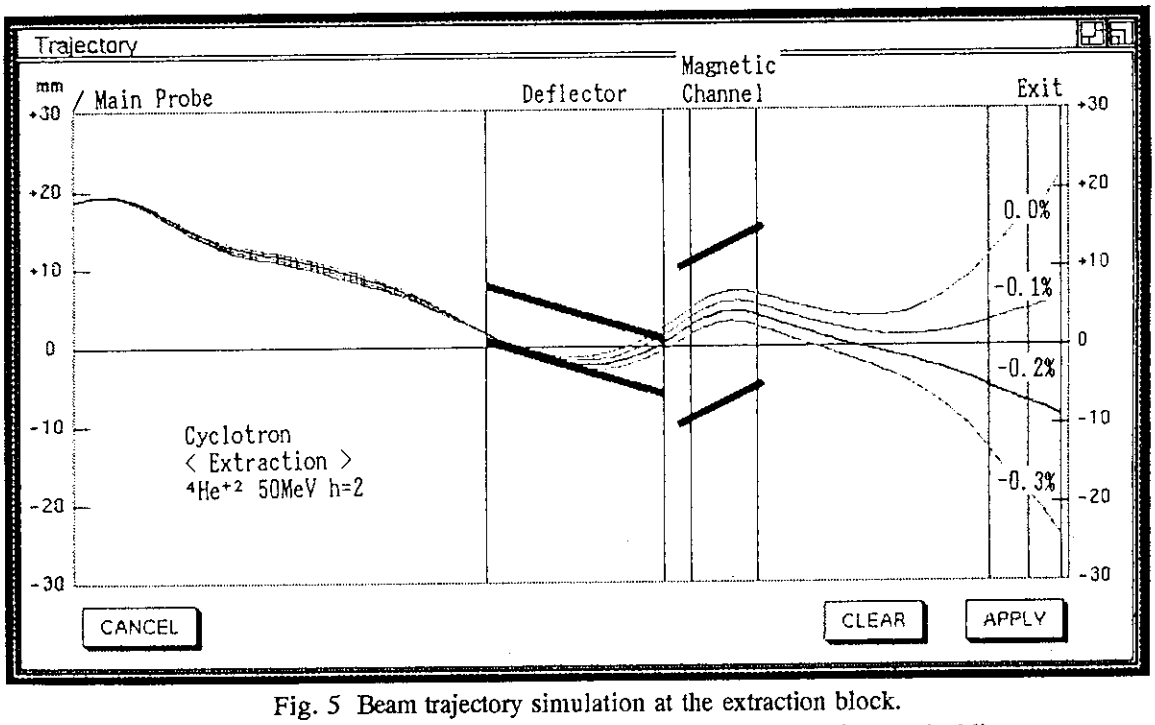

Fig. 5 Beam trajectory simulation at the extraction block.
In this diagram, the spiral beam trajectory is shown as a form of a stretched line.

9.4 Measurements of Beam Characteristics for AVF Cyclotron

S.Okumura, M.Fukuda, T.Agematsu, I.Ishibori, W.Yokota, Y.Nakamura, T.Nara, K.Arakawa
Advanced Radiation Technology Center
Japan Atomic Energy Research Institute

1 Measurement of absolute beam energy

The definite information on the energy of ion particles extracted from an AVF cyclotron is quite important and occasionally mandatory. The ion particle energy inferred from the cyclotron parameters set by the operator should be calibrated by a method ensuring an absolute energy determination.

The energy of the ion particle has been measured absolutely by using the so-called "crossover" technique[1]. This technique is based on scattering kinematics, in particular the variation with the angle of the energy of the particles scattered by elastic and inelastic processes from different target nuclei. It requires a target consisting of a homogeneous mixture of reference nuclei having well-known excited states and projectile nuclei. The absolute energy of the incident particle is obtained from an angle, "crossover angle", at which the recoil projectile particles from light nuclei and the inelastically scattered particles from reference nuclei having well-known excited states have the same energy.

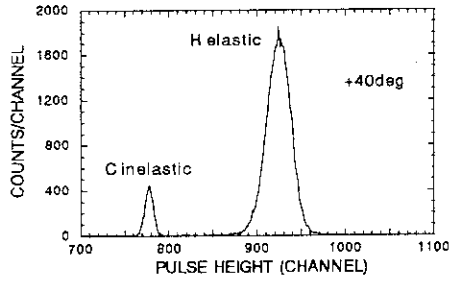

Fig.1. Pulse height spectrum at an scattering angle of 40° for a nominal 10 MeV proton.

A 10 MeV proton was chosen since the crossover angle is relatively large and it is easy to detect the particles at backward angles. A 2.78 mg/cm^2 polyethylene film was used as the target including hydrogen and carbon nuclei to use the 4.439 MeV excited state in carbon. To detect the scattered particles at around the crossover angle, a semiconductor detector was mounted on a movable arm.

Figure 1 shows a typical pulse height spectrum obtained at an scattering angle of 40° with a nominal 10 MeV proton in the scattering chamber at the HE2 target port. The left peak is inelastic scattering on carbon nuclei and the right one is elastic scattering on hydrogen nuclei.

The relationship between the scattered angles and the pulse heights in the both interactions is shown in Fig.2. The crossover angle was evaluated from the crossing point of the interpolating lines for the energies of the elastic and the inelastic scattering. To compensate an asymmetric factor of the scattering geometry, left and right angle measurements were carried out.

The average value of the crossover angle obtained from both angles was 44.3°. The absolute beam energy was evaluated at 9.9 MeV in this case. The uncertainty of the measurement is now under estimation.

We are planning to measure absolute energies for other beam parameters and calibrate the analyzing magnet by the crossover technique.

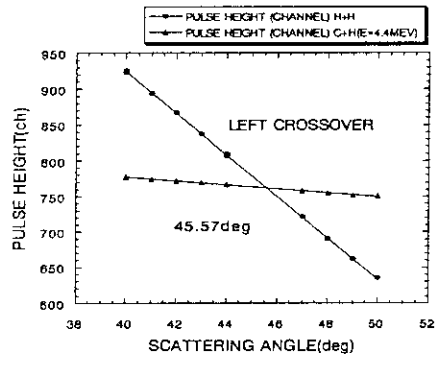

Fig.2. Relationship between the scattering angle and the pulse height for the elastic scattering and the inelastic scattering.

2 Measurement of beam attenuation ratio

Extremely low beam currents below nA region are required in various experiments. Three beam attenuators were installed in the injection beam line of the AVF cyclotron to adjust the beam intensity drastically without changing the cyclotron parameters. A beam attenuator consists of two or

three stainless steel meshes, each of which has an opening ratio of 10^{-1}, 10^{-2} or 10^{-3}. Very low opening ratios less than 10^{-4} can be achieved by combining the meshes in each attenuator. The beam attenuation ratios in the range of the opening ratio from 10^{-1} to 10^{-9} were obtained by measuring the attenuated beam intensity.

The beam attenuation ratios of the beam attenuators[2] were measured to adjust the beam intensity properly. For 10, 20, 45 and 70 MeV H^+ beams, the attenuated beam currents were measured by the Faraday cup installed in the exit of the cyclotron in the opening ratio from 10^{-1} to 10^{-3}. For 260 MeV Ne^{7+} beam, an ionization chamber was used for measuring the opening ratio from 10^{-1} to 10^{-7}. The ionization current was calibrated by a Faraday cup at an beam attenuation ratio of 10^{-1}. For 220 MeV C^{5+} beam, CR-39 track detectors were used to count each ions of the beam and the attenuated currents were estimated from the counts and the exposure time.

The beam attenuation ratios are in agreement with the total opening ratios of the meshes in the order of magnitude, as shown in Fig.3.

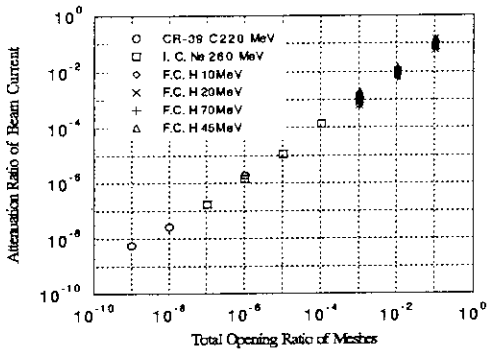

Fig.3. Attenuation ratios of the beam current as a function of opening ratio of attenuators.

3 *Performance of modified beam scanner*

The beam scanner[3] for uniform irradiation of a large area by high-energy intense beams is used for various purposes of materials science. It is composed of a set of electromagnets for horizontal and vertical deflections. The beam is scanned by the magnetic fields varying in triangular waves in a frequency of 50 Hz in the horizontal direction and 0.5 - 5.0 Hz in the vertical one.

Figure 4 shows the wave form of the current supplied to the electromagnet of the horizontal direction. The distortion near the zero-cross point is caused by the transistor switching for polarity change and the distortion near the peak is caused by the induced electromotive force due to relatively high frequency.

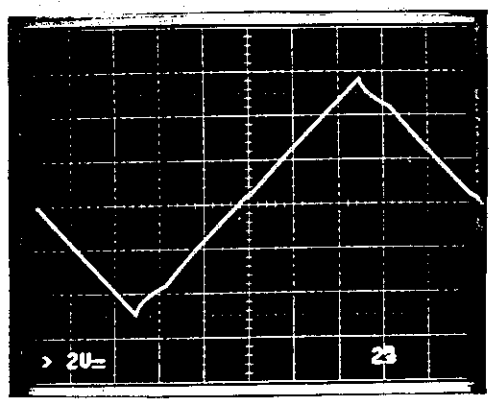

Fig.4. A typical current wave form of the horizontal scanning magnet.

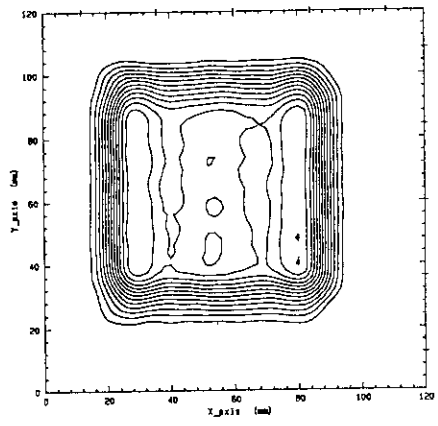

Fig.5. An example of fluence distribution of 45 MeV H^+ beam measured by CTA film dosimeters.

The relative fluence distributions of the scanned beam were measured by cellulose triacetate (CTA) film dosimeter[4]. This measurement showed lack of uniformity in the distribution. So we developed a simulator to evaluate fluence distributions from the scanning conditions. The results calculated by the simulator revealed that the distortions of the current wave forms caused lack of uniformity, as shown in Fig.5.

The beam scanner was modified to decrease the distortions by change of the electrical circuit from the pole switching type to the push-pull one. The current wave form after the modification is shown in Fig.6. The distortions were disappeared in the wave form. The better uniform fluence distribution were measured after the modification as shown in Fig.7.

These measurements showed that the uniformity, in terms of the deviation from the maximum average fluence, was improved from ±15% to ±4%.

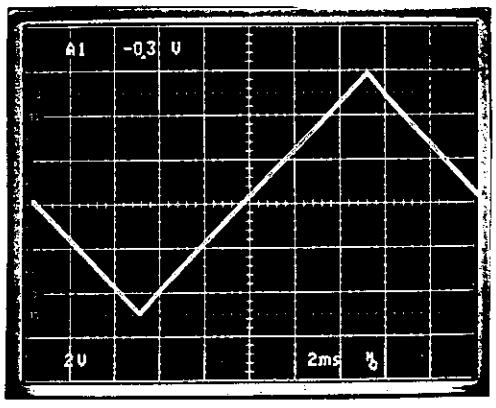

Fig.6. A typical current wave form of the scanning magnet after modification of the beam scanner.

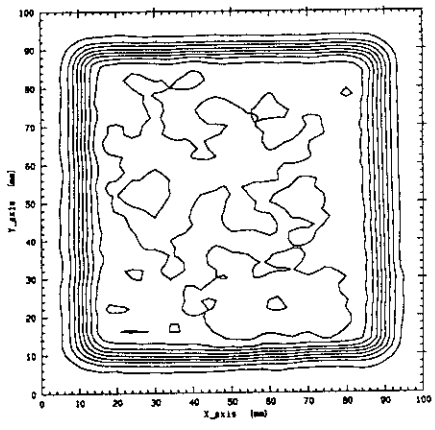

Fig.7. An example of fluence distribution of 175 MeV Ar^{8+} beam measured by CTA film dosimeters after modification of the beam scanner.

4 Real-time Measurement of two-dimensional fluence distribution by PPAC

Film dosimeters have been widely used to measure fluence distributions of scanned ion beams because of the easy handling, but it takes long time for the measurement because of the off-line procedure.

A parallel-plate avalanche counter(PPAC)[5] has been applied to the real-time measurements of two-dimensional fluence distributions in large irradiation fields. The PPAC is a kind of gas proportional counters and has a wide effective area of 120 × 120 mm^2 which is available to detect the incidence position of energetic ion particles. The incidence position on the plane of coordinates can be detected in a charge division method. The position of one ordinate is calculated from the charge ratio measured from the both sides of the electrode which is divided into parallel strips and connected with both neighbors by 500 Ω resistors. The maximum counting rate is about 1k cps in this case because of the long decay time of the output signal from the preamplifier. Therefore, beam attenuators were used in this measurement to reduce the beam intensity drastically.

The first test using the PPAC was carried out to measure fluence distributions of a scanned beam of a 260 MeV Ne^{7+} beam in the irradiation chamber at the LD target port. An example of the fluence distributions measured on irradiation is shown in Fig.8. The two-dimensional fluence distributions could be measured in real time by using the PPAC.

We are planning to measure other kinds of ion beams, especially light ions.

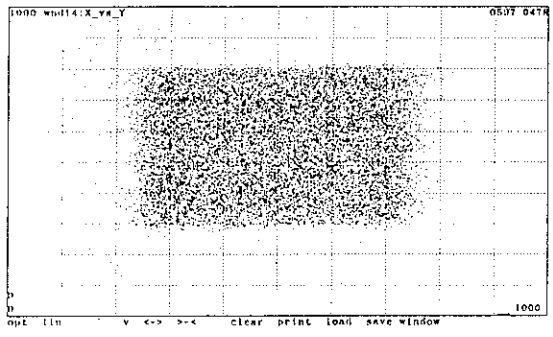

Fig.8. An example of real-time fluence distribution measurements by PPAC. The scanning width is 50 × 50 mm^2. One scale is 11 mm in each direction.

References

1) B.M.Bardin and M.E.Rickey,"Kinematic Method for Determination of Accelerator Beam Energies", Rev. Sci. Instr. 35 (1964) 902-903.
2) S.Okumura et al.,"DEVELOPMENT OF BEAM ATTENUATOR", TIARA Annual Report, Vol.2, 196-197 (1992).
3) K.Arakawa et al., "Beam Scanners", TIARA Annual Report, Vol.1, 31-33 (1991).
4) R.Tanaka et al.,"Effects of Temperature, Relative Humidity,and Dose Rate on the Sensitivity of Cellulose Triacetate Dosimeters to Electrons and γ-Rays", Int. J. Radiat. Tsot., Vol.35, 875-881 (1984).
5) S.Okumura et al., "DEVELOPMENT OF PARALLEL PLATE AVALANCHE COUNTER FOR FLUENCE-RATE MEASUREMENT", TIARA Annual Report, Vol.2, 198-199 (1992).

9.5 Measurements of External Beam Phase Width for 10 and 70 MeV Protons

M. Fukuda, S. Okumura, K. Arakawa and T. Karasawa
Advanced Radiation Technology Center, JAERI

1 INTRODUCTION

A constant orbit method is adopted to determine the acceleration voltage of the JAERI AVF cyclotron. The total turn number of the beams reaches 550 for a harmonic number of h=1, 265.for h=2 and 210 for h=3. RF phase of the internal beam[1] is quite sensitive to field deviations from isochronism because of the large number of turns.

The initial phase width of the beam can be defined with two sets of slits[2] cutting the beam radially on the first turn. The internal beam produced without phase cutting spreads radially by a few centimeters before extraction. Extraction efficiency is limited due to multi-turn extraction, and expected to be improved by confining the phase width. We have measured intensity distributions vs. phase of the external beams for 10 and 70 MeV protons in order to investigate the correlation between the beam phase width and the positions of the phase cutting slits.

2 MEASUREMENT APPARATUS

The external beam phase has been measured with a set of plastic scintillators. The plastic scintillators are installed at the end of a beam line, at 41.2 m from the cyclotron. The telescope-type plastic scintillators are used to distinguish the protons from other particles produced at titanium foil of 14 mg/cm^2. The beam intensity is reduced using beam attenuators[3] to allow for direct proton detection.

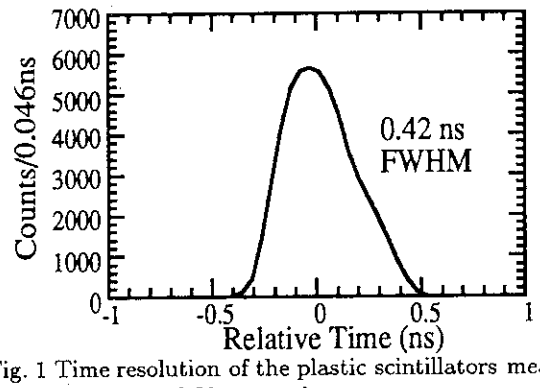

Fig. 1 Time resolution of the plastic scintillators measured with a 70 MeV proton beam.

A time spectrum is obtained by measuring the time lag between signals coming from the detector and the RF reference. Correlating the signals of a pair of scintillators, the time resolution has been measured with a 70 MeV proton beam. The result of this measurement is shown in Fig. 1. The time resolution is 0.42 ns FWHM, which corresponds to an individual resolution of σ=0.12 ns.

3 10 MeV PROTON BEAM

The external beam phase of the 10 MeV protons was measured by detecting the protons directly. A schematic layout of the measuring system is shown in Fig. 2. The initial beam intensity of around 10 nA was lowered by a factor of 10^{-6} with the attenuators. Figure 3 shows the beam phase distributions for the two cases, with and without phase defining slits. Without phase slits the beam intensity distribution is split into several components. The full width of the beam phase reaches 75°, which includes the broadening effect due to the energy spread. The phase distribution for the beam with phase cutting shows two components separated by 18°, which are narrow peaks of 2.2° and 3.4° FWHM phase width.

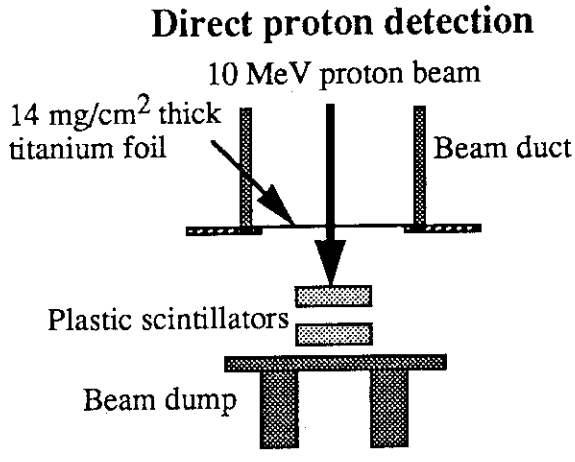

Fig. 2 Schematic layout of the measuring system for a 10 MeV proton beam. The protons were detected directly.

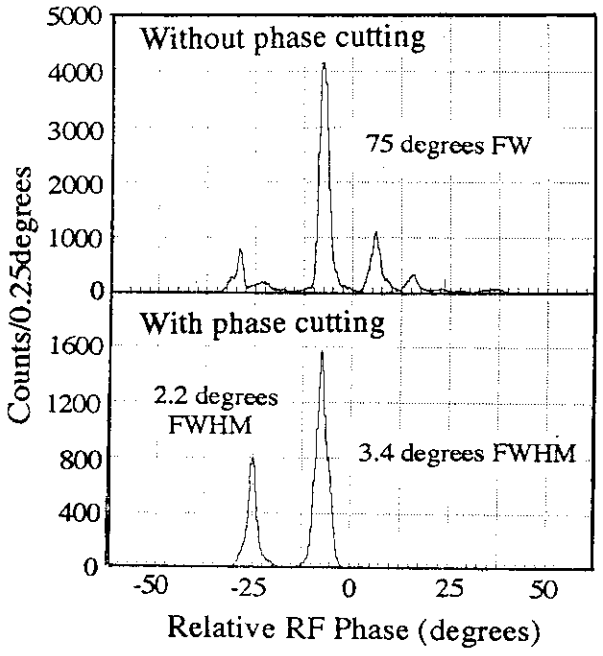

Fig. 3 External beam phase distributions for the 10 MeV protons accelerated using the second harmonic at a RF frequency of 14.970 MHz. Phases are relative, and zeros are not absolute.

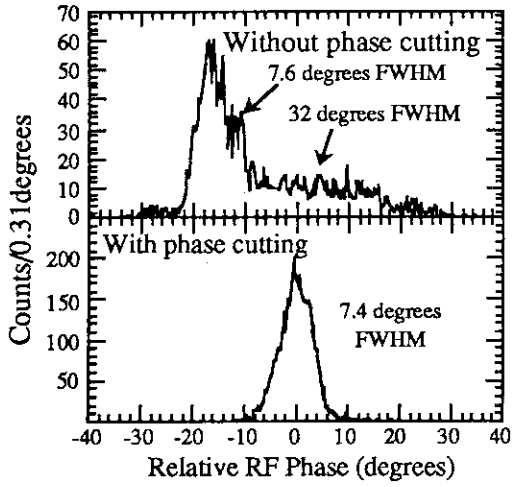

Fig. 5 External beam phase distributions for the 70 MeV protons accelerated using the first harmonic at a RF frequency of 18.919 MHz. Phases are relative, and zeros are not absolute.

4 70 MeV PROTON BEAM

For the 70 MeV proton beam, the beam phase measurement has been carried out by detecting protons scattered elastically from the titanium foil. The layout of the measuring system is shown in Fig. 4. For detecting the scattered protons with internal phase cutting the attenuation factor was only 10^{-1} while it was 10^{-5} without phase cutting. Phase distributions for the beams with and without phase cutting are shown in Fig. 5. For the analysis of the full beam, we assumed the phase spectrum to be composed of two peaks. Phase widths of the two components have been found to be 7.6° and 32° FWHM. The phase width of the beam with phase cutting has been evaluated at 7.4° FWHM.

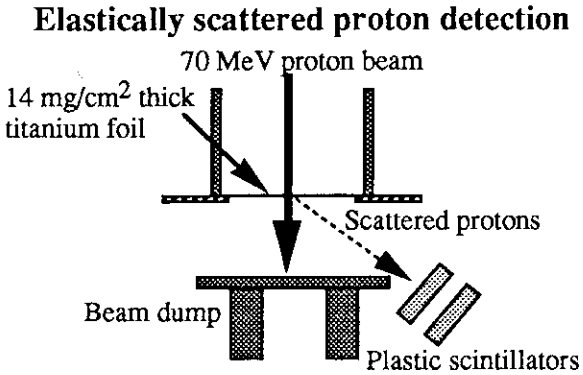

Fig. 4 Schematic layout of the measuring system for a 70 MeV proton beam. The protons scattered elastically from the titanium foil were detected.

5 CONCLUSION

The external beam phase for the 10 and 70 MeV proton beams has been measured with a set of plastic scintillators. A narrow phase width of 2.2° and 3.4° FWHM could be measured for the 10 MeV protons with the beam intensity reduced. External beam phase width of the 70 MeV protons has been found to be reduced to 7.4° with phase defining slits. The external beam phase depends on the internal phase, but also on the particle energy as well as on the transmission probability through the extraction region and the beam transport line. Internal and external beam phase distributions are now being simulated with an orbit calculation program.

References

1) M. Fukuda, et al., "RF Phase Studies of Internal and External Beams for for JAERI AVF Cyclotron", in Proc. of the 9th Symposium on Accelerator Science and Technology, Tsukuba, Japan, August 1993, pp. 306-308.
2) M. Fukuda, et al., "Beam Studies of Injection to Extraction System for JAERI AVF Cyclotron", in Proc. of the 13th Int. Conf. on Cyclotrons and their Applications, Vancouver, Canada, July 1992, pp. 423-426.
3) S. Okumura, et al., "Development of Beam Attenuator", JAERI TIARA Annual Report, Vol. 2, (1992)196.

9.6 PRESENT STATUS AND BEAM ACCELERATION TESTS ON CYCLOTRON

Kazuo ARAKAWA, Yoshiteru NAKAMURA, Watalu YOKOTA, Mitsuhiro FUKUDA, Takayuki NARA, Takashi AGEMATSU, Susumu OKUMURA and Ikuo ISHIBORI

Advanced Radiation Technology Center, JAERI

I. INTRODUCTION

Large AVF cyclotrons, so far, have been used mostly for fundamental nuclear physics and medical application to radiation therapy and radioisotope production. The JAERI AVF cyclotron[1,2] is the first one dedicated to R&D in materials science and other irradiation purposes. These applications of the cyclotron require that many kinds of light and heavy ions can be accelerated in a wide range of energies. To meet the requirement, continuing efforts have been made on new beam development, improvement of beam extraction and transmission, etc.

II. PRESENT STATUS AND DEVELOPMENT

(1) Cyclotron

The AVF cyclotron was smoothly operated for experimental utilization in FY 1993. The beam time for experiments was remarkably increased from 1378 to 2559 hours in FY 1993. Twenty-one kinds of ion species were provided for experiments.

The beam extraction system consists of an electrostatic deflector and a magnetic channel and also of a gradient corrector to focus the beam horizontally. The positions of the deflector and the magnetic channel can be controlled remotely. However, the position of the gradient corrector of a passive type could not be moved remotely. Recently, the gradient corrector was replaced by remote driving type one for easily optimizing a focus the beam horizontally from cyclotron. A RF amplifiers (EIMAC 4CW800B and 4CW50,000E) were also replaced by new ones in the yearly overhaul.

The accumulation of induced radioactivity in the acceleration chamber is making it more difficult to conduct maintenance work inside the cyclotron. The strongest source of radiation is the electrostatic deflector. The septum electrodes of the deflector were replaced by new ones. Furthermore, we prepared a set of new deflector for rapid replacement in case of trouble.

For the protection against radiation hazards, however, it will be necessary to replace some of the strongly activated parts, such as main probe-head, magnetic channel, and magnetic channel probe-head.

The frequency of troubles under cyclotron operation has been relatively low and is gradually decreasing.

III. BEAM DEVELOPMENTS

(1) New Beam Acceleration

The beam acceleration tests have been conducted for 30 MeV H^+, 220 MeV $^{12}C^{5+}$ and 100 MeV $^{16}O^{5+}$. Protons is generated by the multicusp ion source, and other ions by the ECR ion source. The results of the beam acceleration test are summarized in Table 1. The 30 MeV H^+ beam current is limited within 2.2 μA for the present to avoid unnecessary damage of the machine parts. The extracted beam current for $^{12}C^{5+}$ and $^{16}O^{5+}$ ions are 170 nA and 1.7 μA (electrical ampere) respectively.

(2) Extraction Current and Transmission

Particles accelerated and extracted so far are listed in Table 1. The extraction efficiency is defined by the ratio of the beam current measured with the main probe at r=900 mm to that with the Faraday cup (FC) just after cyclotron. The average extraction efficiencies for harmonic 1, 2 and 3 are 50.5 %, 63.2 % and 46.2 %, respectively.

The overall transmission efficiency is defined by the ratio of the beam current with the FC just after analyzing magnet at the injection line to that with FC just after cyclotron. The average transmission efficiencies for harmonic 1, 2 and 3 are 10.6 %, 13.4 % and 6.9 %, respectively. Recently it increased up to 15 - 20 %. The best extraction and overall transmission efficiency was 79 % for 45 MeV H^+ and 22 % for 220 MeV $^{12}C^{5+}$, respectively. The maximum beam currents of heavy ions such as Ne, Ar and Kr mainly depend on the ability of the ion source.

(3) Single Pulse Extraction

The beam chopping system[3] consists of a pulse voltage chopper (P-chopper) and a sinusoidal voltage chopper (S-chopper). The P-chopper was made to chop DC beams from the ion sources into pulse beam in the injection line. The S-chopper was made to extract a single beam pulse after the exit of the cyclotron. The single pulses were successfully extracted for 70 MeV H^+ and 175 MeV $^{40}Ar^{8+}$ ions using a chopping system as shown in Table 2.

IV. RECENT IMPROVEMENT

(1) Beam Attenuator

Three beam attenuators installed in the injection line allow to control the beam intensity injected into the cyclotron. The beam intensities on the targets can be easily controlled in an attenuation rate range of 10^{-1} to 10^{-15}. Each attenuator consists of two or three meshes, each with a hole ratio of 10^{-1}, 10^{-2} or 10^{-3}. The details of this system is reported separately in this report[4].

(2) Pulse Beam Detection System

The pulsed beam experiments require non-destructive methods to monitor the beam during the experimental time and high sensitivity to a wide variety of beams from proton to heavy ions in wide ranges of the energy and the beam intensity. For these reasons, we have developed a highly sensitive beam pulse detection system using a micro channel plate (MCP) with a high signal gain and high time resolution. The pulsed beam can be detected by secondary electrons emitted from a target when the beam passing through it. The system consists of an assemble type MCP (F4655-10, Hamamatsu photonics Ltd.), seven sets of electrodes spaced by insulator rods and targets for the secondary electron emission.

(3) Beam Scanning System

The uniform irradiation of high-energy, intense beam over a large area is required for testing radiation resistance of organic materials and solar cells. The cyclotron beam is two-dimensionally scanned by using a pair of deflection electromagnets. The horizontal scanning frequency is 50 Hz and the vertical one 0.5, 1.0, 2.5 and 5.0 Hz.

Cellulosetriacetate (CTA) film dosimeters has been successfully applied relative measurement of two-dimensional fluence distribution as an integral method for H, He, C, Ar and Kr ions. However, this method does not give fluence distribution in real time.

For these reasons, we calculated the fluence distribution by Simulating the scanned beam dynamics on the basis of the wave form of scanning coil current, then compared the simulated distributions with the measured ones. The both were in good agreement and the beam scanning condition to get good

uniformity was optimized by using this simulation.

At first, the uniformity of the two-dimensional fluence distribution of ion beams was ±15 %, because of the wave form distortion of the excitation current for the scanning electromagnet. An improvement of the power supply of the scanner resulted in a good fluence uniformity within ±4%[5].

(4) Measurement of Fluence Distribution

The fluence distribution of the irradiated area was measured by CTA dosimeters based on the radiation induced optical density change of the film. However, this method does not give fluence distribution in real time. To monitor two-dimensional fluence distribution in real time, we are developing a parallel plate avalanche counter (PPAC) as a monitor of the fluence distribution[4]. The PPAC can detect the incidence positions of the particles within a scanned area of 120 x 120 mm^2 by the charge division method. The two-dimensional fluence distributions under ion beam irradiation was successfully measured by PPAC.

(5) Computer-Based Visual Assistance System

A computer-based operator assistance system was installed for the cyclotron. This system provides a CRT display for cyclotron beam trajectories, permissible setting regions of beam parameters, and searching traces designed to optimize beam parameter adjustment[6]. The details of this system is reported separately in this report.

REFERENCES

1) K.Arakawa, Y.Nakamura, W.Yokota, M.Fukuda, T.Nara, T.Agematsu, S.Okumura, I.Ishibori, T.Karasawa, R.Tanaka, A.Shimizu, T.Tachikawa, Y.Hayashi, K.Ishii and T.Satoh, Proc. 13th Int. Conf. on Cyclotron and Their Applications, Vancouver, Canada, pp.119-122 (1992).
2) K.Arakawa, Y.Nakamura, W.Yokota, M.Fukuda, T.Nara, T.Agematsu, S.Okumura and I.Ishibori, Proc. 9th Sympo. on Accele. Sci. and Tech., Tsukuba, Japan, Aug. pp.202-204 (1993).
3) W.Yokota, M.Fukuda, K.Arakawa, Y.Nakamura, T.Nara, T.Agematsu, S.Okumura and I.Ishibori, Proc. 13th Int. conf. on Cyclotron and Their applications, Vancouver, Canada, pp581-584(1992).
4) S.Okumura, M.Fukuda, W.Yokota, Y.Nakamura, T.Nara, T.Agematsu, I.Ishibori and K.Arakawa, presented at this report.
5) T.Agematsu, S.Okumura and K.Arakawa, JAERI-M 94-071.
6) T.Agematsu, K.Arakawa, S.Okumura, Y.Nakamura, W.Yokota, T.Nara, M.Fukuda, and I.Ishibori, Proc. 9th Sympo. on Accele. sci. and Tech., Tsukuba, Japan, Aug. pp437-439 (1993).

Table 1 Results of Extracted Intensity and Transmission

Particle	Energy (MeV)	Harmonic No.	Frequency (MHz)	Extracted Intensity (eμA)	Extraction Efficiency (%)	Transmission (%)
H^+	10	2	14.97	10	68	12
	20	2	21.03	5.0	77	11
	30	1	12.77	2.2	51	22
	45	1	15.46	30	79	14
	70	1	18.92	5.0	53	12
	90	1	21.14	10	39	2.0
D^+	10	2	10.63	11	29	3.7
	35	2	19.70	40	59	4.6
	50	1	11.76	20	49	7.2
$^4He^{2+}$	20	2	10.67	5.5	69	11
	50	2	16.77	20	62	17
	100	1	11.81	10	32	6.4
$^{12}C^{5+}$	220	2	20.42	0.17	77	22
$^{16}O^{5+}$	100	3	17.98	1.7	34	8.1
$^{20}Ne^{6+}$	120	3	17.70	0.30	31	2.0
$^{20}Ne^{7+}$	260	2	17.48	0.33	70	19
$^{36}Ar^{8+}$	195	3	16.82	2.4	50	10
$^{36}Ar^{10+}$	195	3	16.83	0.10	43	1.2
$^{40}Ar^{8+}$	175	3	15.14	3.0	73	13
$^{40}Ar^{11+}$	330	2	13.68	0.21	49	14
$^{40}Ar^{13+}$	420	2	16.24	0.03	63	13
$^{84}Kr^{20+}$	520	2	11.98	0.045	72	20

Table 2 Results of Single Pulse Extraction

particle	$^{40}Ar^{8+}$	H^+
energy	175 MeV	70 MeV
pulse interval	3.3μs	2.11μs
	4.75μs	1.27μs
pulse width	-	1.95ns
charge	$7*10^{-14}$ C/pulse	$2*10^{-15}$ C/pulse
detector	SSD	Sintilator

9.7 Construction of JAERI 18-GHz ECR Ion Source

W. Yokota, T.Nara, Y.Saitoh, Y.Ishii and K.Arakawa
Advanced Radiation Technology Center, JAERI

Introduction

Ions with mass to charge ratio (M/Q) less than 6.5 can be accelerated by the JAERI cyclotron, and Xe ion may be a limitation with the OCTOPUS source which has been used since the cyclotron facility was completed. On the other hand, the research plan requires heavier ion species including metal ions in wider energy range. We constructed a new ECR ion source (ECR-18) with high performance in generating highly charged ions and metal ions. The basic design of the source is described in the last annual report[1] and elsewhere[2,3]. The detailed designs of the source, electric current sources, a microwave power source and a beam analyzing system were completed by October in 1993. After being manufactured, they were installed in the 2nd ion source room underground of the cyclotron building in February, 1994.

Detailed Source Design and Measured Field

A microwave frequency of 18 GHz was adopted because it may be the highest that can be obtained by a commercially available klystron tube and applied for $2\omega_{ce}$ mode operation by use of room temperature magnets. The maximum magnetic field strength over 1.4 T was a goal for both mirror and sextupole fields. The goal field strength was obtained by calculation and the basic design of the magnets and the plasma chamber was defined in 1992. In the detailed design, some minor changes were made because of technical problems and they are shown in Table 1 together with the final design parameters. Magnetization of permanent magnet strongly depends on manufacture process, and it is difficult to make the best of materials characteristics. To achieve the goal field strength, the thickness of the sextupole magnet was increased by 5 mm as margin. According to this, the larger bores of the mirror coil magnets, in which the sextupole magnet is inserted, was also enlarged. Calculation showed this change little reduced the mirror fields.

Measured mirror field distribution at the highest coil currents is shown in Fig. 1 in comparison with that calculated. The agreement is good both in the shape and in strength. Small displacement of the peaks and disagreement at the valley may be attributed to that the distance between the mirror coils might be shorter in the measurement than in the calculation. On the other hand, maximum value of the sextupole field is about 95 % that of the goal and this does not make $2\omega_{ce}$ resonance over a wide area on the surface of the plasma chamber. However, the field strength is enough for confining plasma, and this failure may not be a problem in actual operations. A picture of the source is shown in Fig. 2.

Beam Analyzing System

The ion beams extracted from the source is focused by an electrostatic einzel lens just downstream of the extraction electrode and ion species are selected by the beam analyzing system. As shown in Fig. 3, the system consists of a 90° analyzing magnet and two chambers for beam diagnosis. The chambers are equipped with a Faraday cup, two pairs of X-Y slits at the focus points of the magnet and two turbo-molecular pumps. A beam profile monitor and an emittance monitor will be installed in the future. The analyzing magnet produces the highest field of 1.7 T and can bend ions with a magnetic rigidity twice as much as the maximum value with which the ions can be accelerated by the cyclotron.

Power Supply

It is generally considered from many experiences that a microwave power of a few hundreds watts is enough for small ECR plasma. In our case, the size of plasma is relatively large and the higher frequency brings about larger power loss in the waveguides. Therefore the maximum output power of the microwave generator was defined at 2.5 kW. Microwave is fed axially into the plasma chamber from the rear end.

Four independent current sources were prepared for the two mirror coils, the solenoid coil and the analyzing magnet. The maximum current is 700 A for the mirror and the solenoid coils, and 125 A for the analyzing magnet.

The total power consumption of the coils and power supplies is about 260 kW at full excitation. Generated heat are removed by a water-cooling system.

Summary

The ECR-18, a beam analyzing system and power supplies have been constructed and installed. Ion generation will be started immediately after high vacuum being obtained in the chambers. The source will be optimized by generation of Ar ions this fiscal year to attain high performance in generating highly charged ions. The metal ion generation method, which has been developed with another ECR ion source now in use, will be applied to ECR-18 in next stage. After completion of development, the source will be connected to the cyclotron.

References

1. W.Yokota, T.Nara, Y.Saitoh, Y.Ishii and K.Arakawa, JAERI TIARA Annual Report 1992 (vol.2), p.179
2. W.Yokota, Y.Saitoh, Y.Ishii, T.Nara and K.Arakawa
Proc. of Int.Workshop on ECR Ion Source, May 6-7, 1993,Groningen ,Netherlands, p.245
3. W.Yokota, T.Nara, Y.Saitoh, Y.Ishii and K.Arakawa, Proc. of the 9th Symposium on Accelerator Sci. and Tech., Aug 25-27, 1993, Tsukuba, Japan, p.92

Table 1 Specification of the new ECR ion source. Parameter values of the basic design are shown if they are different from the final values.

	final design and measured field	basic design and calculated field
Ion Source		
mirror coil (including yoke)		
number	2	
outer diameter	104 cm	102 cm
inner diameter	8.0 cm (smaller)	
	18.5 cm (larger)	18.0 cm
length	27 cm	
number of turn	224	
maximum field	1.4 T (on axis)	
solenoid coil		
number	1	
outer diameter	82 cm	
inner diameter	18.0 cm	17.5 cm
number of turn	206	200
maximum field	0.9 T (on axis)	0.7 T
multipole permanent magnet		
number of pole	6	
material	NdFeB	
thickness	4.5 cm	4.0 cm
length	30 cm	
bore diameter	8.0 cm	
maximum field	1.05 T	1.10 T
(at 0.5 cm distance from inner surface)		
plasma chamber		
length	100 cm	
outer diameter	7.5 cm	
inner diameter	7.0 cm	
Power Supply		
microwave generator		
number	1	
power tube	klystron	
frequency	18 GHz	
maximum power	2.5 kW	
mirror coil current supply		
number	2	
maximum current	700 A	
maximum voltage	67 V	70 V
stability	$1*10^{-3}$	
solenoid coil current supply		
number	1	
maximum current	700 A	
maximum voltage	58 V	55 V
stability	$1*10^{-3}$	

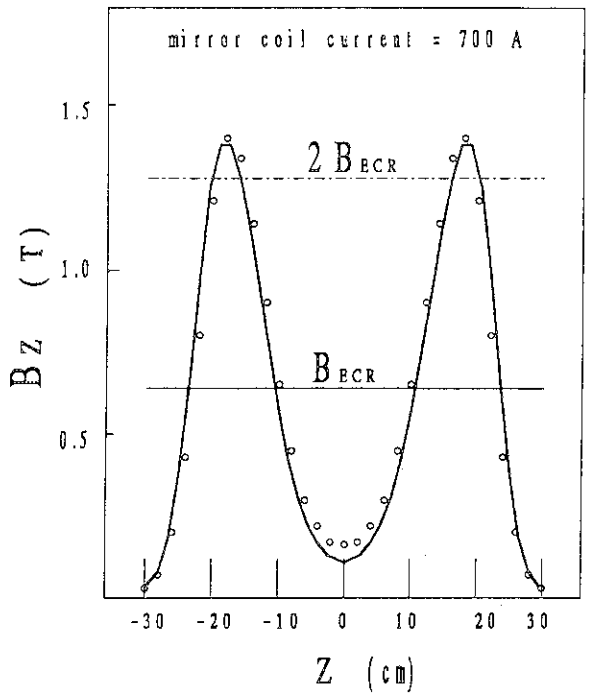

Fig. 1 Mirror magnetic field distribution on the axis: calculated (solid line) and measured (open circle).

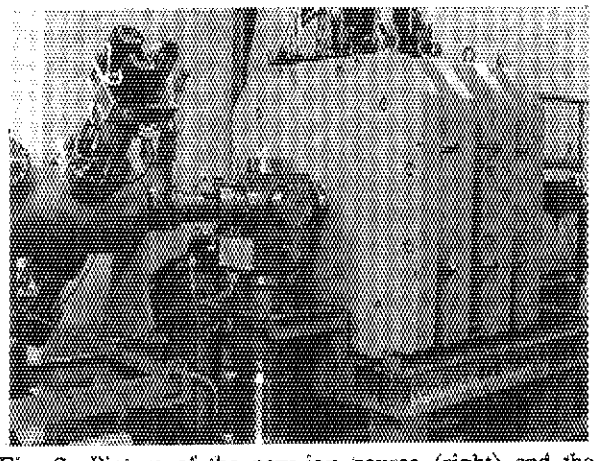

Fig. 2 Picture of the new ion source (right) and the beam diagnosis chamber with a pair of X-Y slits (left).

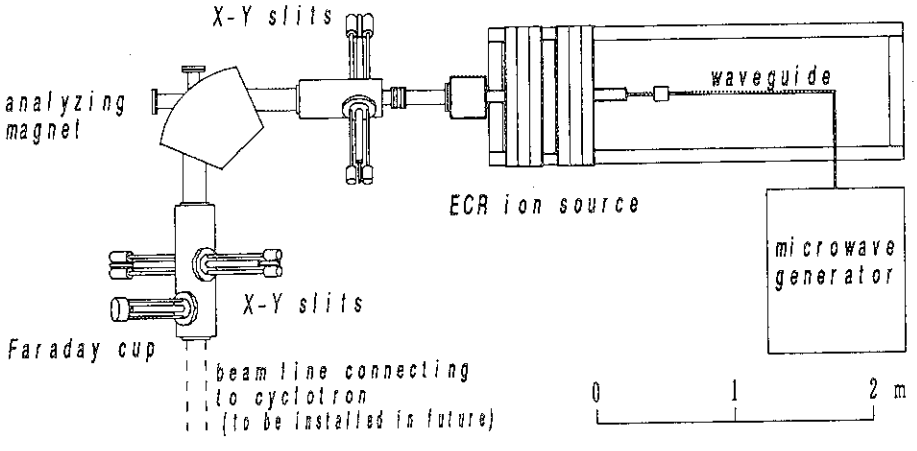

Fig. 3 Schematic layout of the ion source and the beam analyzing system.

9.8 PRELIMINARY MEASUREMENT OF BEAM ATTENUATION BY INTERNAL GASES IN THE CYCLOTRON VACUUM CHAMBER

Yoshiteru NAKAMURA, Ikuo ISHIBORI, Kazuo ARAKAWA
Toshihiro YOSHIDA[2], Yoshitaka ARAKAWA[2]

Advanced Radiation Technology Center, JAERI
Beam Operation Co., Ltd.[2]

I. INTRODUCTION

The pressure in the cyclotron vacuum chamber (VC) should be sufficiently low to reduce the beam loss due to the collision of the accelerated ions with gas molecules. We have estimated the amount of the beam loss in the design of the cyclotron vacuum system[1),2)].

The beam loss is almost proportional to the product of the pressure of residual gas, the cross section[3),4)] of collision and the traveling path of ion beam, and it may bring a serious problem in heavy ion acceleration. So, we are planning to examine the beam attenuation by increasing the internal pressure in VC.

However, there is a fear that the damage caused by discharge may be occurred at the electrodes of a deflector and an inflector, contact fingers in the resonator cavities because of increasing pressure, although our purpose is to measure beam attenuation under the condition of the cyclotron operation. Therefore, we initially procured the basic data when the cyclotron was not operated.

II. MEASUREMENT OF PRESSURE DISTRIBUTION IN VACUUM CHAMBER

We measured first the pressure distribution and gas components in VC, and also carried out a test on pressure control by gas feeding prior to the cyclotron operation.

(1) Method of Pressure Control

In general, there are two methods of pressure control in VC; one is gas feeding method, and the other is variable conductance one. We selected the former method in consideration of the actual structure of the vacuum system. A block diagram for the pressure control is shown in Fig. 1. The setting pressure in a gauge controller (MIG-921) is transmitted to a mass flow controller (CMS-201) through a pressure controller (CMS-101). This system can control the pressure in VC finally by means of regulation of nitrogen gas flow rate from a gas cylinder. A magnetic valve was installed to shut the gas feed quickly by remote control if any trouble such as discharge occurs in VC.

As a first step, we obtained a relationship between the gas flow rate and the

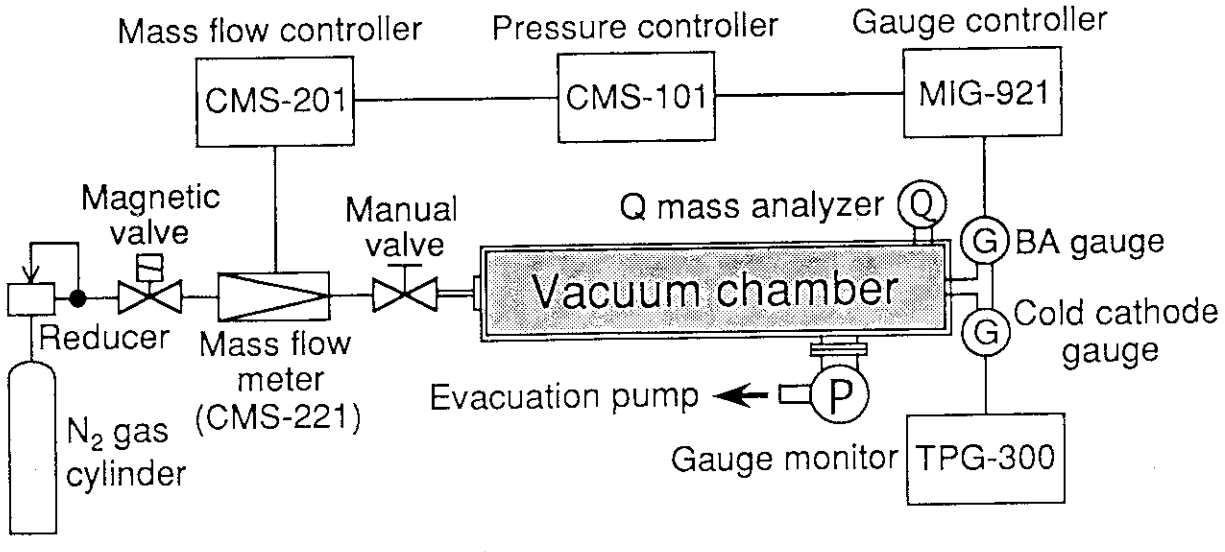

Fig. 1 A block diagram for pressure control in the cyclotron vacuum chamber.

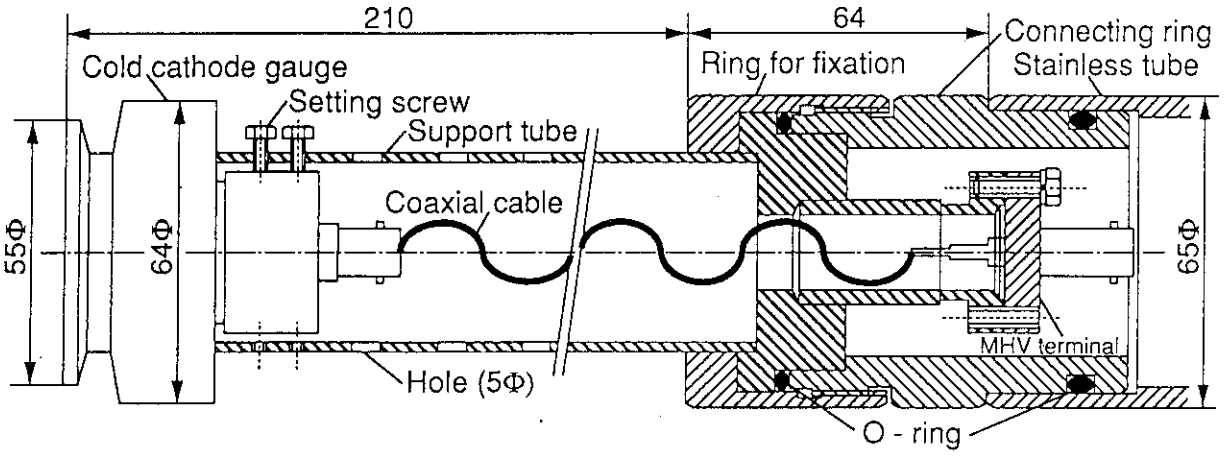

Fig. 2 A drawing of the cold cathode gauge head mounted at the top of the main probe.

pressure, and a pressure distribution in VC by nitrogen gas feeding near No. 2 compensator far from a magnetic suspended turbo molecular pump. The gas flow rate with the unit of standard cc per minute (SCCM) corresponds to setting voltage (V) of the CMS-201 exactly.

(2) Measurement Method of Pressure Distribution

In order to measure the pressure distribution in VC, we reconstructed the top of a main probe so that the radial distribution can be measured easily by the replacement with a vacuum gauge head. A cold cathode gauge (IKR-20, Balzers) built-in a permanent magnet was selected owing to the apprehension of residual magnetic field from the main magnet.

The reconstructed head of the main probe is made of stainless steel, is shown in Fig. 2. The vacuum gauge head is fixed up the same position to the main probe head completely. The main probe equipped with the gauge head can be inserted smoothly up to 170 mm from the center of the cyclotron without vacuum break, since the gauge head with a maximum diameter of 64 mm is a little less than the main probe stem of 65 mm diameter.

(3) Measured Results

Pressure change at two positions in VC is shown in Fig. 3. The pressure at the maximum flow rate of 10 SCCM amounts to 2-3x10^3 Pa which is about 100 times as large as the initial value.

Figure 4 shows the pressure distribution along the radial direction as a

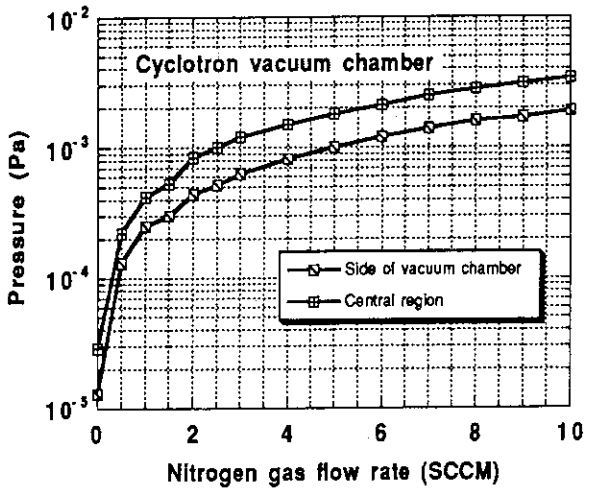

Fig. 3 A relationship between nitrogen gas flow rate and pressure in the vacuum chamber.

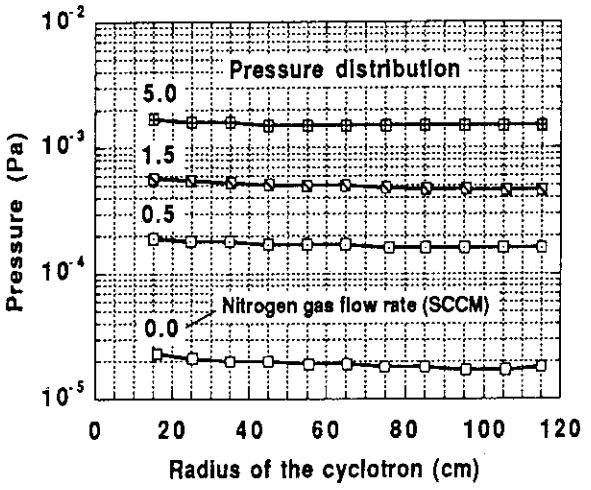

Fig.4 Pressure distributions along the radius direction of the cyclotron.

function of gas flow rate. Though the internal pressure distributions of the cyclotron are roughly flattened independent of the gas flow rate, it can be seen somewhat higher at the central region. We also make sure that the pressure in VC does not depend on the condition of adjacent two gate valves connected to the injection line and beam transport one.

The measured result of gas constituents is shown in Fig. 5 for supply of nitrogen gas into VC. The constituents at the pressure of 2.6×10^{-5} Pa are mainly H_2O^+ and OH^+ without supply of nitrogen gas. On the other hand, the partial pressure of N_2^+ causes predominant contribution at the pressure more than 1.7×10^{-4} Pa under nitrogen gas feeding.

III. FURTHER PLANNING

At the usual operating pressure of about 1×10^{-5} Pa in VC, we have not experienced appreciable attenuation induced by residual gas yet for the accelerated beams such as H^+ 10 MeV, $^{16}O^{6+}$ 160 MeV. Only an example[5] of the beam attenuation has been observed for $^{40}Ar^{8+}$ 175 MeV at the pressure more than 1.1×10^{-4} Pa.

However, we had a trouble that a few contact fingers in the No. 2 resonator were melted by generation of multi-pactoring at relatively high pressure of 1×10^{-3} Pa order.

We have to pay very careful attention for measurement of the beam attenuation effect by gas feeding under cyclotron operation.

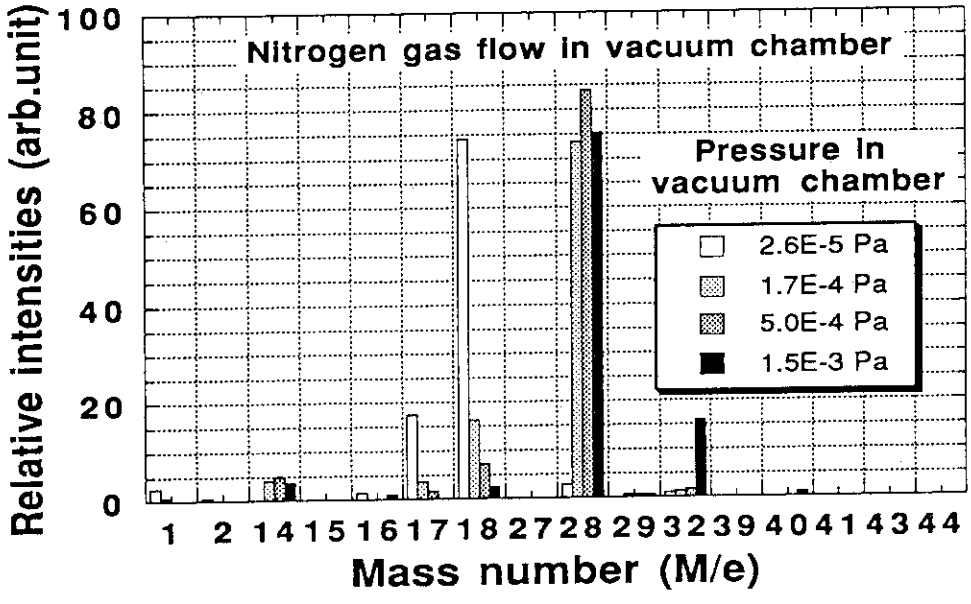

Fig. 5 Distribution of partial pressure in the vacuum chamber.

REFERENCES

1) Y. Nakamura, K. Arakawa, et. al., Proc. 8th Symp. on Accel. Sci. and Technol., Saitama, Japan, p194 (1991)
2) Y. Nakamura, I. Ishibori et. al., JAERI-M 94-007, 74p (1994)
3) H. C. Hensh, I. Feigenbaum, et al., IEEE Trans. Nucl. Sci., NS-32, No. 5, p3797 (1985)
4) J. L. Belmont, Rapport Interne, ISN 86-106, ISN Grenoble (1986)
5) T. Tachikawa, Y. Hayashi, et. al., Proc. Int. Conf. on Evolution in Beam Applications, Takasaki, Japan, p270 (1991)

9.9 Electrostatic Accelerators Constructed in the Second-Phase

S.Tajima, I.Takada, K.Mizuhashi, S.Uno, K.Okoshi,
Y.Saitoh, Y.Ishii, T.Kamiya, T. Suda and T.Sasuga

Advanced Radiation Technology Center, JAERI

1. Introduction

The installation of two electrostatic accelerators[1),2),3)], the 3MV single-ended accelerator (NHV NC-3000B) and the 400kV ion implanter (Nissin NH40SR), was started in TIARA from the beginning of February 1993. They were completed at the end of July 1993 after the acceptance tests and a government inspection. The operation for various experiments with three electrostatic accelerators have been started from January, 1994. This report outlines the new accelerator systems and their performances.

2. 3MV Single-ended Accelerator

The single-ended accelerator provides light ions such as proton, deuteron and helium with an energy range from 0.4 to 3MeV. The profitable characteristics of this machine are as follows; 1) the stability of the terminal voltage is extremely high ($\Delta V/V \leq \pm 1 \times 10^{-5}$), 2) high intensity ion beams are available, 3) electron beam is also accelerated by changing the terminal polarity. The machine consists of a high-voltage generation circuit, a positive ion source, an acceleration tube and a computer control system. The main structure of the accelerator is housed in a pressure vessel of 7.0 m in length and 2.5 m in diameter, as shown in Fig.1. The acceleration tube was separated from the high-voltage generator, in order to remove the effects of alternative electric field and mechanical vibration of the high-voltage generator.

(1) High-voltage generation circuit

The high-voltage generation circuit, illustrated in Fig.2, provide the stable voltage from 0.4 to 3MV. To minimize the voltage ripple the balanced Schenkel circuit was adopted. It is driven at frequency of 41kHz and can deliver the maximum charging current of 1.5mA to the terminal. The Shenkel circuit is generally similar to the Cockcroft-Walton circuit in the point that both circuits generate high-voltage by using multi-stage diode and capacitors.

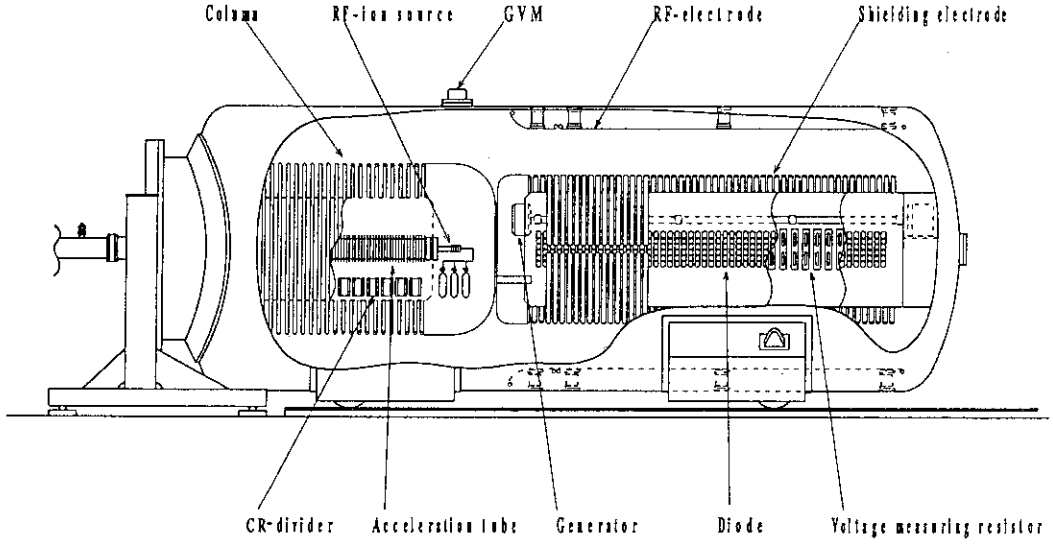

Fig. 1 Structure of the 3MV Single-ended Accelerator

An advantage of the Schenkel in comparison with the Cockcroft is that the voltage ripple does not depend on the number of the stage. The balanced Schenkel circuit arranged with a couple of the circuits is also effective to reduce the voltage ripple caused by the swing of the electric field. A variable inductor is adjusted to take a balance between two circuits. One circuit consists of a RF electrode that provide power to the circuits, fifty seven stage diode units and shield electrodes that form stray capacitance with an opposite RF electrode. The voltage drift is reduced by high gain feed-back circuit. The high accuracy resistors were used, because it is required exactly to measure the voltage for feed-back control.

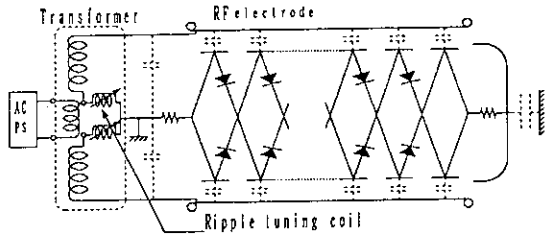

Fig.2 Schematic Diagram of High Voltage Generation Circuit

(2) RF ion source

The RF ion source which can easily generate high-intensity light ions and electron was mounted on the high-voltage terminal. The life time of it was estimated at one year under normal operation. To keep the gaseous plasma, 100 MHz RF power is supplied to the source quarts. There are three bottles for hydrogen, deuterium and helium gases on the terminal. Each gas is fed to source and the flow rate is controlled by the thermo-mechanical valve driven through the insulating rod. The gas load from the ion source are evacuated by a 1500 l/s turbomolecular pump set at the exit of the accelerator vessel through the acceleration tube.

3) Acceleration tube

An acceleration tube assembled eighty four aluminum electrodes and glass insulators is mounted by the acrylic plates on the center axis of the accelerator vessel. Each electrode are divided by the resistors of 200MΩ to make uniform electric field along the tube and protected by the shield rings and the spark gaps. Ions and electron can be accelerated by using this acceleration tube. In acceleration of ion beam current higher than 100μA, some permanent magnets were mounted for electron suppression.

(4) Acceptance tests

The acceptance test have been carried out mainly on following items; 1) high voltage generation, 2) voltage stability and 3) beam transportation.

In the high voltage generation test, a terminal voltage of 3.09 MV, that is 103% of the rated maximum voltage, was kept for 1 hour without sparking. A high voltage meter was calibrated at the threshold energy of 1.880 MeV in the nuclear reaction ^{7}Li (p,n)^{7}Be. The voltage stability was measured for voltage drift and ripple at 3 MV. The voltage drift was measured by recording the error from the reference to the chart recorder for 1 hour and also voltage ripple generated from a CR divider circuit was measured by oscilloscope. Both results were smaller than the guaranteed value of $\pm 1 \times 10^{-5}$.

Beam acceleration tests were carried out by measuring the beam current at the exit of the accelerator. Beam transport tests were also carried out by measuring the current at the end of the beamline SA for ions and SX for electrons (see Fig.7). Both results exceeded guaranteed values for all the ion (electron) species and energies. The results of the acceptance test are listed in Table 1.

3. 400kV ion implanter

The ion implanter is able to generate a wide variety of ions from proton to gold with an energy of 20 to 400keV. The high-voltage terminal equipped with an ion source, an analyzing magnet, turbo-molecular pumps and their power supplies was insulated from ground by four ceramic posts. The structure of the implanter is illustrated in Fig.3. A Cockcroft-Walton circuit with nineteen stages generates high voltage up to 370kV for acceleration. Ion extraction voltage for the ion source is normally 30kV so that the acceleration energy becomes 400keV at a maximum.

Table 1 Results of Acceptance Test for the Single-ended Accelerator

Item	Specification			Measured
High voltage generation	±3.0 MV × 1.03 for 1h			+3.10 MV for 1h -3.09 MV for 1h
Voltage stability	$\Delta V/V<\pm 1\times10^{-5}$			Drift below$\pm 1\times10^{-5}$ for 1h Ripple $\pm 0.975\times10^{-5}$
Beam acceleration	Ion	Energy (MeV)	Current (μA)	Current (μA)
	H	0.4	100	121
		3.0	300	305
	D	0.4	50	75
		3.0	200	220
	He	0.4	50	65
		3.0	200	222
	e	3.0	100	188
Beam transport	Ion	Line	Current (μA)	Current (μA)
	H	SA	100	110
	He	SA	70	75
	e	SX	50	65

Since the high-voltage terminal, the Cockcroft circuit and the acceleration tube were assembled in atmospheric condition. The surroundings were kept in low relative humidity below 60% to prevent spark.

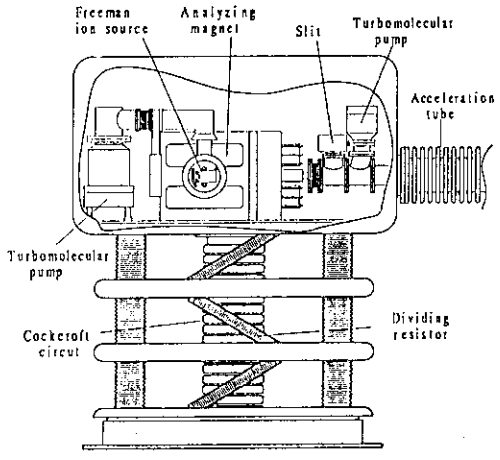

Fig.3 Structure of the 400kV Ion Implanter

A Freeman type ion source can generate a wide variety of ion species with high current. Ion beam is extracted from arc plasma supported with a hot filament in the source. In general, gaseous materials are used to produce the ion, however, solids were also used by using an oven or a spatter electrode. The life time of the filament made from tungsten wire was about 30 hours in normal operation.

To adjust the ion source parameter a local console was installed beside of the implanter in the target room 2. The devices housed in the high-voltage terminal can be controlled either by a center console or by the local one.

The acceptance tests for the implanter were carried out for almost the same items as the single-ended accelerator. All the tests satisfied the guaranteed values as listed in Table 2.

A mass spectrum of Ag ions extracted from the source using the oven is shown in Fig. 4.

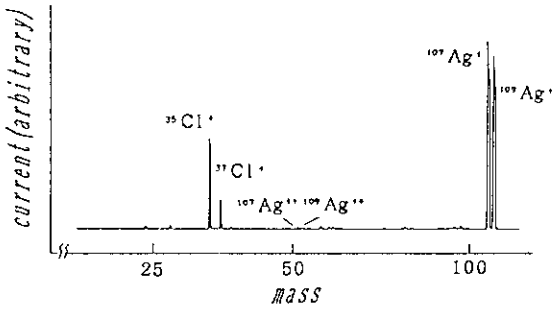

Fig.4 Mass Spectrum of Ag Ions Extracted from Freeman source

Table 2 Results of Acceptance Test for the Ion Implanter

Item	Specification			Measured
High voltage generation	370 kV ×1.03 for 1h			382 kV for 1h
Voltage stability	$\Delta V/V \leq \pm 3\times10^{-3}$			$\pm 1.23\times10^{-3}$ (p-p)
Beam acceleration	Ion	Energy (keV)	Curr. (μA)	Curr. (μA)
	P	400	100	100
	Ar	400	100	100
	As	400	100	100
	Ag	400	100	22
Beam transport	Ion	Line	Curr. (μA)	Curr. (μA)
	P	IC	30	37.5
	Ar	IC	30	36
	As	IC	30	32
	Ag	IC	4	38
Resolution of analyzing magnet	m/Δm≥100			111 for Ag

The silver chloride(AgCl) was used to produce Ag ions. It is able to observe the two isotopes of silver and a little their double charge and chlorine peaks. The resolution of analyzing magnet was calculated at 111 for the spectrum.

4. Control system

Each machine of the single-ended accelerator and the ion implanter is controlled by a work station and a real time CPU(VME) communicated with the programmable logic controllers(PLC) through Ethernet bus, as shown in Fig.5. The work station maneges the whole system and also takes charge of man-machine communication and treatment of operating data. The VME CPU mediates communication between the work station and the PLC as an ended interface on real time. The PLC also has CPU for specific control. Two systems are connected each other by bus so that one operator can control both the accelerators.

As shown in Fig.6, each control console consists of two character displays with mouses and keyboards , three rotary encoders, five assignable meters, four analogmeters and a oscilloscope for beam profile monitoring. An operator can control each accelerator and beam transport devises such as bending magnets and quadruple lenses using by mouse, rotary encoders and keyboard. The device to be controlled is selected by assigning the device pointer on the display using a mouse.

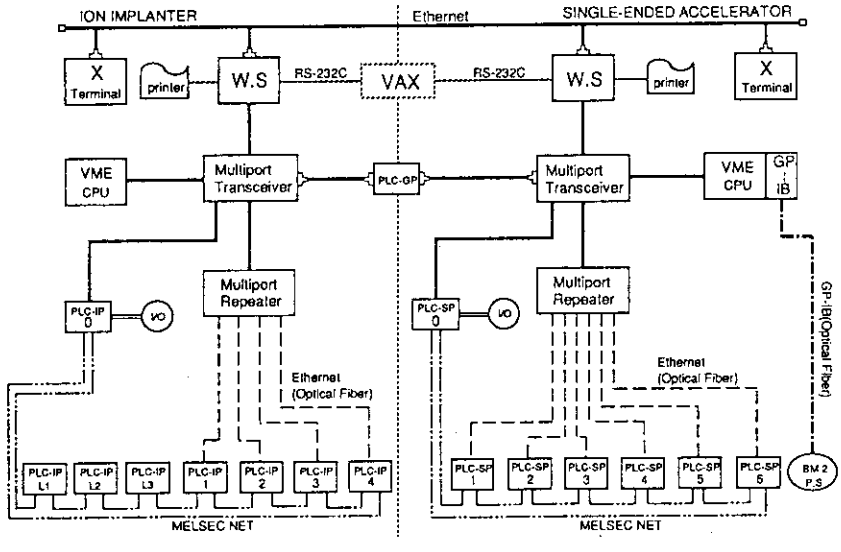

Fig. 5 Architecture of the Control System

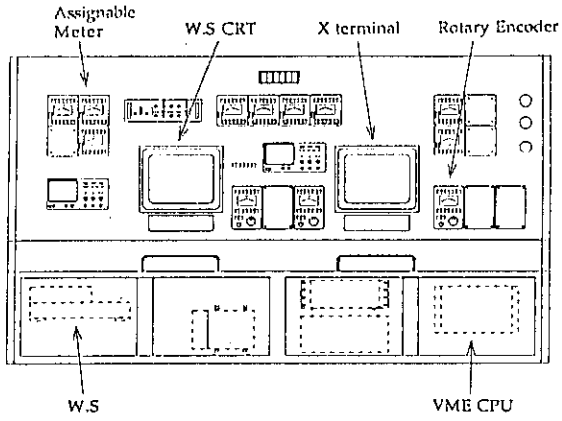

Fig.6 Front View of the Center Console

5. Beam transport system

A beam transport system, shown in Fig.7, was assembled for multiple beam operations of triple and dual beam modes using three or two electrostatic accelerators. The transport system consists of bending magnets, electrostatic and magnetic quadrupole lenses, steerers, Faraday cups, slits, beam profile monitors, scanners, ion pumps, etc.. The single-ended accelerator has four beamlines, SA,SB,SC and SX. The first three were designed for the ion beam to allow for transporting ions of mass number 16 at 3MeV. The SX line was designed only for electron beams below 3MeV. A 90 degree analyzing magnet with radius of 1.5m was installed to form submicron-class microbeams stably. The magnetic field of the magnet was adjusted by using a NMR gauss meter within a resolution of 0.01 gauss. A combination of the magnet and a slit system placed in just behind the magnet is also used for energy stabilization. Two 270 degree magnets were installed to achromatically bend electron beam at a right angle independently of the energy.

The ion implanter has five beamlines, IA,IB,IC,ID and IX. All of them were designed to allow for transporting ions of mass number 200 at 400keV.

In order to observe the beam profiles in real time, vibrating probes were introduced for each beamline. They can provide the beam profiles of X and Y directions with center markers on the oscilloscope. There were three XY-scanners for uniform irradiation to wide target area on the IA, SC and SX line. The maximum scanned area is 100×100 mm^2 for IA and 40×40 mm^2 for SC and SX. The scanning frequency is continuously variable from 1 to 1kHz. To hold the high vacuum in the beamline, an ion pump was assembled for each vacuum section of the beamlines. They were effective and simple to keep the pressure within 10^{-8} torr. As noted above, all the beamline components were controlled and watched by the center console in the control room.

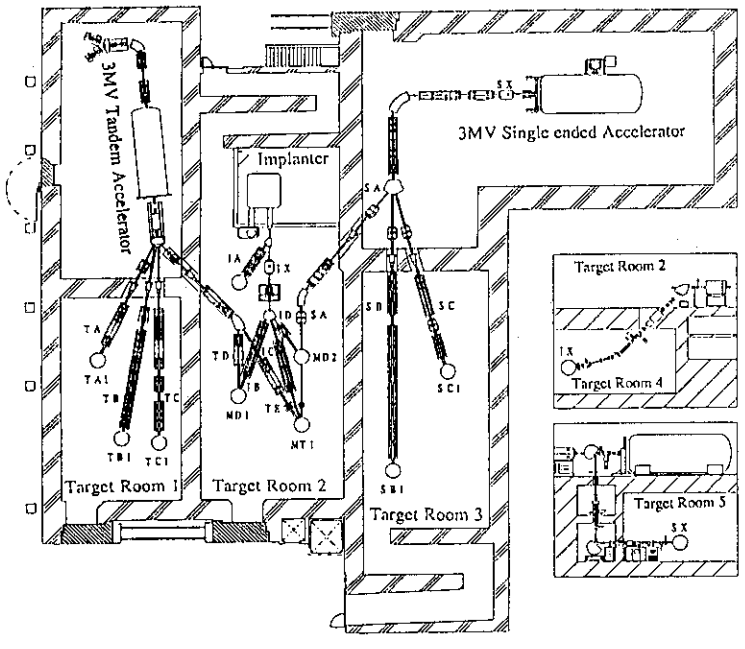

Fig.7 Layout of Beam Transport System in the Multiple Beam Building.

Reference

1) S.Tajima,I.Takada, K.Mizuhashi, Proc. 6th Workshop on Tandem Accelerator and Technology, Fukuoka(1993) p.14
2) Y.Saitoh,S.Tajima,I.Takada,K.Mizuhashi, Nucl.Inst. and Meth. B89(1994) p.23
3) Y.Ishii,S.Tajima,I.Takada,K.Mizuhashi, Proc. BEAMS,Tokyo(1993) p.105

9.10 Safety System of Multiple Ion Beam Irradiation Facility

Kiyoshi MIZUHASHI, Satoshi TAJIMA, Isao TAKADA
Koichi NISHIMURA and Hiromasa WATANABE
Advanced Radiation Technology Center,JAERI

I. INTRODUCTION

Multiple ion beam irradiation facilities composed of three electrostatic accelerators, beam transport lines and five target rooms. The facilities have been in operation from the beginning of 1994. This facility is operated in various modes; (1) independent operations of accelerators in single-beam experimental mode, (2) a dual-beam experiment using two accelerators and a single-beam experiment using another accelerator, and (3) triple-beam experiment using three accelerators.

As the experiments and preparations are performed in prallel at this facilities, many researchers and other workers work in the facility a day.

We designed the safety control and interlocking systems under consideration of these conditions.

II. OUTLINE OF SAFETY CONTROL SYSTEM

It is very important to construct a system keeping safety from radiation hazard without restricting the activity of the workers. In this point of view, a personal access control system[1] (PCS) was introduced in TIARA. PCS is one of devices which constitute the whole safety control system. PCS consists of a non-touch type ID card(oscillator) and receivers. This system makes persons freely work in the radiation controlled areas. At the same time, the list of person working in the area can be searched on CRT of the PCS.

Many devices and components for safety control including PCS are supervised by under a programmable control station.

Followings are some descriptions of the components of safety control system. Figure 1 shows all the components of the safety control system and the relationship among them.

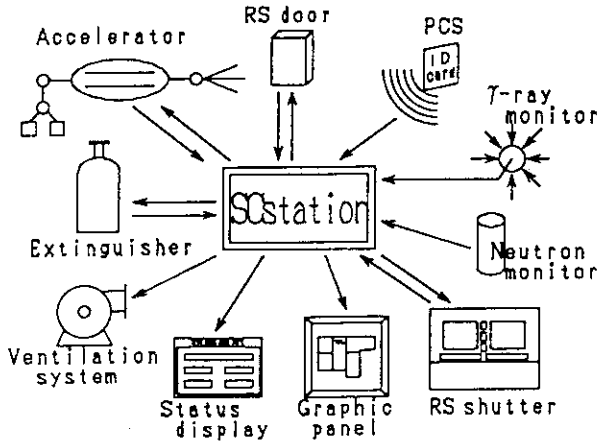

Fig. 1 Safety control system

1. Neutron monitor

A neutron monitor is assembled in each target and accelerator room. When the neutron flux exceeds an allowed value, the beam is automatically stopped by inserting a faraday cup into the beam line.

2. Gamma-ray monitor

Each target and accelerator room have a gamma-ray monitor. When the monitored dose rate exceeds the allowed value even if beam is off, the radiation shielding (RS) door can not be opened.

3. Personal access control system

A PCS has been introduced in the radiation controlled areas. Each target or accelerator room have a couple of antennas which catch radio waves from an ID card and make the control system detect whether any worker is present or not in the room. If the system detects any person in the room, the RS door can not be closed.

4. Radiation shielding door

A person is allowed to enter and leave each target or accelerator room only through the RS door. When the RS door is opened, the accelerator can not be operated and /or accelerated beams can not be transported to the target room. These

doors, also, can not opened during accelerator operation or irradiation.

5. Halon gas extinguisher

The halon gas extinguisher is installed in the target and accelerator rooms in consideration of possibility of electric fire. The halon gas can not be discharged into the room if any workers are in the room or the door opens. The door also can not be opened during the period that the gas are filled in the room.

6. Radiation shield shutter

A radiation shielding (RS) shutter is placed in a radiation shielding wall between accelerator and target rooms. It has role for shielding radiation through beam ducts for gamma-rays and neutrons induced by accelerating beam. When accelerated beams are transported other target rooms, the persons can work in a target room by closing all the RS shutters installed in the surrounding walls. The RS shutters can not be opened by the inhibition signal of the room.

7. Accelerator

Accelerators are allowed to be operated with a "permission signal" from SC station. The permission signal is made from safety side signals as above mentioned components. An "operation" and an "irradiation" signals are made in the accelerator console and these signals are used for the interlock circuit of RS door's.

8. Status display

Each target or accelerator room has a status display at the entrance. It indicates three kinds of informations, that is, "Operation" or "Not operation", "Irradiation" or "Not irradiation", "No admittance" or "Entrance permission". When "No admittance" is indicated, the RS door can not be opened. If the door is opened during operation or irradiation because of any accident, the accelerator is automatically stopped.

9. Graphic panel

All the status of the components equipped with interlocking system for human safety are displayed on a graphic panel. All the components are symbolized and each symbol is usually indicated by LED in blue or red color. The red color means unsuitable condition for accelerator operation or beam irradiation.

The accelerators can be operated in the area which is enclosed by the blue lighting character along the shielding wall in the graphic panel.

III. SAFETY CONTROL STATION

The SC station occupies an important position in the system. Many informations from all the devices are gathered, and all the interlocking logic signals are made by the them at the SC station. All the devices for safety control are under control of the SC station. Figure 2 shows a block diagram of programmable control system.

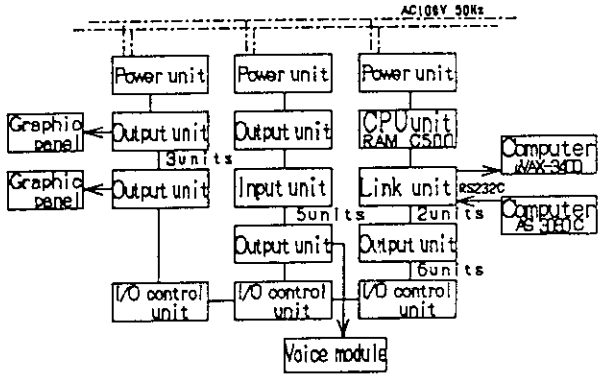

Fig. 2. Programmable control system

This system consists of a CPU unit, twelve output units, five input units, three power units and three I/O control units. The total input and output contacts are 160 and 368 points, respectively. Most points of output contacts are used for the graphic panel which has many LEDs for the status display. The system is connected with two computers by RS-232C interface. The one takes many informations about various conditions of the multiple ion beam irradiation facility from the SC station and the other sends the data of the PCS to SC station for interlock.

IV. INTERLOCKING SYSTEM

1. Operation

Elements of the interlocking system for human safety was formed fifteen signals from nine kinds of device as shows in Fig. 3. The permission for operating the tandem accelerator in triple beam irradiation mode requires that the safety condition of the tandem accelerator room, the target room No.2 and the single-ended accelerator

room are established. In the case of single beam transportation to the target room No.2 from the tandem accelerator, it is not necessary to complete the safety condition for the single-ended accelerator room.

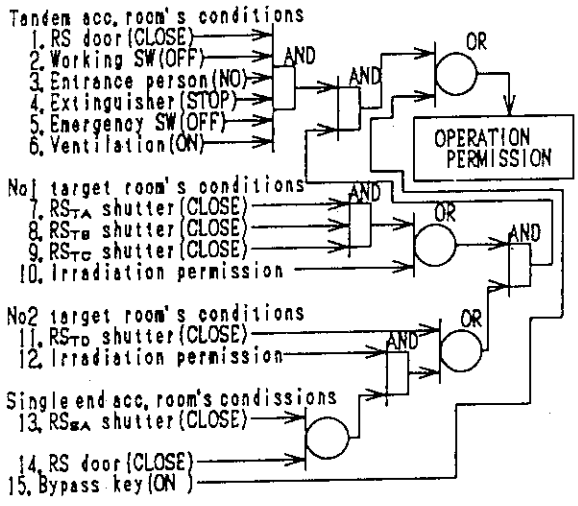

Fig. 3. Operation permission signal for the Tandem accelerator

The irradiation permission signal in Fig.3 is a synthetic signal of all the target room's safety conditions.

Each permission and inhibition signal are connected with normal open and close contact, respectively. All the functions should work on safe side by such connection, if any trouble occurs in the connecting wires, the computers and SC station.

2. Irradiation

In accelerated beam can be transported to a target room on condition that the safety requirements of the target room is satisfied. If the condition is not complete, the irradiation permission signal is not formed and RS shutter cannot be opened. Figure 4 illustrates the irradiation permission signal for the target room No.2.

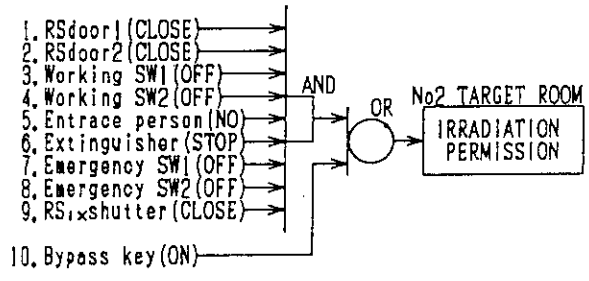

Fig. 4. Irradiation permission signal for the Target room No.2

3. Opening and closing of door

The RS door is interlocked to protect person against the radiation hazard. The RS door can not be opened during the accelerator operation or beam irradiation. Fig.5 illustrates the sequence of the opening and closing permission signals.

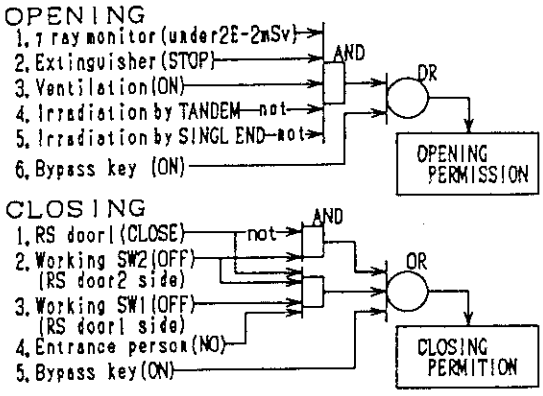

Fig. 5. Permission signal of RS door for the Target room No.2

The RS door has an another interlocking function that any person is left inside the irradiation room. A control circuit of the door interlinks to two principal device. The one is a working switch and the other is PCS. The interlocking of the working switch has a function that the RS door does not close while any person is working in the room. The switch is turned on by the person after opening the RS door.

The relations between the accelerator and the RS door are summarized as follows; the RS door cannot be opened during accelerator operation, and when the RS door open, the accelerator cannot be operated. If the RS door is opened during the accelerator operation, the accelerator is automatically stopped.

V. PRESENT STATUS

The safety system has functioned steadily for a year without any trouble and accident.

REFERENCES

1).Koichi NISHIMURA,et al., JAERI TIARA Annual Report vol.2 (1992) pp.232-233

9.11 Status of the Negative Ion Source for the 3MV Tandem Accelerator

Y.Saitoh, K.Mizuhashi, and S.Tajima
Advanced Radiation Technology Center, JAERI

1. Introduction

Two types of negative ion sources are connected with the 3 MV tandem accelerator. The one is Cs sputter type (nec:SNICS) for most of negative ion species, and the other is RF charge exchanging type (nec: ALPHATROSS) exclusively for negative helium ion. The standard operating condition and maintenance way for the ALPHATROSS has been established [1]. Three technical progress are reported on the SNICS as follows; (1) four new ion species generated by the SNICS could be added to the deliverable ions from the tandem for users, (2) an recovery method of the ionizer poisoned by Ce beam operation has been examined without cleaning and reassembling, and (3) an ion source test stand has been constructed.

2. New ion species

Post-analyzed ion beam currents of four new ion species (As, Se, Bi and Ga) are shown in table 1, and typical post-accelerator charge distributions are shown in fig. 1a and 1b. In the case of Bi, ion beam current became unstable because of the low melting point of 271 °C when the ionizer current was increased up to a normal condition of 20 A. This made us to operate the ionizer under low Cs ionization efficiency. It will be improved to make a cathode by BiO instead of Bi. The acceleration test of oxygen molecular ions was also tried. A negative charged O_2 ion beam of 1 μA was injected to the tandem, and a single positive charged O_2 ion beam could be observed by a beam profile monitor at a terminal voltage of 3 MV, but could not be measured by a Faraday cup.

3. Tungsten effect for recovering ionizer

After operation of lanthanide ion beams, the decrease of beam current from the SNICS has been observed. For example, Ni beam current of 17 μA was observed before Ce beam operation, but it decreased to 5 μA after Ce. This is explained as follows. Neutral Ce atoms sputtered from the cathode cover the surface of the ionizer, and the Cs ionization efficiency of the ionizer decrease, because of its low vaporized pressure and work function. The Ce atoms can not be removed without a extremely high temperature operation or a cleaning and a reassembling of the ion source [2]. It takes almost one day to clean and reassemble the ion source. Such poisoned ionizer could be repaired by sputtering the tungsten cathode. Sputtered neutral W recovered the poisoned ionizer surface because of the low vaporized pressure and high work function. After W operation, Ni beam current was perfectly recovered up to 17 μA.

4. Construction of ion source test stand

An ion source test stand has been constructed to examine and improve performances of ion sources independently from regular operation of the tandem. This system consists of a high voltage deck equipped with an ion source, A 90° mass analyzing magnet with a resolution of 200, and a beam diagnostic system assembly including a Faraday cup and a beam emittance monitor. In usual operation, measurements of ion beam current are made with an extraction voltage of 14 kV corresponding to a negative ion energy of 20 keV. The layout of the test stand is illustrated in Fig. 2.

[1]Saitoh et al., JAERI TIARA Ann. Rep., 1992 (Vol. 2) 207
[2]Roy Middleton, A Negative Ion Cookbook, Univ. Pennsylvania(1989)

Table 1. Beam currents of new ion species (SNICS)

Ion species	As	^{80}Se	Bi	^{69}Ga	^{71}Ga
Beam current	1 μA	10 μA	1 μA	2 μA	0.8 μA

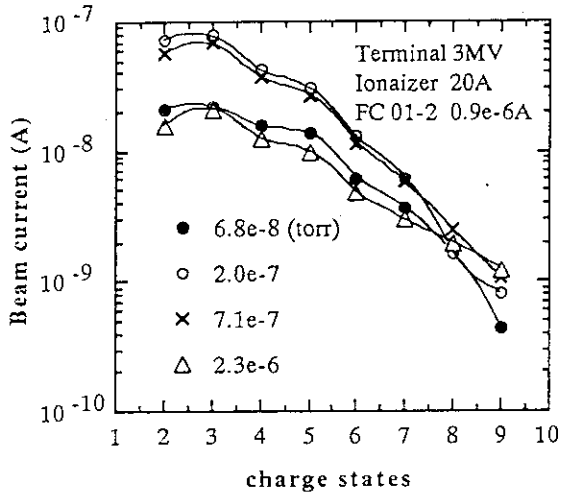

Fig.1-a Ion Beam current of As with respect to stripper gas pressure as a function of charge states

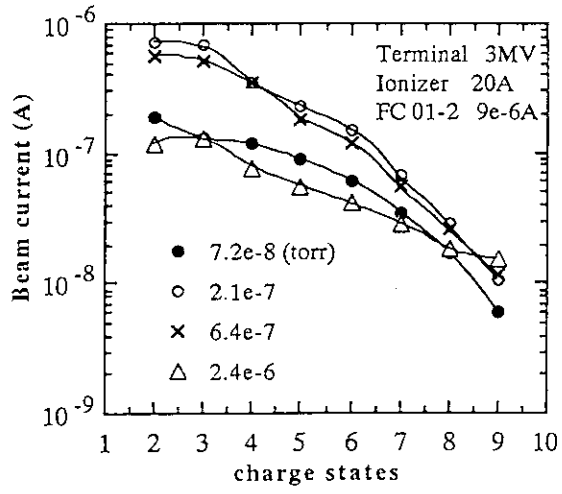

Fig. 1-b Ion beam current of Se with respect to stripper gas pressure as a function of charge states

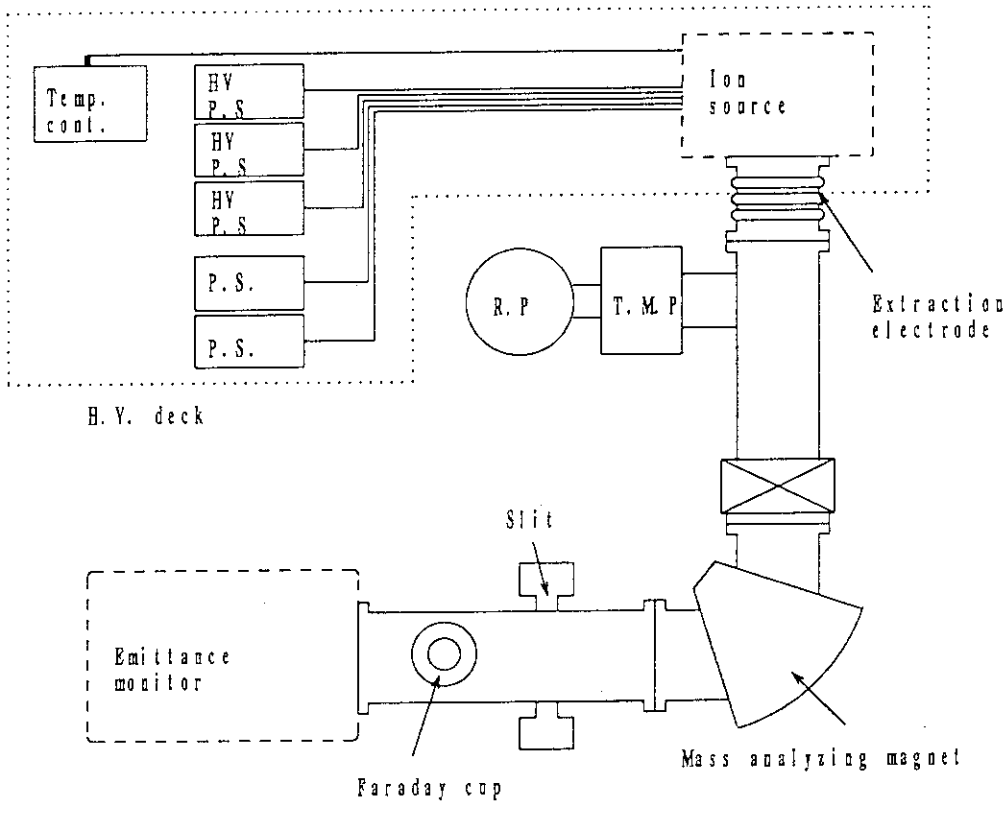

Fig.2 Layout of ion source test stand

9.12 Measurement of Voltage Stability at the Single-ended Accelerator

Y. Ishii, S. Tajima, I. Takada, K. Mizuhashi, Y. Saito, S. Uno, K. Okoshi, T. Kamiya, T. Sasuga, R. Tanaka and E. Iwamoto*
Advanced Radiation Technology Center, JAERI
*Nissin-High Voltage Co.,ltd.

1. Introduction

The 3MV Single-ended accelerator[1], completed in July 1993, is equipped with a light ion microbeam line[2] which is intended to provide a submicron beam. To achieve the submicron beam, the high voltage generator was designed to have a high voltage stability of $\pm 1.0\times10^{-5}$ to minimize the chromatic aberration which is dominated by the energy spread of the accelerated beam. A charging system of symmetrical Schenkel type was selected to meet the stability requirement. However, verification of the very high stability strongly depends on the measurement system, because of the tolerable variation of the terminal voltage is only ±30V at the maximum voltage of 3MV. The stability has so far been measured by using a capacitor pick off(CPO) or a generating volt meter(GVM) in Van de Graaff type accelerators. We selected two types of precise voltage measurement systems. One is a measurement resistor system, and the other is a capacitance resistor(CR) dividing system. We measured the variation of the terminal voltage by using the measurement systems.

2. Single-ended Accelerator

The structure of the inner single-ended accelerator is illustrated in a separate report in this annual report. The high-voltage generator and the accelerating unit are separated from the voltage terminal in order to reduce the influences of electric noise from the charging circuit and mechanic vibration from the motor generator for the high voltage generation. Two types of measurement systems of the terminal voltage were assembled into the accelerator vessel. The one is a voltage measuring resistor system for measuring the voltage drift in the charging unit, the other is a CR dividing system for measuring the voltage ripple in the accelerating unit. To achieve the very high voltage stability, the control system of DC supply was also adopted in the charging system.

3. The Precise Measurement System of Voltage Stability[3]

We measured two types of the very small variations involved in the terminal voltage. The one is the voltage drift, the fluctuation depending on time in long period. The other is the voltage ripple, the variation which arises from the charging system. The voltage ripple varies with high frequencies of the similar order of 42kHz, the frequency of the resonator. The variations have been detected by using CPO and GVM. However, since the variations at the extremely stable voltage is too small, it is difficult to measure the voltage variation reliably by these methods. We adopted a voltage measuring resistor system and a CR dividing system, as shown in Fig. 2.

The voltage measuring resistor system shown in Fig. 1(A) was designed only for measuring the voltage drift. The resistor r_1 connects two resistors of R_1 in parallel. The resistor r_S links 220 stages of the resistor r_1 in series. The resistor r_2 connects 133 stages of the resistor R_2 in parallel. The voltage difference of the resistor r_2 is 7.5V for the terminal voltage at 3MV. We measured a very small variation of the voltage at 3MV for one hour or more. Uncertainties to the resistance values of R_1 and R_2 are less than ±1%, and the temperature coefficient less than 50ppm per degree. A double sealed wire was used for the signal lead between the voltage measuring system and the recorder to reduce noises.

The CR dividing system shown in Fig. 1(B) was designed for measurement of the voltage ripple. The resistor D_1 connects resistor R_3 with capacitor C in parallel. The CR dividing system links 35 stages of D_1 in series. The output voltage of the oscilloscope was calibrated against the voltage indication using the standard DC voltage supply. The variation of the voltage ripple of 450mV indicated on an oscilloscope corresponds to the voltage stability of $\pm 1.0\times10^{-5}$.

4. Results

Figure 2(A) shows the voltage drift measured at 3MV for about one hour. The variation of the terminal voltage was considered to be less than $\pm 1.0\times10^{-5}$.

Figure 2(B) shows the voltage ripple observed as a repeated high-frequency wave from. The ripple at 3MV is evaluated to be less than $\pm 1.0\times10^{-5}$ from the measured amplitude of 440mV.

We are planing to measure the spread of the accelerated beam energy using several nuclear resonance reaction with high energy resolution.

Reference
[1] S. Tajima. at. al. This TIARA Annual Report Number-3 (1994)
[2] T. Kamiya at. al. This TIARA Annual Report Number-3 (1994)
[3] Y. Ishii at. al. Proceedings of the Fourth Symposium of Beam Engineering of Advanced Mattel Syntheses. (1993)105

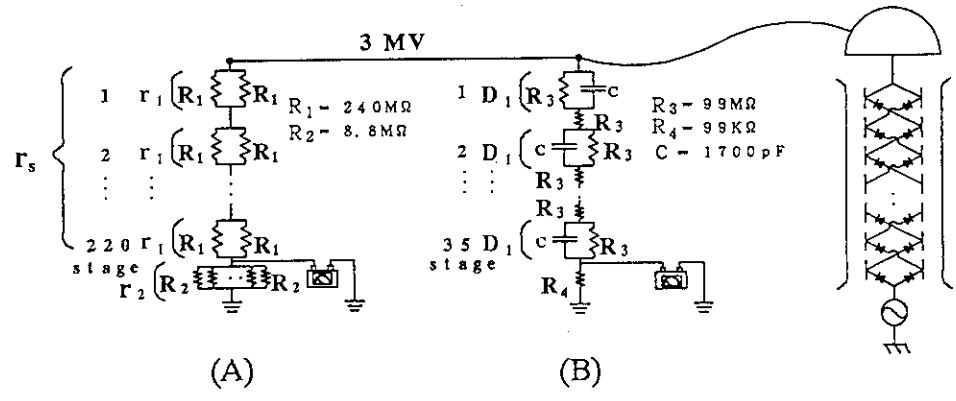

Figure 1 Two types of systems measuring variation of terminal voltage. (A) is the voltage measuring resistor system, and (B) the CR dividing system.

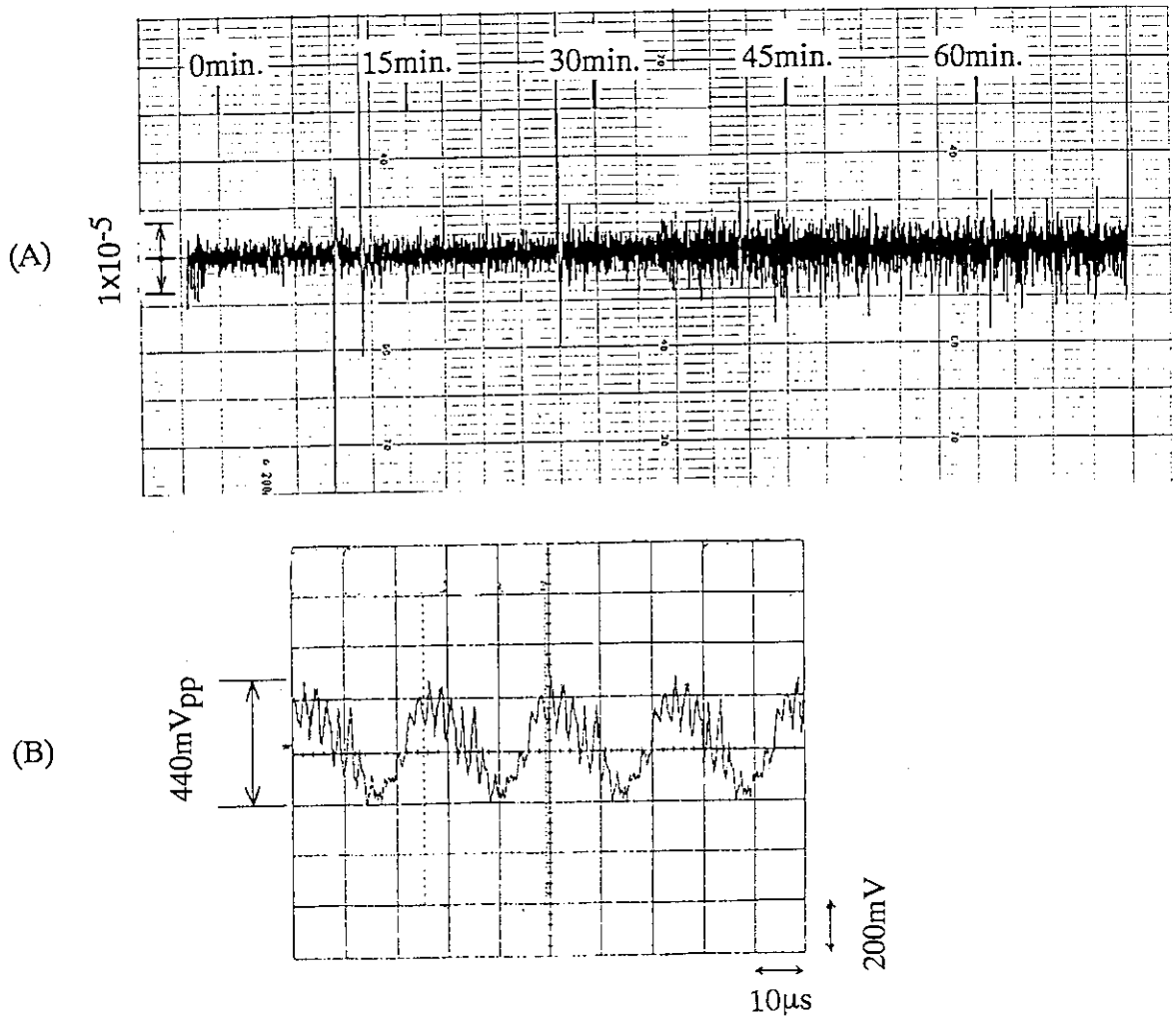

Figure 2 Measured results of stability of terminal voltage. Both results were measured at a terminal voltage of 3.0MV in no-load condition for ion beam current. (A) shows the variation of the voltage drift. (B) shows the voltage ripple.

9.13 Preliminary Study of Ultra Fine Microbeam

Yasuyuki Ishii, Akira Isoya and Ryuichi Tanaka
Advanced Radiation Technology Center, JAERI

1. Introduction

The technique for producing ion microbeam has been developed in several research laboratories in the world. A universal method of producing ion microbeam converged on a beam size of the order of 1μm has been now established by means of some magnetic lenses.

In resent years, the design rule of microelectronics devices is approaching 0.1μm. The analysis of the inner structure of the devices requires fine ion microbeams with a beam size of 0.1μm or less than sub half micron. However, it will be difficult for high-energy ion beams to reduce the focused beam size within sub half micron by using a quadrupole magnetic lens system, mainly because of the limitation of the spherical aberrations due to the construction of the magnetic lens.

To achieve an ultra fine high-energy ion microbeam by breaking through the optical limitation of the magnetic lens, we introduced a new idea of "acceleration lens" which unifies the two functions of beam focusing and beam acceleration, and makes the spherical aberration negligible. This lens system makes an virtual image in the lens system when the ratio of the acceleration energy to the energy of the incident ion beam is large. A fine microbeam is focused at a target as a real image displaced from the virtual image by using an Einzel lens.

2. Formative principle of ultra fine microbeam

An acceleration lens shown in Fig. 1 has a very strong focusing action in the neighborhood of the entrance aperture, and shifts a focusing point in the direction of progress by nearly uniform accelerating electric field in the lens system. Since the region which acts as a lens is small in the entrance of the acceleration lens, the influence of the spherical aberration can be neglected in focusing a fine microbeam. From this reason, a very small virtual image can be formed in the neighborhood of the entrance of the acceleration lens in the accelerating field and the it can be displaced to a real image with a beam size of 0.1μm order. An Einzel lens is installed after the acceleration lens to displace the image.

However, the limitation in the stability of the acceleration voltage makes the energy spread of the accelerated beam increase, which results in the increase of the focused beam size at the target because of the chromatic aberration.

The difficulty can be solved by applying the same high voltage to the center electrode of the Einzel lens and the puller electrode of the ion source, because the energy spread of the accelerated beam is compensated by this arrangement. The chromatic aberration due to the energy spread of the beam extracted from the ion source is also negligible, if the spread is less than 1eV when the acceleration voltage is 100kV. Therefore it is expected that a chromatic aberration free microbeam will be formed at the target.

3. Resent Progress

(1) Acceleration lens and Einzel lens[3)]

Detailed design of beam optics for the acceleration lens and the Einzel lens has been conducted to achieve an ultra fine 100keV ion microbeam at the target. The minimum demagnification factor was estimated at ~0.02 for the acceleration lens. However, the minimization of the factor for the Einzel lens is limited by the increase of chromatic aberration dominating the final beam size at the target. The beam size strongly depends on the design of the acceleration lens system.

(2) Ion source[4)]

Three conditions for the beam incidence into the precise lens system are required to achieve an ultra fine 100keV ion microbeam with a beam size of 0.1μm at the target; (1) the incidence beam is 10μm, (2) the divergence angle

is 3mrad, (3) the energy spread of the incident beam is less than 1eV for the beam energy of 100eV. A test bench of a duoplasmatron type ion source shown in Fig. 2 was made on a trial base for a preliminary study on the possibility to produce a low-energy beam satisfying the above conditions.

We succeeded to extract a high quality 30eV proton beam with a low beam divergence and a narrow energy spread. However, we found that further studies is necessary to improve relatively poor intensity and instability of the extracted beam. On the basis of these results, an improved ion source was designed and manufactured for the microbeam formation test at 100kV.

Reference

[1] A. Isoya: Proc. Int. Conf. on Applications of Nuclear Techniques. P.334 Jun. (1990), Creta, Greece
[2] A. Isoya: Proc Int. Conf. on Evaluation in Beam Applications. P.397 Nov. (1991) , Takasaki, Japan
[3] A. Isoya Proceeding of fifth meeting of TANDEM accelerator and it's applications (1992)120
[3] A. Isoya Proceeding of fifth meeting of TANDEM accelerator and it's applications (1993)66

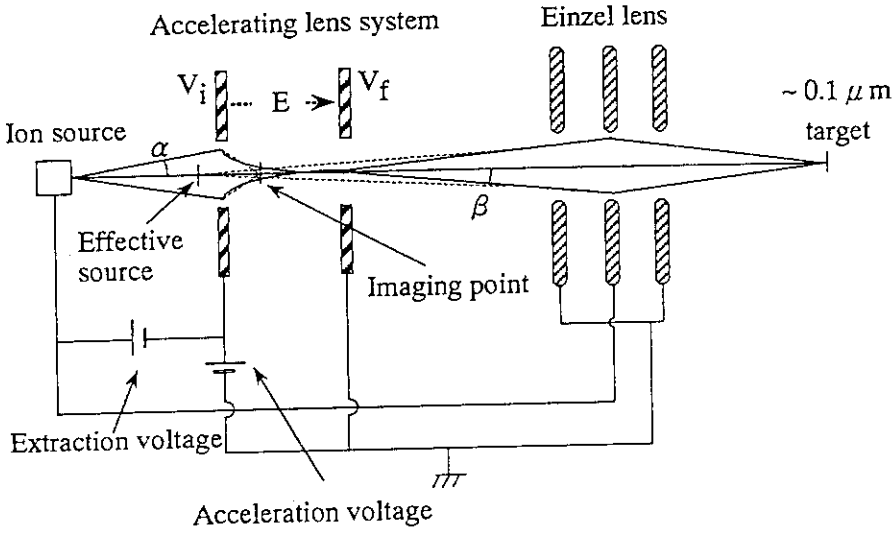

Figure 1 A schematic diagram of optical system of focusing ultra fine microbeam.

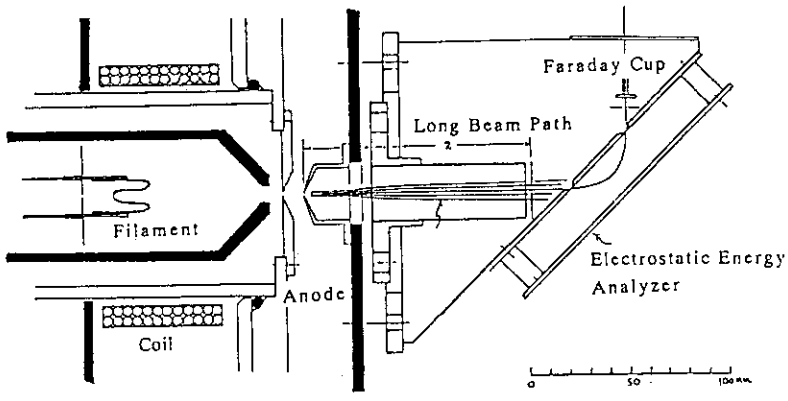

Figure 3 Experimental system of ion source with electrostatic energy analyzer.

10. Status of TIARA 1993

10.1 UTILIZATION OF TIARA FACILITIES

Utilization and Coordination Division,

Advanced Radiation Technology Center, JAERI

1. Introduction

TIARA is a center of the ion accelerator facilities for ion beam applications that is composed of three buildings and four ion accelerators, i.e. an AVF cyclotron, a 3MV tandem accelerator, a 3MV single-ended accelerator, and a 400kV ion implanter. The cyclotron and the tandem accelerator have been served for research applications since FY 1990. The single-ended accelerator and the ion implanter were completed in July 1993 and started for research use in January 1994.

2. Utilization System

TIARA is opened for public use: it receives applications of the experimental subjects once a year from users in wide areas as well as JAERI staffs, and the subjects are approved after official investigation by TIARA General Program Committee(GPC). The utilization day of each accelerator is fairly allotted to the subjects three times per year by Program Advisory Committee under the GPC that are both publicly organized.

Charges for the utilization by visitors are remitted in the case that the outer user have concluded a contract of the joint research (between JAERI and a university or a company) or that of projective joint research between JAERI and universities; the result of research have to be published at the TIARA Research Review Meeting and in the JAERI TIARA Annual report in these cases. There is another system of visitor use with charges but without the publication duty.

3. Experimental subject approved

Number of subjects approved in FY 1993 for the experiment using cyclotron was 52 and that using three electrostatic accelerators was 32. Subject numbers in each research field are shown in Table 1, and those in each category of relations with users are in Table 2.

Table 1. Number of experimental subjects at various research fields.

Fields of Research \ Accelerators	number of subjects	
	cyclotron	eletrostatic accelerators
Materials for space	9	1
Materials for fusion	3	8
Biotechnology	11	4
Functional material	6	15
R I & nuclear chem.	7	0
Radiation chemistry	5	0
Basic technology	9	4
Others	2	0
total	52	32

Table 2. Number of expriment subjects at various relations with users.

Relations with visitors \ Accelerators		number of subjects	
		cyclotron	electrostatic accelerators
JAERI only	Takasaki Establishment	8	9
	others	6	6
Cooperative research with university		11	13
The JAERI-universities collaborative research program		14	3
Joint research with private company or governmental institute		11	1
Cooperative &Joint Researches		2	0
Visitors use with charges		-	-
total		52	32

4. Allotted time to users

Table 3 shows officially allotted time of accelerator utilization to every research field at each period (5-1, 5-2, 5-3) in FY 1993. Table 4 also shows the allotted time to every group classified with the kinds of users. The utilization time is allotted to the user by unit of day; one day means a daytime from 9 a.m. to 6 p.m. in case of the electrostatic accelerators. In case of the cyclotron one day means a daytime (9 a.m. to 6 p.m.) or a night (6 p.m. to 9 a.m.) since the cyclotron has been continuously operated from Monday to Friday.

There is no allotted time in the period of 5-1 for the tandem accelerator and in the periods of 5-1 and 5-2 for the single-ended accelerator and the ion implanter because of the second phase accelerators' construction.

Table 3. Utilization of accelerators in FY 1993 at various research fields.

Fields of Research \ Accelerators	utilization days at each period															
	cyclotron				tandem accelerator				single-ended accelerator				ion implanter			
	5-1	5-2	5-3	total	5-1	5-2	5-3	total	5-1	5-2	5-3	total	5-1	5-2	5-3	total
Materials for space	14.0	18.3	15.5	47.8		7	10	17			0	0			0	0
Materials for fusion	4.0	1.9	2.0	7.9		2	11	13			14	14			9	9
Biotechnology	12.2	8.2	5.2	25.6		7	2	9			0	0			0	0
Functional material	9.0	8.7	6.1	23.8		26	20	46			25	25			17	17
R I & nuclear chem.	5.0	8.0	8.0	21.0		-	-	-			-	-			-	-
Radiation chemistry	5.0	4.2	4.0	13.2		-	-	-			-	-			-	-
Basic technology	21.0	19.2	17.4	57.6		7	10	17			8	8			-	-
Others	0.8	3.5	1.8	6.1		-	-	-			-	-			6	6
total	71	72	60	203		49	53	102			47	47			32	32

Table 4. Utilization of the accelerators in FY 1993 at various relations with users.

Relations with visitors \ Accelerators		utilization days at each period															
		cyclotron				tandem accelerator				singl-ended acceler.				ion implanter			
		5-1	5-2	5-3	total	5-1	5-2	5-3	total	5-1	5-2	5-3	total	5-1	5-2	5-3	total
JAERI only	Takasaki Establishment	16.6	16.4	16.2	49.2		24	18	42			25	25			18	18
	others	7.0	6.0	7.0	20.0		0	12	12			14	14			9	9
Cooperative research with university		4.6	5.1	2.2	11.9		16	10	26			8	8			5	5
The JAERI-universities collaborative research program		24.0	22.3	17.2	63.5		2	1	3			0	0			0	0
Joint research with company or governmental institute		12.8	16.2	11.4	40.4		7	10	17			0	0			0	0
Cooperative &Joint Researches		6.0	5.0	3.0	14.0		-	-	-			-	-			-	-
Visitors use with charges		0	1.0	3.0	4.0		0	2	2			-	-			-	-
total		71	72	60	203		49	53	102			47	47			32	32

10.2 OPERATION OF AVF CYCLOTRON

Kazuo ARAKAWA, Yoshiteru NAKAMURA, Watalu YOKOTA, Mitsuhiro FUKUDA, Takayuki NARA, Takashi AGEMATSU, Susumu OKUMURA and Ikuo ISHIBORI

Advanced Radiation Technology Center, JAERI

The JAERI AVF cyclotron is usually operated weekly. The yearly operation time is divided into three beam-time periods, each of which consists of 11 weeks of beam-times and allocated to experiments by Program Advisory Committee. Three weeks for maintenance and additional beam-times and about two weeks of no operation intervene between the programmed beam-times. The experiment plan and beam-times are allotted for each period. The weekly operation is usually carried out continuously from Monday morning till Friday evening. Regular yearly over-haul was carried out for 4 weeks in the summer.

The total operation time in the FY 1993 was 3247 hours, and monthly operation times are shown in Fig. 1. The percentage of time used for experiments, beam developments, and tuning were 80.2%, 10.5% and 9.3%, respectively. The beam time for experiments was 2559 hours in FY 1993 and remarkably increased from 1378 hours in FY 1992. Twenty-one kinds of ion species including three new ions, $^{12}C^{5+}$ (220MeV), $^{16}O^{5+}$ (100MeV) and $^{84}Kr^{20+}$ (520MeV), were provided for experiments. The accelerated particles and their beam time are also shown in Fig. 2. The beam time for light ions exceeded 50% of all as shown in Fig. 2. A single pulsed beams of H^+ (70MeV) and $^{40}Ar^{8+}$ (175MeV) ions were also provided for experiments using a beam chopping system.

In order to meet the requests from many groups of researchers, the accelerated particles, their energies and the beam course are changed as shown in Table 1.

Table 1 Frequency of particle, energy and beam course change in FY.

FY	Particle	Energy	Beam Course
1992	42	47	64
1993	43	51	123

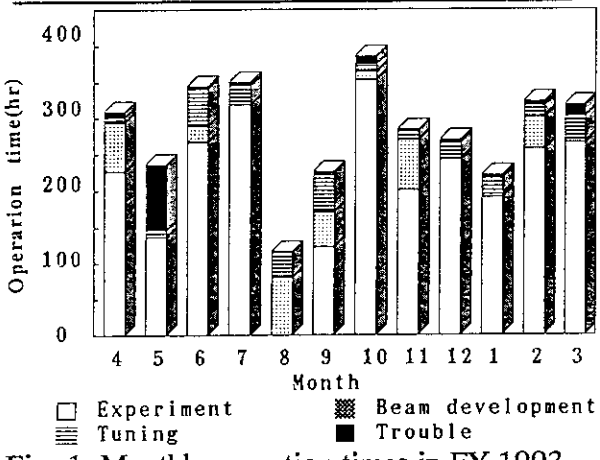

Fig. 1 Monthly operation times in FY 1993.

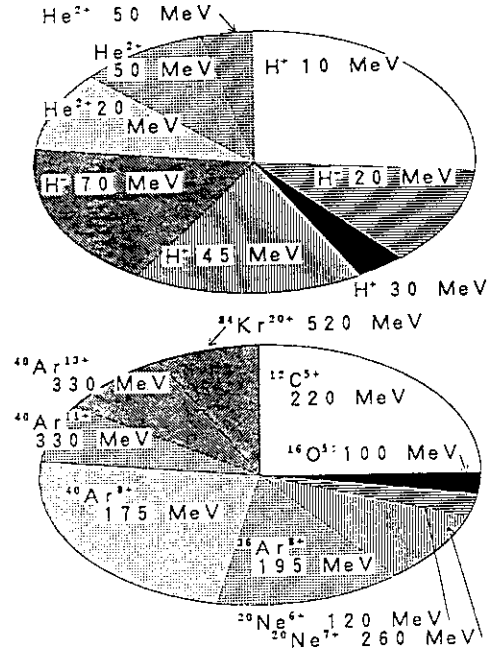

Fig. 2 Percentage of beam time of accelerated ions in FY 1993.

10.3 Operation of the Electrostatic Accelerators

Ion Accelerator Operation Division
Advanced Radiation Technology Center, JAERI

1. Introduction

The second-phase construction of the ion accelerators, the 3MV single-ended accelerator and the 400kV ion implanter, was completed at the end of July, 1993. The tandem accelerator restarted operation for experiments from September, 1993. The single-ended accelerator and the ion implanter started the operation for experiments from January, 1994, after the test operations by JAERI staffs. Various experiments using new accelerators have been started for triple beam irradiation, dual beam experiments, electron irradiation, submicron beam formation and in-situ observation study with an analytical electron microscope.

2. Operation

The three accelerators were smoothly operated according to a beam-time allotment approved in PAC. The tandem accelerator was operated for the beam-time period 5-2 and 5-3 and the other two were only for 5-3. The total yearly operation time in FY 1993 was 804 hours for the tandem, 608 hours for the single-ended and 396 hours for the implanter. The monthly operation time for three accelerators was irrustrated in Fig.1.

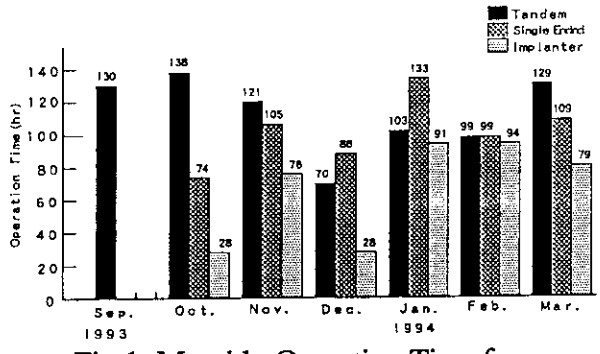

Fig.1 Monthly Operation Time for Electrostatic Accelerators in FY 1993

The tandem provided eighteen ion species such as H, ^{3}He, ^{4}He, C, N, O, Fe, Ni, Au etc.. The single-ended also provided H, D and He ions and electrons. The utilization frequency ratio of He ions reached about 75%.

Because available ion species of the implanter were not so much at the acceptance, they were increased by using various methodes of ion generation during the test operation. Table 1 lists the ion species available for the implanter at the end of FY 1993. The utilization frequency ratios of ion species for three accelerators are shown in Fig. 2.

Table 1 Available Ion Species for the Ion Implanter

Ion Species	Typical Current (μA)
H	2 ~ 10
C	1 ~ 5
O	2 ~ 10
P	5 ~ 30
Ar	5 ~ 30
K	5 ~ 30
Mn	2 ~ 10
As	5 ~ 30
Ag	1 ~ 4

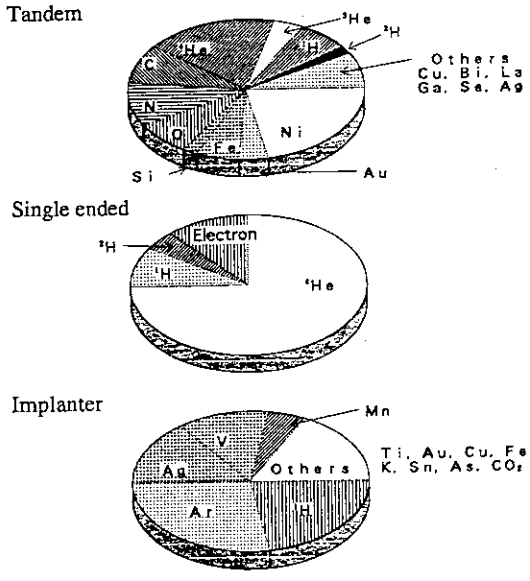

Fig. 2 Utilization Frequency Ratios of Ion Species for Electrostatic Accelerators in FY 1993

10.4 RADIATION CONTROL & RADIOACTIVE WASTE MANAGEMENT IN TIARA

Safety Division & Utilities and Maintenance Division,
Department of Administrative Services, TRCRE, JAERI

1. Radiation Control

1.1 Individual monitoring

(1) Individual monitoring for the radiation workers

Table 1 shows a distribution on effective dose equivalent of the radiation workers in fiscal 1993. The effective dose equivalent of all workers except seven were less than 0.2 mSv (minimum detectable dose equivalent) and the six of the seven workers were under 1 mSv, the other one was exposed 1.5 mSv due to the overhaulding of the cyclotron.

(2) Individual monitoring for the inspect visitors etc. to the radiation controlled areas

Table 2 shows number of persons who have been entered the controlled areas temporally except the radiation workers resisted officially. Individual monitoring for these persons were carried out with TLD and the effective dose equivalent of every entrance person was less than minimum detectable dose.

Table 1. Distributions on the effective dose equivalent in fiscal 1993.

Items	Persons / Periods	Number of persons: 1st quarter	2nd quarter	3rd quarter	4th quarter
Distribution range on effective dose equivalent HE : Effective dose equivalent (mSv)	HE ≦ 0.2	363	392	418	441
	0.2 < HE ≦ 1.0	0	3	4*	0
	1.0 < HE ≦ 5.0	0	1*	0	0
	5.0 < HE ≦ 15.0	0	0	0	0
	15.0 < HE ≦ 25.0	0	0	0	0
	25.0 < HE ≦ 50.0	0	0	0	0
	50.0 < HE	0	0	0	0
Persons for radiation control (A)		363	396	422	441
Exposure above 1 mSv	Persons (B)	0	1	0	0
	(B)/(A) ×100 (%)	0	0.25	0	0
Mass effective dose equivalent (man mSv)		0.0	2.8	1.3	0.0
Mean dose equivalent (mSv)		0.0	0.01	0.0	0.0
Maximum dose equivalent (mSv)		0.0	1.1	0.4	0.0

* The same worker was exposed during 2nd & 3rd quarter.

Table 2. Number of temporary entrance persons to radiation controlled areas in fiscal 1993.

Temporary entrance persons / Persons / Periods	Number of persons: 1st quarter	2nd quarter	3rd quarter	4th quarter	total
Temporary Workers	236	351	350	453	1390
Ispect Visitors	575	588	407	576	2146

1.2 Monitoring of released radioactivities for gas and dust

Table 3 shows the maximum radioactive concentrations and total activities for gas and dust released from TIARA's stack, during each quarter of fiscal 1993. The least amount of ^{41}Ar and ^{11}C were detected for some time on operation of cyclotron, but the radioactive dust released was not detected.

Table 3. Monitoring results of released activities for gas and dust in fiscal 1993.

Nuclide	Items	Periods	1st quarter	2nd quarter	3rd quarter	4th quarter	total
gross-β	dust (Bq/cm^3)	maximum concentration	$<5.5\times10^{-11}$	$<5.8\times10^{-11}$	$<5.7\times10^{-11}$	$<5.5\times10^{-11}$	$<5.8\times10^{-11}$
^{65}Zn	dust (Bq/cm^3)	maximum concentration	$<3.9\times10^{-10}$	$<4.0\times10^{-10}$	$<3.9\times10^{-10}$	$<3.5\times10^{-10}$	$<4.0\times10^{-10}$
	Total released activity (Bq)		0	0	0	0	0
^{41}Ar	gaseous (Bq/cm^3)	maximum concentration	3.1×10^{-4}	$<7.1\times10^{-5}$	$<2.0\times10^{-4}$	$<2.0\times10^{-4}$	$<2.0\times10^{-4}$
	Total released activity (Bq)		2.1×10^{9}	2.0×10^{8}	3.3×10^{8}	1.2×10^{8}	2.8×10^{9}
^{11}C	gaseous (Bq/cm^3)	maximum concentration	$<7.1\times10^{-5}$	–	$<7.1\times10^{-5}$	$<2.0\times10^{-4}$	$<2.0\times10^{-4}$
	Total released activity (Bq)		1.5×10^{7}	–	5.3×10^{6}	7.7×10^{8}	7.9×10^{8}

1.3 Monitoring for radiation dose rate and surface contamination

Radiation dose rate monitoring was routinely carried out in/around the controlled areas and surface contamination monitoring was also carried out. No unusual value of dose rate or contamination was detected. Figure 1 displays a distribution of the dose rate at the controlled area in the cyclotron building as an example.

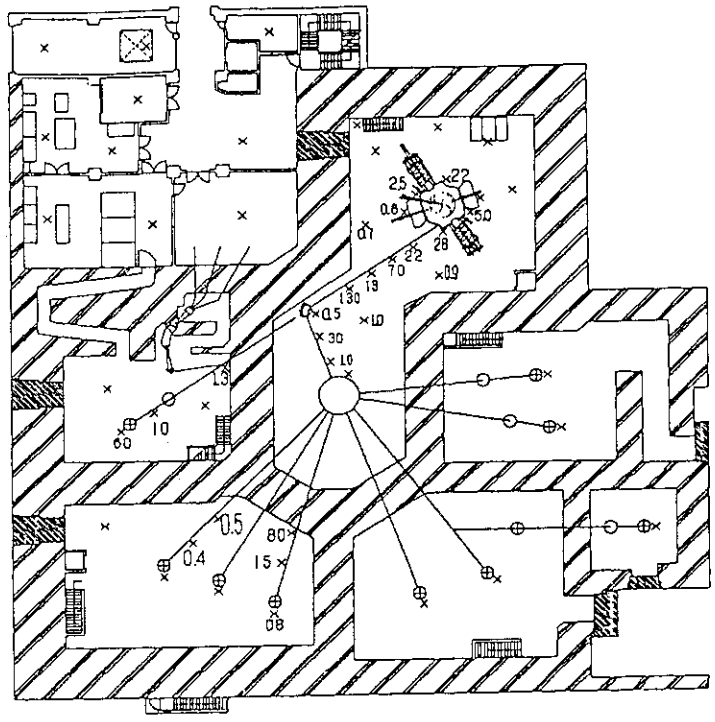

Fig. 1 Dose rate distribution at the radiation controlled area in the cyclotron building.

Date measured :
March 29, 1994
Measuring position :
Indicated with ×
above 1 m from floor
Unit : μ Sv/h
(numerics less than 0.2 μ Sv/h are not indicated)

1.4 Authorized radioisotopes

Table 4(a) shows a list of sealed radioisotopes authorized at the end of fiscal 1993. These isotopes are used in TIARA as checking sources for several kinds of radiation detectors. Seventeen nuclides of unsealed type are also authorized mainly for researches of neutron shielding and RI production, as shown in Table 4(b).

Table 4. List of radioisotopes authorized at the end of fiscal 1993 in TIARA.

(a) Sealed radioisotopes

Authorization No. and Date	Nuclides and amounts	Places used	Place of Strage
No.3469 Aug.30, 1991	^{241}Am 3.7 GBq ×1	Cyclotron Building Light Ion Room 1 to 3 Heavy Ion Room 1 to 3 Cyclotron Vault Light Ion Preparation Room Heavy Ion Preparation Room Heavy Ion Measuring Room Multiple Beam Building Target Room 1 Tandem Accelerator Room	Cyclotron Building
	^{57}Co 370 MBq ×4 ^{119m}Sn 370 MBq ×4	Cyclotron Building ISOL Room Ion Beam Research Building Hot Physics Laboratory	Cyclotron Building RI storage box in ISOL Room

(b) Unsealed radioisotopes

Authorization No. and Date	Places used	Nuclides	Amounts of annual use
No.7790 Nov.24, 1993	Cyclotron Building Light Ion Room 1 to 3 Cyclotron Vault Cyclotron Pit Room Switching Magnet Room Cooling Room Power Distribution Room Hot Work Room Hot Laboratory Semi Hot Laboratory RI Measuring Room ISOL Room Ion Beam Research Building Radiation Measuring Room Hot Physics Laboratory Hot Work Room Hot Chemical Laboratories 1 to 2	^{54}Mn	50 MBq
		^{65}Zn	1 GBq
		^{58}Co	1 GBq
		^{55}Fe	500 MBq
		^{7}Be	1 GBq
		^{75}Se	200 MBq
		^{95m}Tc	200 MBq
		^{139}Ce	600 MBq
		^{11}C	4 GBq
		^{13}N	4 GBq
		^{15}O	4 GBq
		^{52}Fe	200 MBq
		^{61}Cu	200 MBq
		^{133}Xe	300 MBq
		^{186}Re	600 MBq
		^{18}F	4 GBq
		^{127}Pr	3 MBq

2. Radioactive Waste Management

2.1 Solid wastes

Table 5 shows the amounts of solid wastes at various properties and kinds generated in each quarter of fiscal 1993. Main wastes were combustible matter such as gloves and incombustible filters for exhaust air. Compressible wastes were generated mainly by the cyclotron maintenance.

2.2 Liquid waste

Liquid waste was almost waste water ('inorganic' in Table 6) generated with chemical experiments and operation of air conditioning units installed in each room of the first class ratiation controlled area. Larger quantity of the waste water in summer season (2nd quarter) are mainly due to condensed drain from air by operating the units.

Low level waste water is treated by evaporation and condensed water is reused in the controlled area. Only small ammounts of residue are generated by the evaporation because the radiation level is very low and the waste quality is very pure so that the waste can be evaporated to high concentration rate.

The evaporation residue and sludge are solidified by cement in a stainless steel drum. The residue and sludge of ca. 100 liter makes one cement solidify of 200 liter drum.

Table 5. Radioactive solid wastes generated in fiscal 1993.

Items \ Amounts	Amounts of generation in each periods (m^3)					Number of package /drum
	1st quarter	2nd quarter	3rd quarter	4th quarter	total	
Low level	0.02	0.32	0.04	2.47	2.85	
1)Combustible	0.02	0.32	0.04	0.24	0.62	5*
2)Incombustible	0	0	0	2.23	2.23	
Compressible	0	0	0	0.06	0.06	1*
Filters	0	0	0	2.17	2.17	20
Imcompressible	0	0	0	0	0	
Ion exchange resin	0	0	0	0	0	
Cement solidify	0	0	0	0.20	0.20	2*
High level	0	0	0	0	0	0
1)Incombustible	0	0	0	0	0	0

*: 200 liter drum

Table 6. Radioactive liquid waste generated in fiscal 1993.

Items \ Amounts	Amounts of generation in each periods (m^3)					Number of package /drum
	1st quarter	2nd quarter	3rd quarter	4th quarter	total	
Low level	15.71	17.06	8.41	15.79	56.97	
1)Inorganic	15.71	16.92	8.41	15.69	56.73	treatment
2)Organic	0	0.14	0	0	0.14	carry over
Organic	0	0	0	0	0	0
Oil	0	0.14	0	0	0.14	carry over
3)Sludge	0	0	0	0.10	0.10	*
Medium level	0	0	0	0	0	
1)Inorganic	0	0	0	0	0	carry over
2)Organic	0	0	0	0	0	
Organic	0	0	0	0	0	
Oil	0	0	0	0	0	
3)Sludge	0	0	0	0	0	
Evaporation residue	0	0	0	0.10	0.10	*

*: treated to cement solidify

Appendix

Appendix 1. LIST OF PUBLICATIONS

A1.1. Publications in Journal

J01. T.Agematsu, S.Okumura and K.Arakawa
Uniform iradiation system using beam scanning method for cyclotron
JAERI-M **94-071** (1994).
C 9.3 31042

J02. M.Asano, M.Yoshida, M.Tamada, K.Arakawa, M.Fukuda, S.Okumura, T.Agematsu and H.Omichi
Irradiation appartus for preparation of ion track pore films
Radiation, **19** (1993) 19.
T 4.3 31024

J03. T.Chiba, A.Kawasuso, M.Hasegawa, M.Suezawa, T.Akahane and K.Sumino
Positron 2D-ACR study of divacancies in Si
Mat. Sci. Forum (in press)
O 6.6 31027

J04. T.Futagami, Y.Aoki, O.Yoda and S.Nagai
XPS and optical absorption studies on alpha-Al_2O_3 and MgO single crystals implanted with Cr, Cu and Kr ions.
Nucl. Instrum. Meth. B **88** (1994) 261.
O 6.10 off-line

J05. P.Goppelt-Langer, S.Yamamoto, Y.Aoki, H.Takeshita, H.Naramoto, M.Saido, J.Yagyu and N.Ogiwara
High resolution hydrogen measurements using HE-ERD
Nucl. Instrum. Meth. B,
submitted for publication.
T 6.1 32014

J06. M.Hasegawa, A.Kawasuso, T.Chiba, T.Akane, M.Suezawa, S.Yamaguchi and K.Sumino
Positron lifetime and 2D-ACR studies of divacancies in Si
Appl. Phys. (in press)
O 6.6 31027

J07. M.Hasegawa, M.Tabata, T.Miyamoto, M.Fujinami, H.Sunaga, S.Okada and S.Yamaguchi
Positron annihilation in neutron- and electron-irradiated silica glass
Sci. Rep. Res. Inst. Tohoku Univ. (RITU) **40a** (1994) 203.
O 6.6 31027

J08. M.Hasegawa, M.Tabata, T.Miyamoto, Y.Nagashima, T.Hyodo, M.Fujinami and S.Yamaguchi
Positron and positronium in free volume in oxides : silica glass and neutron-irradiated alumina
Mat. Sci. Forum (in press)
O 6.6 31027

J09. A.Kawasuso, M.Hasegawa, M.Suezawa and S.Yamaguchi
Studies of divacancy in Si using positron lifetime measurement
Hyperfine Int. **84** (1994) 397.
O 6.6 31027

J10. A.Kawasuso, M.Hasegawa, M.Suezawa, S.Yamaguchi and K.Sumino
Annealing study of defects induced by electron irradiation of Czechralski-grown Si using positron lifetime technique
Appl. Surf. Sci. (in press)
O 6.6 31027

J11. A.Kawasuso, M.Hasegawa, M.Suezawa, S.Yamaguchi and K.Sumino
Annealing process of vacancies in silicon induced by electron irradiation : Analysis using positron lifetime measurement
Mat. Sci. Forum (in press)
O 6.6 31027

J12. V.V.Krushev, H.Koizumi, T.Ichikawa, H.Yoshida, H.Shibata, S.Tagawa, and Y.Yoshida
Relation between track structure and LET effect on free radical formation for ion beam-irradiated alanine dosimeter
Radiat. Phy. Chem., **44** (1994) 521
O 3.4 31040

J13. H.Kudo, K.Shima, T.Ishihara, H.Takeshita, S.Yamamoto and H.Naramoto
High-energy shadowing effect and its application to atomic and solid stste physics.
Nucl. Instrum. Meth. **B90** (1994) 533.
T 6.5 32025

J14. A.Miyashita, T.Ohyanagi, O.Yoda and K.Murakami
Observation of the initial stage of the laser ablation
IONICS (J. Ion Sci. and Technology) **29**(8) (1994) 29 (in Japanese).
O 6.7 off-line

J15. Y.Nakamura, I.Ishibori, S.Okumura, T.Nara, W.Yokota, M.Fukuda, T.Agematsu, K.Arakawa, K.Mizuhashi, M.Sano, K.Hoshika, T.Satoh, T.Torii and H.Watanabe
Vacuum system for JAERI AVF Cyclotron
JAERI-M **94-007** (1994).
C 9.

J16. Y.Nakamura, W.Yokota, S.Okumura, M.Fukuda, T.Nara, T.Agematsu, I.Ishibori, K.Arakawa, K.Hoshika and T.Satoh
Power supply system for JAERI AVF cyclotron
JAERI-M **94-054** (1994).
C 9.

J17. H.Naramoto and C.W.White
Ion beam analysis on ion implanted insulators
Res. Report of the Institute of Electrical Engineers of Japan (1993) p.41 (in Japanese).
I,S,T 6.2 32015

J18. H.Naramoto, H.Takeshita, Y.Aoki, S.Yamamoto and P. Goppelt-Langer
Ion beam analysis of α-Al_2O_3 crystal implanted with vanadium ions
J. Appl. Phys.
submitted for publication.
I,S,T 6.2 32015

J19. M.Nishizawa and M.Inoue
Mutation induced by radiation in tobacco - Plant type and flower type -
Rep. Soc. Crop Sci. and Breed. in Kinki **39** (1994) 49.
C 2.7 31019/32011

J20. M.Nunogaki, T.Okada, H.Takeshita, Y.Aoki, S.Yamamoto and H.Naramoto
New material surface processing by means of preceding ion/electron and plasma process.
J. Nucl. Sci. and Technol.
(to be published).
T 5.8 32009

J21. T.Ohyanagi, A.Miyashita, K.Murakami and O.Yoda,
Time- and space-resolved X-ray absorption spectroscopy of laser-ablated Si particles
Jpn.J.Appl.Phys. **33** (1994) 2586.
O 6.7 off-line

J22. H.Kudo, K.Shima, T.Ishihara, H.Takeshita, Y.Aoki, S.Yamamoto and H.Naramoto
High-energy shadowing effect and its application to atomic and solid state physics
Nucl. Instrum. Meth. **B 90** (1993) 533.
T 6.5 32025

J23. T.Sekine, A.Osa, M.Koizumi, S.Ichikawa, M.Asai, H.Yamamoto and K.Kawade
Decay of the new isotope ^{127}Pr
Z. Phys. **A349** (1994) 143.
C 7.2 31035

J24. N.Shimatani, K.Kawatsura, S.Arai, T.Shiono, Y.Horino, Y.Mokuno, K.Fujii, H.Takeshita, S.Yamamoto, Y.Aoki and H.Naramoto
High energy Ni ion implantation and thermal annealing for α-SiC single crystal
Nucl. Instrum. Meth. **B 91** (1994) 529.
T 5.14 32026

A1.2. Publications in Proceedings

C01. K.Arakawa, Y.Nakamura, W.Yokota, M.Fukuda, T.Nara, T.Agematsu, S.Okumura and I.Ishibori
Status report on the JAERI AVF cyclotron.
Proc. of the 9th Symposium on Accelerator Science and Technology (Tsukuba, Aug. 25-27, 1993) p.202.
O 9.6/10.2

C02. T.Agematsu, K.Arakawa, S.Okumura, Y.Nakamura, W.Yokota, T.Nara, M.Fukuda and I.Ishibori
Development of visual beam adjustment method for cyclotron.
Proc. of the 9th Symposium on Accelerator Science and Technology (Tsukuba, Aug. 25-27, 1993) p.65.
O 9.3 31042

C03. T.Asakawa, M.Sasaki, M.Yoshimoto, S.Gonda, T.Shiraishi and H.Koinuma
Electrical properties of C_{60} and its partially decomposed thin films fabricated by vacuum evaporation and ion plating method.
Proc. of the Material Research Society, 1994 Spring Meeting (San Farncisco, Apr. 3-8, 1994)
O 5.11 32020

C04. M.Baba, T.Kiyosumi, T.Iwasaki, M.Yoshioka, S.Matsuyama, N.Hirakawa, T.Nakamura, Su.Tanaka, R.Tanaka, Sh.Tanaka, H.Nakashima and S.Meigo
Characterization and application of 20-90 MeV ^{7}Li(p,n) neutron source.
Proc. 1993 Nuclear Deta Symposium, JAERI-M 94-019 (1994) 200.
C 8.3 31048

C05. M.Baba, T.Kiyosumi, T.Iwasaki, M.Yoshioka, S.Matsuyama, N.Hirakawa, T.Nakamura, Su.Tanaka, R.Tanaka, Sh.Tanaka, H.Nakashima and S.Meigo
Characterization and application of 20-90 MeV ^{7}Li(p,n) neutron source at TIARA.
Proc. Int. Conf. on Nuclear Deta for Science and Technology (Gatlinburg, May 1994)
to be published from American Nuclear Society.
C 8.3 31048

C06. M.Fukuda, S.Okumura, K.Arakawa, Y.Nakamura, W.Yokota, T.Nara, T.Agematsu, I.Ishibori and T.Karasawa
RF phase studies of internal and external beams for JAERI AVF cyclotron.
Proc. of the 9th Symposium on Accelerator Science and Technology (Tsukuba, Aug. 25-27, 1993) p.306.
O 9.5

C07. P.Goppelt-Langer, J.P.Biersack, W.Bohne, D.Fink, B.Gebauer, M.Wilpert and Th.Wilpert
Materials analysis using high-energetic heavy ion beams.
Proc. of the 12th Symposium on Ion Beam Technology (Hosei Univ., Tokyo, 1993)
T 6.1 32014

C08. P.Goppelt-Langer, S.Yamamoto, H.Takeshita, Y.Aoki and H.Naramoto
High-energy elastic recoil detection -- Heavy ions for light element analysis --

JAERI Conf. (1994)
(to be published).
T 6.1 32014

C09. K.Harada
Resistant Mechanisms agaist heavy ion beam on radioresistant bacterium. (in Japanese)
Proc. of the 5th Radation Process Symposium (Osaka, Nov.24-25, 1993) p.28.
C 2.11 31023

C10. K.Harada, T.Nakano, R.Kimura, N.Mizuma and M.Saito
Effects of high LET radiation on radioresistant bacterium *Deinococcus radiodurans*. (in Japanese)
Proc. of the Scientific Meeting on the Research Reactor Institute, Kyoto University (Osaka, Feb. 8-9, 1994) p.81.
C 2.11 31023

C11. J.Isoya, H.Kanda and Y.Morita
ESR studies of point defects in synthetic diamond crystals.
Proc. of the 4th International Conference on the New Diamond Science and Technology (Kobe, July 1994) in press.
C 1.8 31025

C12. T.Kato, K.Tomizawa, Y.Takahashi, K.Kuriyama, H.Takeshita, S.Yamamoto and H.Naramoto
Electrical properties of carbon implanted semi-insulating GaAs.
Proc. of the 12th Symposium on Ion Beam Technology (Hosei Univ., Tokyo, Dec. 10-11, 1993) p.125.
T 5.13 32024

C13. H.Koizumi, T.Ichikawa and H.Yoshida
Linear energy transfer dependence of free radical formation in Ion-Irradiated Alanine.
Proc. of the Yayoi Symposium on Ion-Beam Radiation Chemistry (Chiba, Jan. 21, 1994) p.16.
C, O 3.4 31040

C14. Kuriyama, T.Kato, K.Tomizawa, Y.Takahashi, Y.Aoki, H.Takeshita, S.Yamamoto and H.Naramoto
Electrical activation process of C implanted semi-insulating GaAs.
9th International Conference on Ion Beam Modification of Materials Applications (Canberra, Feb. 1995) (to be published in Nucl. Instrum. Meth.)
T 5.13 32024

C15. A.Miyashita, T.Ohyanagi, O.Yoda and K.Murakami
Diagnosis of laser-ablated carbon particles measured by time-resolved X-ray absorption spectroscopy.
Proc. of the International Symposium on Advanced Nuclear Research (Mito, Mar.23-25, 1994) (to be published).
O 6.7 off-line

C16. N.T.My, Y.Aoki, H.Takeshita, S.Yamamoto, P.Goppelt-Langer and H.Naramoto
Ion beam induced luminescence and damage study on single- and poly-crystalline Al_2O_3 :Cr.
Proc. of 6th Japanese-Chinese Bilateral Symposium on Radiation Chemistry (Tokyo, Nov. 6-11, 1994).
O, S 5.9 32016

C17. T.Nakamura, Accelerator shielding research group
Shielding experiment with quasi-monoenergetic several tens MeV neutrons at 90 Mev AVF cyclotron facility, TIARA.
Proc. 1993 Nuclear Data Symposium, JAERI-M 94-019 (1994) 95.
C 8.5 31050

C18. N.Nakao, T.Nakamura, M.Takada, Sh.Tanaka, H.Nakashima, Y.Sakamoto, Y.Nakane, Su.Tanaka and K.Shin
Spectrometry of several tens MeV neutrons penetrated through concrete and iron shields using organic liquid scintillator.
Proc. 1993 Nuclear Data Symposium, JAERI-M 94-019 (1994) 183.
C 8.5 31050

C19. N.Nakao, T.Nakamura, M.Takada, Sh.Tanaka, H.Nakashima, Y.Sakamoto, Y.Nakane, Su.Tanaka, K.Shin, E.Tanabe, T.Shibata, Y.Uwamino and M.Baba
Spectrometry of several tens MeV neutrons penetrating shields using organic liquid scintillator at 90 Mev AVF cyclotron facility, TIARA.
Proc. of the 8th Int. Conf. on Radiation Shielding (1994) Vol.1, p.272.
C 8.5 31050

C20. T.Nara, W.Yokota, Y.Nakamura, M.Fukuda, T.Agematsu, S.Okumura, I.Ishibori and K.Arakawa,
Status of ECR ion source at JAERI.
Proc. of the 9th Symposium on Accelerator Science and Technology (Tsukuba, Aug. 25-27, 1993) p.89.
O 9.7

C21. H.Ohno, Y.Aoki and S.Nagai
Secondary ion mass spectrometry of thin carbon film growth on a low energy hydrocarbon ion beam deposition.

Proc. of The 36th Symposium on Radiation Chemistry (Tokyo, Oct. 1993) p.155.
O 6.9 off-line

C22. H.Ohno, Y.Aoki and S.Nagai
Thin film growth by low energy hydrocarbon ion deposition.
Proc. of The 4th Symposium on Beam Engeneering of Advanced Material Synthesis (Tokyo, Nov. 24-26, 1993) p.175
O 6.9 off-line

C23. T.Ohyanagi, A.Miyashita, K.Murakami and O.Yoda
Dynamic behaviors of laser-ablated Si particles.
Proc. of the International Symposium on Advanced Nuclear Research (Mito, Mar.23-25, 1994) (to be published).
O 6.8 off-line

C24. Y.Sakamoto, H.Nakashima, Y.Nakane, Sh.Tanaka, T.Nakamura, M.Baba, N.Nakao, Su.Tanaka and K.Shin
Shielding experiment with quasi-monoenergetic neutrons between 15 and 90 MeV at 90 Mev AVF cyclotron facility, TIARA.
Proc. of the 8th Int. Conf. on Radiation Shielding (1994) Vol.2, p.809.
C 8.5 31050

C25. S.Sasaki, A.Ushirokawa, Y.Morita and M.Tanaka
Investigation of solar cells for solar power satellite SPS 2000.
ISTS 94-e-29, 19th International Symposium on Space Technology and Science (Yokohama, May 1994)
C 1.5 31005

C26. S.Yamamoto, P.Goppelt-Langer, Y.Aoki, H.Takeshita, and H.Naramoto
Hydrogen analysis in Cu/Nb multilayers using ^{15}N ions
Spring Meeting, The Japan Institute of Metals (Tokyo, 1994) p.52 (in Japanese)
I,S,T 6.3 32017

C27. T.Yamashita, M.Inoue, A.Nakamura, H.Watanabe and A.Tanaka
Characters of interspecific hybrid between *Nicotiana gossei* Domin and *N.tabacum* L., using $^{4}He^{2+}$ beam-irradiated pollen.
Proc., 84th Meeting of the Japanese Society of Breeding (Tokyo, April 1994), Japn. J. Breed. **44**, Suppl. 1 (1994) 187.
T 2.7 31019/32011

C28. W.Yokota, Y.Saitoh, Y.Ishii, T.Nara and K.Arakawa
Designe of 18-GHz ion source at JAERI.
Proc. of the 11th International Workshop on Electron Cyclotron Resonance Ion Sources (Groningen, May 6-7, 1993) p.245
O 9.7

C29. W.Yokota, Y.Saitoh, Y.Ishii, T.Nara and K.Arakawa
Designe of JAERI 18-GHz ECR ion source.
Proc. of the 9th Symposium on Accelerator Science and Technology (Tsukuba, Aug. 25-27, 1993) p.92.
O 9.7

Appendix 2. Type of Research Collaborations

Section of this Report	Research Program Number	Type of Research Collaborations*
1.1	31008	(JAERI)
1.2	31007	(JAERI)
1.3	31009	Joint Research
1.4	32001	(JAERI)
1.5	31005	Joint Research
1.6	31004	Joint Research
1.7	31006	Coop.Res.Univ. /Joint Research
1.8	31025	(JAERI)
2.1	32010	Joint Research
2.2	31014	Joint Research
2.3	31015	(JAERI)
2.4	31016	(JAERI)
2.5	31017	Coop.Res.Univ.
2.6	31018	Coop.Res.Univ.
2.7	31019/32011	Coop.Res.Univ.
2.8	31020	Coop.Res.Univ.
2.9	31021/32012	Coll.Proj.Res.
2.10	31022/32013	Coll.Proj.Res.
2.11	31023	Coll.Proj.Res.
2.12	31051	Joint Research
2.13	31052	Coop.Res.Univ.
3.1	31037	Coll.Proj.Res.
3.2	31038	Coll.Proj.Res.
3.3	31039	Coll.Proj.Res.
3.4	31040	Coll.Proj.Res.
3.5	31041	(JAERI)
3.6	31045	(JAERI)
4.1	31001	(JAERI)
4.2	31002	Joint Research
4.3	31029	Coop.Res.Univ. /Joint Research
4.4	(off-line)	Coop.Res.Univ.
5.1	32018	(JAERI)
5.2	31011	(JAERI)
5.3	31010	(JAERI)
5.4	31026	(JAERI)
5.5	32002 ~ 4	(JAERI)
5.6	32005 ~ 6	(JAERI)
5.7	32007	Coop.Res.Univ.
5.8	32009	Coop.Res.Univ.
5.9	32016	(JAERI)
5.10	32020	Coop.Res.Univ.
5.11	32022	Coop.Res.Univ.
5.12	32023	Coop.Res.Univ.
5.13	32024	Coop.Res.Univ.
5.14	32026	Coop.Res.Univ.
5.15	32026	Coop.Res.Univ.
5.16	32027	Coop.Res.Univ.
6.1	32014	(JAERI)
6.2	32015	(JAERI)
6.3	32017	(JAERI)
6.4	32021	Coop.Res.Univ.
6.5	32025	Coop.Res.Univ.
6.6	31027	Coop.Res.Univ.
6.7	(off-line)	(JAERI)
6.8	(off-line)	(JAERI)
6.9	(off-line)	(JAERI)
6.10	(off-line)	(JAERI)
7.1	31030	(JAERI)
7.2	31035	(JAERI)
7.3	31036	Coll.Proj.Res.
7.4	31036	Coll.Proj.Res.
7.5	32029	(JAERI)
8.1	31046	Coll.Proj.Res.
8.2	31047	Coll.Proj.Res.
8.3	31048	Coll.Proj.Res.
8.4	31049	Coll.Proj.Res.
8.5	32050	Coll.Proj.Res.
9.1	32031	(JAERI)
9.2	32032	(JAERI)
9.3	31042	Joint Research
9.4	31043	(JAERI)
9.5 ~ 9.13	—	(JAERI)
10.1 ~ 10.4	—	(JAERI)

* Joint Research : Joint research with private company or governmental institution

Coop.Res.Univ. : Cooperative research with university

Coll.Proj.Res. : The JAERI-universities collaborative project research program

Appendix 3. Organization and Personnel of TIARA (Fiscal 1993)

1) Organization for the Research and Development of Advanced Radiation Technology

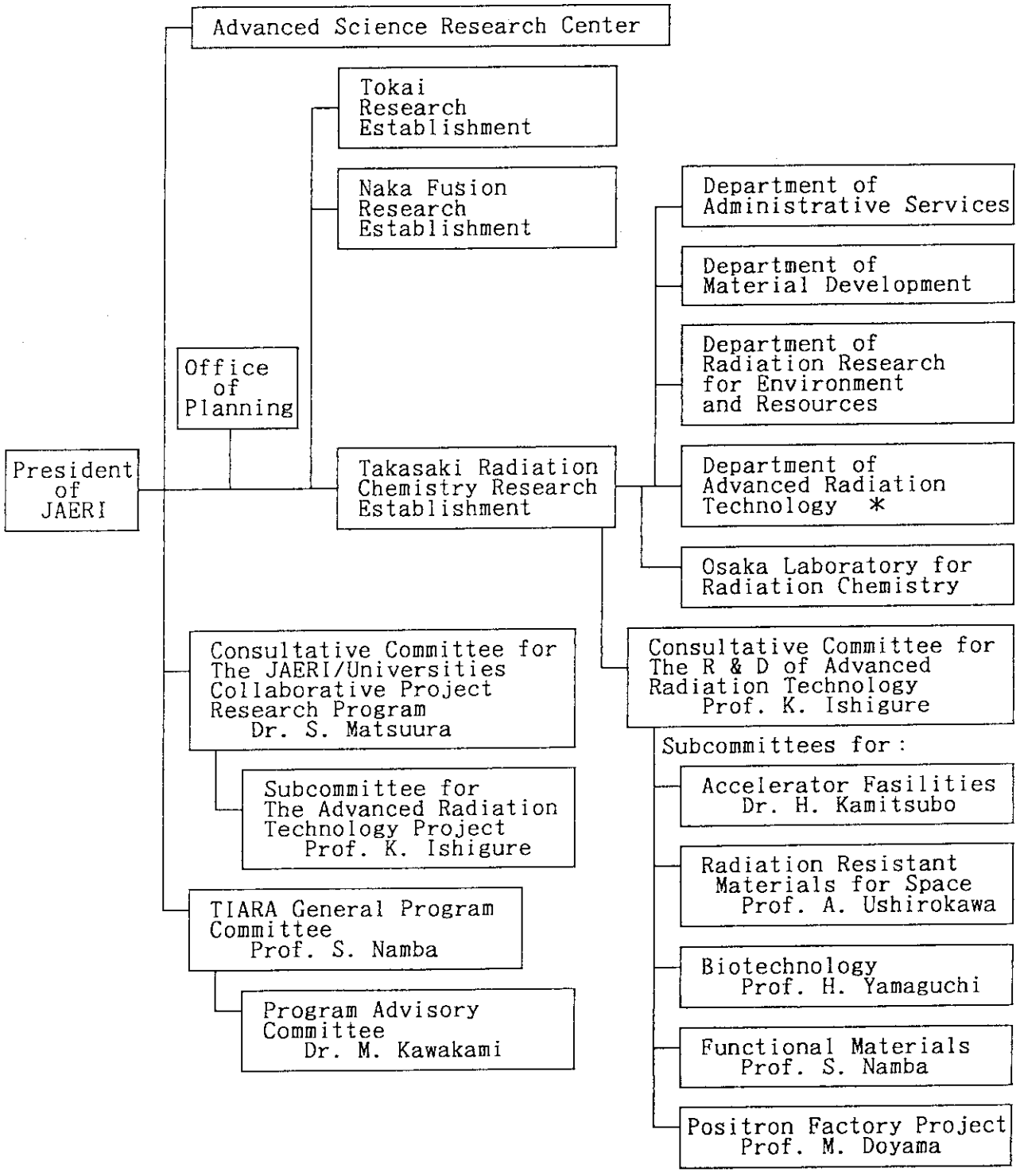

* reorganized to 'Advanced Radiation Technology Center' from fiscal 1994.

2) Administration and Operation of TIARA *

Department of Advanced Radiation Technology

Director	I. Ishigaki	
Deputy Director	R. Tanaka	
Administrative Manager	E. Yamashita	
Staff Member	H. Ehara,	T. Suzuki

Ion Beam Research Administration Division

General Manager	H. Watanabe	
Staff Member	S. Tanaka,	K. Nishimura,
	M. Hosono	

Ion Accelerator Operation Division

General Manager	T. Sasuga	
Staff Member	H. Tachibana	

Group of Cyclotron Operation

Staff Member	K. Arakawa,	Y. Nakamura,
	T. Nara,	T. Agematsu,
	I. Ishibori	

Group of Electrostaic Accelerators Operation

Staff Member	S. Tajima,	I. Takada,
	K. Mizuhashi,	S. Uno,
	K. Ohgoshi	

Ion Beam Engineering Division

General Manager	(R. Tanaka)	
Staff Member	T. Kamiya,	W. Yokota,
	M. Fukuda,	S. Okumura,
	Y. Saito,	Y. Ishii,
	T. Suda	

2) Radiation Monitoring and Control at TIARA

Department of Administrative Services

Safety Division

Staff Member	Y. Iwaya,	K. Sato

3) Radioactive Wast Treatment and Disposal at TIARA

Utilities and Maintenance Division

Staff Member	J. Yoshii,	K. Fukuda

---

* for information, contact to : —
Advanced Radiation Technology Center, Takasaki Radiation Chemistry Reasrch Establishment, Japan Atomic Energy Research Institute
1233 Wakanuki-machi, Takasaki, Gunma-ken, 370-12, Japan.
Tel. : (81)273-46-9600 ~3 ; Facsimile : (81)273-46-9690